



UNIVERSIDAD NACIONAL DE COLOMBIA

A statistical model of fracture due to drying in Bamboo *Guadua angustifolia*

Gabriel Villalobos Camargo

Universidad Nacional de Colombia
Facultad de Ciencias, Departamento de Física
Bogotá, Colombia
2012

A statistical model of fracture due to drying in Bamboo *Guadua angustifolia*

Gabriel Villalobos Camargo

Tesis presentada como requisito parcial para optar al título de:
Doctor en Ciencias Físicas

Director:

Dr. Rer. Nat. José Daniel Muñoz Castaño

Línea de Investigación:

Mecánica Estadística

Grupo de Investigación:

Grupo de simulación de sistemas físicos

Universidad Nacional de Colombia
Facultad de Ciencias, Departamento de Física
Bogotá, Colombia

2012

Dedicada a mi esposa, Andrea Franco,
que hizo lo más bello y generoso,
hacer de mis sueños nuestros sueños,
con quien los días bonitos son hermosos,
y es mi apoyo en los momentos oscuros.

Agradecimientos

Quisiera hacer una mención especial a varias personas muy especiales, cuya ayuda mejoró ostensiblemente la calidad de esta tesis, pues apoyaron con su sabiduría y agudeza acerca de este extenso campo. Primero que todo, al profesor José Daniel Muñoz, mi director, que me introdujo al campo de la Mecánica Estadística aplicada y cuyas ideas me ayudaron a dar forma al camino que es este viaje. La colaboración de los profesores Hans Herrmann, Ferenc Kun, Dorian Linero y Jorge Montoya, quienes ofrecieron un punto de vista experto de diversos temas que fortalecieron la visión y la amplitud de esta investigación. También fue un placer tener enriquecedoras discusiones con el Dr. Nuno Araujo y el Dr. Falk Wittel, quienes aportaron la perspectiva desde su experiencia y conocimiento. Los profesores Lucilla de Arcangelis, Arcesio Lizcano, Walter Liese, Peter Niemz, Richard Murphy y Caori Takeuchi proveyeron valiosos consejos sobre detalles específicos, pero complejos.

Algunos estudiantes, técnicos y amigos me dieron apoyo técnico invaluable, preguntas interesantes y apoyo en los momentos difíciles. Quisiera mencionar especialmente a Camilo Aponte, Carlos Córdoba, Frederic Eberts, Sergio Galindo, Philipp Hass, Gergely Kocsis, Luiz López, Miller Mendoza, William Oquendo, Karla Peña, Melissa Rusinque, Thomas Schneider, Julian Shrenk y Gábor Tímár. En general a los compañeros del grupo de simulación de sistemas físicos y a algunos más, que puedo haber olvidado en este momento.

He sido afortunado de tener el apoyo económico e institucional del pueblo Colombiano, a través de la Universidad Nacional de Colombia y Colciencias. Instituciones externas también apoyaron esta investigación como el ETH-Zurich, el Jardín Botánico de Zurich, la Universidad de Pereira y la Universidad de Debrecen.

No menos importante, ha sido el apoyo de mi familia. Primero, mi mamá Elena que confió en sacar esto adelante, y mi hermano Carlos Fernando. A mi papá, cuyo ejemplo siempre llevo presente al tomar todas las decisiones. Una mención muy especial para Guillermo, Graciela y Marcela, quienes siempre nos dieron su apoyo incondicional. A Lunita, que siempre me recordó que es lo más importante. Y finalmente, el amor y sacrificio de mi esposa Andrea, quien ha estado conmigo en las situaciones maravillosas tanto como en las incomprensibles.

Resumen

El presente trabajo propone y analiza modelos estadísticos de fractura inspirados en la geometría y en los mecanismos de secado del tejido parenquimatoso de *Guadua angustifolia*, un bambú andino que es usado ampliamente en las industrias de la construcción y las artesanías. Los modelos propuestos son dos-dimensionales, y su geometría es similar a aquella de un corte perpendicular al culmo de la guadua; la dirección en la que las deformaciones tienen lugar. Un primer conjunto de modelos propuestos analizan el primer estado del secado, en el que las células se hallan saturadas con agua (llamada *agua libre*) y un frente capilar avanza de célula a célula. Un segundo conjunto de modelos se usa para investigar las fracturas inducidas en la segunda etapa del secado, cuando el agua (llamada *agua ligada*) dentro de las paredes celulares mismas se evapora; las fracturas dependen entonces del secado uniforme. Los modelos numéricos muestran que el proceso de fractura inducido por capilaridad se puede modelar como percolación invasiva, con un frente de secado moviéndose de célula a célula; con dimensión fractal del cluster de células secas en el momento de percolación tiene el valor de $91/48 \approx 1.896$. En el proceso de fractura inducido por la contracción muestra una transición de fase bien definida, en la cual la cantidad de desorden estructural es el parámetro de orden: a valores bajos del desorden, el proceso de fractura es dominado por una fractura macroscópica que aparece al comienzo, mientras que para valores más altos del desorden, el proceso de fractura procede en pequeñas fracturas que eventualmente se fusionan generando la ruptura en el sistema. En el valor de la transición, la distribución de tamaños de avalanchas es una ley de potencias cuyo exponente es -2.6 ± 0.08 , en total concordancia con el valor de campo medio de $5/2$ del modelo de haces de fibras. Más aún, un análisis de escalamiento finito provee un colapso de los diferentes datos en una única forma funcional para el tamaño promedio de la avalancha $\langle \Delta_{max} \rangle$, identificándolo como parámetro de orden, con valores de $\beta/\nu = 1.4$ y $1/\nu \simeq 1.0$, y el promedio de la tasa $\left\langle \frac{m_2}{m_1} \right\rangle$ del segundo y primer momentos m_2 y m_1 de la distribución de tamaños de avalancha, muestra comportamiento similar a aquel de la susceptibilidad de una transición de fase continua, con $\gamma/\nu = 1.$, $1/\nu \simeq 0.9$. Estos resultados sugieren que la transición de fase inducida por el desorden en el proceso de rompimiento de la lámina, corresponde a una nueva transición de fase cuyos exponentes críticos caracterizan probablemente una nueva clase de universalidad. Este resultado puede tener implicaciones profundas en la comprensión de las fracturas debidas al secado en películas delgadas, como es el caso de superficies con pintura, capas delgadas de madera, filmes uv y anti reflectivos en los procesos de

manufactura de vidrios y de películas delgadas, y es consistente con el hecho de que los materiales exhiben una estructura desordenada son más resistentes que aquellos con una regular. Los estudios numéricos presentados aquí se complementaron con mediciones experimentales que soportan la hipótesis que propone que el encogimiento es la principal causa del proceso de fractura del bambú. Los resultados obtenidos de los modelos propuestos proveen una percepción aguda en los procesos estadísticos de secado, con implicaciones que pueden ir hasta el campo de la ciencia de materiales. Constituye, entonces una contribución valiosa y original al campo de los modelos estadísticos de fractura.

Palabras clave:

Modelos estadísticos de Fractura, bambú *Guadua angustifolia*, método de los elementos discretos, modelos de elementos finitos, transiciones de fase, escalamiento finito, fractura.

Abstract

This work proposes and analyzes statistical models of fracture inspired in the geometry and drying mechanisms of the parenchymatous tissue of *Guadua angustifolia*, an Andean bamboo widely used in the construction and handicraft industries. The proposed models are two-dimensional, resembling the geometry of the tissue in a plane perpendicular to the culm, where most deformations take place. A first set of models is proposed to analyze the first stage of drying, when all cells are saturated with water (called *free water*) and a capillary front advances from cell to cell. A second set of models are used to investigate the fractures induced in the second drying stage, when the water (called *bond water*) inside the cell walls themselves evaporates and the fractures are driven by a uniform shrinkage. Our numerical studies show that the fracture process induced by capillarity can be well modeled by invasion percolation, with a drying front moving from cell to cell and a fractal dimension of $91/48 \approx 1.896$ for the cluster of empty cells at percolation. In contrast, the fracture process induced by shrinkage shows a well-defined phase transition, with the amount of structural disorder as control parameter: At low disorders, the breaking process is dominated by a macroscopic crack at the beginning, while at high disorders the fracturing proceeds in small-sized micro-cracks which eventually merge and break the layer. At the transition, the avalanche size distribution becomes a power law with exponent -2.6 ± 0.08 , in agreement with the mean-field value $5/2$ of the fiber bundle model. Moreover, good quality data collapse from the finite-size scaling analysis show that the average value of the largest burst $\langle \Delta_{max} \rangle$ can be identified as the order parameter, with $\beta/\nu = 1.4$ and $1/\nu \simeq 1.0$, and that the average ratio $\left\langle \frac{m_2}{m_1} \right\rangle$ of the second m_2 and first moments m_1 of the avalanche size distribution shows similar behavior to that of the susceptibility of a continuous transition, with $\gamma/\nu = 1.$, $1/\nu \simeq 0.9$. These results suggest that the disorder induced transition of the breakup of thin layers corresponds to a novel continuous phase transition, with critical exponents characterizing probably a new universality class. This remarkable outcome can have deep implications in the understanding of drying-induced fractures of thin films, like painted surfaces, thin wood layers, anti reflective and UV-protecting coatings on glasses and thin-film manufacturing processes, and is consistent with the fact that materials exhibiting a disordered structure are often more resistant than others with a regular one. This numerical studies are complemented with experimental measurements supporting the hypothesis that proposes the shrinkage as the main fracture process in Bamboo. The proposed models' results provide great insight into the statistical physics of drying, with impli-

cations that may go far into the field of materials sciences. It constitutes, therefore, a valuable and original contribution to the field of statistical models of fracture.

Keywords:

Statistical models of fracture, bamboo *Guadua angustifolia*, discrete element method, finite element model, phase transitions, finite size scaling, fracture.

Contents

Contents	5
List of Figures	8
1 Introduction	20
1.1 Guadua and fracture	20
1.2 Statistical models of fracture	23
1.3 This work	25
2 Bamboo and drying	29
2.1 Guadua physiology	30
2.1.1 Vascular bundles	33
2.1.2 Fibers	35
2.1.3 The parenchyma cell	38
2.2 Engineering of drying in wood and bamboo	42
2.2.1 Continuum models	43
2.2.2 Guadua, experimental drying and mechanical characteristics	46
2.3 The physics of drying	48
2.3.1 Chemical potential	48
2.3.2 Capillarity	50
2.3.3 Drying dynamics	52
2.4 Drying effects on the bamboo tissues	54
2.4.1 Plasmolysis	54
2.4.2 Drying and cell collapse	55
3 Fracture, critical phenomena and statistical models of fracture	57
3.1 Elasticity	57
3.2 Fracture	61
3.2.1 Continuum applied mechanics	62
3.2.2 Analytical models of fracture	63

3.3	Critical Phenomena	64
3.3.1	Fluid system	64
3.3.2	Ising model phase transition	65
3.3.3	Universality and critical exponents	66
3.3.4	Percolation	67
3.3.5	Finite size scaling	69
3.4	Statistical models of fracture	70
3.4.1	Fiber Bundle Models	70
3.4.2	Random Fuse Networks	76
3.4.3	Beam models	79
3.4.4	Crackling noise	81
3.4.5	Applications of Finite size scaling	82
4	Simulation methods	88
4.1	Computational models and object oriented programing	89
4.2	The discrete element method	89
4.2.1	Basic elements of DEM	91
4.2.2	Sphero-polygons	92
4.2.3	Sphero-polygons for the simulation of fractures due to capillary forces . .	96
4.3	The finite element method	97
4.3.1	Elasticity FEM problem formulations	98
4.3.2	Strain-displacement equations	99
4.3.3	The plane frame element, PFE	100
4.3.4	Voronoi construction: gathering of guadua structure and random lattice generation	101
4.4	Pore network models	103
4.4.1	General description	104
4.4.2	Physical evidence of “drying rules”	104
5	Capillary pressure statistical mechanics model	107
5.1	Honeycomb lattice non-trapping invasion percolation	107
5.2	Dynamic Model	110
5.2.1	Model Description	110
5.2.2	Fracture statistics for different drying dynamics and disorder distributions	115
5.2.3	Crack sizes and system spanning fractures	120
5.3	Analysis	121
6	A statistical model of fracture due to shrinkage, the Cell Network Model of fracture	122
6.1	The Model	122
6.1.1	Homogeneous model, Hexagonal geometry	125
6.1.2	Inhomogeneous model, Voronoi Geometry	125
6.1.3	Distributions of breaking thresholds	125
6.2	Evolution	127

6.3	Breakup process	128
6.3.1	Avalanche dynamics	128
6.3.2	Distributions of humidity decrement between consecutive avalanches . .	130
6.3.3	Fraction of remaining junctures	131
6.4	Damage	133
7	A theoretical statistical model of fracture due to shrinkage	136
7.1	Introduction	136
7.2	Model construction	137
7.3	Breakup Process	139
7.4	Avalanche dynamics	142
7.5	Discussion	146
8	Experimental evidence of avalanches of breakings during Bamboo drying	150
8.1	Moisture content	151
8.2	Acoustic emission measurements	151
8.3	Microscopy measurements	155
9	Conclusions	157
	Bibliography	164
	A Numerical constants	176
	B Publications	179
	Index	187

List of Figures

1.1	Two constructions by Simón Vélez, Architect. Guadua culms were used as the construction structural material. (Left) “Puente en la China” (Bridge in china).[Vél]. (Right) , 2009 Simón Vélez, Principal Prince Claus Award in the Netherlands [Kra11].	20
1.2	A picture of the parenchyma tissue of guadua, from [LVV ⁺ 03].	22
1.3	(Left) Geometry of the fracture model. The cell walls, green, are modeled as beams that go between the junctions, red. (Right) Pore network model for drying dynamics. The cells are joined together by pores, whose widths distribute randomly. At any drying stage, there will be some cells filled and some will be empty.	26
2.1	A bamboo forest near Milan, Italy.	29
2.2	(Left) Internode structure of bamboo (a) the culm, including the longitudinal axis z commonly used in wood studies; (b) vertical section, showing the hollow interior and the culm wall; (c) the node (d) cross section, showing also the radial and tangential directions r , t . (modified from a sketch in [Jan81]). (Right-up) Bamboo culms, the red square marks the culm wall. (Right-down) A section of the culm-wall of Guadua bamboo, the dark spots correspond to the fiber sheaths, the light material to the parenchyma tissue. .	30
2.3	(Left) A cut of a young culm wall of Guadua Angustifolia [LVV ⁺ 03]. Fiber sheaths corresponding of xylem and phloem are covered by brown fibers. The dark green cells around them correspond to young fibers not yet lignified, the light green cells further away correspond to the parenchymatous cells. (Right up)Three dimensional view of culm tissue with vascular bundles embedded in ground parenchyma in <i>Oxytenathera abyssinica</i> , from [Lie98] (Right down)Two metaxylem vessels in a bamboo with separating rim and adjoining parenchyma cells, from [Lie98]	31
2.4	(Left) Zoom of the fiber bundle of Guadua, transverse cut. From [LVV ⁺ 03] (Center) Vascular bundle of the bamboo species <i>Gigantocloa levis</i> , showing the fiber caps (1), metaxylem (Mx), Phloem (Ph),protoxylem (Px), and free fiber strands (2). [LVAG06] (Right) A cross section of a vascular bundle of bamboo [Xu10]	32
2.5	(Left) Fiber Bundle. (Right) Structure of the fibers and the microfibers of bamboo, from [FTDG ⁺ 11]	32
2.6	(Right) Schematics of water flow. [Coc06]	34

2.7	(Left) Vascular bundles per area, as function of internode number, either at the inner or outer side of the culm wall [ON09] . (Center)Volume fraction of fibers, as function of radial coordinate, for different node numbers [Ama97] . (Right) Bamboo fiber sheaths are composed of conducting tissue, and fibers. This is a snapshot of both a small and a big bamboo fibers, and a parenchyma cell. The length of the black vertical line in the lower left corner is 100 μm , [Lie98]	35
2.8	(Left) Thickening of bamboo culm cell wall, from [GKM04]. A), Elongating culm (less than 6 months old), B) Young culm (1 year old), C) Mature Culm (3 years old). (Center)Poly-laminate structure of the thick-walled bamboo fiber. Fibril angle at the left, notation of wall lamella at the right [Lie98]. (Rigth) Micro-fibril distribution [YJHS08]	36
2.9	Chemical composition of bamboo, from [Li04]. The hollo-cellulose column contains both α -cellulose and hemicellulose. Some alcohol toluene solubles may also be hot water solubles. Furthermore each column has to be calculated from different samples, since the procedures to collect them are destructive. Finally, the authors do not report error bars.	37
2.10	Tissue development observed with either polarized light (A,C,E,G,I) or phloroglucinol-HCl staining (B,D,F,H,J) for <i>Dendrocalamus asper</i> , [GM05]. Scale bars, 200 μm <i>Up</i> : Lignification starts in the fiber surrounding vascular tissues, and continue in the inward direction. <i>Down</i> : The increase in birefringence, with cell evolution is linked with the presence of secondary cell walls.	37
2.11	The plant cell. [Nob09]	38
2.12	Parenchyma consisting of both elongated and cube shaped cells. The horizontal axis is along the bamboo axis (z direction) and the vertical axis in the radial direction, for a sample of 270 $\mu m \times 180 \mu m$. From this picture we estimated the parenchyma cell wall width as $4 \pm 0.6 \mu m$, the cell width as $30 \pm 0.8 \mu m$ -same as the depth for cube shaped cells- and a depth of $108 \pm 0.6 \mu m$ for elongated cells. Picture from [Lie98]	39
2.13	(Left) Turgor pressure, from [JM00]. (Right) Tricellular junction with inter cellular space [WB07]	39
2.14	(Left)Nanoindentation load displacement curve for the fiber cells of <i>Phyllostachys edulis</i> , from [ZJLL09] (Right) Cane cross section during drying. (A) dried at 20 C and 65% relative humidity for 2h. (B) Dried for 4 h. The bar corresponds to 200 μm . Arrow, radial direction [OKY07]. (Right) Detachment of a hemicellulose loop when two cellulose fibrils to which it is attached are separated by a local tensile component, from [AJ08] . .	40
2.15	(Left) Unaspirated bordered pit in a sapwood tracheid. Inside diameter, 18 μm , torus diameter 9 μm , openings 1 μm in the tangential direction and up to 2 μm in the radial direction. [Sia84] (Right)Pit pairs, (a) simple. (b) bordered pits, commonly between two prosenchyma cells, (c) half bordered pit, commonly between parenchyma and prosenchyma cells. [Sia84]	41
2.16	Drying process in porous media, from [Whi77]	43

2.17	(Left) Moisture content (with 1 corresponding to 100%) for a drying half-slab of wood of $2\text{ cm} \times 1\text{ cm}$ dimensions, as a function of thickness. Different curves correspond to different drying times (0.5 h, 1h, 2h, 4h, 6h, 8h, 10h 12h, 14h and 15h respectively from higher moisture content towards lower). The external temperature is set at a constant value of 60 Celsius. (Right) Central plane moisture content temperature field evolution, bottom up corresponding to 0h, 2h, 4h, 6h, 8h, 10h and 15h respectively. Taken from [PT02].	44
2.18	Isotherm curves for mosa bamboo, for various internode samples [ON09]	46
2.19	(Left) Flexural breaking test, from [GMABS07]. (Right) Construction of the test probes, [MAGBS07].	47
2.20	The bamboo culm mechanical properties vary both on the height of the culm and on the radial direction. [YJHS08]	48
2.21	(Left) Laplace overpressure inside an spherical droplet. (Center) Laplace force per unit length $\vec{\gamma}$. (Right) Determination of the contact angle θ_E [GBWQ04]	50
2.22	Advancing angle when the drop is inflated, receding angle when the drop is deflated, from [GBWQ04]	51
2.23	Free water evaporation from wood. (a) The surface tension on the air-water interface is interpreted as a force per unit length. (b) - (c) Siau, [Sia84], argues that the surface tension magnitude changes when the water evaporates: goes from an initial value in (b), increases to a maximum when the surface has the curvature equal to the inverse of the pore width; and then is reduced again, when the radius is larger. Notice that as the Laplace's pressure accounts for the difference between the liquid and the air, the arrows that are depicted in the horizontal walls and the lower one would not be present in a saturated porous medium. (e) - (g). This implies that widest pores dry first, including bubbles inside the system, as smaller pores "pump out" water from wider ones. (h) - (i) This may cause the wood to contract.	53
2.24	(Left) Position of plasma membrane during plasmolysis, from [Nob09]. (Right) Höfler diagram. Shows the relationship between the water potential ψ^i , the hydrostatic pressure P^i , and the osmotic pressure Π^i in a plant cell for various protoplast volumes, from [Nob09].	54
2.25	(Left) Cross section of a cane during drying, dried at 20 C and 65% relative humidity for (A) 2 hours, (B) 4 hours, from [OGT04]. The arrow indicates the radial direction. (Center) Change in relative thickness of cane during drying as function of moisture content, from [OGT04]. (Right) Drying induced fractures, as seen by confocal laser [SMO09] . .	55
3.1	Young's experiment	58
3.2	Constitutive law for (a) ideal plasticity. The yield point is marked as F_n . After it has been reached the young modulus is preserved, but some deformation d is no longer revertible. (b) a mild steel. From [Her91]	59
3.3	Convention for defining $\sigma_{\alpha\beta}$, from [Her91]	60
3.4	Schematic representation of the study of fracture on different length scales. From [HR90]	61

3.5	Fracture modes, from [ANZ06].	62
3.6	(Left) a)Fluid. Projection of the PVT surface on the PT plane, b) Magnet. Projection of the HMT surface on the HT plane. (Right) Isothermal cross sections of the PVT surface. The exponent δ is a measure of the degree of the critical isotherm.[Sta87]	65
3.7	Liquid-gas coexistence curve for many fluids become identical when the axes are rescaled with the critical values of density and temperature [Gug45].	67
3.8	The conductance of each bond is a randomly distributed variable. From [HR90]	68
3.9	Sketch of phase diagram for a real gas. The point marked “C” is the critical point, from [HR90]	68
3.10	(Left) A Fiber bundle, consisting in N horizontal fibers clamped at an end and subject to a loading parallel to the fibers on the other. All the fibers have the same elastic constant E , but may have a different strength $\sigma_{i,max}$, as this variable is drawn from a probability distribution. Initially, each fiber is subject to the same fraction of the total force, F/N which can be larger than $\sigma_{i,max}$ for some fibers which have to be taken out of the simulation. A steady state occurs when the load felt by every fiber is below its strength, causing a global displacement of the bundle of magnitude x . (Right) Force as a function of displacement for a FBM. The red curve corresponds to a case in which displacement is controlled, then each time a fiber is broken there is a drop on the load felt by the system. In the case that force is controlled, the system follows the red line until a drop. Then the load is maintained at this fixed value (black line) until the load is increased above this local threshold. [PHC10].	71
3.11	Macroscopic constitutive behavior for a fiber bundle with GLS [KRHH06]	72
3.12	Distribution D of burst sizes Δ obtained in a computer simulation of 10^7 fibers. A line of slope of -0.5 is plotted to guide the eye. [KRHH06]	73
3.13	Constitutive behavior of the model, with annealed disorder without residual stiffness at $a = 0.8$, for different k_{max} , from [KRHH06].	74
3.14	Avalanche size distributions for different values of k_{max} and a when fibers have remaining stiffness and annealed disorder. $N = 1600$ fibers, averages made over 2000 samples. Vertical axis $D\Delta$ is the number of avalanches of size Δ , from [KRHH06].	75
3.15	Phase diagram for the continuous damage model with remaining stiffness for both types of disorder, from [KRHH06].	76
3.16	Characteristic timescales t_r and t_f of the fiber bundle model for the Basquin’s law system. Below a certain σ_l the deformation of the system converges to a limit with a characteristic relaxation time t_r . Above it, there is a lifetime of the system t_f . From [KCAH08]	77
3.17	(left) Random fuse network. The lattice is tilted at 45° from the bus bars [HR90]. (Right) Current response of an Ohmic resistor, [BC06].	77
3.18	Burst size distribution on the random fuse model, from [PHH05].	79
3.19	From [Her91]	79

3.20	(Left) space of disorder magnets, renormalization picture. The scale free system sits in a fixed point, i.e., maps to itself through renormalization. At its left and right large “infinite” avalanche systems or small avalanche systems are located. (Middle) structure of the avalanche of Sethna’s model. (Right) Values of the different exponents that characterize the fracture for sethna’s model. From[SDM01]	81
3.21	Scaling of avalanche shapes. (Left) Voltage pulse, proportional to the number of domains flipped, as a function of time during a single large avalanche. (Center) Average avalanche shapes for different durations for sethna’s model. (Right) Experimental data of magnet crackling voltage. [SDM01]	82
3.22	(Left) Thin crack, with length $2a$ subject to stress σ_0 .(Right) Scaling plot m vs γ for different system sizes L . Data collapse for $x = 0.089$. [VAH08]	83
3.23	Rescaled plot of mass distributions of various pressure values. The dashed line indicates the fitted power law with exponent $\tau = 1.55 \pm 0.03$ [HWK06].	84
3.24	Fragmentation of spheres. (Left) Front view of reconstructed spheres, showing the fragments with different colors, for different initial speeds. (Right) Mass of the largest and the second largest fragment and average fragment mass as function of impact velocity. From [CWKH08].	85
4.1	Collection of bodies, discretization into finite elements, changing configurations and possible fragmentation [SdBH04]	90
4.2	Regularized smooth treatment of a contact [SdBH04]	92
4.3	(Left) An sphero-cow, constructed by means of smoothing out a polygon based on straight lines (black lines, at the left), to get a smoothen out blue cow. [AM08] (Right) Opening, sphero-polygon construction. Upper panel shows the effect of erosion, the initial set defined by the interior of the black square gets reduced to that of the red square. The middle panel shows the effect of dilation, an initial black square gets augmented to the red sphero-polygon with rounded edges. To obtain and sphero-polygon which is a subset of the initial one, the opening has to be constructed by applying first erosion and then dilation, as shown in the last panel.	93
4.4	(Left) Four different snapshots of the simulation of a Minkowski cow bounding on a simple landscape. (Right) Up, normalized linear kinetic energy and rotational energy of a “gas” of 400 Minkowski cows confined to a rectangular box, which settles to average values. The horizontal lines correspond to the expected values from statistical mechanics. Down, normalized energy distribution of the particles, the line corresponds to the Maxwell-Boltzmann distribution. [AM08]	95
4.5	Simulation of the motion of grains in a silo, for two shapes of grains. (Left)(Center-Left) For circular grains a change in the opening of the silo only changes the flow of particles; (Center Right)(Right) instead, for the complex shaped grains a change of the opening can cause jamming- or an arc inside of the sample. [AM08]	95
4.6	The regular lattice used for the model of [Chapter. 5].(Left) Red and Blue numbers, the coordinates in the lattice; Green, neighboring cells; aquamarine, numbering of the cell walls. (Right) Neighbours of a cell wall, in magenta; Junctures, in yellow; Wall node numbers, in green.	96

4.7	Collision Vertex-Edge between two walls. The distance d , in magenta, corresponds to the overlapping.	96
4.8	The deformation field and the shapes of the elements for a problem of orthotropic elasticity in 2D by means of PEFiCA (an open code finite element implementation, written by Prof. Dorian Luis Linero, [Lin09])	98
4.9	(Left) A plane frame Element, showing the nodal displacements. The angle θ describes the orientation of the element. (Right) Each of the nodes and their local displacements, the overline coordinates correspond to the element coordinates.	100
4.10	Construction of the voronoi lattice corresponding to the real parenchyma tissue. (Left) A picture from the guadua drying, taken from [LVV ⁺ 03]. (Center-Left) the cells are recovered by applying a mask to the imate. (Center-Right) using the centers of the cells, a triangulation can be constructed. (Right) the voronoi lattice is built by intersecting the lines perpendicular to those of the triangulations. The final voronoi tessellation is seen in[Fig. 4.11].	101
4.11	(Left) Voronoi lattice build from a photo of bamboo parenchyma tissue. In green the voronoi cells that will correspond to the cells. The cell walls (in white) suffer capillary pit forces perpendicular to them. The tessellation was done using Triangle[She96]. (Rigth) An inhomogeneous lattice, build by displacing the center nodes in an hexagonal lattice and calculating the closest neighbours by means of a Delaunay triangulation, [Fig. 4.11], used in [Chapter. 6].	102
4.12	Voronoi generation. (Left) Inside each hexagon from the original lattice, build a circle. Take a random point from inside each of the circles. (Center) Make a triangulation, by drawing rects from the points to those in the neighboring circles. (Rigth) The voronoi construction is finished by taking the perpendicular lines to those of the triangulation and extending them until they find another rect.	102
4.13	Modeling of pore space by a network of pores (sites) and throats (bonds), from [Pra02] .	103
4.14	(Left) Liquid flow due to <i>capillary pumping</i> . (Center) Boundary layer over the network and state of pores and throats, (Right) A given state of the drying interface. From [SMT08]	103
4.15	Probability distribution of of finding a burst of sizes s ($2D$), or A ($3D$), from [XDSW08]	105
5.1	Snapshots of percolation drying systems. In gray the empty cells, light blue the drying front cells, and dark blue the inner cells. (Chapter cover) System of linear dimension $L = 200$, at the percolation time. (This page) A system of linear dimension $L = 24$: (Left) Initial state, the drying front corresponds only to upper and lower rows. (Right) State of the system at percolation time.	108
5.2	Average size of the emptying cluster at percolation time, as function of the linear size of the system. Black points correspond to the size of the cluster for invasion percolation. The red points include the forces and detachments, from section 5.2. Dashed black line corresponds to a power low of 1.8, the known value for invasion percolation from the literature.	109

5.3	(Left) Forces acting on the system. 1. Cohesive junctures lamella. 2. Contact forces due to neighboring cells. 3. and 4. Cohesive forces in keeping the cells walls together. (Right) Capillarity causes a difference of pressure that can be represented as a force acting on those walls on the air-water drying front set of cells which have not plasmolyzed. Key: Gray cell, empty; Light blue cell, drying front; Dark blue cell, inner; colored wall, are not delaminated and the color-scale represents the magnitude of the force; black wall, delaminated.	111
5.4	Uniform distributions of either breaking thresholds (σ) or pit opening widths (δ) are characterized by a center value (C_σ, C_δ) and a width (W_σ, W_δ).	111
5.5	Snapshots of an non-homogeneous system with $4 < \sigma < 4.2$, with a distribution of pits characterized by a disorder $\xi = 0.7$: (Left) $\tau = 49$, drying starts; (Middle) $\tau = 114$ some fractures appear on those walls which belong to the drying front; (Right) Final state, some isolated cracks have appeared. Color key: Gray cell, empty; Light blue cell, drying front; Dark blue cell, inner; colored wall, are not delaminated and the color-scale represents the magnitude of the force; black wall, delaminated.	113
5.6	Snapshots of an non-homogeneous system with $4 < \sigma < 4.2$, with a distribution of pits characterized by a disorder factor $\xi = 0.7$ (Left) $\tau = 434$, more cracks are generated on the cells belonging to the drying front; (Middle) $\tau = 849$ final state of the system after the drying process has finished; (Right) Individual cracks, characterized by different colors.	114
5.7	Homogeneous system of linear size $L = 30$, $\sigma = 4$, for 300 instances of the system, and several values of the amount of disorder of the pit pore size distributions ξ_{pit} . (Left) Average avalanche size as function of the drying cell time τ , shows that a constant rate of delamination, which starts early and reaches higher values for larger amounts of disorder. (Right) Avalanche size distributions, show exponential behavior.	117
5.8	Homogeneous system of linear size $L = 30$, $\sigma = 4$, for 300 instances of the system, and several values of the amount of disorder of the pit pore size distributions ξ_{pit} . (Left) Distributions of Energy released in the breakings. For small values of energy the distributions peak in discrete values. (Right) Distributions of final sizes of cracks. The slope of the blue line is -1.98 ± 0.16 , and that of the cyan is -0.75 ± 0.06 ; the flattening comes as higher avalanches happen for higher disorders.	117
5.9	Inhomogeneous system of linear size $L = 40$, $4.0 < \sigma < 4.2$, for different values of the amount of disorder of the pit pore size distributions ξ_{pit} , averaged over 300 instances. (Left) Average avalanche size as function of the drying cell time τ , shows that a constant rate of delamination, which starts early and reaches higher values for larger amounts of disorder. (Right) Avalanche size distributions, show exponential behavior.	118
5.10	Inhomogeneous system of linear size $L = 40$, $4 < \sigma < 4.2$, for several values of the amount of disorder of the pit pore size distributions ξ_{pit} . (Left) Distributions of Energy released in the breakings. For small values of energy the distributions peak in discrete values. (Right) Distributions of final sizes of cracks, the slope of the set $\xi = 0.5$ is calculated as -1.87 ± 0.18 , and for the cyan -0.77 ± 0.06 ; the flattening comes as higher avalanches happen for higher disorders.	119

5.11	Drying time τ needed to dry the sample as function of the disorder of pore pits. The value is constant, independently of the disorder, which implies that the drying process is not affected by the fracturing. Notice that the error bars are one order of magnitude lower than the values.	119
5.12	Size of the system spanning crack as a function of the size of the system. The slope is different from the percolation one, thus showing that the fracture process is not related to percolation. A disorder value of $\xi = 0.9$ and 300 instances for large systems and 50 for smaller ones were used; however not all the samples had a spanning crack along the sample.	120
6.1	A) Bamboo culms [Lin], B) Small <i>Guadua angustifolia</i> board showing the fibers embedded into the parenchymatous tissue and their distribution: more dense at the outer than at the inner side. C) 3D Bamboo culm structure. Fiber bundles align along the axis of the culm ([Lie98]). D) 2D photography of the <i>Guadua</i> parenchyma ([LVV ⁺ 03]).	123
6.2	Upper left, the plane frame element spanning between the nodes i and j , arbitrarily oriented by an angle θ . Each node has two translational and one rotational degree of freedom. Lower left, two contiguous cells. Right, structure of the CNMF (not at scale). The hexagons represent the cells and the junctures are arranged into triangles. Hashing represents fixed boundary conditions.	123
6.3	Snapshots of the system, for a $L = 5$ geometry. Left(5 steps), a gap appears due to the breaking of some junctures at the center of the sample. Middle, 7 time-steps, right 17 time-steps.	125
6.4	Snapshots of the system, for a $L = 8$ geometry. (Left) A few junctures have been removed, causing small displacements of the remaining ones; as for instance the one in the coordinates $x = 0.01$, $y = 0.024$. (Right) As the evolution continues, the removed junctures cause larger displacements in the network.	126
6.5	Initial network, for the case of an inhomogeneous lattice. The disposition of the cells resemble the randomness in the parenchyma tissue of <i>guadua</i>	126
6.6	Log-log plot of number of events of avalanche size s ($N(s)$) as function of avalanche sizes (s) for the CNMF, for several centers of distribution of breaking thresholds, homogeneously distributed. (Left) A power law with exponent $-2.93(9)$ is gather for a breaking threshold of 0.35 (for an explanation on the units, see Sec. 6.3.1), the breaking thresholds are given by the control parameter is defined in (Eq.6.5) (Right) Histogram of avalanche sizes for several widths of the homogeneous threshold distribution centered at $0.35EA$, for different widths.	129
6.7	Log-log plot of number of events of avalanche size s ($N(s)$) as function of avalanche sizes (s). (Left) Several Weibull distributions of the breaking thresholds, with values of the shape parameters m between 1 and 10. The straight line corresponds to an slope of -2.9 . (Right) Inhomogeneous lattice geometry, the control parameter is the global breaking threshold. The straight line corresponds to an slope of 2.5.	129

6.8	Histogram of Normalized Humidity decrements between consecutive avalanches h_{btw} , for different maximum humidity changes Δh_{max} (which is proportional to the Cell Wall strain, (Eq.6.4)). For a maximum humidity change of 25 (in arbitrary units) the slope is fitted to $-0.188(5)$, while for a maximum humidity change of 200 it is $-0.074(1)$. The system corresponds to regular lattice geometry, with breaking thresholds given by (Eq.6.6).	130
6.9	Histogram of humidity increments between successive avalanches. (Left) Breaking thresholds following several Weibull distributions, with m between 1 and 10. The green line corresponds to a fit of the series of shape $m = 2$, with slope $-0.45(2)$. The blue line to that for $m = 10$, with slope $-0.63(2)$ (Right) For an inhomogeneous lattice geometry the slope in semi-log axis is $-1.04(2)$.	131
6.10	Number of intact fibers as function of the humidity change for several homogeneous distribution of the breaking threshold with different widths (semi log). The line is drawn only to guide the eye, the data points are the symbols. The system corresponds to regular lattice geometry, with breaking thresholds given by (Eq.6.6). <i>Inset</i> , linear axis.	132
6.11	Scaled fraction of intact fibers as function of the humidity change (in units of max humidity difference) for different system sizes.	132
6.12	Histogram of avalanche sizes for damage parameter $a=0.1$ and several maximal numbers of failures, k_{max} . The bolder line (slope $-2.98(7)$) fits for avalanche sizes between 1 and 7, while the thinner line (slope $-2.1(1)$) fits for avalanche sizes between 7 and 60. The breaking thresholds have a homogeneous threshold distribution centered at $0.35EA$	133
7.1	(Left) Example of initial randomized geometry. (Right) Uniformly distributed breaking thresholds are centered at $C = 1$ with half-width W . The amount of strength disorder is controlled by varying the value of W between 0 and 1.	138
7.2	First large avalanche for three different widths of disorder, showing how the narrower breaking distributions favor the appearance of large fractures. (Left) $\xi = 0.01$, (Center) $\xi = 0.1$, (Right) $\xi = 0.3$. [VLM11, VKLM11].	139
7.3	The relative length reduction $\langle \alpha \rangle$ of springs as a function of time for several values of the amount of disorder ξ . The system size was set to $L = 30$. Data values are binned with a bin size $\Delta t = 1$ and $\Delta t = 16$ for $0 < t < 10$ and for $t > 10$, respectively.	140
7.4	Average number of steps t_f needed to reach the shrinkage value of $\alpha_f = 0.7$, for different values of the disorder ξ , for a system of size $L = 30$.	141
7.5	Arithmetic average of avalanche sizes $\bar{\Delta}(\alpha)$ as function of the shrinkage α for different values of disorder ξ . Each curve is the average over several instances of the system. <i>Inset</i> For very high disorders (for example $\xi = 1.0$), there is a single maximum, corresponding to a single large avalanche, just at the start. This first maximum disappears close to the transition value of disorder $\xi_c = 0.6$ and, thereafter, a second local maximum appears. For all cases, there is an exponential relationship between $\bar{\Delta}$ and α at the end of the process.	142
7.6	Avalanche size distributions $N(\Delta) \propto P(\Delta)$ for a system of linear extension $L = 30$, for several values of disorder ξ . <i>Inset</i> avalanche size distribution at the critical point ξ_c , where a good quality power law is obtained.	143

7.7	Arithmetic average of the largest avalanche, for different system sizes, as a function of the disorder of the system ξ . The different data curves collapse in a single shape when the transformation is applied, implying: $\xi_c = 0.4$, $\beta/\nu = 1.4$ and $1/\nu = 1$. <i>Inset</i> Original data without rescaling.	144
7.8	Arithmetic average of the largest $\langle \Delta_{max} \rangle$ and second largest $\langle \Delta_{max}^{2nd} \rangle$ avalanches for different system sizes, as a function of the disorder ξ	145
7.9	Scaling plot of the average avalanche size $\langle m_2/m_1 \rangle$. By rescaling the two axis with appropriate powers of L , all curves obtained for different L values collapse on the top of each other for $\gamma/\nu = 1.$, $1/\nu = 0.9$ and $\xi_c = 0.4$. The inset shows the original data before rescaling.	147
8.1	Moisture content as function of drying time, for two sets of experiments. Black points corresponds to the measurements of moisture content averaged over 4 segments of internode culm of 1 cm of width. An exponential fit with timeconstant $-0.4(3) 1/b$ is shown in dashed line. The red diamonds correspond to moisture content over a single 10 cm segment, with the red line being an exponential fit with timeconstant $-0.10(3) 1/b$	152
8.2	Snapshots of the sample 1, at different times during drying, along with enlargements of one of the two catastrophic cracks that appeared on this sample. (Upper left) Minute 41, no visible cracks. (Upper Right) Minute 79, two cracks are clearly visible. (Lower left) Minute 105. (Lower right) Minute 157, large deformation of the ring.	153
8.3	(Color Online). Examples of voltage on the microphone, blue continuous line (proportional to the sound intensity), and set noise threshold. a) A cascade of small sized breakings. b) A single large crack. (Sounds included as supplementary material.)	154
8.4	(Left) Experimental squared voltage size distributions $N(\Delta)$. The line drawn has a slope of -1.2 . (Right) Experimental waiting times between consecutive avalanches.	155
8.5	(Color online) (Left) Experimental scatter plot of energy as function of avalanche timespan. (Righth) Experimental averaged energy release per avalanche as function of time.	156
8.6	Zoom, amplified 57 times a fiber bundle and surrounding parenchyma tissue. (Left) Before drying.(Right) After drying.	156
9.1	(Left) Polygonal, inhomogeneous cellular lattice model geometry, [Fig. 4.11](Right)Randomized triangular lattice model geometry. [Fig. 7.1]	158
9.2	(Left)Arithmetic average of avalanche sizes $\Delta(\alpha)$ as function of the shrinkage α for different values of disorder ξ [Fig. 9.2] (Right) Scaling plot of the average avalanche size $\langle m_2/m_1 \rangle$. By rescaling the two axis with appropriate powers of L , all curves obtained for different L values collapse on the top of each other for $\gamma/\nu = 1.$, $1/\nu = 0.9$ and $\xi_c = 0.4$. [Fig. 9.2]	160

9.3	(Left) Capillary front model snapshots of percolation drying systems. In gray the empty cells, light blue the drying front cells, and dark blue the inner cells. [Fig. 5] (Right) Capillary induced fractures model. Key: Grey cell, empty; Light blue cell, drying front; Dark blue cell, inner; colored wall, are not delaminated and the color-scale represents the magnitude of the force; black wall, delaminated.[Fig. 5.3]	160
B.1	Poster, presented at the 2009 Conference on Computational Physics, Taiwan	180
B.2	Talk, presented at the 2010 Conference on Computational Physics, Norway	181
B.3	Poster, presented at the 2010 iupap conference on statistical mechanics STATPHYS24, Australia	181
B.4	Article, Computer Physics Communications. 2010.	182
B.5	Article, Computer Physics Communications. 2010.	183
B.6	Poster, presented at School and Conference on Mathematics and Physics of Soft and Biological Matter The Abdus Salam International Centre for Theoretical Physics - ICTP, Trieste, Italy 2 - 13 May 2011	184
B.7	Talk, presented at the Seminar Computational Physics for Engineering Materials, Zurich Switzerland, April 2011.	185
B.8	Article, Physical Review E. 2011.	186



“Iglesia sin religión, interior” (Cultless church), Simón Vélez, Architect. Guadua culms were used as the construction structural material. [Vél]

Introduction

1.1 Guadua and fracture

Guadua angustifolia is an Andean Bamboo generally used both as a construction material (structural beams and walls) and as a raw material for handicrafts (furniture and vessels) throughout Colombia [Jan81, AVB93]. In fact, most part of the Andean landscape in Colombia, with his mountains and valleys, is painted with the light-green color of Guadua. As in all bamboos, Guadua structure is optimized to withstand stresses along its axis, with a high Young modulus in this direction, and to bend elastically on the perpendicular direction. The fibers, oriented along the axial direction of the culm and embedded in a soft parenchyma tissue, are more abundant towards the outer side than to the inner one. Due to this characteristics, Guadua is considered a functionally graded material . [SWP06].



Figure 1.1: Two constructions by Simón Vélez, Architect. Guadua culms were used as the construction structural material. (Left) “Puente en la China” (Bridge in china).[Vél]. (Right) , 2009 Simón Vélez, Principal Prince Claus Award in the Netherlands [Kra11].

Guadua plant grows fast: a shoot of about 3 years old is considered mature. Guadua structures can be quickly assembled, and they can provide temporal constructions to relief zones.

This was the case of Pereira’s Cathedral, which was built in Guadua by the architect Simón Velez after a 6.2 Richter-scale magnitude earthquake destroyed the previous construction in 1999, leaving hundreds of homeless people in the Colombian coffee region[Elt01]. Moreover, Guadua forests play a crucial ecological role, fostering native species, helping to regulate the water cycle, consuming CO_2 , and injecting water back into the soil (in fact a Guadua tree injects two liters of water at night for each liter it drains during the day). Nowadays, Guadua experiences a revival as structural material for building gorgeous houses. [LVV⁺03]

The main cause of Guadua failure, both for structural and handicraft uses, is the occurrence of cracks along the axis; which may even propagate across nodes. When the drying process is poorly performed, micro-cracks appear in the inner wall of the culm and propagate to the outer surface. These cracks do not compromise the structural bending resistance of the beam, but on the long run they make the structure harder to maintain. This is specially critical for furniture and handicrafts, where the appearance of the good is spoiled. The macroscopic drying of Guadua has been thoroughly studied. In his Ph.D. thesis[MA06], J.A. Montoya performed a systematic study of the drying conditions of Guadua for both solar and oven dryers. He concluded that the most relevant element to prevent cracks is a careful drying schedule, consisting on different drying stages in which both temperature and air moisture content are carefully controlled. This procedure drives the Guadua to the final environmental conditions of placement and use. ¹

The fracture process of bamboo depends on its structure, reviewed on [Section. 2.1]. In summary, the bamboo stem (or culm) is a hollow cylinder, surrounded by the cortex and surrounding a hollow space, the lacuna. It is composed of three different tissues: vascular bundles, carrying on sap and water; fibers, giving support to the main structure, and a soft parenchymatous matrix tissue, allowing the culm to bend [Fig. 2.4]. This last tissue, the *Parenchyma*, is the one where fractures occur. Guadua tissues are aligned along the direction of the culm, even periodically repeated from section to section. Thus, the shrinkage of guadua shows different values in the three directions: $\alpha_l = 0.8 \pm 0.1$ along the culm, which is negligible; $\alpha_t = 10.6 \pm 2.7$, for the tangential direction, and $\alpha_r = 7.0 \pm 1.0$, for the radial direction [Section. 2.2.2]. Therefore, the models for drying induced fractures can be treated as *2D* problems in the radial-tangential plane. In such a section, the parenchyma tissue appears as a random array of (almost) hexagonal cells of approximately similar sizes [Fig. 1.2]. Walls of adjacent cells are joined together by a middle lamella, and every three neighbor cells meet together at the so called *tri-cellular junctures*. These ones are the points where silica accumulates, when the bamboo gets older, and where the fracture is easier to take place.

Wood (and bamboo) drying is a process which has two main stages: a first removal of free water and a second removal of bond water. Free water removal starts when the vessels are emptied by the action of gravity, just after harvest. Afterward, the water from inside the living cells will also drain out. This is possible because all parenchyma cells are connected by small pores called

¹The traditional handling of Guadua in Colombia, in contrast, lays far away from that optimal treatment. Guadua culms are harvested early in the morning, when the plant has injected most of the water content back into the soil. Then they are left inclined in the forest for several days in order to allow the sugars to ferment, in a process called *avinagrado* (seasoning), with the hope that the alcohols and acids so generated will prevent future bug attacks. Next they are dried outdoors, with strongly changing conditions between day and night, for several days [MA06]. It is not a surprise that such handling will lead to cracks in the final product.

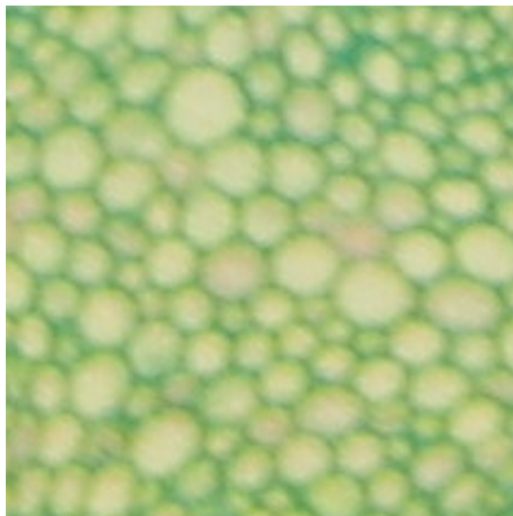


Figure 1.2: A picture of the parenchyma tissue of guadua, from [LVV⁺03].

pits The Reynolds number of this process (see Appendix A) is of the order of 10^{-3} ; therefore, the flux is laminar. In this stage capillarity plays a central role, because meniscus with radii of the order of the pits' sizes appear on the drying front. The second stage of drying consists on the removal of the bound water from the small capillaries inside the cell walls themselves, until the sample attains the equilibrium moisture content. At this stage, all cells are connected to the air across the pits, and the drying is driven by diffusion.

In the wood literature there are two main hypothesis describing the appearance of macroscopic cracks during the drying of cellular materials: *collapse of the soft tissue*, due to the capillary forces acting on the parenchyma cells[Sia84]; or *shrinkage driven fractures*, caused by the uneven change in the shape of wood due to the dissipation of the water from within the cell walls [PJKJ01]. The microscopic interactions defining the two fracture mechanisms by drying are drastically different. The capillary model implies that the forces only appear at the drying front, where some cell walls have air at one side and water at the other side. On the contrary, in the shrinkage model every cell wall in the system is in contact with air and can dry by evaporation. The main transport mechanism here is diffusion, but - if the process is slow enough - it has time to equilibrate and all cells can shrink at the same time, due to the loss of bond water. In fact this second procedure is different from several fracture mechanisms (collision, shear, etc) in which the stresses start on the boundary and transfer thereafter the material inside. In the poaceas, like bamboo, both mechanisms take place, one at each drying phases. For the *Arundo donax* (also known as Giant cane), another giant grass of the same family as the bamboos (*Poacea*), the collapse induced fractures have been shown to be caused by drying [OGT04]. As bamboo is a composite material with both parenchyma tissue (soft) and fiber sheaths (stiff), capillary forces during drying may cause large enough forces within the matrix material as to produce cell tissue collapse, micro-cracks or even macro-cracks. In this mechanism, the most relevant force that an individual cell suffers during the drying process is the capillary force that appears in the newly

formed interfaces [Sia84], [Fig. 2.23]. On contrary of bamboos, softwoods' main components are tracheids cells and rays, both having a relatively high Young modulus and low water content with respect to the parenchyma tissues of bamboos. Therefore, softwoods' drying does not generate collapse of the cells, instead it induces fractures only due to the shrinkage.

The fracture process depends on several different elements: air moisture content, drying temperature, preservative soaking proportions, material porosity, to name but a few. The continuum engineering of wood drying takes all of them into account to build computational models of drying at the tissue level, [PT02]. The process of fracture is studied by means of macroscopical models that follow the evolution of the elasticity tensor, and propose failure conditions ($F(\sigma_{ij}) = 0$, reviewed in [Section. 3.2.1]). In this work I do not pursue this path. In contrast, the general approach of statistical mechanics is to propose simplified models (i.g., taking the interactions only to first order and to first neighbors) in order to analyze individual aspects of the problem. The application of statistical mechanics to the study of materials lead to the statistical models of fracture. Breaking of materials is a process that is driven by the disorder at the microscopic scale. The statistical models of fracture approach is to put the focus on the fluctuations of the statistical observables of the system and the impact that it has on the structure, on the contrary to the material science approach in which the average quantities are the focus.

1.2 Statistical models of fracture

The goal of the study of statistical models of fracture (SMF) is to characterize the global fractures by providing macroscopic quantities, and relate them to the microscopic interactions. As mentioned by Alava et. al. [ANZ06], the first systematical account of fracture was made by Leonardo da Vinci, when he studied tension tests on metal wires and noticed that longer wires failed earlier than shorter ones (which could be due to the fact that longer wires have a larger chance of having weak spots). The influence of fluctuations on fracture would have to wait until the works of Griffith, [Gri20] to appear in the scientific literature. This work would be later systematized by Weibull [Wei51], proposing a distribution of failure thresholds that still is widely used in the description of fracture. Some authors claim that the Griffith theory is similar to the classical theory of nucleation in first-order phase transitions [ZRSV99a, GacP95, RK89].

In an statistical model of fracture the breakup process of a continuous body is studied by a discretized model of interacting parts of the system. The steps of the system's evolution are called *discretization*, in which the geometry of the constituent parts and their interactions before failure are defined; *failure law* of a single element, which gives the way the constituent elements detach; and *distribution rule*, which takes into account the redistribution of the forces that act on the boundary of the object among the remaining elements. One of the first, and most relevant SMF is the Fiber Bundle Model (FBM for short). It was proposed in the 1920's by Pierce, but was first described in terms of statistical quantities by Daniels in 1945 (the main results are reviewed in [Section. 3.4.1]). The process they describe is the breakdown of a rope (or metal cable) which holds some weight, taking into account its inherent structural disorder. In the discretization the rope is described as a set of N parallel non interacting fibers, each of which holds a fraction N/L of the total load. The failure law says that each of the fibers fail at a given strength threshold σ_i ,

taken from a random distribution. When a fiber fails, the load it holds has to be taken by the others, by a distribution rule. The two more common cases are to give this load to everybody (Global Load Sharing), or only to the neighbors (Local Load Sharing). The evolution of the system consists in taking increments in the global load until an element fails and shares its load; this could cause other elements to fail, in an avalanche. The breakdown process of fiber bundle has a phase transition, whose order parameter is the fraction remaining fibers which are still intact. When the system approaches breakdown, the distribution of avalanche sizes follows a power law distribution denoting a scale free phenomena, which was analytically proven by Hemmer et. al to have a power of $-5/2$, $N(\Delta) \propto \Delta^{-5/2}$ [HH92]; with Δ the size of the avalanche. There is agreement in the literature that this power law distribution marks a phase transition for the model. In [ZRSV97], the fraction of unbroken fibers is taken as the order parameter of the system and, therefore, a first order phase transition is suggested. Other authors, [MGP00], define the probability of triggering further breakings given an individual failure as the order parameter, and thus define it as a second order phase transition (see also [PHC10], [ANZ06] and [Section. 3.4.1]). Fiber bundle models have also been used to study creep, the response to solids to a constant load; showing how two different universality classes appear depending on the interaction rule for the fibers: either continuous with power law divergences for global load sharing, or abrupt for local load sharing, [KMHH03]. In more general cases of FBM with different kind of redistribution rules among neighbors, the structure of the phase transitions change, as shown in [HZH08], in which the distribution of forces is anisotropic; [RKH08], where degradation is introduced by allowing a fiber to fail more than once; [HKPK08], where strong inhomogeneities are introduced by having some unbreakable fibers, which implies two power law regimes characterized by either $5/2$ or $9/4$ exponents (for a review, see [KRHH06]).

Another successful SMF is the random fuse network model (RFM). In this case, the system is defined as an array of fuses, set up in a square lattice, having random failure thresholds. A current applied to two extremes of the lattice in bus bars is steadily increased, until the fuses start to fail. The redistribution of the current by a burned fuse is taken into account automatically by the calculation of the Kirchhoff laws in the system. This model shows a power law distribution of avalanches, with $N(\Delta) \propto \Delta^{-3}$ [PHH05], [Section. 3.4.2]. In the context of the random fuse model, Zapperi et. al. proposed to change the focus of the fracture process from a thermally activated process to study the effect of the *quenched* disorder inside of the sample, [ZRSV99a]. He finds a first order phase transition in which the control parameter is the effective medium constant ϕ , and the susceptibility is the average avalanche size m . The RFM presents a scalar view of fracture. This can be extended to a vectorial representation. An example is the Beam Models in which the medium is discretized by beams, [Section. 3.4.3]. They represent fracture by a solution of the Lamé equation, and thus are useful in studying the three breaking criteria in fracture.

In some statistical models of fracture the phases of the system are easy to spot. For instance, in [SDM01], Sethna introduces the term *crackling noise* to describe a phase transition between two kind of sound events: popping, individual failure events as in pop-corn; and snapping, in which many constituent elements fail at once, as the breaking of a piece of chalk. Crackling occurs in between, with avalanches taking every size. An example of this behavior is the famous

Richter law of earthquakes, which predicts that the distribution of sizes of earthquakes follows a power law distribution. This law is a clear example of the fact that there is a simpler universal relation driving the phenomena, irrespective of the different mechanisms that cause either the large avalanches (continental plate displacements) or the small ones (dirt on the crack).

The statistical models of fracture have also been useful in studying the relationship between the microscopic degrees of freedom and macroscopic characteristics. Two examples are Paris's Law, [VAH08], relating the velocity of an expanding crack to the microscopic damage; and shell fragmentation [HWK06, CWKH08], characterizing the breaking of egg shells and Christmas balls by critical exponents. In the case of cracks due to collision of two objects, the phase transition occur between a state with surface cracks, and another one ruled by cracks that percolate across the sample, as discussed in [CWKH08, GCC99, Cha06, DAKH04]. Almost all mentioned SMFs share the common aspect that the loading is caused by tension or traction, but in general by forces applied at the boundaries. In the 2D models this implies that the loading on individual elements is not isotropic.

Beyond the field of fracture, statistical mechanics has also been used to study the process of drying, as in the models of *invasion percolation*. A porous material is modeled there as a set sites and bonds, and the invasion of one fluid by another is a stepwise process depending on the bond's widths. For this process a fractal dimension of $91/48$ is found at the time that percolation is achieved. This process relies on the capillary forces that appear in the drying interfaces, a subject that has been reported also experimentally, [XDSW08].

1.3 This work

The objective of this thesis is to propose and analyze statistical models of fracture inspired in the geometry and drying mechanisms of the parenchymatous tissue of *Guadua angustifolia*. The proposed models are two-dimensional, resembling the geometry of the tissue in a plane perpendicular to the culm, where most deformations take place. A first set of models is proposed to analyze the first stage of drying, when all cells are saturated with water (called *free water*) and a capillary front advances from cell to cell. A second set of models are used to investigate the fractures induced in the second drying stage, when the water (called *bond water*) inside the cell walls themselves evaporates and the fractures are driven by a uniform shrinkage. Both the Finite Element Method (FEM) as well as the Discrete Element Method (DEM) are used to perform the simulations. Our numerical studies show that the fracture process induced by shrinkage shows a well-defined phase transition, with the amount of structural disorder as control parameter: At low disorders, the breaking process is dominated by a macroscopic crack at the beginning, while at high disorders the fracturing proceeds in small-sized micro-cracks which eventually merge and break the layer. Moreover, good quality data collapse from the finite-size scaling analysis show that the average value of the largest burst $\langle \Delta_{max} \rangle$ can be identified as the order parameter, and that the average ratio $\left\langle \frac{m_2}{m_1} \right\rangle$ of the second m_2 and first moments m_1 of the avalanche size distribution shows similar behavior to that of the susceptibility of a continuous transition. In contrast, the fracturing process induced by capillarity can be well modeled by invasion percolation.

This book is organized as following. The first [Chapter. 2] is devoted to the biology and drying mechanisms of *G. angustifolia*. [Chapter. 3] summarizes the more relevant statistical models of fracture for this study, after a short review of the basic concepts on elasticity and critical phenomena. The simulation methods used in this research are described in [Chapter. 4]. The forthcoming chapters present the results of my research and are ordered in the same time sequence of the drying process. [Chapter. 5] is devoted to the simulation of fracture propagation during the free water removal, when fractures driven by capillary forces may take place. [Chapter. 6] presents two FEM models for shrinkage that closely resembles the actual geometry of the parenchymatous tissue of *G. angustifolia*. In contrast, [Chapter. 7] introduces a DEM model for shrinkage that over-simplifies this geometry, but allowing for intensive statistical studies. This is the model that clearly shows the phase transition mentioned above. A final chapter [Chapter. 8] contains the result of two experiments on the drying of bamboo, identifying microscopic structural changes and measuring the acoustic emissions by fracture. I conducted this series of experiments while at the ETH in Zurich, so the material used is not *G. angustifolia*, but a similar Bamboo (*Phyllostachys edulis*). The main conclusions are recorded in [Chapter. 9], and two appendices list the values of numerical constants employed in the simulations and the publications derived from this doctoral thesis.

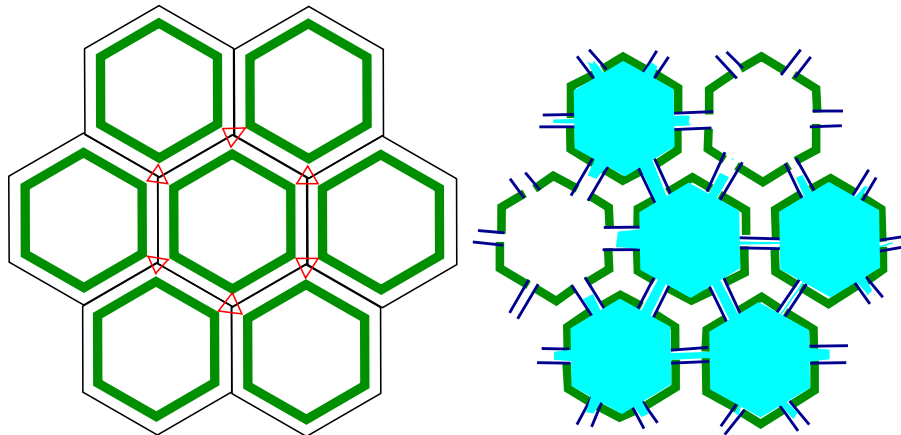


Figure 1.3: (Left) Geometry of the fracture model. The cell walls, green, are modeled as beams that go between the junctions, red. (Right) Pore network model for drying dynamics. The cells are joined together by pores, whose widths distribute randomly. At any drying stage, there will be some cells filled and some will be empty.

The proposed models' results provide great insight into the statistical physics of drying, with implications that may go far into the field of materials sciences. It constitutes, therefore, an original contribution of statistical models of fracture.



Mauricio Pardo's reconstruction of a Renault 4 car with bamboo culms, [Iv][Elt10]

Bamboo and drying

The giant bamboos are angiosperm plants belonging to the family of Poacea, also known as the grass family. Grasses are woody plants, more primitive than herbaceous ones. They have their dividing cells (meristematic tissue) close to the nodes, allowing continued growth after the tip has been removed. Along with bamboos, many other species of grass have been domesticated; namely the grain cereals, wheat rice, oats, sugar cain and sorghum [Sch97].



Figure 2.1: A bamboo forest near Milan, Italy.

With several different species thriving in the tropical jungles across the globe, giant bamboos not only play an important ecological role, they also provide a very resistant, cheap and fast to harvest wood replacement with uses ranging from handicrafts to structural building beams and

columns. In this chapter I will discuss the state of the art knowledge about bamboos in general and *Guadua angustifolia* in particular.

2.1 *Guadua* physiology

The bamboo plant is composed by roots, stem (also called culm), leaves and fruits. The culm itself is a hollow cylinder whose hollow inner space is called the lacuna. A succession of nodes separate the culm in individual sections, [Fig. 2.2]. In the outer side of the culm there is the cortex, which impermeabilizes and protects the inner tissues. A cylindrical coordinate system with the z direction along the longitudinal axis of the culm is customary to use in wood studies (sometimes called simply the axial direction).

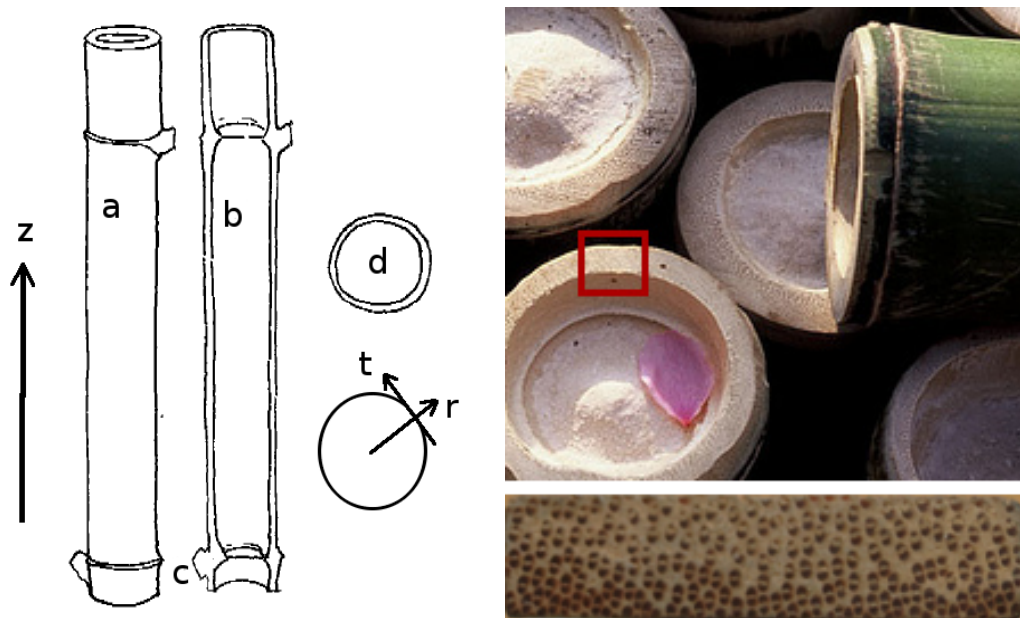


Figure 2.2: (Left) Internode structure of bamboo (a) the culm, including the longitudinal axis z commonly used in wood studies; (b) vertical section, showing the hollow interior and the culm wall; (c) the node (d) cross section, showing also the radial and tangential directions r , t . (modified from a sketch in [Jan81]). (Right-up) Bamboo culms, the red square marks the culm wall. (Right-down) A section of the culm-wall of *Guadua* bamboo, the dark spots correspond to the fiber sheaths, the light material to the parenchyma tissue.

The different kind of cells that can be seen in a transverse cut of the culm wall are depicted in [Fig. 2.4]. The vascular bundles (xylem, phloem and fibers) are embedded among the parenchymatous cells [Lie98]. Their percentages are: *Vascular bundles* (or conducting tissue, about 40%), *fibers*, (8%) and *parenchyma cells* (about 52%) [GL74]. This tissues have a preferred orientation: aligned along the z axis, in the longitudinal direction. Unlike wood, bamboo does not have rays to allow diffusion in the radial direction.

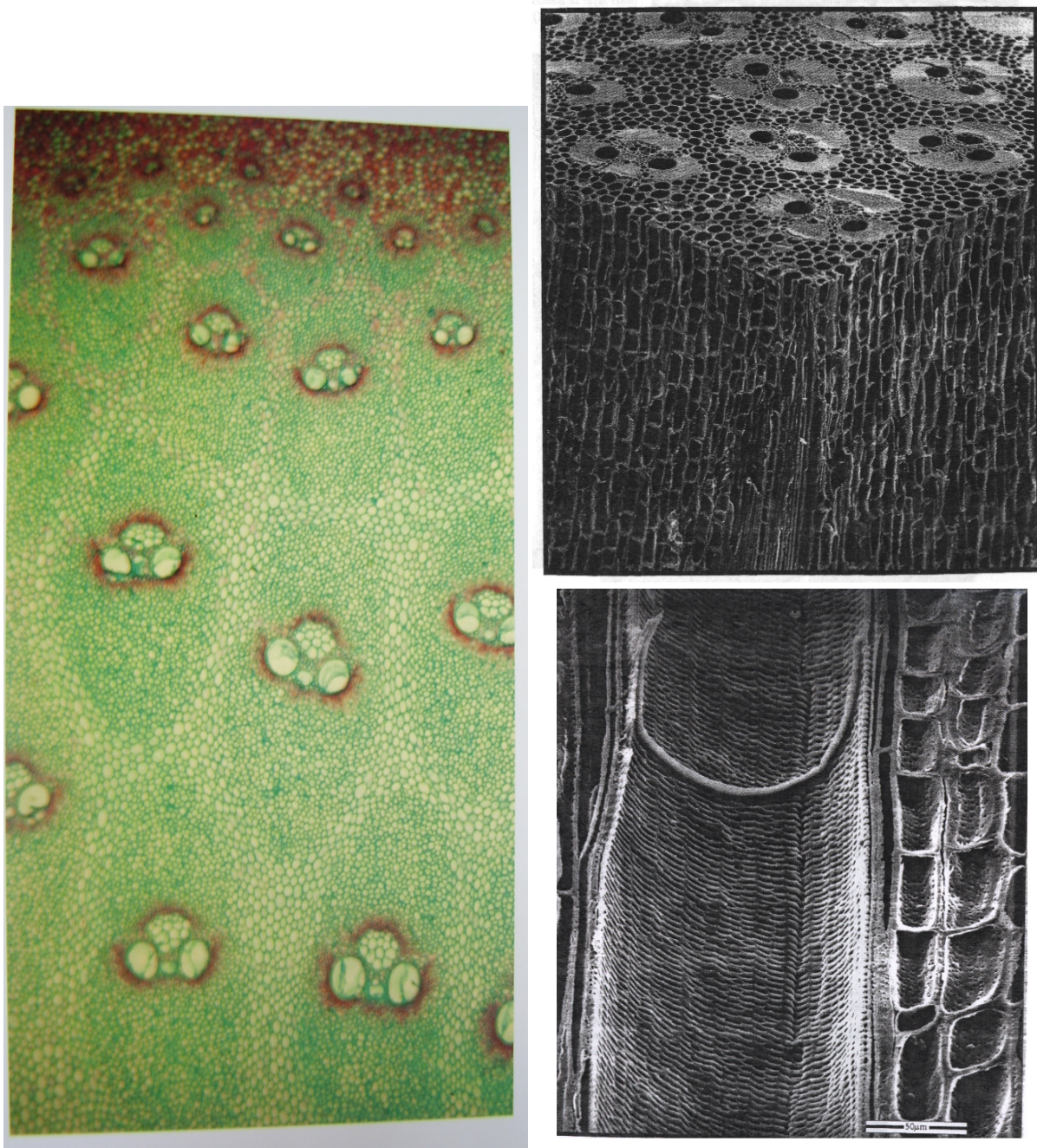


Figure 2.3: (Left) A cut of a young culm wall of *Guadua Angustifolia* [LVV⁺03]. Fiber sheaths corresponding of xylem and phloem are covered by brown fibers. The dark green cells around them correspond to young fibers not yet lignified, the light green cells further away correspond to the parenchymatous cells. (Right up) Three dimensional view of culm tissue with vascular bundles embedded in ground parenchyma in *Oxytenathera abyssinica*, from [Lie98] (Right down) Two metaxylem vessels in a bamboo with separating rim and adjoining parenchyma cells, from [Lie98]

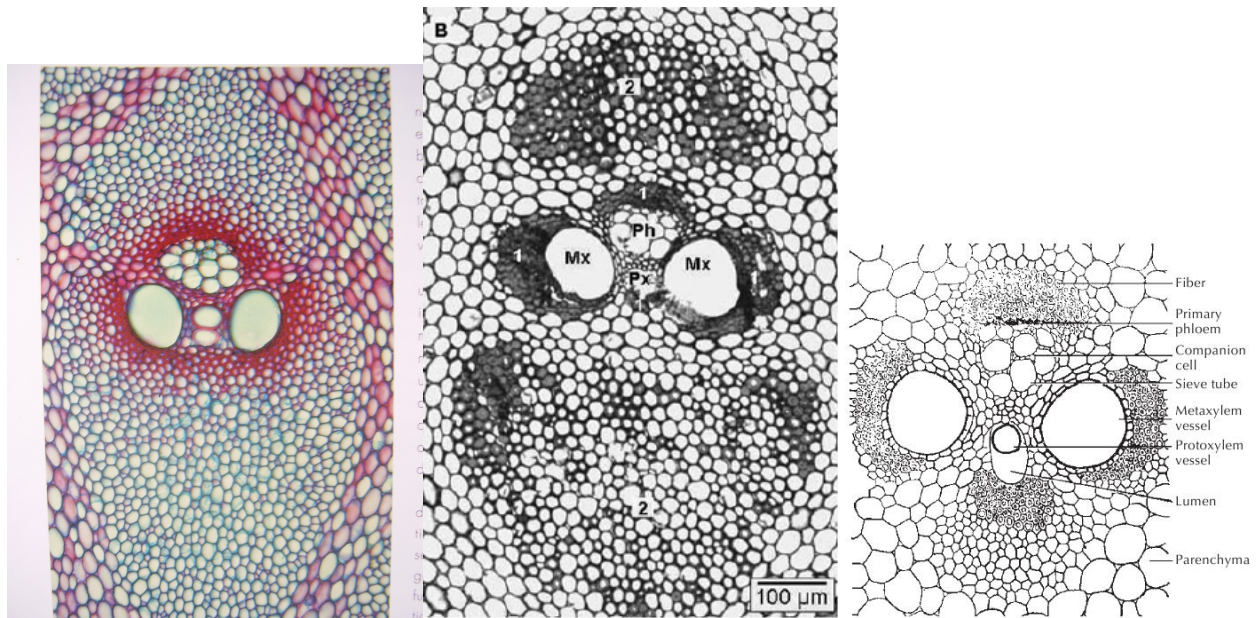


Figure 2.4: (Left) Zoom of the fiber bundle of *Guadua*, transverse cut. From [LVV⁺03] (Center) Vascular bundle of the bamboo species *Gigantocloa levis*, showing the fiber caps (1), metaxylem (Mx), Phloem (Ph), protoxylem (Px), and free fiber strands (2). [LVAG06] (Right) A cross section of a vascular bundle of bamboo [Xu10]

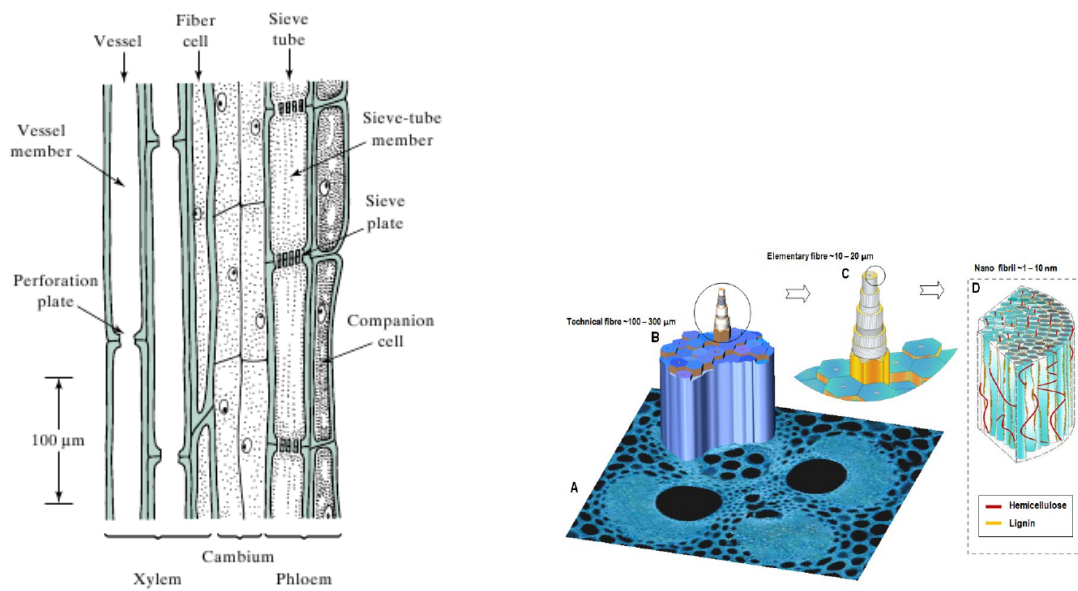


Figure 2.5: (Left) Fiber Bundle. (Right) Structure of the fibers and the microfibrils of bamboo, from [FTDG⁺11]

Part	outer	inner
Top	4.4	9.8
Middle	3.8	7.8
Base	3.1	5.0
Mean	3.8	7.5

Table 2.1: Vessel (metaxylem) cross sectional area of bamboo *Guadua angustifolia* var. *sur* (as % of total area of the cross section), edited from [Lie98], also in <http://www.inbar.int/publication/txt/tr18/default2.htm>

2.1.1 Vascular bundles

In a living plant there are two paths for water, xylem and phloem, forming the fiber sheath (see [Fig. 2.3], [Fig. 2.4],[Fig. 2.5]). The former takes the water from the roots to the leaves in a process called *Cohesion - Tension*¹. The rate of transport in xylem is about $10\text{ cm}/\text{min}$ [Zim83]. In phloem transport occurs through the sieve elements, which are living cells. The transport rates are about $1\text{ cm}/\text{min}$, and can be either upwards or downwards. The rate is mainly affected by solute concentrations between the sources of solutes and their sinks in the plant body.

In bamboo there are two kinds of xylem: the metaxylem vessels and the protoxylem. The former is about $25\ \mu\text{m}$ width, and works in an adult plant; the latter being used mostly in the early stages of development. Metaxylem is usually surrounded by one or two layers of lignified parenchyma cells, and are connected by pits. The vessel cells in the metaxylem are connected through a perforation plate, which is mostly plane.[Fig. 2.5] In the living plant, the sap moves through the vessels, and this is also the main path of movement of free water during drying. Their cross sectional area and size varies with height and distance to the culm, as shown in [Tab. 2.1] for *Guadua Angustifolia*. The cross sectional area of the vessels varies between $10000(\mu\text{m})^2$ (a radius of $100\mu\text{m}$), and $30000(\mu\text{m})^2$, from the outer to the inner side of the culm. The pit openings are around $2\mu\text{m}$ in length.

Long-distance water transport in trees

The *cytoplasm* of the plant cells is surrounded by the lipid bilayer *plasmalemma membrane*, in contact with the rigid cell wall, formed of cellulose and hemi-cellulose micro-fibrils. It is a solution with high solute concentration. The membrane is permeable to water molecules and selectively permeable to solutes, enabling water uptake by osmosis, although the permeability

¹The pores in the leaves through which transpiration takes place are about 5 nanometers width, creating a meniscus. A capillary of this width would suffice to hold a column of water one order of magnitude more than taller trees, but the xylem that is connected to them is wider, or the order of 10^{-4} . What holds the water inside the xylem? First, the cohesive forces in water may suffice to hold the column together. Besides this, the xylem itself is hydrophobic, not allowing water to escape. On top of that the xylem has plates that reduce its width, which would prevent any bubble that may enter in there to propagate thorough the whole system. Lastly the living plant may have mechanisms to repair such embolisms.[Coc06, TZ02] What is important to our problem is that a cut down *Guadua* culm without leaves will not be able to physically hold water inside by capillary forces throughout but that may be there by distances of up to the meters in the xylem.

of the bilayer is low. It gets enhanced by the *aquaporins*, that is specific water channel proteins. The cytoplasm of different molecules is connected through *plasmodesmata*, thus defining a water compartment, called the *symplasm*. The water outside of it, forms a second compartment: the *apoplasm* [Fig. 2.8].

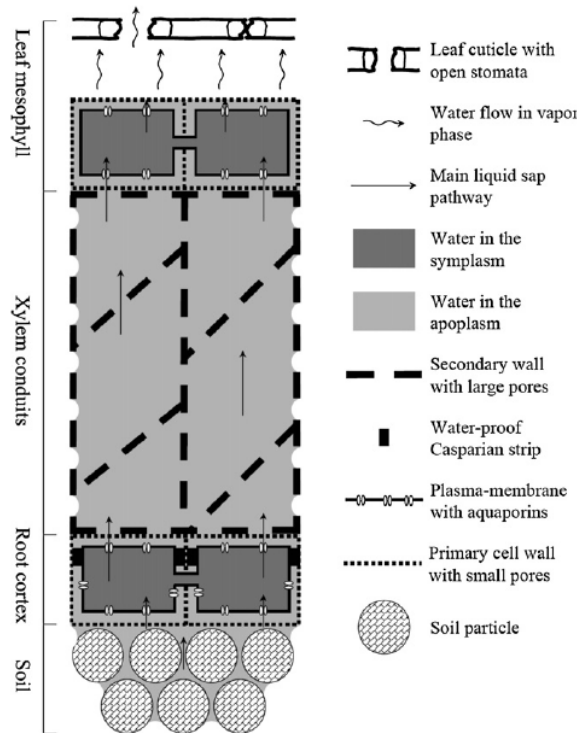


Figure 2.6: (Right) Schematics of water flow. [Coc06]

The *xylem* is the tissue that is devoted to long-distance water transport. It contains cells, called tracheids, where the lateral walls have been reinforced by a deposit of lignin (a hydrophobic polymer) and the cytoplasm has disappeared. The cell end walls may be completely missing, forming large conduits called vessels. They are capillaries of various dimensions, (1mm to several meters length, 10 to 400 μm diameter). These cells are dead, so they have no membranes. This water body is called the *apoplasm*.

The water moves due to gradients in hydrostatic pressures, $F = K \cdot \Delta P$, F the bulk water flow (kg s^{-1}), K a diffusive coefficient. Water flow from inside the bilayer (symplasm) towards the cell wall (apoplasm) are driven by the difference of *osmotic potential* $\Delta\Pi$, and the reflection coefficient σ , as $F = K \cdot (\Delta P + \sigma \Delta\Pi)$. Tree roots enhance their contact area by using hairs. Water flow goes mostly to the symplasm, as the apoplasm pathway is interrupted by an hydrophobic deposit: *The Casparian Strip*. The roots also have aquaporins allowing easy access to the symplasm. This also allows the tree to control the uptake of ions from soil and, then, water flows to the leaves through the xylem conduits [Fig. 2.6]. Because xylem lacks plasmalemma membrane, they also lack cytoplasm, so they are made of dead cell walls, increasing their hydraulic efficiency.

They also have many pores, called *pits*, which are fundamental to the water interchange between cells [Coc06].

2.1.2 Fibers

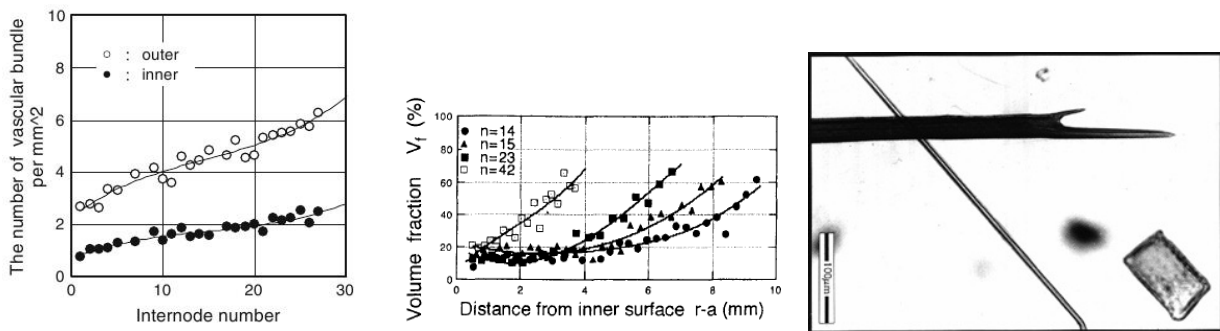


Figure 2.7: (Left) Vascular bundles per area, as function of internode number, either at the inner or outer side of the culm wall [ON09]. (Center) Volume fraction of fibers, as function of radial coordinate, for different node numbers [Ama97]. (Right) Bamboo fiber sheaths are composed of conducting tissue, and fibers. This is a snapshot of both a small and a big bamboo fibers, and a parenchyma cell. The length of the black vertical line in the lower left corner is 100 μm , [Lie98]

The number of fiber bundles, also called fiber sheaths or vascular bundles, increases with respect to the internode number [Fig. 2.7](Left). They are thicker and less abundant towards the lacuna, with respect to the outer side of the culm. [Fig. 2.4] and [Fig. 2.7](Left)(Center). This uneven distribution of fibers increases the mass density of the culm towards the exterior, because fiber sheaths are denser than parenchymatous tissue. Optical image analysis has been used to establish the aspect ratio RT (Radial - Tangential) as well as the area percentage of fiber sheaths as function of total area, for a transversal cut of *Moso bamboo*, as a function of the node number, either for the inner side or the outer side of the culm [KAN11]. Between nodes 10 and 20 the aspect ratio RT is close to 1.5 for outer and 1.0 for inner, while the area (equal to the percentage of mass of fibers) goes from 0.5 at the outer side to 0.3 at the inner one. The bamboo fibers have lengths ranging between 1.04 mm, in *Phyllostachys nigra* to 2.64 mm in *Bambusa vulgaris*. *Guadua angustifolia* fibers have an average length of 1.60 and a width of 11 μm [Lie98] [Fig. 2.7].

The fiber sheaths are embedded in a softer tissue, called parenchyma. Parenchyma cells may *collapse* during the free water removal stage of drying, usually due to unappropriated drying treatments [OGT04] [Fig. 2.14].

Mechanical characterization of the fiber cell wall

Bamboo fiber cell walls have a multilayered structure, which is established during the first year of development of the plant, continuing until the third one. Thickening of the fibers results from deposition of new layers which gives a high degree of heterogeneity in layer patterns, and

is caused by two mechanisms: firstly, the addition of lignin to the cell walls with aging, starting by the fiber cell walls, and later also in the parenchyma cells; secondly, the addition of more secondary walls in bamboos than in softwoods, [GKM04, Bha03, Lie98, GM05], see [Fig. 2.8].

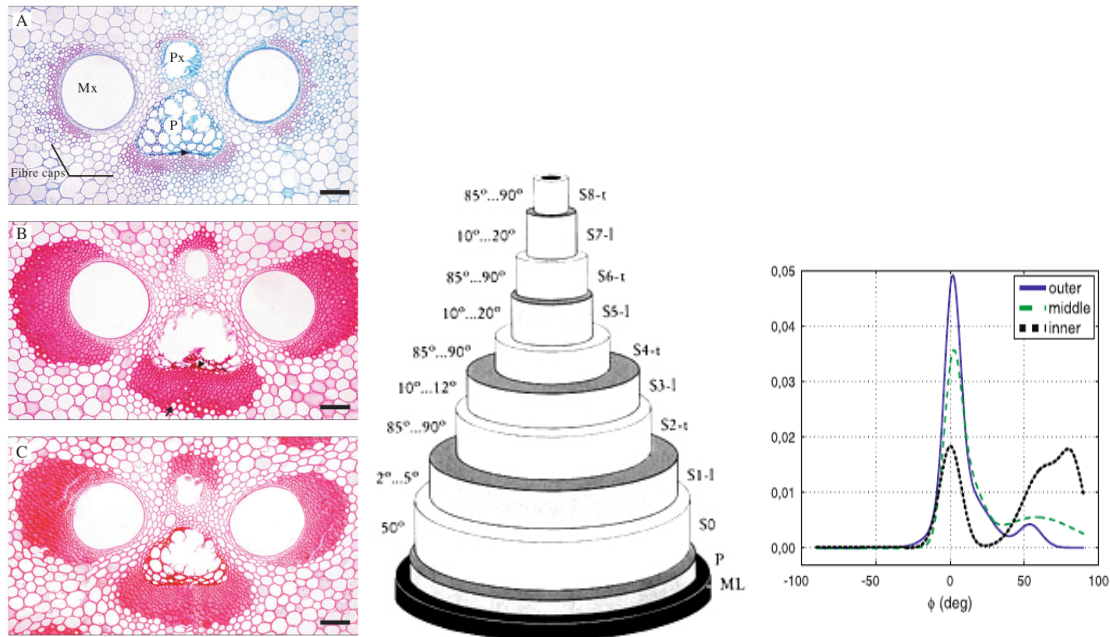


Figure 2.8: (Left) Thickening of bamboo culm cell wall, from [GKM04]. A), Elongating culm (less than 6 months old), B) Young culm (1 year old), C) Mature Culm (3 years old). (Center) Poly-laminate structure of the thick-walled bamboo fiber. Fibril angle at the left, notation of wall lamella at the right [Lie98]. (Right) Micro-fibril distribution [YJHS08]

Chemical composition of Bamboo and micro-fibril angle

Bamboo chemical components, like wood, are primarily cellulose, hemi-cellulose, and lignin. In smaller percentage also different resins, tanins, waxes and salts. [Li04] Related to the position across the cell wall, the main components have been characterized as seen in [Fig. 2.9]. Both lignification and appearance of second layers on the cell walls of bamboo occur with the maturation of the cells. At the end, lignin distribution among the parenchyma cells can be regarded as homogeneous, as seen in [Fig. 2.10] and [LHH⁺02].

The presence of cellulose cristal depends on the distance towards the center of the culm, i.e., the radial coordinate. The authors of [YJHS08] show how both the percentage of crystallinity and the length of the cristals increase from the inner to the outer part of the culm; specifically the lengths go from $247 \pm 10 \text{ \AA}$, $303 \pm 10 \text{ \AA}$ up to $328 \pm 10 \text{ \AA}$. The crystallinity, goes from $32 \pm 3\%$, $43 \pm 3\%$ up to $40 \pm 3\%$.

The *micro-fibril angle* is defined as the angle between the micro-fibrils in the cell wall and the fiber angle, and is measured in a 4.5 years old bamboo. For *Moso bamboo* the distributions of micro-fibril angle are bimodal, one peak at very small angles and another at large ones. In the

Age	Location	Ash	Hot Water Solubles	Alcohol-toluene Solubles	Lignin	Holo-cellulose	α -cellulose
		%	%	%	%	%	%
One	Bottom	1.82	5.83	3.32	21.98	68.92	46.52
	Middle	1.94	5.07	2.86	22.11	70.84	47.30
	Top	1.95	5.14	3.48	21.26	71.95	47.51
Three	Bottom	1.30	6.33	4.17	23.21	68.58	46.21
	Middle	1.36	6.91	4.38	23.95	72.69	46.82
	Top	1.41	7.43	5.21	23.71	73.82	46.99
Five	Bottom	1.26	4.89	6.61	22.93	69.94	46.08
	Middle	1.30	5.19	6.81	22.97	72.50	47.65
	Top	1.35	5.84	7.34	23.02	73.65	47.91
Three ^l	Epidermis	4.09	9.19	5.99	22.41	63.14	41.71
	Outer	0.54	5.26	3.15	24.30	69.94	49.02
	Middle	0.65	7.25	4.25	21.79	65.84	45.08
	Inner	0.88	9.33	5.78	22.57	64.54	42.84

Figure 2.9: Chemical composition of bamboo, from [Li04]. The holo-cellulose column contains both α -cellulose and hemicellulose. Some alcohol toluene solubles may also be hot water solubles. Furthermore each column has to be calculated from different samples, since the procedures to collect them are destructive. Finally, the authors do not report error bars.

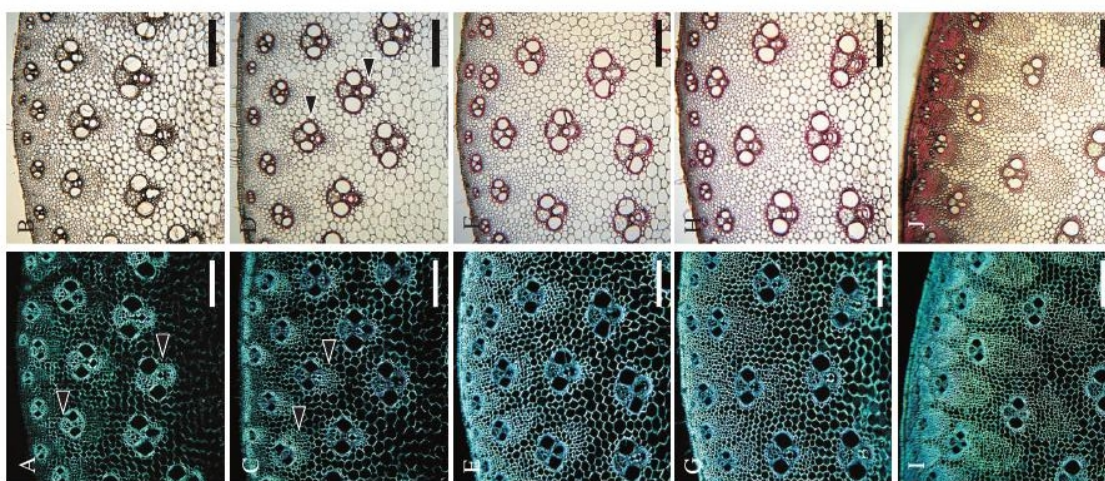


Figure 2.10: Tissue development observed with either polarized light (A,C,E,G,I) or phloroglucinol-HCl staining (B,D,F,H,J) for *Dendrocalamus asper*, [GM05]. Scale bars, $200\mu\text{m}$ Up: Lignification starts in the fiber surrounding vascular tissues, and continue in the inward direction. Down: The increase in birefringence, with cell evolution is linked with the presence of secondary cell walls.

middle and outer section of the cell wall (see [Fig. 2.20]) most fibers lie along the fiber axis, while at the inner side large values of the microfibril angle are dominant.

For *Phyllostachys vidiiriglaucescens* the micro-fibrils of a one year old culm for both parenchyma cells and fibers where studied. For the former transverse micro-fibrils as well as some at 70% were found, as well as S and Z helices. For fibers they report micro-fibrils with an angle of 60%, transverse and axially aligned microfibers, see [Fig. 2.8] and [CM00].

2.1.3 The parenchyma cell

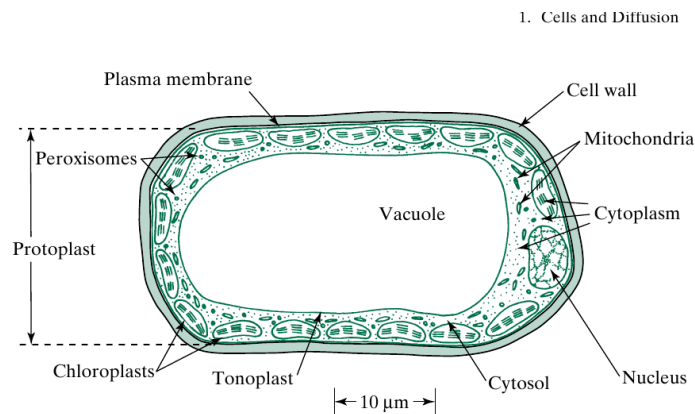


Figure 2.11: The plant cell. [Nob09]

As every plant cell, the living material or parenchyma cells (called *Protoplasm*), is surrounded by a protective layer (the *the Cell Wall*); in some cases it even has an internal reservoir for water, organic and inorganic solutes called the *Vacuole*. [Fig. 2.5] The cell wall is made mostly of cellulose, which gives rigidity to the plant and is highly permeable to water. It has a width of about $4 \mu m$, (see [Fig. 2.12] and [LVAG06]), is mostly composed of cellulose and surrounds the whole cell providing it with structural stability and protection. While alive, the stability of the cell is being sustained both by the stiffness of the cell wall and by the osmotic pressure inside the lipid bilayer.

Between the cell wall and the protoplasm there is a *plasma membrane*, a bi-lipid layer with embedded protein structures which control the flux of ions and organic molecules needed by the cell. Most advanced plant cells also have another membrane, called the *tonoplast*. Its main function is to surround and isolate an inner vacuole, pushing the cell organelles closer to the outside of the cell and providing turgor pressure. The tonoplast has a similar structure to the plasma membrane but it has many more aquaporins (organelles that control the flux of water across the bi-lipid layer) [Nob09, CM94].

Three neighboring cells join together at the tricellular *junctions*, [Fig. 2.13]. Made mostly of pectic polysaccharides, their role in the living cell is to hold together neighboring cells by distributing the turgor forces [CJ11]. The cell wall between two neighbouring cells is also joined by the middle lamella, and structure coming from the genesis of the cells which also provides some structural stability to the union of the cells.

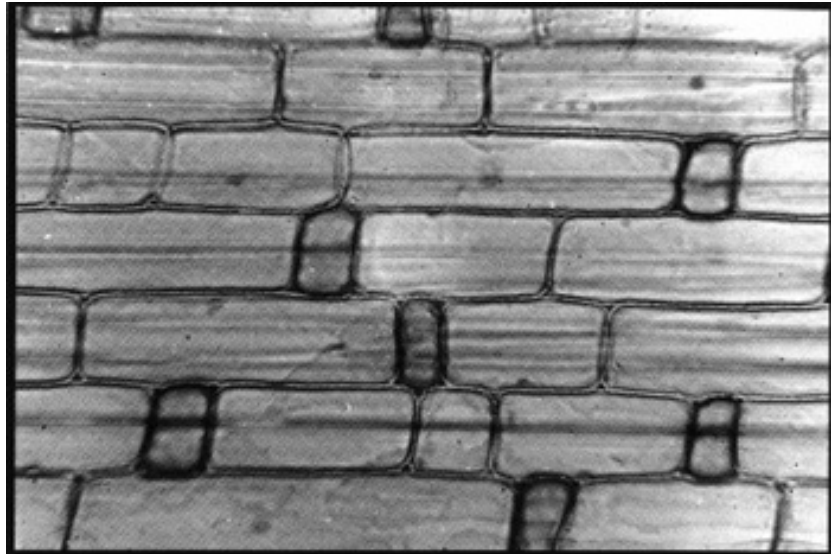


Figure 2.12: Parenchyma consisting of both elongated and cube shaped cells. The horizontal axis is along the bamboo axis (z direction) and the vertical axis in the radial direction, for a sample of $270 \mu\text{m} \times 180 \mu\text{m}$. From this picture we estimated the parenchyma cell wall width as $4 \pm 0.6 \mu\text{m}$, the cell width as $30 \pm 0.8 \mu\text{m}$ -same as the depth for cube shaped cells- and a depth of $108 \pm 0.6 \mu\text{m}$ for elongated cells. Picture from [Lie98]

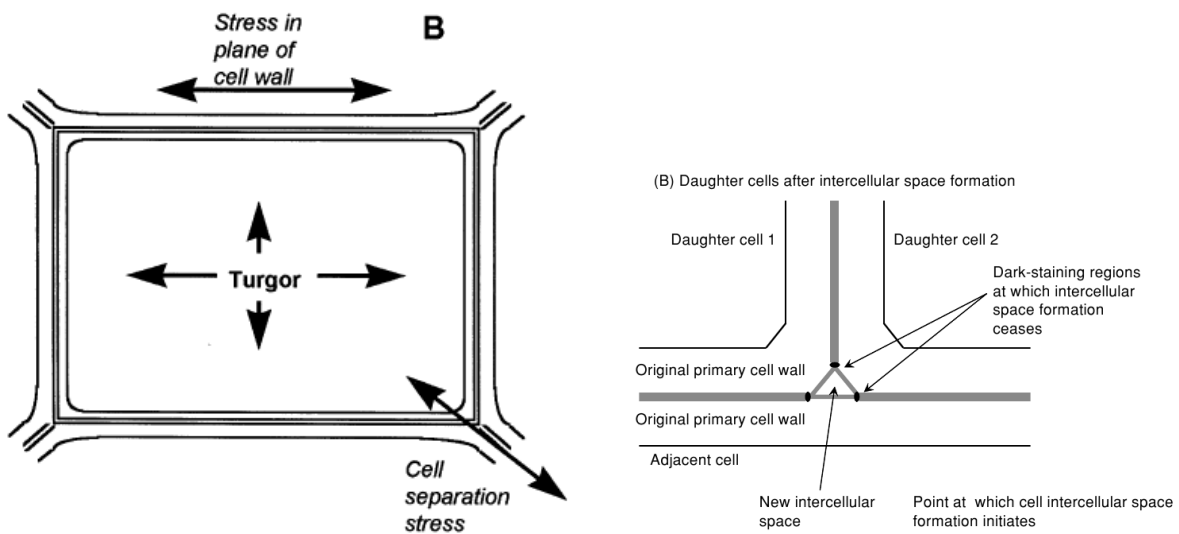


Figure 2.13: (Left) Turgor pressure, from [JM00]. (Right) Tricellular junction with inter cellular space [WB07]

Parenchyma cells are smaller towards the outer and inner parts of the culm wall. They can be either elongated in the vertical direction (20 to 80 μm length, to 25 to 40 μm tangential and radial directions) or cube-like shaped. Parenchyma tissue arranges in columns in which there are often larger cells followed by smaller ones. The shorter have denser cytoplasm, thinner walls without lignification. The parenchyma cells are usually connected through pits with plasmodesmatal contacts, located in the tangential walls. Around the metaxylem vessel there are small parenchyma cells with many pit openings. They are the cell's storage tissue, so starch can be abundant in them. Also remain active throughout the life of the culm and their walls get thickened with age. The more abundant moisture content in the base of the culm has been attributed to the higher water storage capacity of the parenchyma cells, which are more abundant at the base than at the top of the culm [Lie98].

Mechanical properties of parenchyma cell

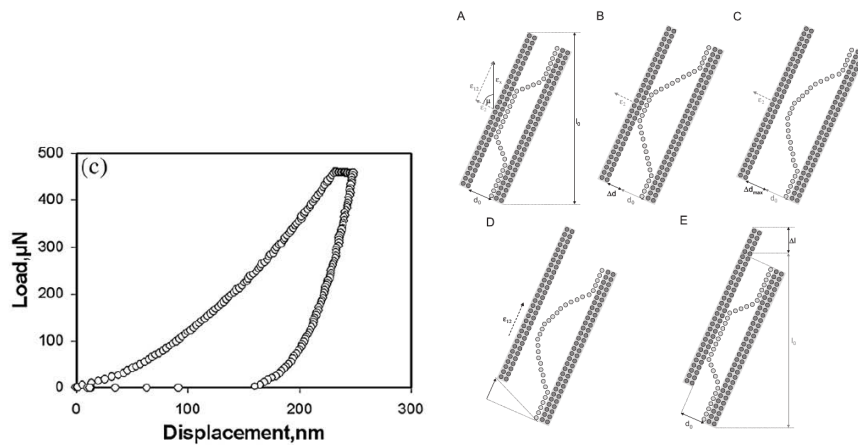


Figure 2.14: (Left) Nanoindentation load displacement curve for the fiber cells of *Phyllostachys edulis*, from [ZJLL09] (Right) Cane cross section during drying. (A) dried at 20 C and 65% relative humidity for 2h. (B) Dried for 4 h. The bar corresponds to 200 μm . Arrow, radial direction [OKY07]. (Right) Detachment of a hemicellulose loop when two cellulose fibrils to which it is attached are separated by a local tensile component, from [AJ08]

Nanoindentation experiments in the Cell Wall of Bamboo fibers and Bamboo parenchyma of *Phyllostachys edulis* have been carried out by [ZJLL09], with the results of the Hardness and Young Modulus shown in the [Tab. 2.2]. While elastic modulus is different for parenchyma or fiber cell walls, the hardness would be roughly the same. The authors also claim that the fiber constitutive behavior is ductile, showing a linear segment, and plastic deformation leading to irreversible damage, as seen in the [Fig. 2.14]. These results are somehow contradictory with those reported by [OKY07] (citing Chuma et al) for *Phyllostachys pubescens*, in which density and tensile strength for parenchyma are found to be one order of magnitude less than that of fibers; with Young's modulus is even two orders of magnitude less [Tab. 2.3]. There is no agreement on the exact values for the elastic constants for the tissues of the cell wall of bamboos.

Bamboo Component	Hardness (GPa)	Elastic Modulus (GPa)
Fiber cell wall	0.44 ± 0.09	10.4 ± 1.8
Parenchyma cell wall	0.43 ± 0.22	3.4 ± 1.3

Table 2.2: Hardness and elastic modulus from nanoindentation tests, *Phyllostachys edulis*, from [ZJLL09]

Bamboo Component	Density (g/cm^3)	Young's Modulus (GPa)	Tensile strength (MPa)
Fiber	1.57	48	498
Parenchyma	0.45	0.26	73

Table 2.3: Features of fiber and parenchyma for *Moso bamboo*, from [OKY07]

Moreover, Keckes as cited by Jarvis [AJ08], shows that even after this permanent deformation, the Cell Wall may restore its original elastic modulus, by a model called Molecular Velcro. The idea is that at the yield point, the structures of the cell wall may debond thus creating a large deformation. But this structures can bond again (as a velcro), thus restoring the elastic modulus while there is a permanent deformation. [Fig. 2.14]

Pit pairs

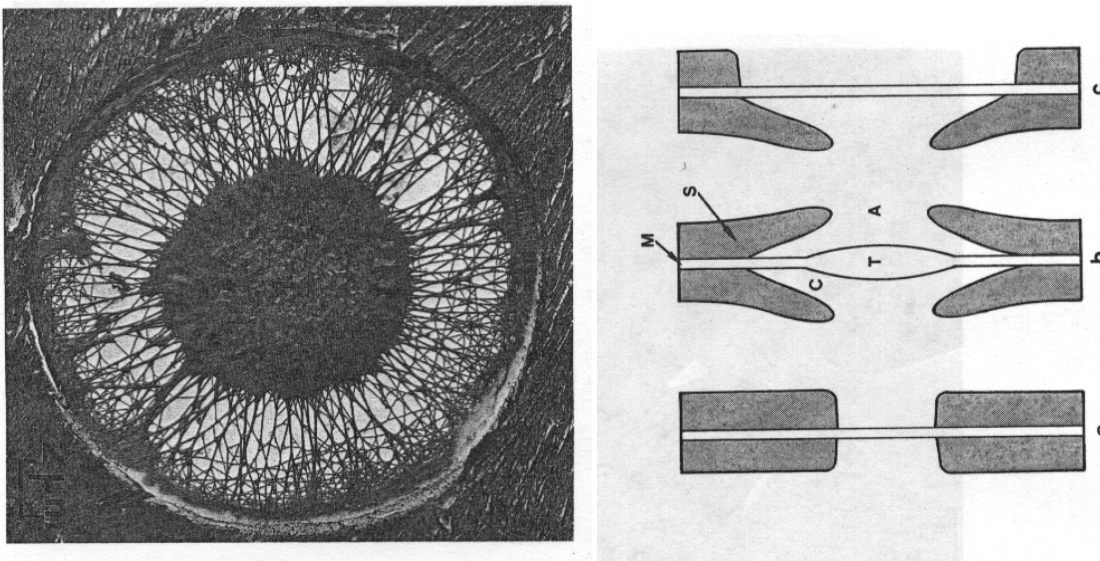


Figure 2.15: (Left) Unspirated bordered pit in a sapwood tracheid. Inside diameter, $18\mu m$, torus diameter $9\mu m$, openings $1\mu m$ in the tangential direction and up to $2\mu m$ in the radial direction. [Sia84] (Right) Pit pairs, (a) simple. (b) bordered pits, commonly between two prosenchyma cells, (c) half bordered pit, commonly between parenchyma and prosenchyma cells. [Sia84]

Pits are gaps in cell wall of adjoining cells. They consist in an absence of the cell wall together

with a pit membrane. There are three types of pit pairs, as shown in [Fig. 2.15]. As the holes in the pit pairs constitute the smallest lumens between neighboring cells, they will be crucial to our model of drying: the capillary surfaces of smallest radius will appear at them. These forces can be strong enough as to cause a detaching of the pit membrane towards one end of the pit pair. This model, known as the aspiration model was proposed in [HT67]. The capillary radius of water is initially bigger than that of the pit. As water evaporates, smaller meniscus appear inside the pit structure, creating tensions that can move the pit membrane into the second cell [Sia84].

2.2 Engineering of drying in wood and bamboo

Drying of wood is a large industry for which a extense body of knowledge has been published. In this section I will present some terms for the reader that has no experience on the subject.

Saturated Vapor Pressure is defined as the equilibrium partial pressure of evaporating water in contact with air.

Relative Humidity is the ratio between vapor pressure in air to saturated vapor pressure:

$$H = p/p_0 \times 100\%. \quad (2.1)$$

Moisture content Moisture content is the quantity of moisture in wood, as a percentage of oven-dry mass.

$$M = \frac{w_g - w_o}{w_o} \quad (2.2)$$

with w_g the moist mass, and w_o oven dry mass.

Equilibrium moisture content , EMC. The equilibrium moisture content corresponds to the amount of liquid present in the wood at a given value of moisture in the air, after transient effects have disappeared. This humidity is either free or bond water; the former being physically sorpted and present in the voids of the plant while the later is chemically sorpted staying inside the walls. As the EMC depends on the porosity of the material, it also shows dependence on the drying history: previous incomplete drying cycles may have left trapped air bubbles inside of the sample. The functional relationship between equilibrium moisture content and humidity is called *sorption isotherm* [Sia84].

Water in plants can be held by either surface tension effects (called absorbed), or by stronger chemical (hydrogen) bonds (adsorbed). [Wal06] **Absorbed** water is found in the cell lumens and intracellular cell spaces, and is called free water. **Adsorbed** water is found within the cell wall and in the interior of the cell itself.

Fiber Saturation Point(FSP) is defined as moisture content at which the cell is saturated with bond water in the cell walls with no free water in the lumens; in other words, when there

is no absorbed water. Another operational definition has been proposed. Since the mechanical properties of wood changes dramatically when it is dried beyond FSP, it has been redefined just at the point of drying in which the mechanical properties sharply change [Sia84].

2.2.1 Continuum models

In 1977, Whitaker [Whi77] presented a model in which drying is regarded as a coupled problem of heat, mass and momentum transfer. Instead of taking into account the specific geometry of the porous material, the three phases of water (solid phase, called σ ; gaseous phase -vapor plus air-, called γ ; and liquid phase, called β), are represented by continuous fields. The method to obtain the fields is called *homogenization*, and consist in taking averages of the different quantities inside predefined discretized volume segments \mathcal{V} , represented in [Fig. 2.16].

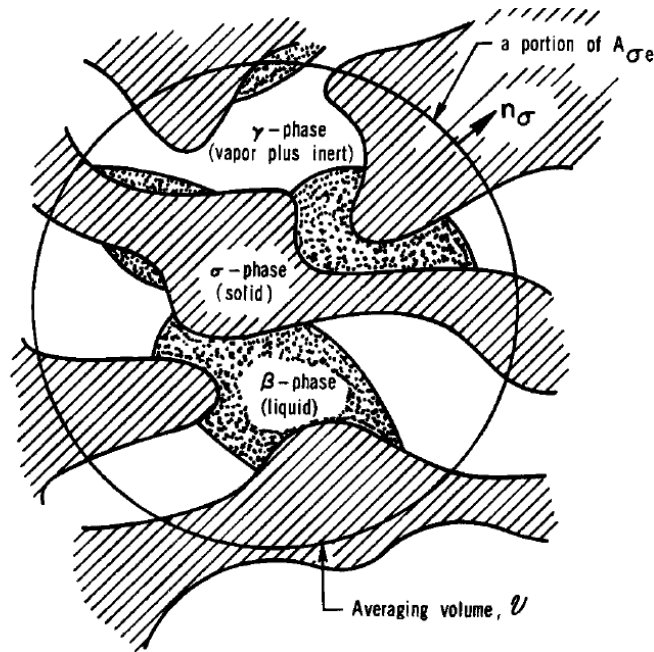


Figure 2.16: Drying process in porous media, from [Whi77]

The differential equations that the three fluids follow are the continuity equation, Newton's second law, and the thermal energy equation, written as:

$$\frac{\partial \rho_i}{\partial t} + \nabla \cdot (\rho_i \vec{v}_i) = r_i \quad (2.3)$$

$$\rho \frac{d\vec{v}}{dt} = \rho \vec{v} + \nabla \cdot \mathcal{S} \quad (2.4)$$

$$\rho \frac{dh}{dt} = -\nabla \cdot \vec{q} + \frac{dp}{dt} + \nabla \vec{v} : \vec{\tau} + \phi \quad (2.5)$$

with ρ the density, i a sub-index indicating species “i”, \vec{v} the velocity, r_i the rate of creation of quantity ρ_i (due to chemical reactions or evaporation), \mathcal{S} the stress tensor, h the enthalpy, $\vec{\tau}$ the viscous stress tensor, p the pressure, \vec{q} the heat flux, and ϕ a source or sink of electromagnetic radiation. The model then specifies the suitable conditions of the different phases.

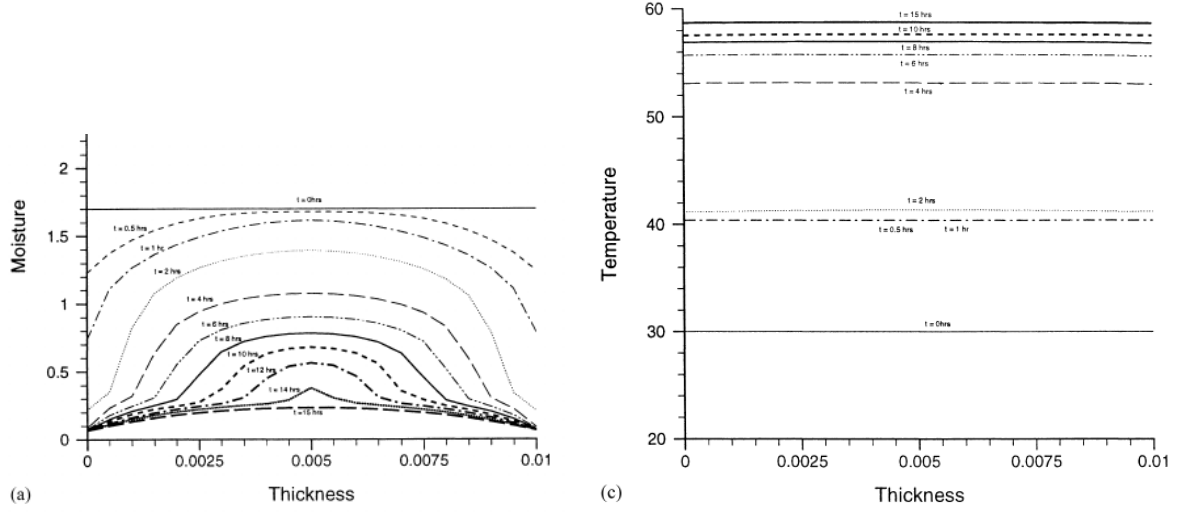


Figure 2.17: (Left) Moisture content (with 1 corresponding to 100%) for a drying half-slab of wood of $2\text{ cm} \times 1\text{ cm}$ dimensions, as a function of thickness. Different curves correspond to different drying times (0.5 h, 1h, 2h, 4h, 6h, 8h, 10h, 12h, 14h and 15h respectively from higher moisture content towards lower). The external temperature is set at a constant value of 60 Celsius. (Right) Central plane moisture content temperature field evolution, bottom up corresponding to 0h, 2h, 4h, 6h, 8h, 10h and 15h respectively. Taken from [PT02].

For solid phase the velocity is zero $v_\sigma = 0$ and there are no sources or sinks, i.e., the solid porous material remains still and unchanged. Then only a heat flux equation is needed, and (Eq.2.5) reads:

$$\rho_\sigma \left(\frac{\partial h_\sigma}{\partial t} \right) = -\nabla \cdot \vec{q}_\sigma + \phi_\sigma.$$

A simplification assumes that enthalpy is a linear function of temperature, and heat capacity is constant: $h = c_p T + \text{constant}$:

$$\rho_\sigma c_{p\sigma} \left(\frac{\partial T_\sigma}{\partial t} \right) = k_\sigma \nabla^2 \mathcal{S} + \phi_\sigma \quad (2.6)$$

The liquid phase has a single component, therefore the continuity equation (Eq.2.3) reads:

$$\partial \rho_\beta t + \nabla \cdot (\rho_\beta \vec{v}_\beta) = 0 \quad (2.7)$$

A further simplification used in these models is to assume the liquid phase as incompressible and with negligible viscous dissipation, which simplifies the heat transfer equation (Eq.2.5) to:

$$\rho_\beta c_{p\beta} \left(\frac{\partial T}{\partial t} + \vec{v}_\beta \cdot \nabla T_\beta \right) = k_\beta \nabla^2 T_\beta + \phi_\beta$$

For the **gas phase** Whitaker takes into account the two different components, air and water vapor, with two continuity equations derived from (Eq.2.3). He further assumes that there is no chemical reaction in this phase (no sinks or sources). For each species:

$$\frac{\partial \rho_i}{\partial t} + \nabla \cdot (\rho_i \vec{v}_i) = 0 \quad (2.8)$$

and similarly for the whole gas, as the density and momentum of this is the sum of those from each phase:

$$\rho_\gamma = \rho_1 + \rho_2 \quad (2.9)$$

$$\rho_\gamma \vec{v}_\gamma = \rho_1 \vec{v}_1 + \rho_2 \vec{v}_2 \quad (2.10)$$

The velocity \vec{v}_i is written as the sum of the average mass velocity and the diffusion velocity. The Fick's Law ($\rho_i \vec{u}_i = -\rho_\gamma \mathcal{D} \nabla (\rho_i / \rho_\gamma)$) is also taken into account, to obtain:

$$\frac{\partial \rho_i}{\partial t} + \nabla \cdot (\rho_i \vec{v}_\gamma) = \nabla \cdot \left(\rho_\gamma \mathcal{D} \left(\frac{\rho_i}{\rho_\gamma} \right) \right) \quad (2.11)$$

with \mathcal{D} a diffusion coefficient of the gas phase into the solid phase. The thermal energy equation 2.5 for this case takes the form:

$$\rho_\gamma c_{p\gamma} \left(\frac{\partial T_\gamma}{\partial t} + \vec{v}_\gamma \cdot \nabla T_\gamma \right) = k_\gamma \nabla^2 T - \nabla \cdot \left(\sum_{i=1}^N \rho_i \vec{u}_i \bar{h}_i \right) + \phi_\gamma \quad (2.12)$$

where the heat capacity of the gas phase $c_{p\gamma} = \sum_{i=1}^N \frac{\rho_i}{\rho_\gamma} \bar{c}_{pi}$, and the Fourier's law was used.

Perré and collaborators had built a computer model based on this set of continuum field equations, including as boundary conditions the initial moisture content and temperature schedules that correspond to the drying of different types of wood. In their work the material characteristics as capillary pressure, bond liquid diffusivity and thermal conductivity are inferred from image analysis, homogenization and experimental observation (see [PT02] and references therein). Using a finite element method they are able to find the moisture content, internal temperature and pressure fields during the drying process.

The main goal of this kind of models is to forecast the position of the drying front during the process of drying. While the existence of such frontier between a wet porous material and a dry one has been predicted and measured in the literature, these numerical models provide a different approach and an easier way to gather data about the drying process. A plot of such

surface for a 2D model is shown in [Fig. 2.17]. The price paid by such result is to deal with a complex model, with several different parameters, and in which the measured quantities are not necessarily completely independent on the initial conditions. The objectives of continuous methods are then complementary of those of the present work, which is devoted to analyze and ponder the different mechanisms of fracture from a more analytical point of view.

2.2.2 Guadua, experimental drying and mechanical characteristics

Like in wood, the foremost quantity needed to understand the changes of the mechanical properties of bamboo during drying is the *fiber saturation point* FSP; as the sorption, moisture capture inside of the sample due to the humidity in the atmosphere, affects the Young modulus of the material. The value of the FSP given the measurement uncertainty is also called fiber saturation zone. In [MA07], the fiber saturation point of the bamboo species *Phyllostachys pubescens* Mazel is measured in the range of 32% to 34% equilibrium moisture content.

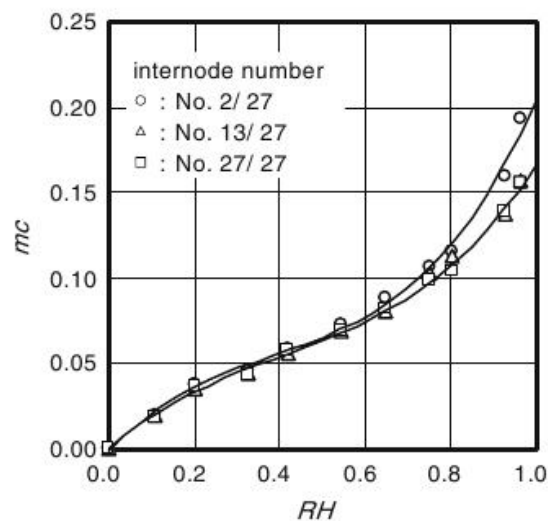


Figure 2.18: Isotherm curves for mosa bamboo, for various internode samples [ON09]

In bamboos, fiber distribution has little effect on the water adsorption properties, as seen on the equilibrium moisture content as function of relative humidities for different internode numbers, as can be seen in [Fig. 2.18].

Prof. Montoya has also characterized the material properties of Guadua. In [GMABS07] he presents results on the measurement of the Young modulus as a function of: age of the plant, atmospheric moisture content and sample height position in the culm. He finds that the flexural elastic modulus lies in the range of 11700 to 13266 N/mm^2 and that the breaking stress increases with decreasing humidity, from 87981 N/mm^2 at a relative humidity of 85% to 122917 N/mm^2 at 65% of relative humidity (both measurements made at a Temperature of 20 Celsius). The measurements are made by means of macroscopic test samples (“probetas”), shown in [Fig. 2.19].

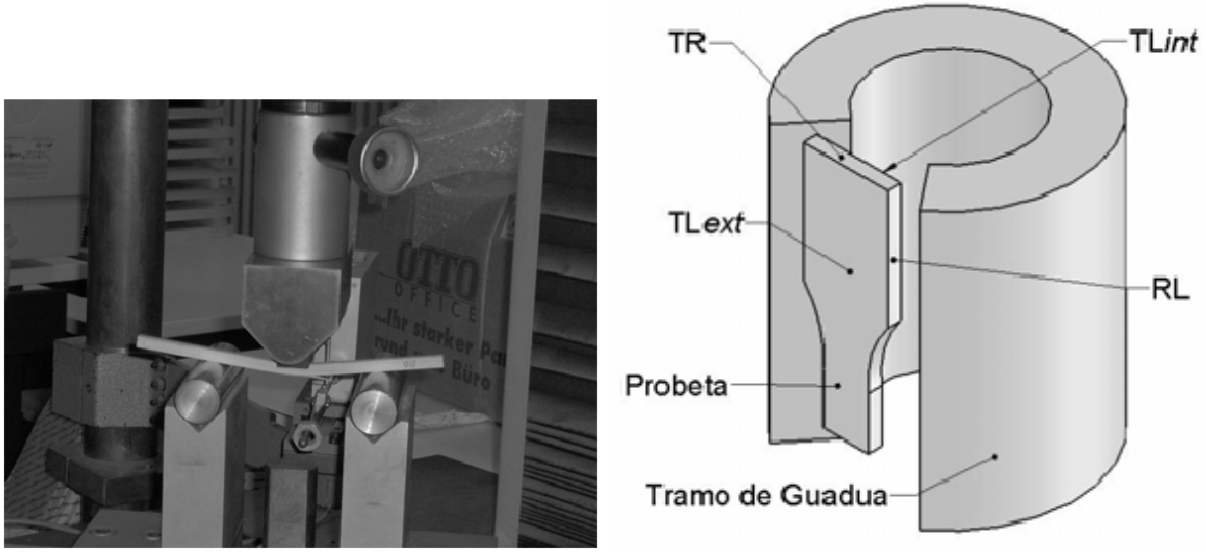


Figure 2.19: (Left) Flexural breaking test, from [GMABS07]. (Right) Construction of the test probes, [MAGBS07].

The Brinell indentation test provides information about the hardness of the material. The indenter is a sphere of 10 *mm* radius made of steel or tungsten, which is pressed against the bamboo sample by exerting a force of 29 *kN*. The observable quantity of this experiment is the diameter of the indentation. In [MAGBS07], Brinell tests for different orientations of a test probe are made. As one expects, the inside of the culm is softer than the outside (21 to 24 at the inner side N/mm^2 against 30 to 40 N/mm^2 at the outer side). This tests also confirm the increase in hardness due to lowering the relative humidity. [GMABS06].

The drying induced shrinkage of bamboo culms as a macroscopic material is different on the three main directions, radial, tangential and longitudinal. For *Moso bamboo* it has been measured as function of the moisture content, from the water saturation point to oven dry condition (0 moisture content); with measurements picked at different points with respect to the culm center (see [Fig. 2.20]). In [YJHS08], You and collaborators authors report that the shrinkage in the tangential direction varies with the radial direction, with outer layers having higher values than inner ones, from 7.4% down to 5%. The longitudinal shrinkage has a single value at less than 2%. From this results You concludes that the bamboo fibers resemble late-wood of conifers, while parenchyma would resemble early-wood.

In [MA06], Montoya presented experimental results of guadua drying induced shrinkage. Using culm samples of 15*mm* longitudinal, 30*mm* tangential and 8*mm* radial dimensions, he measured shrinkage while monitoring the sample weight (corresponding to the equilibrium moisture content in the sample), at different environment moisture values. The expansion coefficient α is defined as the percentage difference between the length in the wet condition l_w and the dry sample length l_0 :

$$\alpha = \frac{l_w - l_0}{l_0} \times 100(\%), \quad (2.13)$$

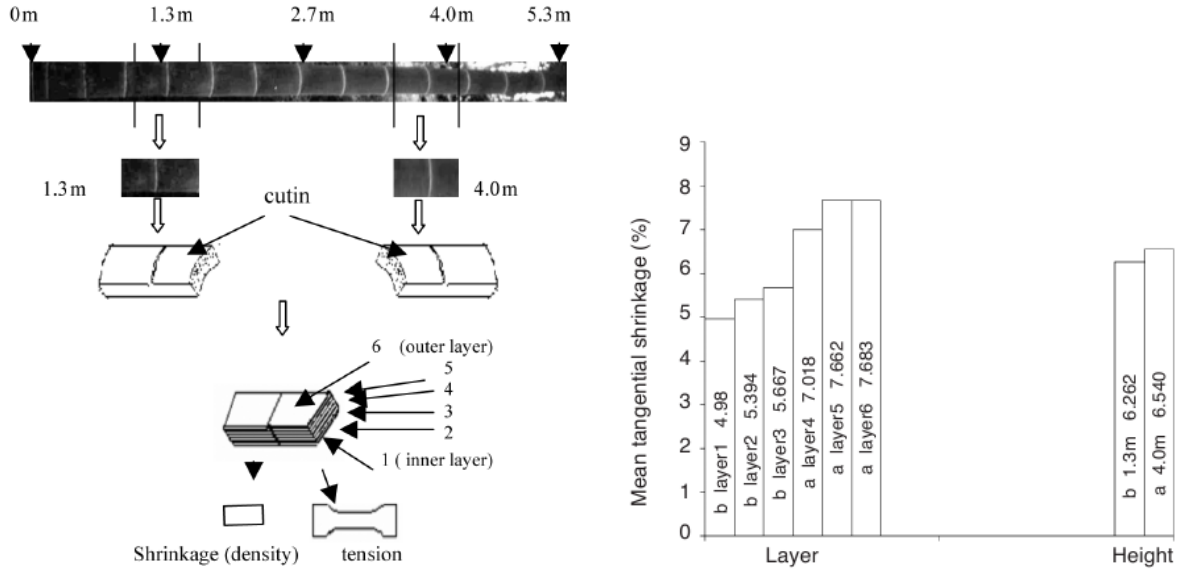


Figure 2.20: The bamboo culm mechanical properties vary both on the height of the culm and on the radial direction. [YJHS08]

where the wet condition corresponds to an moisture content of 85%. For the tangential direction he obtains $\alpha_t = 10.6 \pm 2.7$, for the radial direction $\alpha_r = 7.0 \pm 1.0$ and for the longitudinal direction $\alpha_l = 0.8 \pm 0.1$. This implies that drying induced shrinkage in bamboo *Guadua Angustifolia* occur primarily on the radial-tangential plane. Therefore the model I introduce will disregard the deformations in the longitudinal direction.

2.3 The physics of drying

2.3.1 Chemical potential

Water flows in the bamboo due to pressure and osmotic gradients. Thermodynamics describes this flux of particles by means of the chemical potential: The difference in chemical potential equals the potential barrier that will bring two neighbor systems into diffusive equilibrium. In general for a species j , the chemical μ_j potential is given by

$$\mu_j = \mu_{j0} + \underbrace{RT \ln a_j}_{\text{concentrtn. gradient}} + \underbrace{\bar{V}_j P}_{\text{pressure gradient}} + \underbrace{m_j g h}_{\text{grav. pt. ntl.}} \quad (2.14)$$

$$= \mu_{j0} + \bar{V}_j (P - \Pi_s - \tau) + m_j g h \quad (2.15)$$

Here \bar{V}_j is the molal volume of the species j , i.e. the differential increase in the volume of the system when a differential amount of species j is added to the mixture when keeping everything

else fixed, $\bar{V}_j = \left(\frac{\partial V}{\partial n_j} \right)_{T,P,E,h,n_i}$. As a first approximation, one can take just the volume per mole of substance (for water $\bar{V}_w = 18 \times 10^{-6} m^3 mol^{-1}$). The *gravitational pressure*, m_j is the mass per mole, for water $0.018016 kg mol^{-1}$. As the relevant distances are of the order of $1 \mu m$ it generates pressures of the order of $9.8 mPa$.

The activity a_j is defined as the product of a constant γ (which fulfills $0 < \gamma \leq 1$) and the concentration: $a_j = \gamma_j c_j$. The *concentration gradient* can also be written as a function of the osmotic and the matric potentials:

$$RT \ln a_j = -\bar{V}_w \Pi = -\bar{V}_w \left(\overbrace{\Pi_s}^{osmotic} + \overbrace{\tau}^{matric} \right) \quad (2.16)$$

While the osmotic potential Π increases with the concentration:

$$\Pi_s = RT \sum_j c_j \quad , \quad (2.17)$$

the water activity decreases when more solutes are added. The *Matric Potential* is related to the presence of interfaces, due to colloids or membranes, which decreases the thermodynamical activity of the water. In such cases, water has less tendency to react chemically in the bulk or to escape to the surrounding vapor phase:

$$\tau = -\frac{RT}{\bar{V}_w} \ln \gamma_w \quad (2.18)$$

As a first approximation, water inside the plant can be taken as a homogeneous mixture for which the osmotic pressure does not change the water flux.

The *Laplace pressure* will give the difference between the hydrostatic pressure inside of the filled cells and the atmospheric pressure due to the presence of the water air interface. Its value is given by the relationship $\Delta P = 2\gamma \times C$, where C is the curvature, in general: $\frac{1}{R_1} + \frac{1}{R_2}$, where R_1 and R_2 are the principal radii of the surface. For a sphere $\Delta P = \frac{2\gamma}{R}$. If R equals the size of a pit hole (about $10^{-6} m$ from the graph [Fig. 2.15]) and the surface tension for water-air is $72 mJ/m^2$, then²

$$\Delta P = \frac{2\gamma}{R} \approx \frac{146 \times 10^{-3} N/m}{1 \times 10^{-6} m} = 146 kPa = 0.146 MPa \quad . \quad (2.19)$$

Summarizing, the Laplace pressure will be the determinant force in the first stages of drying. Actually, one of the methods to avoid cracks in bamboo drying is to add a surfactant to the water where culm is immersed for chemical treatment before drying. [Sia84]

Water Potential:

²The reader may wonder how a cell may sustain forces this high. Don't forget that Laplace's overpressure is related to capillary interfaces, and only appear during drying. At a living plant, the symplasm is a continuous body of water and therefore there is no interface and no Laplace overpressure. Besides this, the cell wall is a very rigid material with a reported elastic modulus around $28 GPa$ [OWA06].

The chemical potential per unit volume of water is:

$$\mu_w = \mu_w^* - \bar{V}_W \Pi + \bar{V}_W P + m_w g h \quad (2.20)$$

From which the water potential is defined as:

$$\Psi = \frac{\mu_w - \mu_w^*}{\bar{V}_W} = P - \Pi + \rho_w g h \quad (2.21)$$

$$\Psi = \Psi_P + \Psi_\Pi + \Psi_h \quad (2.22)$$

Water will flow in the direction of lowering the water potential.

2.3.2 Capillarity

The surface tension is responsible for the stable shapes that take liquids, as droplets of oil above water and soap bubbles. Its physical origin is the unfavorable energy state that the molecules of the surface of the liquid have in relation with those in the bulk of the liquid. In the midst of the liquid molecules interact with neighbors at all directions, on the contrary surface molecules lack neighbors at the interface side. The units of *surface tension* $\gamma [=] K g \cdot s^{-2}$ allow two interpretations. For one side, γ can be interpreted as the energy that has to be supplied to increase the surface area of the interface between liquid and gas on a droplet, as is depicted in [Fig. 2.21] (left). On the other hand, think of a rigid frame that takes the shape of three sides of a rectangle, while the other side is a rod free to move in the frame. If this is dipped in a mixture of glycerin, water and soap, a film is created. $\vec{\gamma}$ is a force (per unit length) normal to the rod in the plane of the surface and directed toward the liquid, which pushes the rod in the direction of the liquid [Fig. 2.21] (center)

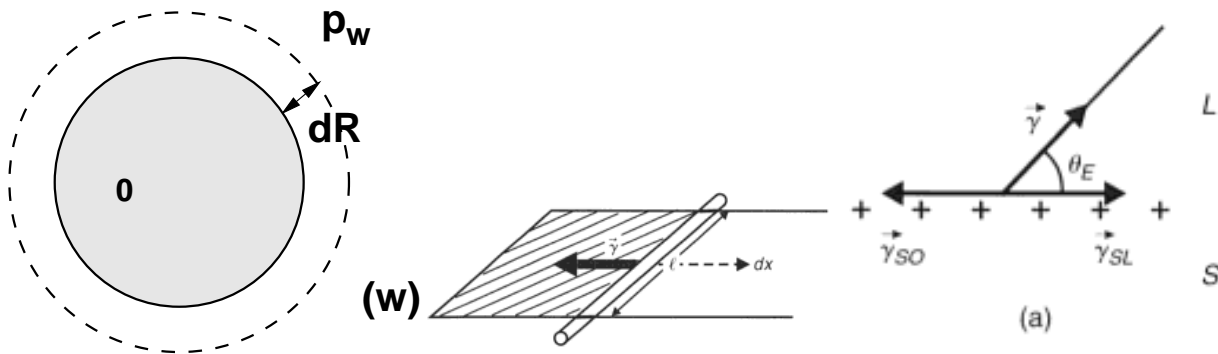


Figure 2.21: (Left) Laplace overpressure inside an spherical droplet. (Center) Laplace force per unit length $\vec{\gamma}$. (Right) Determination of the contact angle θ_E [GBWQ04]

The surface tension will be the source of overpressure existing inside drops and bubbles. For instance take a sphere of oil which has a surface area A , and is immersed in water. If we want to change the area by a differential dA , by means of a displacement dR , the pressure of the oil

against the surface will generate a positive work and the pressure of the water a negative work. The sum of this two has to equal the change of energy of the surface. In equilibrium this adds up to zero, so one can calculate the difference between the pressures:

$$\Delta p = p_o - p_w = \frac{2\gamma_{ow}}{R} \quad (2.23)$$

More generally, Laplace generalized this for any surface. *The increase of hydrostatic pressure Δp that occurs upon traversing the boundary between two fluids is equal to the product of the surface tension γ and the curvature of the surface $C = \frac{1}{R} + \frac{1}{R'}$:*

$$\Delta p = \gamma C = \gamma \left(\frac{1}{R} + \frac{1}{R'} \right) \quad (2.24)$$

The bamboo drying deals with triple interfaces water-air-solid. In this context *total wetting* represents the case in which a small quantity of liquid in contact with the surface spreads completely. If it creates a droplet in the surface there will be *partial wetting*. The physics beyond this is related to the energy needed to create a surface: the spreading parameter is defined as the subtraction of the energy of the dry substrate minus the energy of the wet substrate. For the partial wetting it is also important to know the angle that makes the interface between solid, liquid and air. There is a surface tension at each interface, that can be interpreted as a force. The *Law of Young-Dupré* relates the contact angle with the energy of the three interfaces (see [Fig. 2.21](Right)):

$$\gamma \cos \theta_E = \gamma_{SO} - \gamma_{SL} \quad (2.25)$$

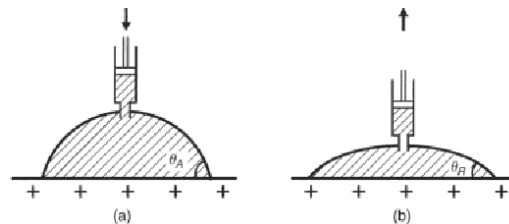


Figure 2.22: Advancing angle when the drop is inflated, receding angle when the drop is deflated, from [GBWQ04]

The contact angle is not unique. Take a droplet on top of a surface. Suppose you add water to the droplet by means of a syringe. The triple point will not move instantly, the contact angle may grow first up to a value called the advancing angle. Pumping water out of the droplet allows to find the receding angle [Fig. 2.22]. This hysteresis is the cause of droplets to get stuck inside capillaries (as in a straw). For the water front inside a porous medium this will give a sort of stability, as the receding surfaces have to get to the receding angle before start moving.

2.3.3 Drying dynamics

Drying of cellular material happens by a succession of different stages, described in the literature, and shortly reviewed in [Section. 2.2]. The first stage of drying consists on the removal of the free water: the moisture content that is hold by physical processes to the plant. It is divided in two sub-stages. A first one starting right at the moment that the plant is sawed (or after it has finished the soaking on preservative solutions). Most of the water in xylem and phloem is drained out by the action of gravity. On the contrary, both water content inside the cell themselves, as well as the water adsorbed within the cell walls still remains. There is very little information on the literature about this first sub-stage of drying, since it has proven not to have a large impact on the crack initiation. Therefore, the literature is focused into different stages (see, for example, [Nie08]). The present research does not study this sub-stage.

The second sub-stage of drying is driven by evaporation, and creates a capillary interface that recedes cell by cell into the stem. Parenchyma cells are connected by small holes known as pits, of the order of 1 or 2 μm , creating a single body of water. When the drying interface gets to a pit, it generates a surface with a curvature of the order of the size of the pit, causing a Laplace under-pressure inside the cells [Fig. 2.23]. This under-pressure can be high enough as to collapse a cell, if the wall stiffness is not strong enough to stand it. In fact, one handling method to reduce the risk of fracture in drying bamboo culms is to add a surfactant to the water solution, in order to decrease the surface tension and the magnitude of this under-pressure [Sia84]. A cell will only collapse if detaches of the neighboring cells at the tricellular junctures. A second stage of drying is driven by diffusion of water among the cell walls, and from them to the atmosphere. The water loss causes shrinkage of the cell walls, which turns into the shrinkage of the bamboo structure.

Let me start by focusing on the first drying stage. To understand the way capillary forces affect the drying dynamics, think of the cell that is being emptied is modeled as if it was an almost filled capillary tube, subject to evaporation over the air-water interface [Fig. 2.23] (b-d). Towards the beginning of the drying process the radius of curvature is larger than the radius of the opening of the pore. As water evaporates, the radius of curvature decreases until it is equal to the radius of the pore. At this point both the curvature as well as the capillary pressure are at a maximum (the radius at a minimum), as any further evaporation will decrease the curvature (increasing the radius).

The way this may affect drying is shown in [Fig. 2.23] (e-l). Initially almost all the lumens will be filled with water, with probably a few bubbles of different sizes. Drying takes place at the air exposed surfaces. Wider capillaries will dry first as the Laplace pressure generated at smaller pores will be higer, so smaller pores will pump water out of wider ones[XDSW08]³

³ [XDSW08] studies the drying of a porous medium by means of creating a sample of particles in a liquid which can be studied by optic means. In their work they proved that during drying the first capillary bonds that dry are those with a bigger radius, as is assumed for pore network simulations. There are two stages of drying, during compactification the particles aggregate and pack into structures creating the network of pores. During the second phase there are invasions of bursts of drying. They measure the probability of the bursts as a function of the area, and get a power-law distribution. The authors claim this to be in agreement with invasion percolation. The functional form found is:

$$P(A) = A^{-\alpha} e^{-A/A^*}, \quad (2.26)$$

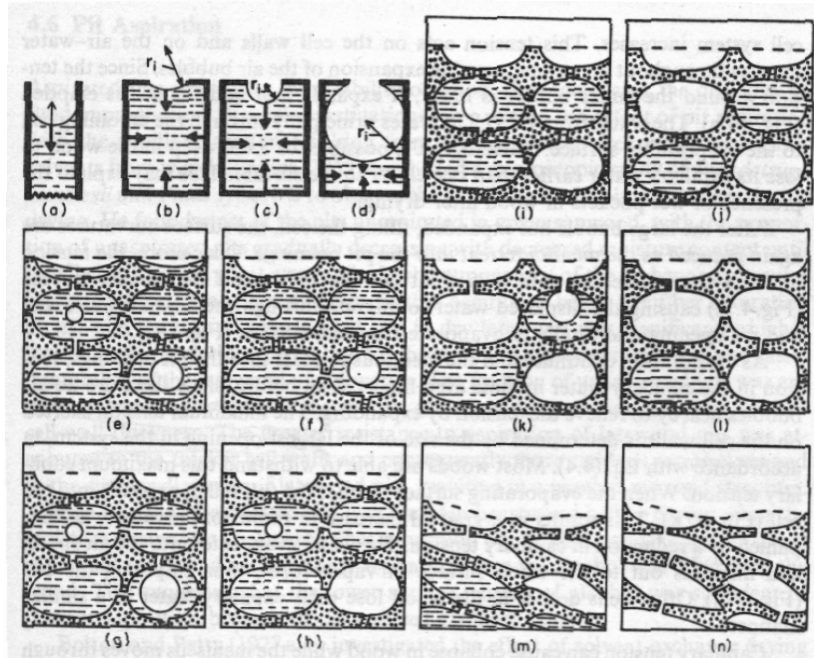


Figure 2.23: Free water evaporation from wood. (a) The surface tension on the air-water interface is interpreted as a force per unit length. (b) - (c) Siau, [Sia84], argues that the surface tension magnitude changes when the water evaporates: goes from an initial value in (b), increases to a maximum when the surface has the curvature equal to the inverse of the pore width; and then is reduced again, when the radius is larger. Notice that as the Laplace's pressure accounts for the difference between the liquid and the air, the arrows that are depicted in the horizontal walls and the lower one would not be present in a saturated porous medium. (e) - (g). This implies that widest pores dry first, including bubbles inside the system, as smaller pores “pump out” water from wider ones. (h) - (i) This may cause the wood to contract.

After the surface cells are emptied, the bigger air bubbles (in case they exist) will increase in size until they occupy the whole cell they are in [Fig. 2.23](g-h), until all cells with a bubble are emptied [Fig. 2.23](j). Afterward, the wider capillaries will start emptying, followed by the cells they are attached to. The maximum tension exerted on the cell walls is determined by the size of the smallest opening in the system. The capillary induced pressure has been studied numerically in other system: a virus during desiccation [CDM⁺09]; in that case the capillary pressure is also seen as a cause of collapse.

The factors that influence collapse in plant cells are:

1. Small pit-membrane openings create high capillary tension during drying (and they also reduce permeability).
2. High surface tension of the liquid being evaporated, so a way to reduce the collapse is to

with $\alpha = 1.6 \pm 0.1$, $A^* = 850 \pm 150 \mu m^2$.

reduce the surface tension of the liquid being evaporated.

3. Low density tissues with weaker cell walls.
4. Elevated temperatures reducing the cell wall strength.

2.4 Drying effects on the bamboo tissues

2.4.1 Plasmolysis

A living cell at equilibrium will have hydrostatic pressure (of about 1 MPa [Nob09]) in its interior that will give rigidity to the cell wall. This phenomenon is called *turgor pressure*. A reduction of the water potential and subsequent volume loss is represented in [Fig. 2.24]. This can lead to plasmolysis: the separation of the plasma membrane from the cell wall. On a plasmolyzed cell, the water in the symplasm can not transmit forces to the cell walls. In the capillary model of [Chapter. 5] this is taken into account by applying a deformation threshold after which the plasmolyzed cells do not suffer from hydrostatic applied forces.

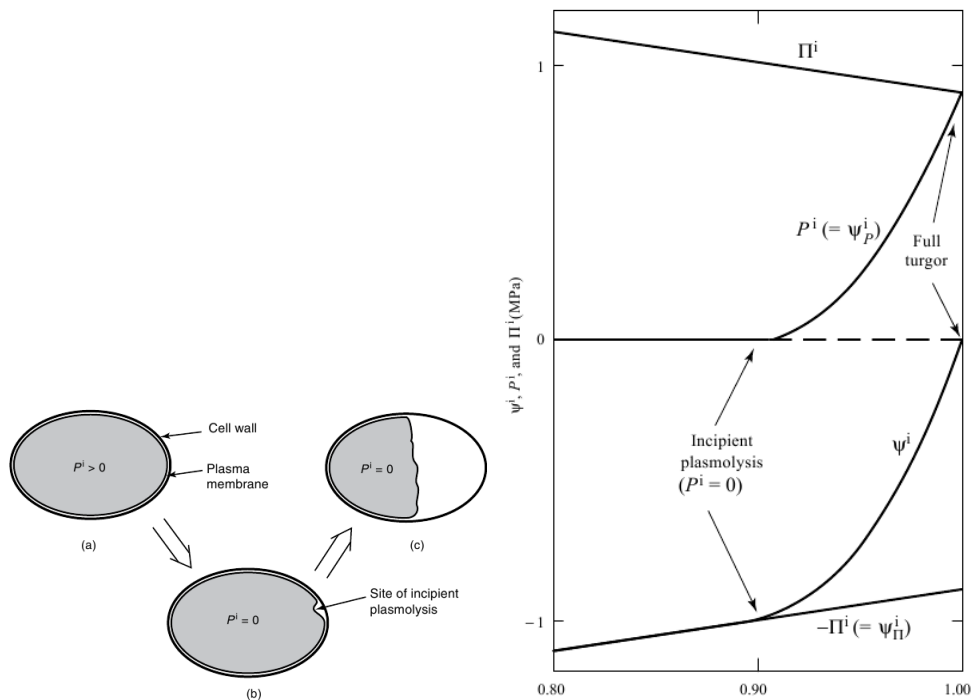


Figure 2.24: (Left) Position of plasma membrane during plasmolysis, from [Nob09]. (Right) Höfler diagram. Shows the relationship between the water potential ψ^i , the hydrostatic pressure P^i , and the osmotic pressure Π^i in a plant cell for various protoplast volumes, from [Nob09].

2.4.2 Drying and cell collapse

Obataya et. al., [OGT04, OGP05], studied the inhomogeneous shrinkage of Green cane due to the collapse of parenchyma cells. For the relative thickness, they found that moisture reduction between 200% and 20% resulted in a 10% thickness reduction [Fig. 2.25], [OGT04]. More interestingly, the shrinkage was found to be inhomogeneous, due to the collapse of parenchyma cells, as shown in [Fig. 2.25]. High temperatures and the waxy epidermis of bamboos are also a cause of collapse of parenchyma cells, so the authors recommend to do a fast drying by means of low humidity content, and to remove the nodes to prevent collapse. Drying induced fractures have been captured by means of laser scanning microscopy, by Sakagami [SMO09].

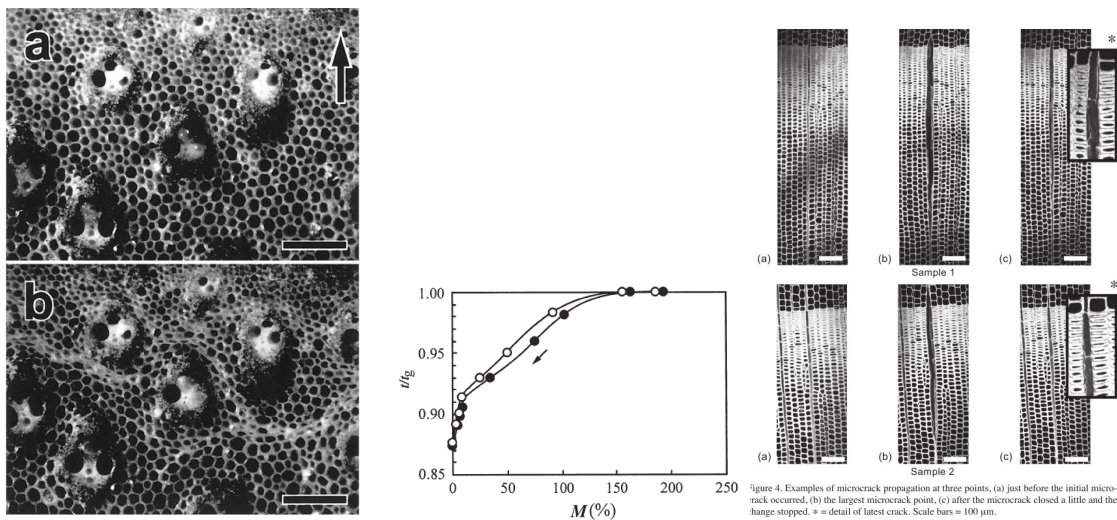
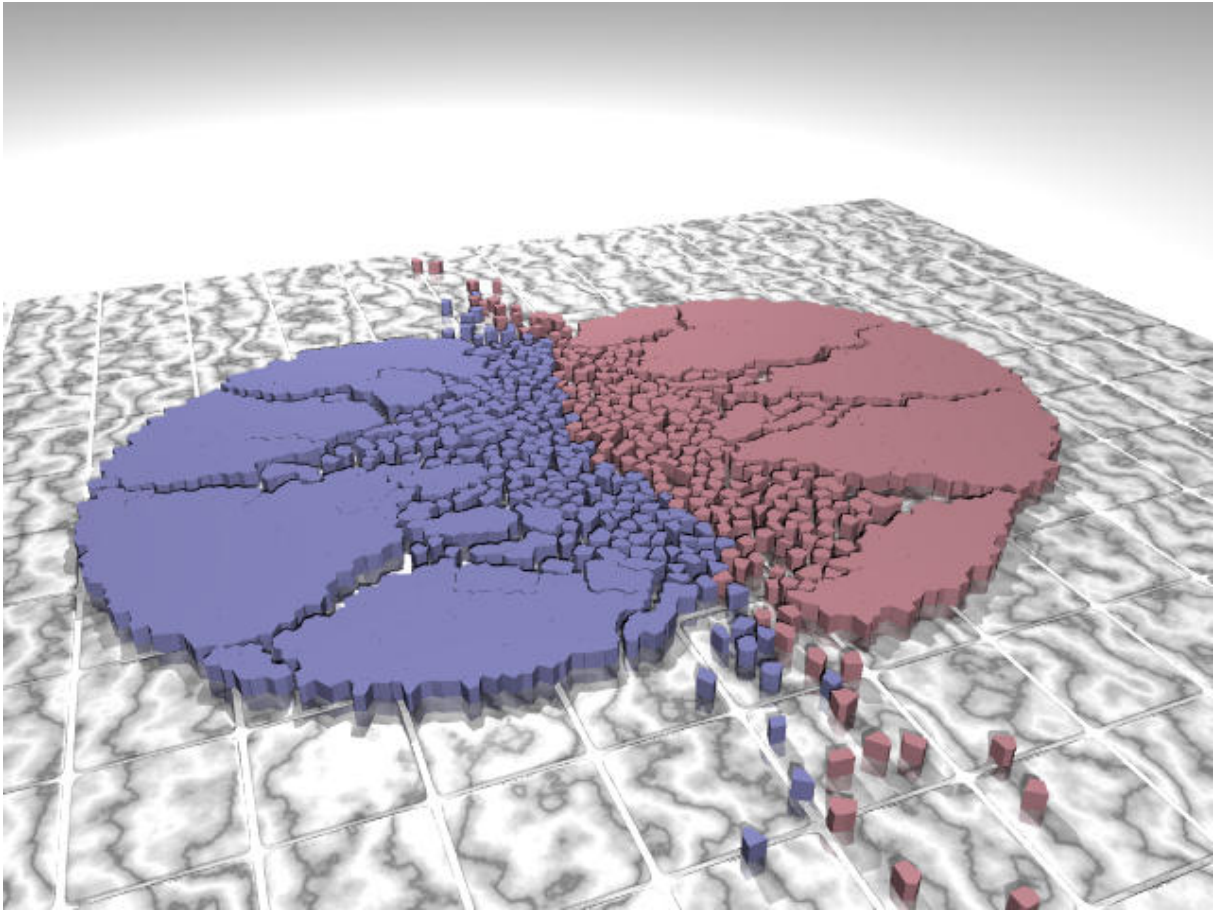


Figure 2.25: (Left) Cross section of a cane during drying, dried at 20 C and 65% relative humidity for (A) 2 hours, (B) 4 hours, from [OGT04]. The arrow indicates the radial direction. (Center) Change in relative thickness of cane during drying as function of moisture content, from [OGT04]. (Right) Drying induced fractures, as seen by confocal laser [SMO09]

For woods it has been proven in the literature how high drying temperatures (more than 60 Celsius) both increase the drying speed, but also generate more cracks. The reason is that the cell wall softens when temperature is higher than 60 Celsius at a moisture content of around 30 %, and this threshold varies with moisture content [Lab08]. The relative effect of this two different mechanisms, either uneven shrinkage or capillary induced collapse, will be the subject of the study of the methods proposed in the following chapters.



Fragmentation of solid disks due to impact, [WKHK04, HWK06, CWKH08]

Fracture, critical phenomena and statistical models of fracture

The field of statistical models of fracture provides a clever and insightful way to study fracture. In the present chapter I start by making a review of basic concepts of elasticity and fracture, in order to clarify the notation [Section. 3.1][Section. 3.2]. The interested reader can follow any of the standard textbooks on the subject [SH06, HR90, GSS06]. In [Section. 3.3] I present a short review devoted to the results of the theory of critical phenomena which are more related to the field of fracture. The literature of this subject is quite extensive, the interested reader may check the textbooks: [Car88, BC06, Her10]. In the final section of this chapter I present some more recent results from the theory of statistical models of fracture, that are specially relevant to the models to be shown in the next chapters of this thesis [Section. 3.4]. Some classic review articles in this field are: [HR90, ANZ06, PHC10].

3.1 Elasticity

In a deformable elastic body the relative distance between any two material points \vec{r}_{i-j} changes when there is a change in the external forces \vec{f}_{ext} (also called loads). Displacement gradients, strains ϵ , are related to changes in load intensities, stress σ , and their rates through the constitutive laws.

If the history of loading and unloading is the same, that is the loaded body recovers its original configuration after the forces have been removed, it is called elastic. Then the stress-strain curve shows no hysteresis. If the relationship is linear it is called linearly elastic. Furthermore if the mechanical properties of the body do not depend on position of the material point, it is called homogeneous. If they are independent of direction, will be isotropic, otherwise would be anisotropic. A subset of anisotropic elastic bodies are the orthotropic elastic, for which some or all of the properties differ in mutually orthogonal directions. In such a case Young's experiment provides the definition of Hooke's law: for an homogeneous block of size $w \times w \times l$ subject to

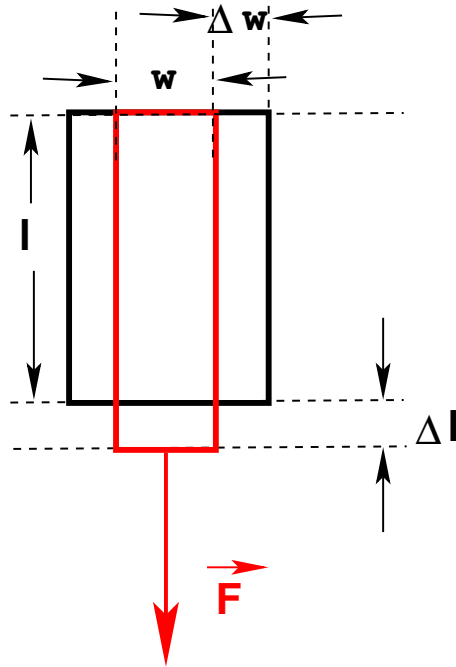


Figure 3.1: Young's experiment

a uniaxial force F , the stress σ is given by:

$$\sigma = \frac{F}{w^2} = Y \frac{\delta l}{l} = -\frac{Y}{\nu} \frac{\delta w}{w} \quad (3.1)$$

with Y the Young modulus and ν the Poisson ratio [Fig. 3.1].

If the deformation causes energy dissipation the response of the system will be delayed, introducing a characteristic delay time τ_d into the problem. This is called viscoelasticity or viscoplasticity, depending on whether the charge is above or below the yield point.

A material is called *brittle* if there is a threshold called *ultimate stress*, such that the material breaks if the strain is larger than it. For a *ductile* material there is also a threshold for which the constitutive relationship is no longer linear, and it is called the *yield strength* σ_Y . After the loading takes the material pass this point there will be remnant deformations when the solid is unloaded. A ductile material breaking point is also called the ultimate stress, see [Fig. 3.2]

The *strength* of the material is either yield stress or ultimate stress at fracture, depending on the situation. This concepts have meaning when the body material, geometry, temperature and the stress state are known: a sheet of paper is brittle to tension but will be ductile to compression. (see, for example, [vK11]). This transition may also depend on the temperature and speed of deformation.

At any time during deformation, the solid can be parametrized by a set of coordinates \vec{r} , while for the coordinates of the undeformed I will use in this text the unprimed notation \vec{r}' . The *displacement field* is defined in the literature by $\vec{u} = \vec{r}' - \vec{r}$. The *symmetric strain tensor* is defined

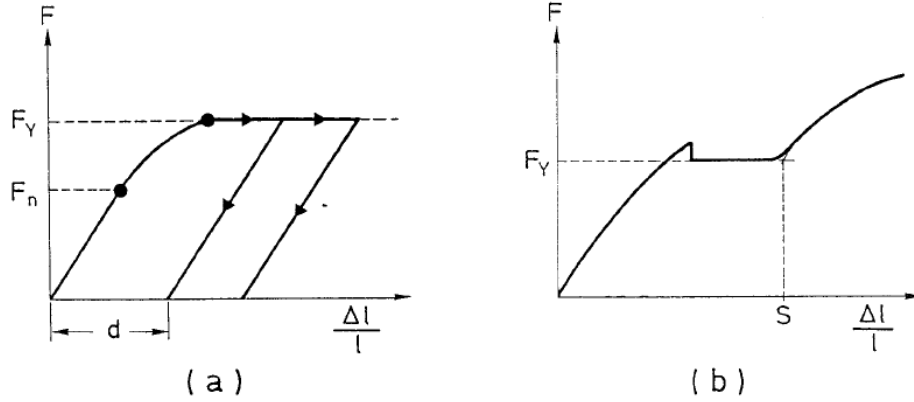


Figure 3.2: Constitutive law for (a) ideal plasticity. The yield point is marked as F_n . After it has been reached the young modulus is preserved, but some deformation d is no longer revertible. (b) a mild steel. From [Her91]

as:

$$\epsilon_{ik} = \frac{1}{2} \left(\frac{\partial u_i}{\partial x_k} + \frac{\partial u_k}{\partial x_i} \right). \quad (3.2)$$

At equilibrium the internal forces acting on an elastic body will vanish, only *tractions* (surface forces) and body forces will be taken into account. Then

$$\vec{F}_i = \int_V (b_i + \sum_j \frac{\partial \sigma_{ij}}{\partial x_j}) dV \quad (3.3)$$

Where σ_{ij} is the stress tensor. The body is in an stable condition when this forces add up to zero. For a linear elastic solid, the linear relationship between strain stress is described by the equation:

$$\sigma_{ij} = \sum_{k,l} \mathbb{C}_{ijkl} \epsilon_{kl}, \quad (3.4)$$

where I used the common notation for the elastic module tensor: \mathbb{C}_{ijkl} . In the case of isotropic medium the stress can only depend on the invariants: $\sum_{\alpha} \epsilon_{\alpha\alpha}$, $\sum_{\alpha\beta} \epsilon_{\alpha\beta} \epsilon_{\beta\alpha}$ and $\sum_{\alpha\beta\gamma} \epsilon_{\alpha\beta} \epsilon_{\beta\gamma} \epsilon_{\gamma\alpha}$, so the theory is invariant under coordinate transformations. The energy is a quadratic form of the strain:

$$E = \frac{1}{2} \left(2\mu \sum_{\alpha\beta} \epsilon_{\alpha\beta} \epsilon_{\beta\alpha} + \lambda \left(\sum_{\alpha} \epsilon_{\alpha\alpha} \right)^2 \right) \quad (3.5)$$

λ and μ are the Lamé constants, related to Young and Poisson by:

$$\lambda = \frac{Y\nu}{(1-\nu)(1-2\nu)} \text{ and } \mu = \frac{Y}{2(1+\nu)} \quad (3.6)$$

The Hooke's law reads:

$$\sigma_{\alpha\beta} = 2\mu\epsilon_{\alpha\beta} + \lambda\delta_{\alpha\beta} \sum_{\gamma} \epsilon_{\gamma\gamma} \quad (3.7)$$

The elastic tensor simplifies to:

$$\mathbb{C}_{ijkl} = \lambda\delta_{ij}\delta_{kl} + \mu(\delta_{ik}\delta_{jl} + \delta_{jk}\delta_{il}) \quad (3.8)$$

$\sigma_{\alpha\beta}$ is a force per unit area. The convention is that for a square shaped volume element, oriented as shown in the figure [Fig. 3.3], the force acts in the β direction for a surface whose normal is oriented in the α direction.

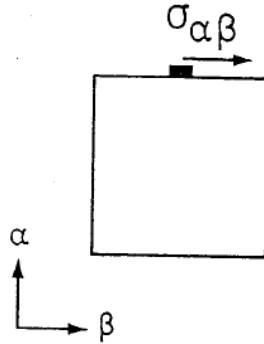


Figure 3.3: Convention for defining $\sigma_{\alpha\beta}$, from [Her91]

The equation of motion, from (Eq.3.3), reads:

$$\rho\ddot{u}_{\beta} = \sum_{\alpha} \partial_{\alpha}\sigma_{\alpha\beta} + f_{\beta} \quad (3.9)$$

In absence of body forces, $\nabla \cdot \sigma = \sum_{\alpha} \sigma_{\alpha\beta} = 0$, thus one obtains the equation for the displacement field:

$$(\lambda + \mu)\nabla(\nabla \cdot \vec{u}) + \mu\nabla^2\vec{u} = 0 \quad (3.10)$$

Which is called Lamé or Navier equation. If each volume element is allowed to rotate, the rotation being described by the variable ϕ , the problem is called asymmetric (Cosserat) elasticity. Strain, in this case, is given by:

$$\epsilon_{\alpha\beta} = \partial_{\alpha}u_{\beta} - \sum_{\gamma} \varepsilon_{\alpha\beta\gamma}\phi_{\gamma} \quad (3.11)$$

with ε the totally antisymmetric tensor. The torsion tensor is defined as:

$$k_{\alpha\beta} = \partial_{\alpha}\phi_{\beta} \quad (3.12)$$

Stress and moment are:

$$\sigma_{\alpha\beta} = (\mu + \alpha)\epsilon_{\alpha\beta} + (\mu - \alpha)\epsilon_{\beta\alpha} + \lambda\delta_{\alpha\beta} \sum_{\gamma} \epsilon_{\gamma\gamma} \quad (3.13)$$

$$\mu_{\alpha\beta} = (\gamma + \delta)k_{\alpha\beta} + (\gamma - \delta)k_{\beta\alpha} + \eta\delta_{\alpha\beta} \sum_{\gamma} k_{\gamma\gamma} \quad (3.14)$$

Where α and β describe the asymmetry. In this case the equations of motion in equilibrium or Cosserat equations, are:

$$(\mu + \alpha)\nabla^2 \vec{u} + (\lambda + \mu - \alpha)\nabla(\nabla \vec{u}) + 2\alpha\nabla \times \phi = 0 \quad (3.15)$$

$$(\gamma + \delta)\nabla^2 \vec{\phi} + (\beta + \gamma - \delta)\nabla(\nabla \vec{\phi}) + 2\alpha\nabla \times \vec{u} - 4\alpha\vec{\phi} = 0 \quad (3.16)$$

For $\alpha = 0$ the Lamé equation is recovered.

3.2 Fracture

Four different disciplines study fracture, namely: applied mechanics, engineering, materials science and statistical mechanics. In relation to the length-scales they are interested in, Herrmann proposes an overlapping categorization that I reproduce in [Fig. 3.4]. Statistical mechanics should also be included ranging through all length-scales.

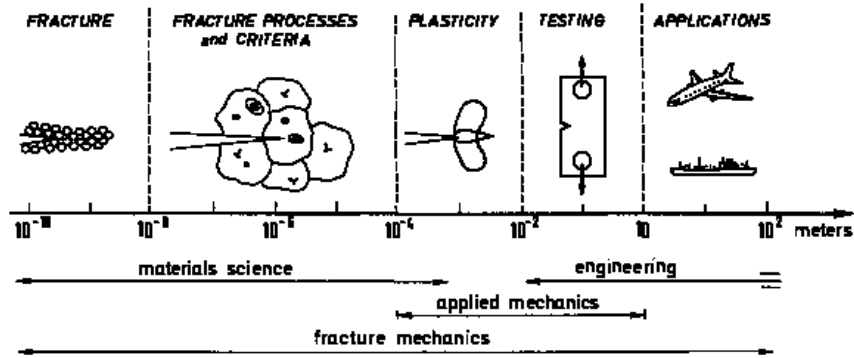


Figure 3.4: Schematic representation of the study of fracture on different length scales. From [HR90]

The question all these disciplines want to answer is: why do materials break? since the early works of Leonardo da Vinci it is known that fracture initiation and grow show strong size effects: a long wire in tension is more likely to break than a short one. These size effects are caused by the disorder of the material, and thus they have to be accounted for by statistical methods and models. *In this context, fracture can be seen as the outcome of irreversible dynamics of long-range interacting, disorder system* [ANZ06].

3.2.1 Continuum applied mechanics

From the point of view of continuum applied mechanics, *crack initiation* is a highly nonlinear problem; while the existing crack has to be accounted as a boundary condition for the elastic strain, its shape does also depend on the stress field acting on it. Moreover, depending on the loading conditions, three fracture modes are defined in the literature: (I) Tensile, (II) Shear, (III) Tearing [Fig. 3.5]. Any loading can be treated as combination of these three modes.

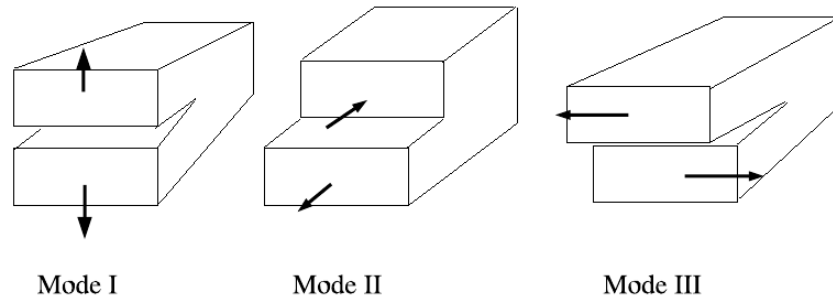


Figure 3.5: Fracture modes, from [ANZ06].

Although the criteria for failure growth describe a singularity in the stress field, in the real material there will be non-linear and inelastic effects that prevent “infinite forces”. The *Fracture process zone* is defined as the volume (or area in 2D cases) that surrounds the crack, and in which nonlinear effects take place. Assuming that the actual state of strain or stress of the material uniquely determines the behavior, even when it is close to the failure limit, a *failure condition* is usually defined in the literature as:

$$F(\sigma_{ij}) = 0 \text{ or } G(\epsilon_{ij}) = 0. \quad (3.17)$$

The *failure surface* is the graphical representation of this subset of the six dimensional stress space.

Different approaches to define the failure condition have been used in the literature. For example, the strain energy failure condition, due to Griffith, assumes a given crack geometry and computes the stress field acting on it (see, for example, [ANZ06]). The analytical calculation looks for the energy that is needed to open an elliptical crack, and sets it as a threshold value to make the process favorable.

Strain energy [Gri20] Fracture, as thermodynamics dictates, will only be possible whenever it is energetically favorable. For instance in 2D the elastic energy stored in an elliptic crack of length a is

$$E_{el} = -\frac{\pi \sigma a^2}{2E} \quad (3.18)$$

with E elastic modulus, σ the applied stress. The surface energy associated to breaking the molecular bonds is

$$E_{surface} = 2a\gamma \quad (3.19)$$

with γ the surface tension. Total energy has to diminish for the process being viable:

$$\frac{dE}{da} = -\pi\sigma^2 \frac{a}{E} + 2\gamma < 0 \quad (3.20)$$

$$\sigma \sqrt{\pi a} > \sqrt{2E\gamma} \quad (3.21)$$

Other failure conditions are:

Maximum Normal Stress Criterion (W.J.M. Rankine, H.Lamé, C.L. Navier) The material is characterized by two values: tensile strength σ_t and compressive strength σ_p . Diagonalization of the stress tensor gives directions in which the stress are maximum, the so called principal stress. Failure occurs if the maximum principal stress reaches σ_t or the minimum principal stress reaches $-\sigma_p$. The failure surface is a cube in the stress space. This hypothesis describes brittle failure of materials.

Principal strain (Saint-Venant and Bach) The failure occurs at a critical strain ϵ_t . By assuming linear elastic behavior until failure, the resulting failure conditions are:

$$\sigma_i - \nu(\sigma_j + \sigma_k) = \sigma_t \text{ where each } i, j, k \text{ is one of } 1, 2, 3 \quad (3.22)$$

The failure surface is a pyramid with the apex at $\sigma_1 = \sigma_2 = \sigma_3 = \sigma_t / (1 - 2\nu)$.

For drying induced cracks in either thin films or cellular materials cracks initiation comes always from tensile forces. Therefore in the models presented in this work, the failure condition for the different models is that of a threshold value for tensile strength.

3.2.2 Analytical models of fracture

In some special cases the fracture problem, that is the shape evolution of the fracture as function of time and the boundary conditions, has been solved analytically. The description of those models falls beyond the scope of this thesis, so only some key results will be shortly reviewed. Consider first a bundle of fibers with quenched disorder in the form of N_d defects with different strength failure thresholds σ_i , all of them being fatal. The problem of fracture of this system is called *extreme statistics*. It can be shown that the cumulative strength distribution takes the form:

$$1 - F(\sigma) \simeq \exp[-V\rho P(\sigma)], \quad (3.23)$$

where $P(\sigma)$ is the probability distribution of strength of the defects, V is the sample volume and ρ is the defect density.

In general, the set of assumptions usually needed to get closed analytical results are too restrictive for the goals of the present work; therefore I will not pursue them. The interested reader is referred to the review articles and textbooks on the subject (as [Chi05, SH06, HR90, GSS06, Her91] and references therein).

3.3 Critical Phenomena

In this section I present a review of the theory of critical phenomena. For a thorough study, some books are available, as [Her10].

Matter can exist in four different phases, namely solid, liquid, gas and plasma. The same substance can change between some of these states, as the ubiquitous example of liquid water, ice and water vapor. The process of change between phases is called a *phase transition*, and it may be sharp (as the case of liquid opalescence) or gradual, as water evaporation at boiling.

Rigorously speaking, phase transitions corresponds to the set of points of the parameter space in which the thermodynamic potential, or some of its derivatives, becomes non analytic. But *such a non-analyticity can arise only in the thermodynamical limit, when the size of the system is assumed to be infinite* ([Her10]), as for any finite system the partition function consists on a sum over countable function of its parameter, so therefore is always analytic.

In the language of P. Ehrenfest, phase transitions are classified by the degree of the derivative of the thermodynamic potential with respect to the control parameter that first exhibits discontinuity. The intuition of this definition is still used in research to guide scientists through defining the kind of transition taking place, even more when there is no agreement.¹ The more modern classification just defines the phase transition as being *continuous*, when there is no latent heat involved or *discontinuous* when there is latent heat involved. *Critical phenomena* is the study of non-analytic properties of system near a phase transition, and the place of the phase space where it takes place is called a *critical point*.

The physical observable that define the distinction between different phases of the system is called an *order parameter*, and it may not be unique for a given phase transition. Two common examples of phase transitions include the liquid-solid-gas phase transition of water, and the magnetization phase transition in the Ising model.

3.3.1 Fluid system

The equation of state of a fluid system $f(P, \rho, T)$ is usually visualized by the projections on the $P\rho$, PT and ρT planes. In the PT plane the three different states of matter and the lines that represent equilibrium between the phases can be easily distinguished. [Fig. 3.6]

The point where the vapor pressure curve ends [Fig. 3.6] is called the critical point, and its coordinates will be the critical temperature, density and pressure (T_c, ρ_c, P_c) . Beyond this limit, there is no physical difference between liquid and gas phases of the fluid.

For a fluid system there is a difference in density between the liquid phase and the gas phase. Furthermore, for temperatures below T_c , this difference in densities is represented as a flat section of the curve P vs T ; which denotes the coexistence of these two phases in equilibrium. From the point of view of criticality, the difference between the liquid and the gas density acts as an *order parameter* of the liquid gas critical point: "*... a quantity which is non-zero below the critical temperature and zero above it will be seen as a common feature associated with the critical points of a wide variety of physical systems.*" [Sta87]. The flattening of the isotherms in this diagram

¹As is the case of FBM, see [ANZ06, PHC10].

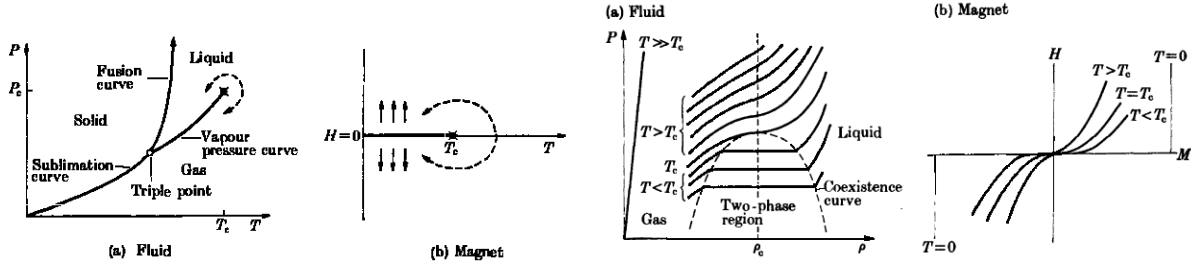


Figure 3.6: (Left) a) Fluid. Projection of the PVT surface on the PT plane, b) Magnet. Projection of the HMT surface on the HT plane. (Right) Isothermal cross sections of the PVT surface. The exponent δ is a measure of the degree of the critical isotherm.[Sta87]

indicate that the isothermal compressibility, defined by

$$\chi_T = \rho^{-1} \left(\frac{\partial \rho}{\partial P} \right)_T, \quad (3.24)$$

diverges to infinity close to the critical point.

3.3.2 Ising model phase transition

The Ising model describes the magnetization of a material discretized by spins lying on the intersection of a square lattice. The interactions between the spins are defined by the Hamiltonian E :

$$E = -J \sum_{\langle i,j \rangle} s_i s_j - H \sum_{i=1}^N s_i, \quad (3.25)$$

then the partition function is:

$$Z = \sum_{\{s_i = \pm 1, i=1, \dots, N\}} e^{-\frac{E}{k_B T}}, \quad (3.26)$$

where s_i represents the spins, and the size of the lattice side is L . H , represents an external magnetic field. The strength of the interaction linking pairs of spin sites $\langle i, j \rangle$ is given by the constant J . The material magnetization is:

$$m = \langle s_i \rangle = \frac{1}{Z} \sum_{\{s_i = \pm 1, i=1, \dots, N\}} s_i e^{-\frac{E}{k_B T}}, \quad (3.27)$$

and can be regarded as an order parameter of the system. In the absence of external field, $H = 0$, the two phases are: ferromagnetic, with $m \neq 0$; and paramagnetic, with $m = 0$. The two directions of the spin are completely equivalent, so the positive and negative spins can be interchanged, $s_i \rightarrow -s_i$; this is called the *Ising symmetry*, Z_2 .

When the system is in the ferromagnetic phase, the material has a magnetization aligned into a certain direction. There is no physical reason to choose any direction, i.e., there is no a priori way to deduce from first principles and boundary conditions which direction will be settled. On any real ferromagnetic magnet the magnetization direction can be regarded as a random binary variable. The disappearance of the symmetry, associated with the establishment of the system's magnetization orientation is called *spontaneously symmetry breaking*.

On the contrary, if $H \neq 0$, there are always some dipoles in the direction of the field. A finite magnetization in the direction of the external field is always present, even at high temperatures.

3.3.3 Universality and critical exponents

The goal of any scientific theory is not simply to describe, neither only to predict the behavior of nature; but to provide a thorough conceptual framework which can also provide answers and links to different unrelated questions. Universality in statistical physics is a clear example. It has shown how physical systems which are completely different at the microscopic level of interactions share the same global behavior; depending only on general characteristics as dimensionality, symmetry, and presence of long-range interactions. Renormalization group is the theory of statistical physics devoted to the study universality. It does it by means of analyzing the fluctuations that happens on a range of length-scales, near a critical point. It has been used in fields as elementary particles, turbulence in fluids, distribution of earthquakes and configurations of polymers.

Following the discussion as presented in [Her10], lets consider the liquid-gas phase transition. For a reduced temperature defined as:

$$t = \frac{T - T_c}{T_c}, \quad (3.28)$$

the specific heat, at fixed volume, in the thermodynamical limit, near the critical point behaves as:

$$C_V = C_{\pm} |t|^{-\alpha}, \quad (3.29)$$

with C_+ (or C_-) refers for $t > 0$ ($t < 0$). Furthermore, the compressibility at fixed temperature

$$\chi_T = \left(\frac{1}{\rho} \frac{\partial \rho}{\partial p} \right)_T, \quad (3.30)$$

where $\rho = N/V$ is the density, also behaves also as a power law:

$$K_T = K_{\pm} |t|^{-\gamma}. \quad (3.31)$$

The liquid-gas transition's order parameter is the difference between gas and liquid densities along the coexistence curve:

$$\rho_L - \rho_G = \rho_c (-t)^{\beta}. \quad (3.32)$$

At the critical isotherm the pressure also scales as a power law:

$$\frac{p - p_c}{p_c} = \left| \frac{\rho_L - \rho_G}{\rho_c} \right|^\delta. \quad (3.33)$$

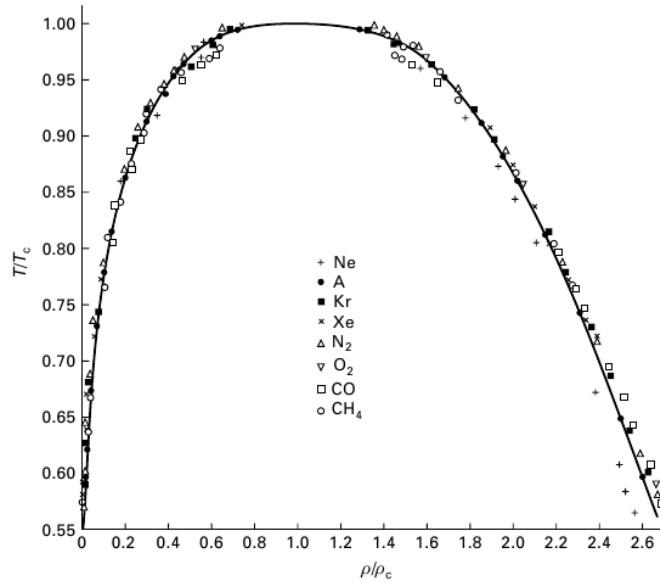


Figure 3.7: Liquid-gas coexistence curve for many fluids become identical when the axes are rescaled with the critical values of density and temperature [Gug45].

The constants α, β, γ and δ , that define the power laws, are not completely independent real numbers; instead they are the same for several different phase transitions. Therefore, they are called *universal*. For instance, the liquid-gas coexistence curves for many fluids fall into the same shape under an scaling of axis by the critical values of density and temperature, as was shown by Guggenheim (see [Fig. 3.7]). The power laws near the critical point can be derived by the *scaling* hypothesis. For the magnetization, for instance, the free energy per unit volume can be assumed as:

$$f(T, H) = |t|^{1/\nu} \Psi_{\pm} \left(\frac{H}{|t|^{\mu/\nu}} \right) \quad (3.34)$$

from this assumption, power laws for magnetization, specific heat and susceptibility arise.

3.3.4 Percolation

The Kirchhoff model is composed by a network of resistors arranged on a quadratic section of a square lattice (see [Fig. 3.8]). The upper and lower boundaries maintain a voltage difference V . The lattice is tilted with respect to the boundaries.

Broadbent and Hammersley (see reference at [HR90]) showed rigorously that this network will not conduct if the concentration of conducting bonds is smaller than some *non zero critical*

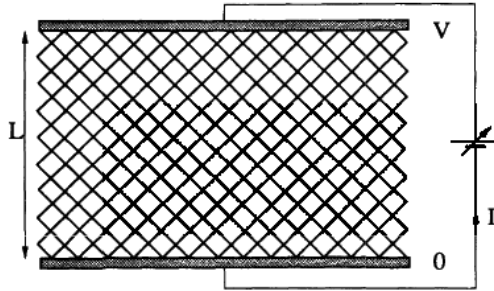


Figure 3.8: The conductance of each bond is a randomly distributed variable. From [HR90]

value. It is intuitively obvious that the conductance will be reduced, what is not so clear is that it drops to zero before $p = 0$. This implies that conductance is not an analytic function for all p , it is singular for some $p = p_c$, which is called the *percolation threshold*.

More generally, take a d -dimensional infinitely large regular lattice of a given topology. There will be a bond present with a probability p absent with probability $q = 1 - p$. Clusters of present bonds will be defined as the sets of bonds which are connected between them: given any two in the set, there is a path that only includes present bonds in the set that goes from one to the other. For the network to conduct, there has to be a cluster that spans through the network, between the boundaries. Above percolation threshold p_c this cluster exists, otherwise it does not. This is the case of bond percolation. Another case will be that of site percolation. In this the subject of study are the nodes, which are present with probability p , or absent with $q = 1 - p$. The clusters are defined in the same way, and a threshold -different to that of the bond percolation- can be found.

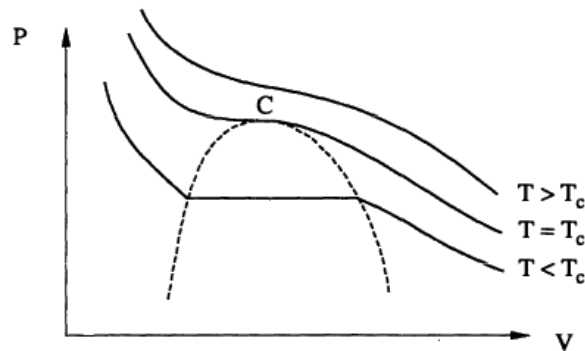


Figure 3.9: Sketch of phase diagram for a real gas. The point marked “C” is the critical point, from [HR90]

While percolation theory was being introduced, the statistical physics community was starting to focus on second order phase transitions or critical points. The figure ([Fig. 3.9]), shows a sketch of the phase diagram of a real gas. If the temperature is above the critical value, there is no

pressure for which the gas liquidifies, before T_c there is. Close to the critical point the gas develops critical opalescence: looks milky. This is due to the fact that it contains liquid droplets with a broad size distribution. In the sixties, a general scaling theory was developed for the behavior for physical systems close to critical points. The percolation threshold p_c is a critical point in the same sense as was described. For a bond percolation problem, taking an infinite regular lattice, the main geometrical property of interest is the cluster size distribution n_s . It gives the distribution of clusters of size s per bond, defined as the probability that a bond belongs to a cluster of size s . The normalization of probabilities implies:

$$q + \sum_{\text{finite } s} s n_s + P_\infty = 1 \quad (3.35)$$

with P_∞ the probability that a bond belongs to the infinite cluster. p_c in this context, is called an *order parameter*, above it P_∞ is non zero and for $p < p_c$, $P_\infty = 0$. This equation also implies that the sum has a similar singularity in p at p_c . This is described by a non-integer *critical exponent* β :

$$P_\infty = A_1(p - p_c)^\beta + \text{not singular terms} \quad (3.36)$$

near the critical point. The other moments of the cluster size distribution will also show singular behavior near p_c :

$$\sum_{\text{finite } s} n_s = A_0(p - p_c)^{2-\alpha} + \dots \quad (3.37)$$

$$\sum_{\text{finite } s} s^2 n_s = A_2(p - p_c)^{-\gamma} + \dots \quad (3.38)$$

where α and γ are critical exponents. Their main property is that the values only depend on the spatial dimensionality of the lattice, not on the type or whether it is site or bond percolation. This property is known as *universality*. In ordinary *critical phenomena* there can only be found a few different universality classes. All systems belonging to the same universality class share the same critical exponents. Further reading [HR90].

3.3.5 Finite size scaling

The analytic models of phase transitions forecast the emergence of discontinuities in the thermodynamical functions (at the critical value of the thermodynamic quantities), only for infinite systems, i.e., when the system dimensions tend to infinity. The correlation length ξ , which may be defined as the length scale of the exponential decay with distance of the order parameter correlating function $e^{-r/\xi}$, diverges at the second order critical point. This implies that for a system of finite size L , as long as ξ/L is small, the effects on the thermodynamical quantities are of the order of $O(e^{-L/\xi})$.

When the system gets close enough to the critical point, $\xi \approx L$, the correlation length tends to the size of the system, so finite-size effects will be of major concern. For example, if the sample is finite and $\xi \gg L$, it will be effectively zero dimensional. The finite-size effects will tend to average the singularities over the region of the parameter scale such that $\xi \approx L$.

Finite size scaling is a technique proposed by Fisher, and studies the way this rounding up happens [Fis71]. Take the three length scales involved in a finite-size system are: ξ , L and a microscopic length a . The thermodynamic quantities depend on the ratios ξ/a , and L/a . *The finite-size scaling hypothesis assumes that close to the critical point the microscopic length drops out* [Car88]. A quantity like the susceptibility χ , which varies as $\xi^{\gamma/\nu}$ for an infinite system, scales as a finite system of size L as:

$$\chi = \xi^{\gamma/\nu} \phi(\xi/L), \quad (3.39)$$

$$= L^{\gamma/\nu} \tilde{\phi}(L^{1/\nu}(T - T_c)) \quad (3.40)$$

with $\phi(u)$ a scaling function that goes to zero when the argument goes to zero. If the system is one-dimensional, χ is an analytic function of T . $\tilde{\phi}(v)$ is a smooth function peaked at $v = v_0$, with the peak localized at the value $T = T_c + v_0 L^{-1/\nu}$. The finite-size scaling hypothesis gives the values of the constants that define the critical exponents of the infinite system.

3.4 Statistical models of fracture

In the previous section the jargon of phase transition was introduced, in order to provide a background for the reader to get into the subject of the statistical models of fracture. Several authors, including Sethna, Zapperi, Herrman and Hansen have used the language and tools of statistical mechanics to understand the physics of failure of materials. In this section I will present some of this models.

3.4.1 Fiber Bundle Models

The failure resistance of stressed fibered materials depends on the way the load is distributed among fibers and their individual characteristics. In bamboo, for example, fibers are supposed to carry most of the load because of its higher elastic modulus. The fiber bundle models (abbreviated in the literature as FBM), present an idealization of a real fibered material. The elements of a FBM [Dan45, PB00, PC03, Sor89] are:

Discretization: The solid can be represented by a set of parallel fibers, aligned regularly. They support only longitudinal deformation.

Failure law: Each fiber is brittle (linearly elastic until failure), all have the same young modulus (E), fiber breaking is instantaneous and a broken fiber would not recover.

Load sharing rule: The load previously hold by a broken fiber is distributed among the remaining ones. It may be (i) global load sharing (GLS) in which the load is homogeneously distributed. In this case is possible to find closed analytical forms. (ii) The load may be distributed only on the closest neighbors. This is called local load sharing (LLS).

Distribution of failure thresholds: The fiber strength σ_i is a random variable with probability $p(\sigma_{th})$ which distributes as $P(\sigma_{th}) = \int_{\sigma_{th-min}}^{\sigma_{th-max}} p(x) dx$. It represents the disorder of the

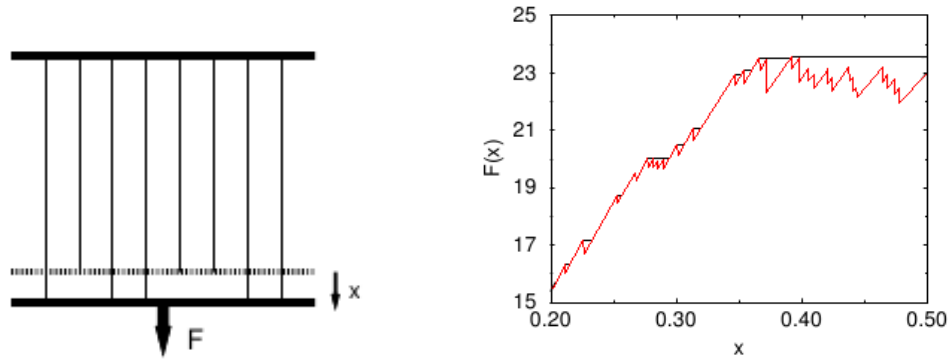


Figure 3.10: (Left) A Fiber bundle, consisting in N horizontal fibers clamped at an end and subject to a loading parallel to the fibers on the other. All the fibers have the same elastic constant E , but may have a different strength $\sigma_{i.max}$, as this variable is drawn from a probability distribution. Initially, each fiber is subject to the same fraction of the total force, F/N which can be larger than $\sigma_{i.max}$ for some fibers which have to be taken out of the simulation. A steady state occurs when the load felt by every fiber is below its strength, causing a global displacement of the bundle of magnitude x . (Right) Force as a function of displacement for a FBM. The red curve corresponds to a case in which displacement is controlled, then each time a fiber is broken there is a drop on the load felt by the system. In the case that force is controlled, the system follows the red line until a drop. Then the load is maintained at this fixed value (black line) until the load is increased above this local threshold. [PHC10].

inhomogeneous material. Examples of distributions used are the uniform distribution between 0 and 1, and Weibull distribution $P(\sigma_{tb}) = 1 - \exp\left(-\left(\frac{\sigma_{tb}}{\lambda}\right)^m\right)$.

Time dependence: To model creep rupture and fatigue, the strength has to be time dependent. [Col56, SA98, MGMP01]

Loading can be done by either changing strain or stress; which corresponds to the experiments in which either the strength or the deformation of the bundle are controlled. If the independent variable is ϵ , a given strain value for every fiber implies also a given strain, as $\sigma_i = E\epsilon$. Intact fibers with strength thresholds below the given σ_i would then break, but since strain is fixed this does not cause a redistribution of the load over the remaining fibers, i.e. there is **no load sharing**. Fibers with strain threshold $\sigma_{trs} > \sigma_i$ are intact. The constitutive relation $\sigma(\epsilon)$ is:

$$\sigma(\epsilon) = E\epsilon \overbrace{[1 - P(E\epsilon)]}^{\% \text{ of intact fibers}}, \quad (3.41)$$

shown in [Fig. 3.11].

When the strain per remaining fibers $\sigma = F/N$, is the independent variable, the procedure consists in increasing its value either by fixed discrete steps or by the least amount needed for one fiber to break. The breaking of one or more fibers decreases N , the number of remaining ones, thus causing an increase in the load that each of them feels; redistribution that itself may lead

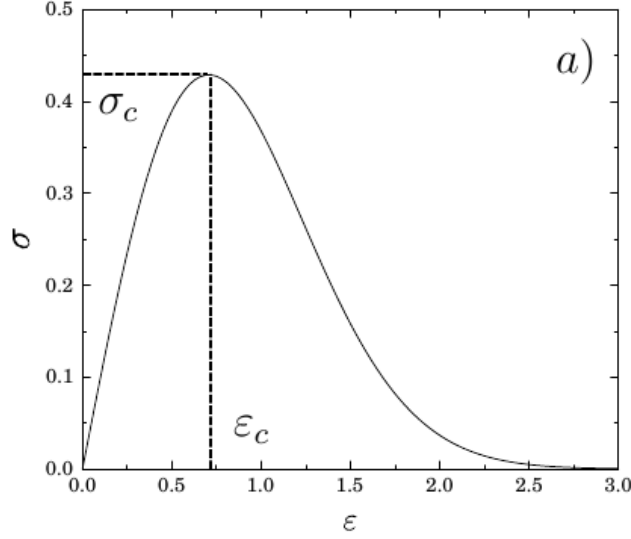


Figure 3.11: Macroscopic constitutive behavior for a fiber bundle with GLS [KRHH06]

to some more breakings in a recurrent way. In other words, a small strain increase may generate a burst of several fiber breakings, which ends either by leaving some intact fibers who hold the total stress, or by a fatal breakdown of the bundle. The constitutive curve can only be realized up to a maximum, the catastrophic failure stress.

For GLS it has been shown analytically that the constitutive curve has a definite maximum, defining a critical strain ϵ_c and stress σ_c , for an infinite system. The critical value is finite, and can be approached by finite systems, since $\sigma_c(N) \rightarrow \sigma_c(\infty)$, when $N \rightarrow \infty$. Hemmer and Hansen proved [HH92] that the distribution of burst of sizes $N(\Delta)$ of a GLS FBM has a *universal* power law behavior in the limit $N \rightarrow \infty$:

$$D(\Delta) \approx \delta^{-5/2}, \quad (3.42)$$

[Fig. 3.12] independently of the disorder distribution.

The local load sharing (LLS) constitutive relation follows the one for GLS, but macroscopic failure occurs at lower critical stress. For $N \rightarrow \infty$, $\sigma_c(N) \rightarrow 0$ as $\frac{1}{\ln(N)}$. In this case there is a rapid decrease of $D(\Delta)$, and dependence on the disorder P .

For a fiber bundle model with global sharing rule, as fibers approach the point of macroscopic failure under a quasi statically increased load, the microscopic quantities (e.g. the burst size distribution) show a scaling behavior typical of continuous phase transitions [HP00, KHH97, HH92]. As some macroscopic quantities (as Young modulus) at the same time also suffer a finite jump, it is suggested that the macroscopic failure of GLS systems is analogous to first order phase transitions close to a spinodal [ZRSV99b, ZRSV99a, ZRSV97].

Some applications of fiber bundle models include the study of the effect of anisotropical stress distribution, in the sense that fibers close to a failed one get a redistribution of stress not only dependent on the distance, as in $\Delta\sigma_{add} = r^{-\gamma}$, but in which a parameter α is used to tune

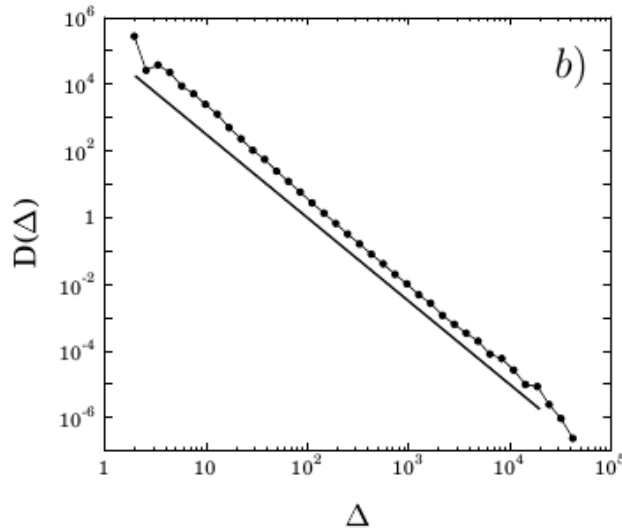


Figure 3.12: Distribution D of burst sizes Δ obtained in a computer simulation of 10^7 fibers. A line of slope of -0.5 is plotted to guide the eye. [KRHH06]

the relative importance of the x and y manhattan distance to the broken fiber. Hidalgo et.al. find that the two different behaviors that appear for the system mediating between Global-Load-Sharing like system to a Local-Load-Sharing at a fixed value of $\gamma_c = 2$, [HZH08]

In [KMHH03] studied Creep, the response of solids to a constant applied load, by both analytical and numerical calculations. First, Kun et.al. showed how, by changing the external load on the system, a partially failed but infinite lifetime state or a finite failure state can be triggered. Interestingly, the authors found that changing the range of interaction of the fibers two universality classes for creep rupture could be identified: for global load sharing the transition is continuous, characterized by power law divergences; for local load sharing the transition is abrupt, with no scaling.

Continuum Damage Fiber Bundle Models

Fiber composites loaded parallel to their axis show a degradation process in which the constitutive curve $\sigma(\epsilon)$ has a plateau before the macroscopic failure. This can be associated to fibers with hierarchical structure or to debonding from the fiber to the adjacent matrix (as in fibers from parenchyma cells). A way to model this behavior is to modify the fibers' failure law by assuming gradual degradation. This is implemented by setting a damage threshold at which the given element gets its Young modulus reduced in a discrete step.

Take for instance a system consisting on N parallel fibers with identical young modulus E , and random failure thresholds σ_{th}^i , $i = 1, \dots, N$. Fibers have linear elastic behavior up to failure threshold, at which the fiber's stiffness is reduced to aE (with $0 < a < 1$), rather than of completely removing it. Instead, there is a maximum number of allowed failures per fiber, k_{max} , at which the stiffness is not reduced anymore. Furthermore, depending on the physical situation that needs to be modeled different models are obtained by changing several parameters:

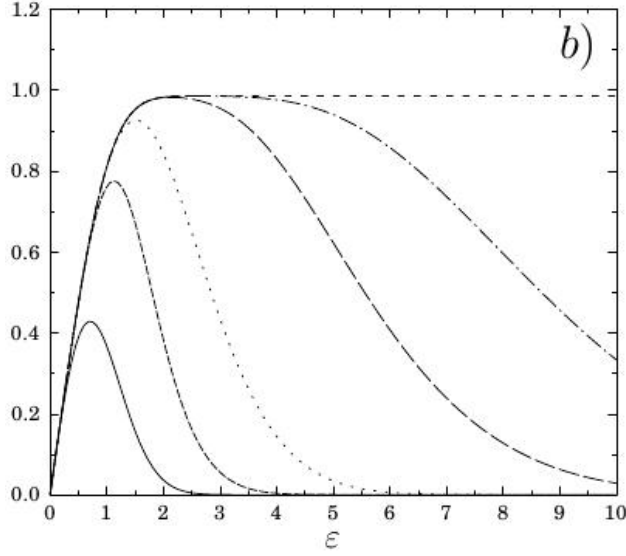


Figure 3.13: Constitutive behavior of the model, with annealed disorder without residual stiffness at $a = 0.8$, for different k_{max} , from [KRHH06].

for instance, damage thresholds may be quenched (fixed at the beginning) or annealed (chosen randomly at each failure); load redistribution can be either global or local; and loading can be done by fixed stress or strain [Fig. 3.10](Right). In the latter, the load of a fiber that has failed i times is given by:

$$f_i(\epsilon) = Ea^{k(i)}\epsilon. \quad (3.43)$$

The macroscopic constitutive behavior of the material, i.e. the load on a fiber at a given strain, is:

$$F/N = \epsilon \left(\sum_{k=0}^{k_{max}} a^k P_k(\epsilon) \right). \quad (3.44)$$

Where a , the damage parameter, and k_{max} the maximum number of times a fiber is damaged, are free parameters which can be used to recover a range of fiber bundles found in literature. If the fibers are not removed, at a number of failures of k_{max} a fiber's stiffness is fixed in the value $Ea^{k_{max}}$. This means that the bundle as a whole develops a residual stiffness, causing the strain-stress curves to tend to straight lines. If the fiber is removed from the simulation (stiffness reduced to zero) after a number of breakings have been reached, the threshold is called k^* . There will be no residual stress but a plateau at a maximum stress for the material. [Fig. 3.13].

The simulations show different kinds of avalanche activities, characterized by different shapes of avalanche size distributions. For a system of remaining stiffness, annealed disorder and Weibull parameters $m = 2$, $\lambda = 1$, the histogram $D(\Delta)$ of avalanche sizes Δ is shown in [Fig. 3.14]. For $k_{max} = 1$ and small a , the model recovers the global load sharing dry fiber bundle model, power laws with exponent $\alpha = 5/2$). Increasing a for fixed k_{max} only gives larger number of avalanches: parallel straight lines. But there is a *critical value* for a , a_c , such that for $a > a_c$ and

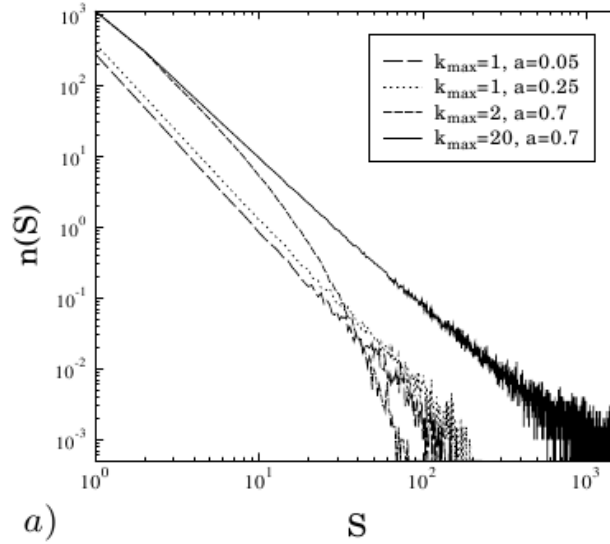


Figure 3.14: Avalanche size distributions for different values of k_{max} and a when fibers have remaining stiffness and annealed disorder. $N = 1600$ fibers, averages made over 2000 samples. Vertical axis $D\Delta$ is the number of avalanches of size Δ , from [KRHH06].

for k less than a specific $k_c(a)$ the avalanche size show exponential distribution, but if k takes a value above $k_c(a)$ the distribution takes power law with exponent $\beta = 2.12 \pm 0.05$.

There is a phase diagram that summarizes the properties of avalanches related to the parameters of the model. Three regimes exist. If damage parameter a is smaller than a_c , dynamics of avalanches is close to a dry fiber bundle model, characterized by a power law of exponent $\alpha = 5/2$. For $a > a_c$, the avalanche size distribution depends on k_{max} . A curve of $k_c(a)$ in the phase diagram separates two regimes: bellow the curve avalanches with exponential shape are obtained. Above it, a power law of avalanches with constant exponent $\beta = 2.12 \pm 0.05$, which is different from the mean field exponent $\alpha = 5/2$.

Universality and Basquin's law of fatigue

On [KCAH08], F. Kun et.al. studied the fatigue fracture of heterogeneous materials by focusing on the microscopic mechanisms of the fatigue process with relation to the time evolution. This was done by means of two models, one based on discrete elements and another one based on fiber bundles. The goal was to study the Basquin's law, which states that the lifetime t_f of a samples increases as a power law when the external load amplitude decreases, $t_f \propto \sigma_0^{-\alpha}$, where α is called Basquin's exponent.

For the fiber bundle model, the authors studied a mean field fiber bundle model, with two failure criteria, either immediate breaking or aging. Healing was introduced in the system by means of a parameter γ which controlled the rate of damage accumulation. Both the FEM and the DEM showed agreement with the experiments, as shown in [Fig. 3.16]. Furthermore, they showed how, as a consequence of healing, a finite fatigue limit emerges; at which the system goes

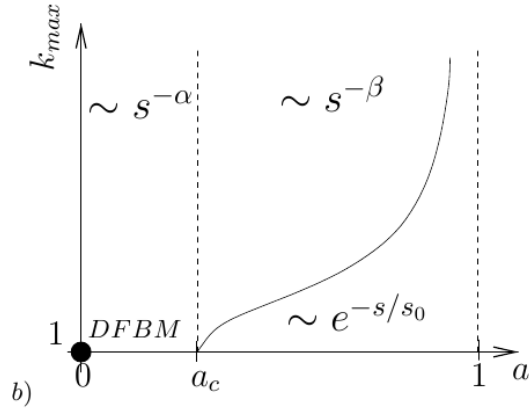


Figure 3.15: Phase diagram for the continuous damage model with remaining stiffness for both types of disorder, from [KRHH06].

through a continuous phase transition. Two different phases are possible, one characterized by finite time failure, and one in which the system has infinite lifetime. At the micro-level the authors find avalanche activity, with bursts of local breakings followed by damage sequences. They demonstrate analytically how this activity is characterized by universal power law distributions, which in turn implies that the non-universality of Basquin's law at macroscopic level is due to the degradation process of the material. In the case of the shrinkage induced drying, we will show how a continuous phase transition is obtained between an isolated cracks phase and a long crack phase. In contrast to what is seen here, in that model the disorder has an important role as the control parameter of the transition.

3.4.2 Random Fuse Networks

The random fuse network models, proposed by L. de Arcangelis et.al, is an idealized way to describe the breaking process in a 2D system by means of a regular network of fuses and isolators who have random burning thresholds [DARH85]. A network of fuses has a fixed voltage difference applied to two borders, as seen in [Fig. 3.17]. The voltage in the system is increased until one of the fuses traspases its burning threshold and is blown. Kirchoff laws are solved again for the new network, and the calculation of the fuses burning is calculated again. When the avalanche of breakings stops the voltage is increased again, and the rules are repeated. The process ends when there is no longer a conducting path between the two electrodes. Both conductivity of the network and the voltage needed to break the hottest fuse are monitored.

The relationship between the random fuse models (RFM) and elasticity comes from the analogy between the Ohm's and Hooke's laws. In a RFM the current in the network is the result of the discretization of the Laplace's equation $\nabla^2 V = 0$, given the system boundary conditions, which can be thought as a simplification of the Lamé equations [ANZ06]. The structural disorder is introduced in the RFM as either: random thresholds, taken from a probability distribution; random dilution, of a fraction of links at the beginning; or random conductivities for the

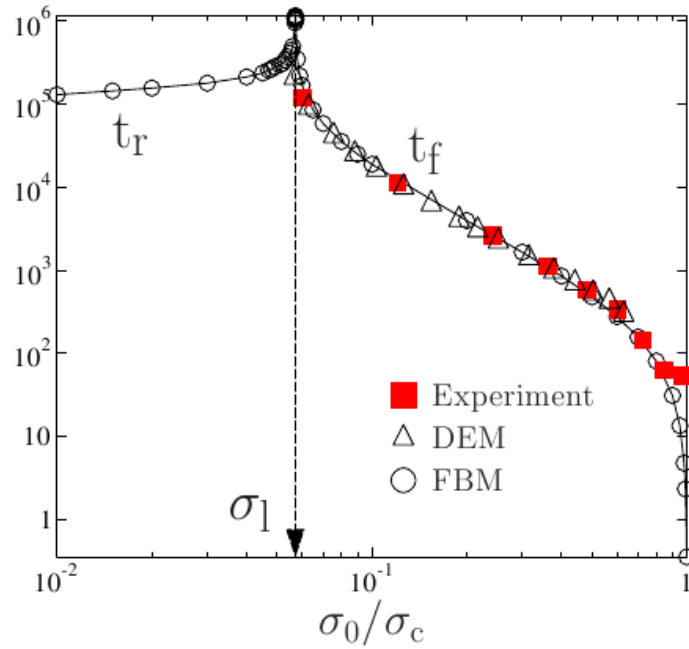


Figure 3.16: Characteristic timescales t_r and t_f of the fiber bundle model for the Basquin's law system. Below a certain σ_l the deformation of the system converges to a limit with a characteristic relaxation time t_r . Above it, there is a lifetime of the system t_f . From [KCAH08]

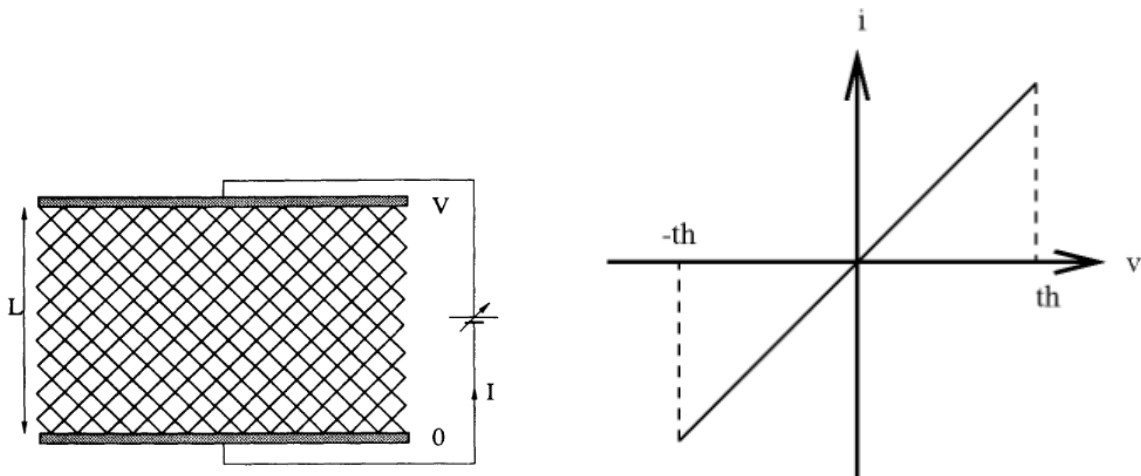


Figure 3.17: (left) Random fuse network. The lattice is tilted at 45° from the bus bars [HR90]. (Right) Current response of an Ohmic resistor, [BC06].

fuses.

The Random fuse model has been used to study different aspects of the breaking of materials. In [ZRSV99a] Zapperi et.al. showed how the avalanche process in the breakdown of a material is preceded by avalanche events, described by scaling laws, and estimated the values of the exponents. Breakdown is characterized by a discontinuity of macroscopic properties of the material, indicating a first-order transition. To construct the order parameter, the dissipated energy on each bond is taken into account,

$$E(I, \{\sigma\}) = \frac{1}{2} \left(\frac{I^2}{G(\{\sigma\})} - \sum_i \sigma_i D_i^2 \right), \quad (3.45)$$

with $G(\{\sigma\})$ the total conductivity of the lattice, which can be given by effective medium theory defining a constant ϕ , as:

$$G(\{\sigma\}) = 2\phi - 1, \quad (3.46)$$

The effective medium theory constant ϕ of this case behaves as an order parameter and scales as:

$$\phi - \phi_c \propto (f_c - f)^{1/2}, \quad (3.47)$$

where $f \equiv I/L$ is the current per unit length. The authors also show how the avalanche size distributions take a distribution of the form:

$$P(m) \propto m^{-\tau} f(m(f_c - f)^x), \quad , \quad \tau = \frac{3}{2} \quad x = 1 \quad (3.48)$$

For instance, the average avalanche size as function of the voltage applied to the bus bars. Zapperi et.al. showed that it follows a power law with increasing bus voltage, with $\langle m \rangle$ is proportional to the ‘‘susceptibility’’, $d\phi/df$:

$$m \propto (V_c - V)^{-\gamma} ; \quad \gamma = 1/2 \quad (3.49)$$

Pradham et.al. have shown how the avalanche distribution for the random fuse model follows a universal power law distribution that goes from an exponent of $\eta = 3$, when all the avalanches are recorded; to $\eta = 2$, when they are measured only after 2/3rds of the fuses have blown [Fig. 3.18] [PHH05].

Damage mechanics

Damage mechanics consists in describing the evolution of scalar damage field $D(\vec{x})$, for local variations of the Hooke law of the material. Internal micro-cracking of the material is encoded in the variation of this field D . Furthermore, the two point correlation function over the scalar field D is constructed; leading to the definition of correlation lengths along and perpendicular to the fracture ξ_{\parallel} and ξ_{\perp} .

For instance, in [PLZA09] the authors study the plastic yielding in disordered media using the random fuse model. If the dynamics is regarded as a minimum energy problem they show how the correlation function shows self-affine roughening $C_l(l) = \langle |h(x+l) - h(x)|^q \rangle \approx l^{q\eta_q}$, with $\eta_q = 2/3$ for any moment q .

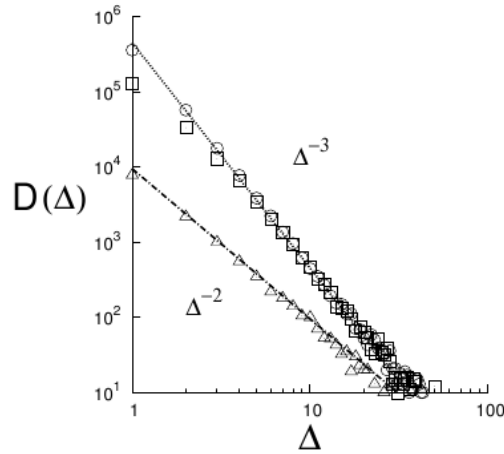


Figure 3.18: Burst size distribution on the random fuse model, from [PHH05].

3.4.3 Beam models

The fracture models of statistical physics usually rely on a mathematical simulation of lattice models. The medium is represented by springs or beams, the disorder imposed by random failure thresholds or randomly removing some links. For instance, [HH89] models the process of fracture by means of a numerical solution of the Lamé equation: the equation of elasticity for an isotropic linear medium (Eq.3.10):

$$(\lambda + \mu)\delta(\delta \cdot \vec{u}) + \mu\delta^2\vec{u} = 0,$$

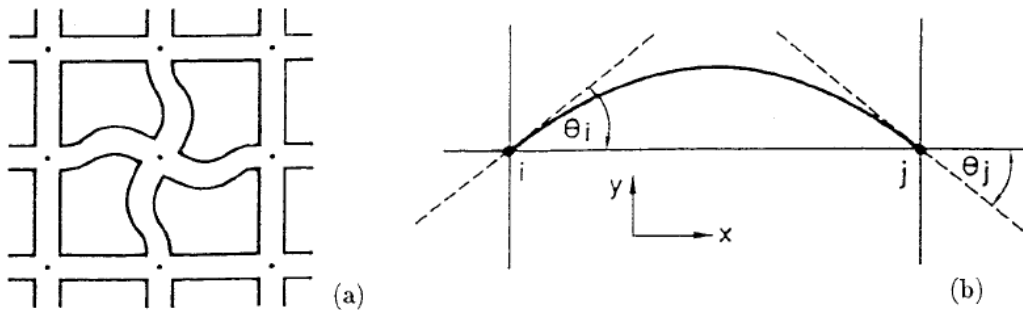


Figure 3.19: From [Her91]

which are called *beam models*. They represent a discretization of the Cosserat continuum equations (Eq.3.15), in which the degrees of freedom are the two coordinates for each site (x_i, y_i) and the rotation $z_i = l\phi_i$ (with $\phi \in [-\pi, \pi]$ the angle -0 in the undeformed condition- and l is the length between the nodes -usually taken as 1-) [Her91]. The links between sites are beams with

cross section A . Prof. Herrmann decomposes forces into tractions f along the axis of the beam, shear forces s , and bending moments m_i, m_j at the ends i and j . For the horizontal beam:

$$f = a(x_i - x_j) \quad (3.50)$$

$$s = b(y_i - y_j + \frac{1}{2}(z_i + z_j)), \quad (3.51)$$

$$m_i = cb(z_i - z_j) + \frac{1}{2}b(y_i - y_j + \frac{2}{3}z_i + \frac{1}{3}z_j) \quad (3.52)$$

$$a = YA \quad (3.53)$$

$$b = \left(\frac{1}{GA} + \frac{l^2}{12YI} \right)^{-1} \quad (3.54)$$

$$c = \frac{YI}{l^2GA} \quad (3.55)$$

where G is the shear modulus, I the inertia (see [Fig. 3.19]). The boundary conditions usually consist in fixed displacement of border nodes to zero. Finally, the stability condition (sum of forces and torques equal to zero) gives the discretized equations for each site.

Prof. Herrmann argues that, since the stress on any existing crack is zero normal to the surface of the crack, it grows in the direction perpendicular to the surface, and it does at the point where the strain parallel to the crack is largest. Different possibilities of growth dynamics correspond to every different kind of microscopic mechanisms for energy transport away from the growing tip.

In [Her91], Prof. Herrmann studies a finite square lattice system of linear size L , subject to shear from top and bottom. First, he defines a micro crack and solves for the Lamé equation. Then, he studies three different breaking criteria; Criterion I describing a brittle material, Criterion II and III describing short time memory related to fast stress corrosion effects. Using the sand box method (count the number of broken beams inside a box of length l around the first broken beam and plot it as a function of l in a log-log plot), he finds that the fractal dimension of the cracks is larger than one; its specific value depending on the breaking criteria (due to the competition between global stress and the direction of local growth imposed by the lattice anisotropy).

Summarizing, this computational approach allows to numerically calculate the fractal dimension of a crack for a given elastic model. This has been useful because it is very difficult to capture the shape of a fracture up to the microscopic level needed to calculate the fractal dimension. A more fundamental issue is the question of the role that the fractal shape of the fracture has on the mechanical properties of the material, as the roughness. As stated in [CBI98], the main conclusion of the fractal nature of the crack is the fact that the process are scale independent. But as for the specific relation with the mechanical properties there is still much work to do to elucidate the actual relation.

3.4.4 Crackling noise

In an insightful review article [SDM01], Sethna et.al. describe the way renormalization group theories have been used to tackle the study of “how things crackle”; describing crackle noise as a distribution of intensity sizes of noise events whose histogram follows a power law, i.e., does not have a characteristic size scale. Examples of crackling noise include the Barkhausen noise in a magnet, the magnitudes of avalanches of earthquakes and the sound of a crumpled paper. As renormalization group theories deal with the way the evolution laws of a system changes as measurement are made under larger and larger size scales, it is possible to study self-similar evolution laws (i.e. those who look the same at different length scales). This is done by the process of coarse-graining the models and measuring the properties of the new models, which is equivalent to a mapping of the space of physical systems into itself.

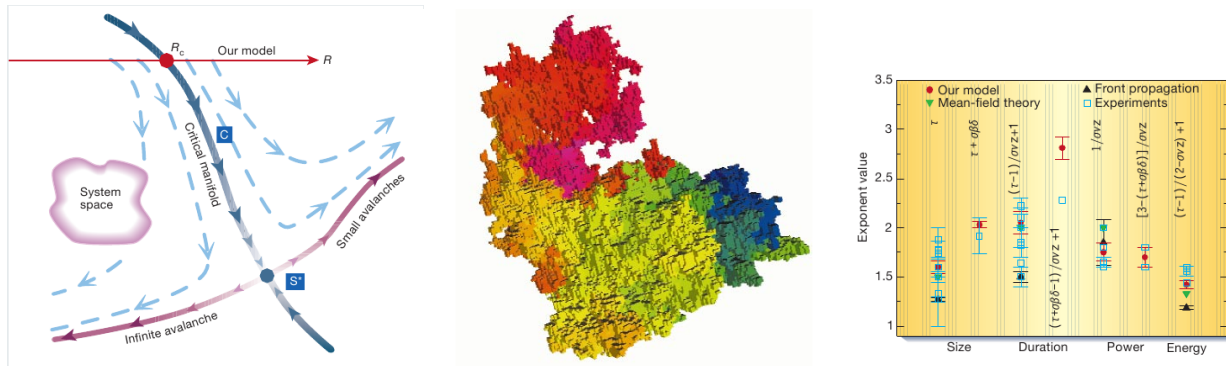


Figure 3.20: (Left) space of disorder magnets, renormalization picture. The scale free system sits in a fixed point, i.e., maps to itself through renormalization. At its left and right large “infinite” avalanche systems or small avalanche systems are located. (Middle) structure of the avalanche of Sethna’s model. (Right) Values of the different exponents that characterize the fracture for sethna’s model. From[SDM01]

Crackling noise in this context is described as the transition between snapping, a situation in which a single fatal crack occur, i.g., breaking a piece of chalk; and popping, a situation in which small individual breakings accumulate continuously. The scale invariance of this process is exemplified by the known Gutenberg-Richter law for earthquake magnitudes: a histogram of the number of earthquakes as function of its magnitude follows a power law. It also means that even though the specific details that account for a large earthquake (continental plate displacements) are intrinsically different to those that cause the small earthquakes, the system does not show a characteristic size scale. Therefore the whole dynamics of the system can be explained by means of a simpler model, which can be obtained by coarse graining the original system. Even more, many other systems may fall into the same category and share the same dynamics, corresponding to the same universality class.

To prove their point, Sethna et. al. use a toy model for a magnet in which individual spins pointing up or down sit on a lattice. The force felt over all spins on a sub-domain of it is given by:

$$F = H(t) + \sum_{neighbors} JS_j + h_i \quad (3.56)$$

with $H(t)$ and external field, J the coupling constant with neighbors, and b_i a normally distributed random variable of standard deviation R , which represents the disorder of the system. For $R \gg J$ the avalanches are small, and most domain flips happen independently (popping). For $R \ll J$ a large avalanche of neighbors snapping at once happens. There is a R_c , in which avalanches of flippings in all scales happen. In a more general way, avalanches can be thought as rearrangements of the system between neighboring metastable states.

The basic critical exponents characterize the scale free behavior of different parameters. The typical length of the largest avalanche scales proportional to $(R - R_c)^{-\gamma}$. At R_c the probability of having an avalanche of size S is $S^{-(\tau+\sigma\delta\beta)}$. The fractal dimension of the avalanches is $1/\sigma\nu$, so the spatial extent of an avalanches is proportional to $s^{\sigma\nu}$. The values of the exponents compared to the experiments are shown on [Fig. 3.20].

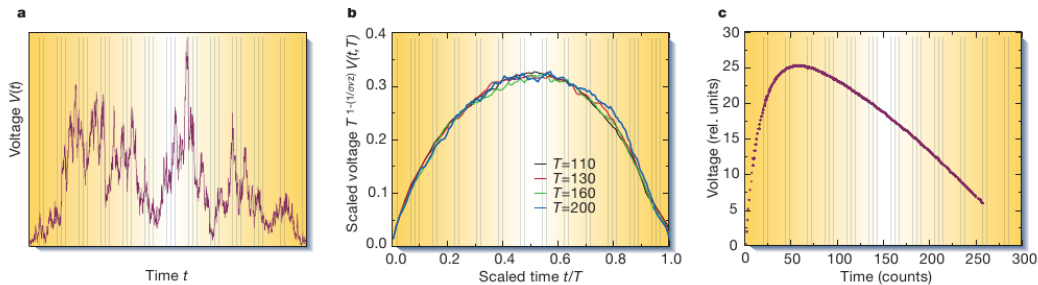


Figure 3.21: Scaling of avalanche shapes. (Left) Voltage pulse, proportional to the number of domains flipped, as a function of time during a single large avalanche. (Center) Average avalanche shapes for different durations for sethna’s model. (Right) Experimental data of magnet crackling voltage. [SDM01]

Beyond the power laws, self-similarity can be spotted on some time depending characteristics. In magnets, for instance, the distribution of sizes S of all avalanches of duration $T < S >_{experiment}(T)$ can be measured and compared with the models. Furthermore the time history of avalanches $V(T)$, the number of flipping domains as function of time, is averaged over all avalanches of fixed duration. Universality is expressed in the collapse of all this functions into a single shape.

3.4.5 Applications of Finite size scaling

Statistical mechanics methods applied to fracture look for ways to bridge the knowledge between the microscopic interactions of a material and the macroscopic behavior. In what follows, I will review some results in which statistical mechanics has been used in this way.

Paris’ law derivation

Take a medium with a very long but sub-critical crack of length $2a$. Paris’ law states that the velocity of growth of the crack is proportional to the power law of the crack intensity factor; characterized by a material dependent exponent m ,

$$\frac{da}{dt} (\Delta K)^m = C(\Delta\sigma \sqrt{a})^m. \quad (3.57)$$

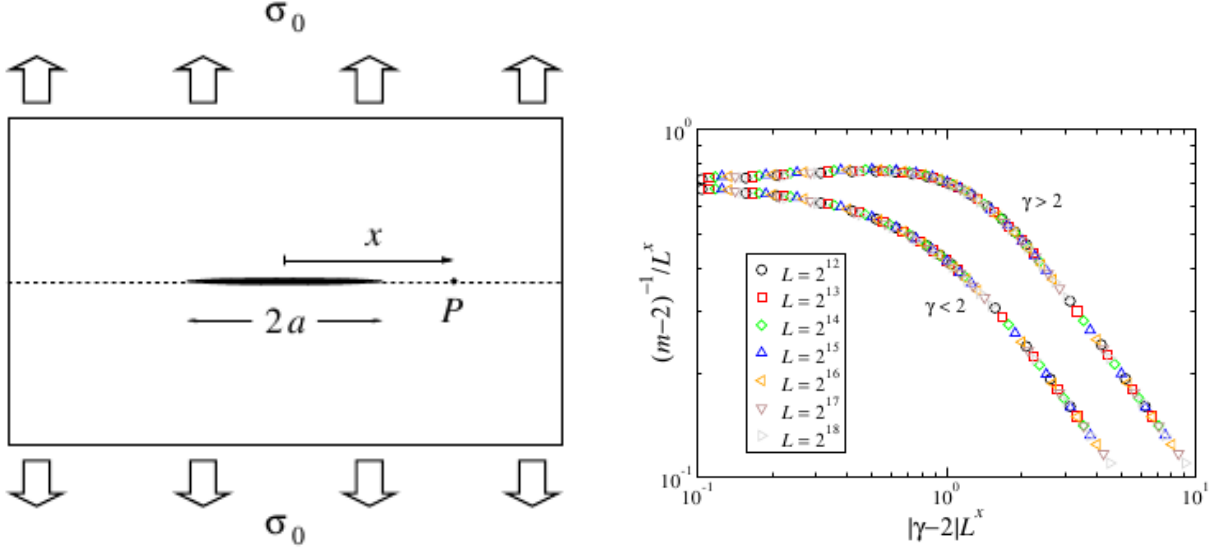


Figure 3.22: (Left) Thin crack, with length $2a$ subject to stress σ_0 . (Right) Scaling plot m vs γ for different system sizes L . Data collapse for $x = 0.089$. [VAH08]

In [VAH08], Vieira et.al. consider whether it is possible to establish a direct connection between microscopic damage accumulation and Paris' law. In order to do this, they assume that the damage can be described as being increased by discrete steps whose magnitude is given by the number of cycles during which the crack as a length of $2a$, and an exponent γ ,

$$\delta F(x;a) = f_0 \delta t [\Delta\sigma(x;a)]^\gamma. \quad (3.58)$$

Under this assumptions, the authors conclude by an analytical calculation that as the size of the system grows, $L \rightarrow \infty$ there is a relation between the exponent of Paris's law m and the parameter γ that gives the step increase (or in other words, which describes the damage accumulation law). This asymptotic relation has two different regimes, differentiated by a critical value $\gamma_c = 2$:

$$m = \begin{cases} 6 - 2\gamma & \text{for } \gamma < \gamma_c \\ \gamma & \text{for } \gamma > \gamma_c \end{cases}. \quad (3.59)$$

which they check by the finite-size scaling hypothesis:

$$\frac{1}{m(L) - 2} = \begin{cases} L^x \mathcal{F}_-(|\gamma - 2|L^x), & \text{for } \gamma < \gamma_c \\ L^x \mathcal{F}_+(|\gamma - 2|L^x), & \text{for } \gamma > \gamma_c \end{cases} \quad (3.60)$$

by means of a numerical simulation, whose results are shown in [Fig. 3.22], highlighting the high quality collapse for the two different regimes.

Fragmentation

Fragmentation is the breaking of particulate materials into small abundant pieces. The shell fragmentation has been studied both experimentally and numerically in the literature. Because of the violence of the process, fragmentation observations are usually restricted to the final state, and the fragment size is the main characteristic quantity. For egg shells either dropped or imploded, Herrmann et.al. [HWK06], have found that the distribution of fragment sizes shows a power-law behavior, independently of the way energy is given to the collision, which microscopic interactions are relevant and which length scales are involved. The exponent depends only on the dimensionality of the system. If $F(m)$ is the mass distribution of fragments, $F(m)\Delta m$ is the probability of finding a fragment with mass between m and $m + \Delta m$. They experimentally find a power law behavior with fragment mass distribution for explosion experiments:

$$F(m) \propto m^{-\tau}, \quad (3.61)$$

with $\tau = 1.35 \pm 0.02$. The numerical simulations vary the pressure of the explosion as a parameter and measure the mass distributions. The different curves of $F(m)\bar{M}^\delta$, with \bar{M} is the average fragment mass and $\delta = 1.6 \pm 0.03$, collapse on the same functional form; giving validity of the scaling:

$$F(m) \propto m^{-\tau} f(m/\bar{M}), \quad (3.62)$$

as shown in [Fig. 3.23].

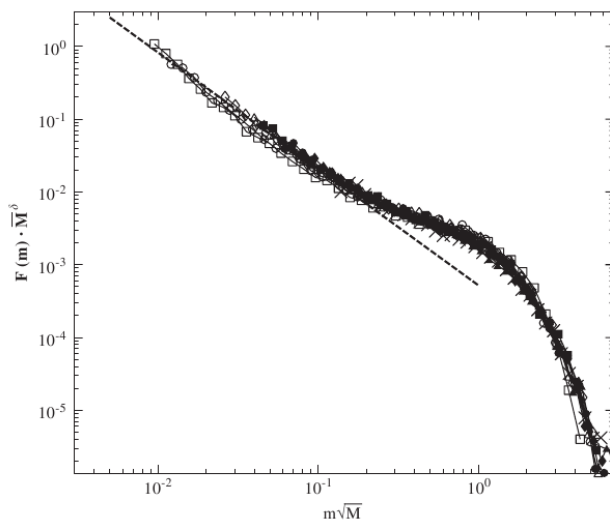


Figure 3.23: Rescaled plot of mass distributions of various pressure values. The dashed line indicates the fitted power law with exponent $\tau = 1.55 \pm 0.03$ [HWK06].

Also, in [CWKH08], Carmona et.al. studied the the evolution of meridional cracks generated in the fragmentation process of spheres. The important quantities in this study are the mass of the largest fragment, the mass of the second largest fragment and the average mass. The breaking of spheres is shown to have different regimes, regarding on the initial kinetic energy of

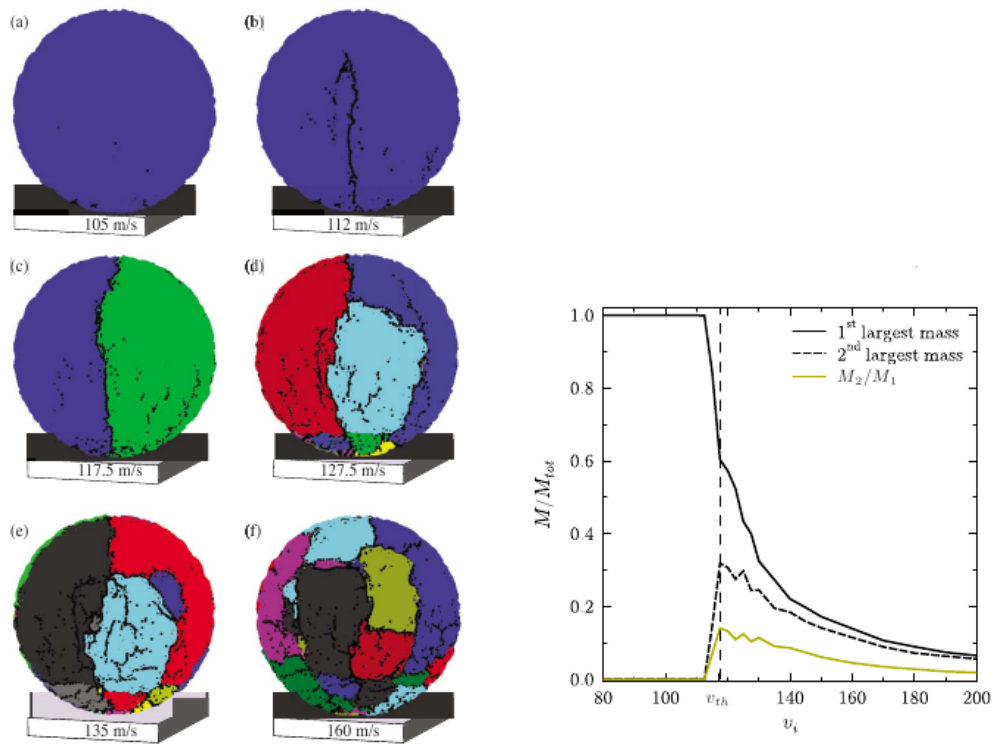
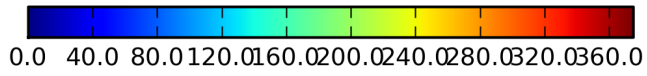
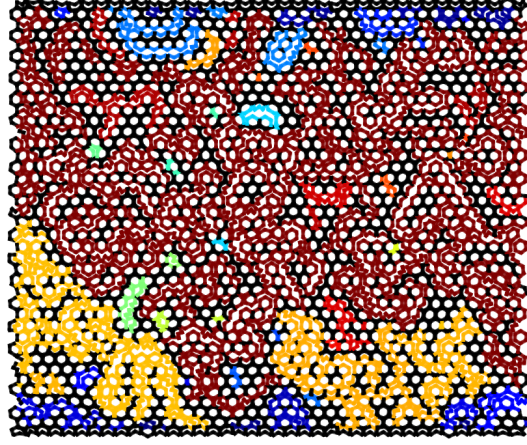
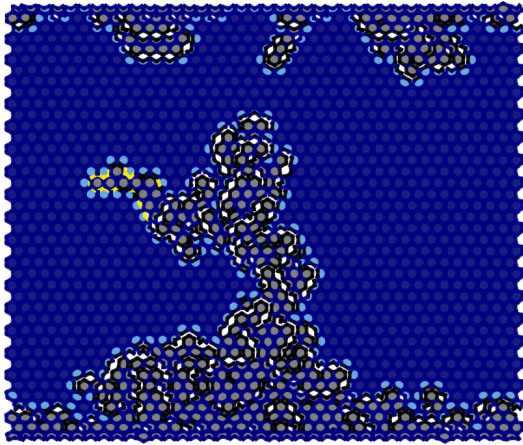


Figure 3.24: Fragmentation of spheres. (Left) Front view of reconstructed spheres, showing the fragments with different colors, for different initial speeds. (Right) Mass of the largest and the second largest fragment and average fragment mass as function of impact velocity. From [CWKH08].

the system. Below a certain value there is a *damaged* or fractured regime, in which the largest fragment has almost the whole mass of the system; the second one being orders of magnitude smaller. With increasing the kinetic energy of the collision, above a certain threshold a *fragmented* state arises; the largest fragment reduces considerably in size, with an increment of the second largest [Fig. 3.24].

$\tau=339$

$\xi=0.9$



Simulation methods

The modeling, from a statistical mechanics point of view, of the different stages of drying of the bamboo calls for different computational methods. Take first the process of the movement of the free water and the capillary forces that happens in the first stage of drying. In order to gauge the possible effects that this has on the breaking, it is necessary to know the position of the drying front with respect of the lattice of hexagonal cells, by taking into account the fluxes due to the pores between neighbouring sites. This is known in the literature as *Pore Network Methods* model. As important as the water flow it is to know the actual position of the cell walls during drying. This calculation is more efficiently and easily performed by means of a *Discrete Element Method* (DEM) simulation, [Chapter. 5].

In [Chapter. 6] I model the effect of shrinkage on the breaking statistics, taking into account two conditions: firstly, the geometry of the cell has to be preserved; secondly, the microscopic model of the cell wall has to reproduce the Lamé equations in the macroscopic limit. For this reason I chose to model the cell wall as a plane frame element in the framework of *Finite Element Method* (FEM).

The last chapter that contains a computational calculation is [Chapter. 7], which includes a simpler implementation of the shrinkage. Using again a DEM model, I studied a more general account of shrinkage loosing the previously imposed restrictions. This implementation turned out to be more capable of handling larger system configurations and the results showed a behaviour similar to what could be attained in the FEM model with smaller systems.¹

In the present chapter I present a brief introduction to these methods, focusing on the mentioned applications. I start by discussing the computational models in general, following the description of the methods.

¹The gain in efficiency using DEM instead of FEM models is counterintuitive; while the latter uses an optimized package to solve the matrix equation corresponding to the structure, the former was programmed by using a simple Verlet algorithm. My guesstimate is that the DEM code is better optimized at compiler time, thus allowing for a more efficient use of the modern processors; counter-weighting the gains provided in using a library in the FEM case.

4.1 Computational models and object oriented programming

One of the ways in which computational physics has been successful is the solution of complex mathematical models by means of numerical methods. In the case of the kinematics of sets of complex objects, for instance, these equations are the differential equations of motion of each of the constituents of the system. The forces themselves can be either derived from a Hamiltonian of the system under consideration, for integrable systems, or even to depend on the observables of the system under consideration.

Under the paradigm of *object oriented programming*, OO, there is a direct analogy between the physical object under study and its representation in the computer. The program is organized in base of “objects”, structures in the memory of the computer for which the programmer defines both data fields and methods. The former define the physical variables that are needed by the object, while the latter models the interactions between the objects. The analogy between the physical model and the computer code makes the OO program easier to code and the computer algorithm resembles the one describing the real physical interactions. As an example, a object oriented program to study the 3 body motion of the earth and Jupiter under the influence of the gravitational field of the sun will have the object “planet”. This in turn will have as data fields: mass, \vec{R}_{CM} , \vec{V}_{CM} ; and as methods $\vec{f}_{i,j}$, which will denote the gravitational force felt by the planet given the other planet.

The numerical integration algorithms provide ways to solve a coupled set of differential equations and boundary conditions that describe in general a physical problem. To do so, they discretize the domain of the problem into several steps and starting from the initial condition provide new values of the variables that are exact up to and approximation value that is given as an order of the step. A common example is the Runge-Kutta order 4 integration method, whose accuracy is of the order of $O(\Delta x^4)$. The structure of *Hamiltonian systems* provide further restrictions that can be incorporated into the integration method. For them a set of initial conditions of the system corresponds to a section of the phase space. Now, under Hamiltonian evolution the phase space area is preserved, although deformed, i.e., the evolution of the system is symplectic. The numerical algorithms that take advantage of the symplectic nature of the phase space of the Hamiltonian systems are also known as symplectic. Examples are the Leap-frog and Verlet Algorithms. In the present thesis I have chosen to use the last one.

The programming language that I have used in this work is C++. It is a mature language widely used both in academia as well as in the applied engineering fields. Some excellent references to this language include the famous book by Deytel [DD09] and a more recent and well written reference and introduction, publicly available at the website [Sou07]. The compilation of all the different codes that were used in this thesis was performed by means of the fast and libre GNU compiler, [SC03].

4.2 The discrete element method

Discrete element methods, shortly DEM, are a set of modeling techniques used to simulate and study the dynamics of a collection of deformable bodies of arbitrary shape. DEM models de-

scribe computationally the inherently discontinuous media by means of a discrete approach. The constraints to the motion of such bodies may be fixed, as for example a gas of hard spheres subject to stay inside a box; or, in general, continuously varying [SdBH04]. DEM methods have been very successful in the simulation of the movement of molecules and atoms, and in such case the method is known as Molecular Dynamics (shortly MD). There the subtleties of the specific models come from the interaction forces between the atoms; the Lennard-Jones potential is commonly used in the literature.

DEM examples include breaking solids, a solids immerse in sticky material, or elastic collision of several bodies. During the course of the evolution of the system, DEM bodies collide and establish or break contacts among them, according to rules which are specific to each problem. The contact forces are applied between those DEM objects which are linked, i.e., the instantaneous configuration of all the particles of the system defines the dynamics of the objects. In the model to be presented on the chapter [Chapter. 5], as the initial configuration of the cells provides an ordered lattice, the definition of the contact forces only calls for the neighboring cells.

On certain cases the physical system under study imposes discreteness on the timescales. Take for instance a hard sphere gas simulation. If it is rare enough, most of the spheres will have long times between collisions; most of the time their trajectories correspond to straight lines. At a given specific time of the simulation, there is no need to use a timestep which is smaller than the smallest collision time between all the spheres in the system. This is what is called an event-driven simulation. Depending on the problem at hand, different approaches of the method are used to tackle the jumps in speeds at collisions, and the spatial inhomogeneities.

DEM also can take into account deformations, by means of constitutive laws. They are specially useful for simulations involving a large number of bodies, on which the contacts change or cannot defined a priori. Finally, they are useful to finding the complex behavior to arise from the microscopic interactions.

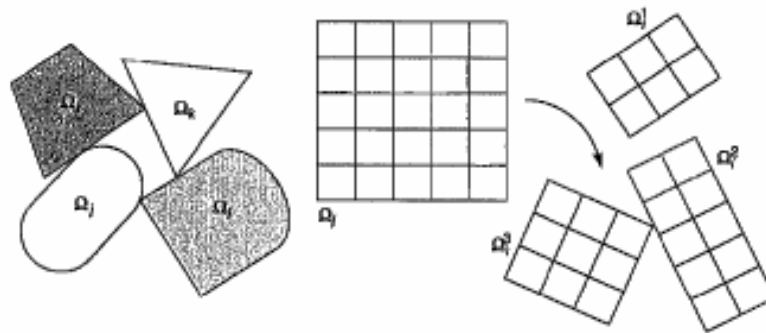


Figure 4.1: Collection of bodies, discretization into finite elements, changing configurations and possible fragmentation [SdBH04]

An operative definition of DEM models characterizes it as any computational modeling framework which:

1. Models finite displacements and rotations of the bodies, by integration of the equations of the motion.
2. Calculates the forces, including the information of the current configuration of the system (say for contact forces), and takes into account detachments between bodies, if necessary.
3. Recognizes new contacts and neighbors of the elements automatically, if necessary.

4.2.1 Basic elements of DEM

Force calculation: The elements of the DEM may feel body forces, as gravity, or also contact forces due to the interaction with their neighbours. Therefore, the force calculation depends on the position of every element, the neighbors and the contacts among them. It is usually the heaviest computational step in DEM simulations. For undeformable collision of bodies, the force law is regularized by changing the infinite steep slope that defines a hard sphere into a finite one; smoothing out the interaction (see [Fig. 4.2]). In the DEM model for the capillary flux, [Chapter. 5], this is implemented by taking a penetration depth. For the statistical model of shrinkage, [Chapter. 7], it is not necessary to take it into account.

Integration of the equations of the motion: After knowing the forces acting on the elements, the differential equations of the motion can be obtained from the Newton, Lagrange or Hamiltonian formulation; along with the introduction of dissipative forces, i.e., those that do not come from a potential. The calculation of the state of the system, is accomplished by an integration algorithm. In the present chapter the symplectic Verlet algorithm suffices [Section. 4.2.1].

Time evolution: Two different routines for time evolution can be used on a DEM, namely time driven or event driven. In the former, a single time-step is defined for the evolution of the system, independently of the dynamics and configuration of the system. This method is commonly used in the modeling of dense packings, in which most of the particles are interacting with their neighbors all of the time, and is used in the calculation of the breakings due to shrinkage of the cell walls in [Chapter. 5]. In event driven DEM, as mentioned before, there is a certain time lapse during which no interactions between the particles in the system take place. Since dynamics is usually the most expensive part of the simulation, it is computationally cheaper to solve the kinematics of the particles using a single time-step equal to the waiting time to the next collision.

The Verlet algorithm Given a Hamiltonian system with generalized coordinates q_i and momentum p_i :

$$H(q_i, p_i) = T + V, \quad (4.1)$$

with T the kinetic energy and V the potential energy, the equations of the motion are written as:

$$\dot{p}_i = -\frac{\partial H}{\partial q_i} ; \quad \dot{q}_i = \frac{\partial H}{\partial p_i} \quad (4.2)$$

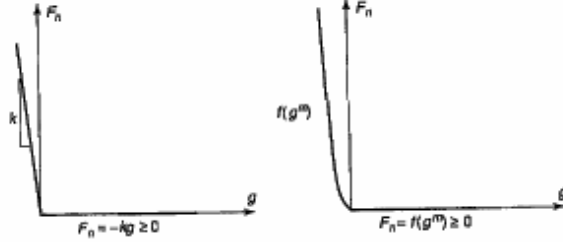


Figure 4.2: Regularized smooth treatment of a contact [SdBH04]

Symplectic algorithms integrate the equations of the motion at each step:

$$\dot{p}_i^{(k+1)} = \dot{p}_i^{(k)} + a_k F_i^{(k)} \delta t \quad ; \quad q_i^{(k+1)} = q_i^{(k)} + b_k \dot{p}_i^{(k+1)} \delta t, \quad (4.3)$$

where $F_i^{(k)} = -\delta V(q_i^{(k)})/\delta q_i^{(k)}$ [Tob07]. Different values of M , a_k and b_k correspond to different algorithms. For instance, the Verlet algorithm is obtained by $a_0 = a_1 = 1$, $b_0 = 2$, $b_1 = 0$, obtaining:

$$\dot{p}_i^{(2)} = \dot{p}_i^{(0)} + \frac{1}{2} (F_i^{(0)} + F_i^{(1)}) \Delta t \quad ; \quad q_i^{(2)} = q_i^{(0)} + \dot{p}_i^{(0)} \Delta t + \frac{1}{2} F_i^{(0)} (\Delta t)^2. \quad (4.4)$$

This is the algorithm of my choice for the simulation of the motion of the cell walls, in [Chapter. 5]; and the shrinkage, in [Chapter. 7].

4.2.2 Sphero-polygons

In [AM08], Fernando Alonso-Marroquín introduced the now widely used method of sphero-polygons. The problem at hand is the simulation of dynamics of colliding rigid bodies first studied by Hertz, in [Her82], and which is of great scientific and technological application in the field of granular materials. The simplest such simulation is that of the bouncing of a sphere over a hard floor. One way to take into account the deformation of the ball at the time of the collision is to assume that the sphere does not deform but overlaps with the flat floor; the force of interaction being a function of the fraction of the radius of the sphere that belongs to the overlapping region. Numerically, the solution of the equations of the motion of the sphere is done rather easily, using the instantaneous overlapping distance between the sphere and the floor to get the motion of the sphere. It is an usual project for students of beginner classes of numerical methods to solve the problem of a gas of rigid bodies.

Before Alonso-Marroquín, the simulation of motion of objects of more complex shapes involved the decomposition of the object into polyhedrons and calculate the overlapping between two neighbouring objects by means of impulse based methods or dynamic constrains. These methods are quite complex to program and computationally expensive. His idea was to take a complex object and smooth out the 2D boundary or the 3D surface, in such a way that at the end it consists only on flat surfaces and segments of arc (in 3D, segments of a sphere). In this

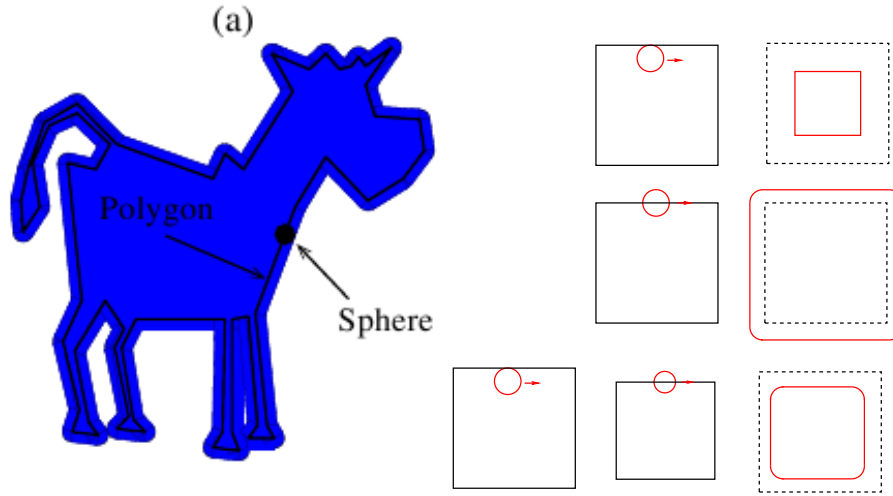


Figure 4.3: (Left) An sphero-cow, constructed by means of smoothing out a polygon based on straight lines (black lines, at the left), to get a smoothen out blue cow. [AM08] (Right) Opening, sphero-polygon construction. Upper panel shows the effect of erosion, the initial set defined by the interior of the black square gets reduced to that of the red square. The middle panel shows the effect of dilation, an initial black square gets augmented to the red sphero-polygon with rounded edges. To obtain and sphero-polygon which is a subset of the initial one, the opening has to be constructed by applying first erosion and then dilation, as shown in the last panel.

way, the interaction between complex objects turns out to be as simple as the sphere-hard floor problem stated at the beginning.

Sphero-Polygons construction

Let me start by discussing the 2D version, for simplicity. Think of the plane as a set of points; the shapes of the objects under study are subsets of the plane in the shape of closed polygons. Now, an opening of this set is defined as:

$$A \circ B = (A \ominus B) \oplus B, \quad (4.5)$$

where \ominus denotes *erosion* and \oplus *dilation*, two geometrical operations that I will describe now. A dilation of one set A by another set B corresponds to extend A by adding all the points obtained by swapping B through the A 's border. This is, it corresponds to the operation:

$$(A \oplus B) = A \cup \left(\bigcup B_i \right), \quad (4.6)$$

where each B_i is constructed by displacing the set B in such a way that its center, x_i , belongs to the border of A . The set $\{B_i\}$ is the set of all such B_i , i.e., for every x_i in the surface of A .

On the contrary, erosion would be the set obtained by swapping B through the border of A and removing all the points of A that are in one of the B_i sets. Explicitly speaking:

$$A \ominus B = A - \bigcup B_i \quad (4.7)$$

The surfaces constructed in such a way will have flat segments, the edges; and segments of and arc (segments of a sphere), the vertices. The latter are defined by the center point of the circle (sphere). An example of the operation for the smoothing out of a polygonal cow is shown in [Fig. 4.3].

Forces

To obtain the forces due to the collision of the sphero-polygons, Alonso-Marroquín and collaborators first consider all the vertex-edges distances between the polygons. Take sphero-polygons SP_i , and SP_j , which contain polygons P_i and P_j and disk radii's r_i and r_j . The polygons are defined by the vertices $\{V_i\}$ and edges $\{E_i\}$. The vertex-edge overlapping distance is:

$$\delta(V, E) = \langle r_i + r_j - d(V, E) \rangle, \quad (4.8)$$

with $d(V, E)$ the euclidean distance between the vertex V and the edge E . The force acting on particle i by particle j is:

$$\vec{F}_{ij} = \sum_{V_i E_j} \vec{F}(V_i, E_j) + \sum_{V_j E_i} \vec{F}(V_j, E_i), \quad (4.9)$$

where $\vec{F}(V, E)$ is the force between vertex V and edge E . The torque over particle i given by particle j is given by:

$$\tau_{ij} = \sum_{V_i E_j} (\vec{R}(V_i, E_j) - \vec{r}_i) \times \vec{F}(V_i, E_j) + \sum_{V_j E_i} (\vec{R}(V_j, E_i) - \vec{r}_i) \times \vec{F}(V_j, E_i), \quad (4.10)$$

with \vec{r}_i the center of mass of particle i and \vec{R} the point of application of the force: the middle point of the overlap between the vertex and the edge:

$$\vec{R}(V, E) = \vec{X} + \left(r_i + \frac{1}{2} \delta(V, E) \right) \frac{\vec{X} - \vec{Y}}{\|\vec{X} - \vec{Y}\|}, \quad (4.11)$$

Example, a sphero-cow silo

In [AM08] Alonso-Marroquín and collaborators implemented a test of the spheropolygon model by using a complex “sphero-cow” shaped grain to run simulations both of colliding grains inside a box as well as simulations of an emptying silo.

Firstly, the grains are constructed following the algorithm just discussed here, in [Fig. 4.3]. The simplest simulation consists in calculating the collision of a single sphero-cow grain with a rough floor, [Fig. 4.4] (Left). The authors also show the distribution of energy and speeds of a gas of 400 sphero-cows confined to a rectangular box. The evolution of total and rotational

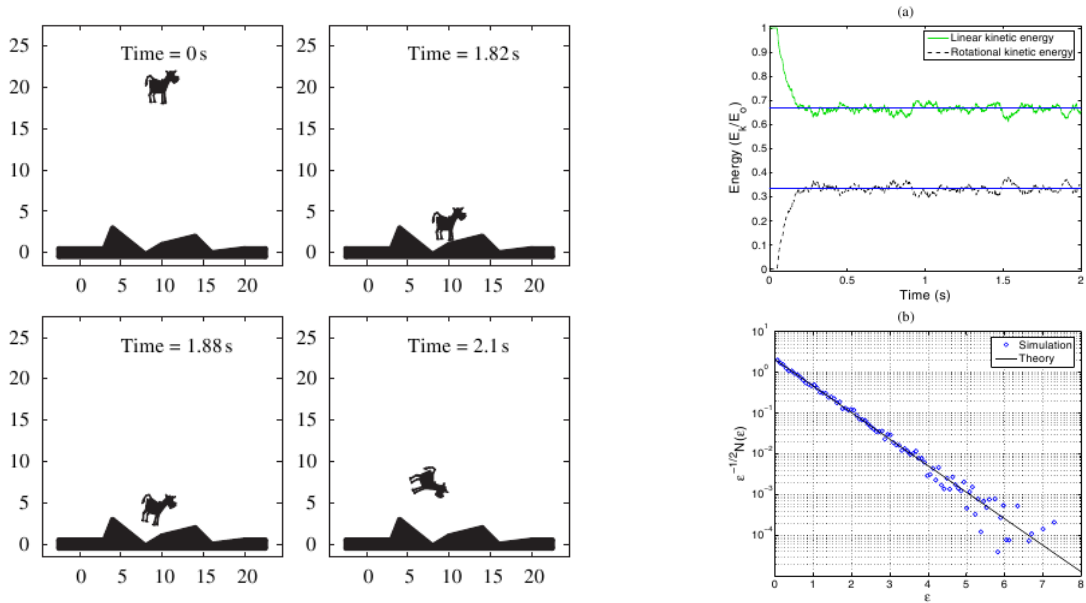


Figure 4.4: (Left) Four different snapshots of the simulation of a Minkowski cow bounding on a simple landscape. (Right) Up, normalized linear kinetic energy and rotational energy of a “gas” of 400 Minkowski cows confined to a rectangular box, which settles to average values. The horizontal lines correspond to the expected values from statistical mechanics. Down, normalized energy distribution of the particles, the line corresponds to the Maxwell-Boltzmann distribution. [AM08]

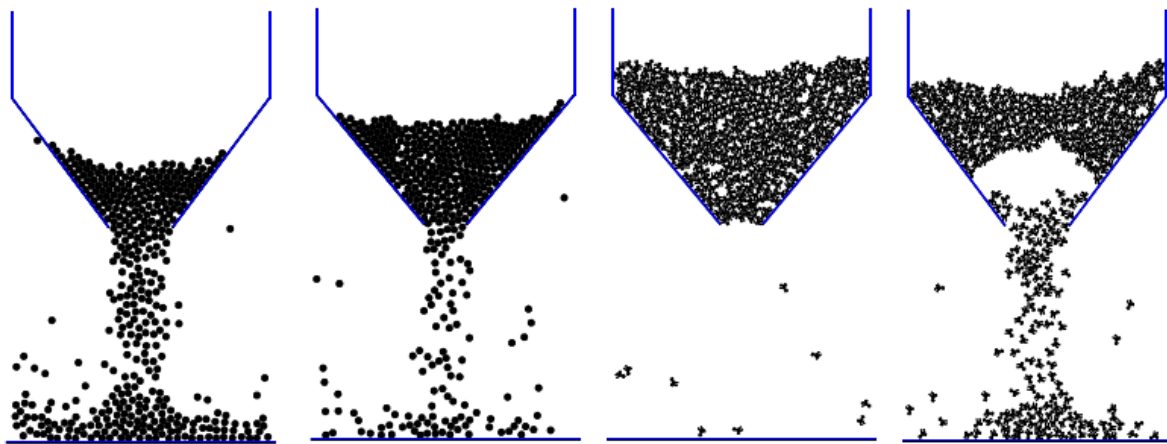


Figure 4.5: Simulation of the motion of grains in a silo, for two shapes of grains. (Left)(Center-Left) For circular grains a change in the opening of the silo only changes the flow of particles; (Center Right)(Right) instead, for the complex shaped grains a change of the opening can cause jamming- or an arc inside of the sample. [AM08]

kinetic energy falls into the expected value for statistical mechanics, and the energy distribution follows the Maxwell-Boltzmann distribution.

Lastly, the silo simulation shows how the change in the opening the throat controls the appearance of jamming for the complex grains; in contrast to a simulation in which they are simple spheres, for which there is no jamming.

4.2.3 Sphero-polygons for the simulation of fractures due to capillary forces

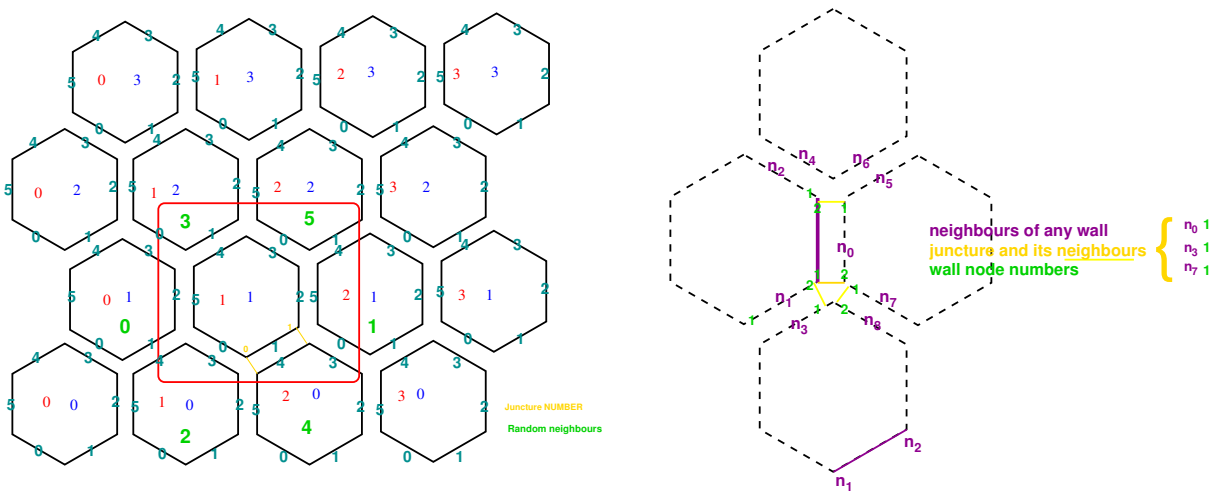


Figure 4.6: The regular lattice used for the model of [Chapter. 5].(Left) Red and Blue numbers, the coordinates in the lattice; Green, neighboring cells; aquamarine, numbering of the cell walls. (Right) Neighbours of a cell wall, in magenta; Junctures, in yellow; Wall node numbers, in green.

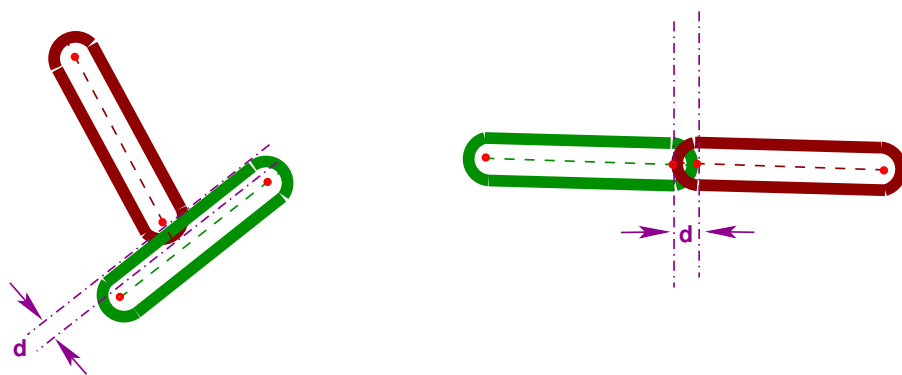


Figure 4.7: Collision Vertex-Edge between two walls. The distance d , in magenta, corresponds to the overlapping.

In [Section. 5.2], [Chapter. 5], the basic elements of the DEM are the cell walls, CW. The geometry is shown in [Fig. 4.6](Left). Two integers represent the position of each cell inside the lattice. For every cell the CW are numbered starting by the lower-left one, in counterclockwise

way. A cell has six neighbours, which are numbered 0, for the left neighbour; 1, for the right neighbour; 2 and 4, for the lower-left and lower-right neighbours; 3 and 5 for the upper-left and upper-right neighbours. This numbering is useful for randomly choosing a neighbour of a cell.

The neighbours of a CW are portrayed in [Fig. 4.6](Right): the first neighbour is the CW of the front cell; second and third neighbors, the previous and next CW of the same cell; fourth and fifth neighbors, the front CW from second and third neighbors; sixth and eighth neighbors, the next and previous CW from the first neighbor; seventh and ninth neighbors, those in the front of sixth and eighth neighbors. These are the only CW linked to a cell, since all other CW are so far away from it that it is pointless to calculate the interactions with them.

The Vertex-Edge collision and Vertex-Vertex collisions between two CW are depicted in [Fig. 4.7]. In the left panel, the Vertex-Edge collision, the overlapping is the distance d , defined as the fraction of the radius of the circle that overlaps the straight line. In the right panel, the Vertex-Vertex collision, this overlapping distance d corresponding to the fraction of one circle inside the other, is shown.

4.3 The finite element method

The *finite element method* is a numerical procedure that provides numerical solutions to a wide range of physical problems: heat transfer, fluid mechanics and solid mechanics problems. The models are represented by a set of integral-differential equations whose domain is a geometric space of arbitrary shape. Although for some problems there are already analytical solutions that are applicable mostly for very symmetric geometries of the domain, the main strength of FEM is that it can handle complicated geometries and give an approximate solution. The FEM solution for the problems with analytical solutions can be used as benchmarks of the model. Its applications include solving the diffusion equation (both for heat transfer and for fluid mechanics) and the elastic and inelastic deformation in 2D or 3D. Several different implementations of the method can be found in the literature and on the Internet; their license terms covering the whole spectrum of possibilities, commercial, free and/or open. One such package is PEFiCA, written by Prof. Dorian L. Linero in order to teach the method for post-graduate students, see [Lin09].

The objective of the Finite Element Method model is to find an approximate solution of the problem, defined in the domain of the problem; which can be of a cumbersome geometry. Firstly, the geometry is discretized into smaller sections of simple shapes. The function that solves the problem is built by continuous piecewise smooth functions defined in the segments. Different boundary conditions for the same problem will need different matching parameters between the piecewise functions. By means of an integral formulation (Galerkin's method, sub-domain method, for instance) a system of algebraic equations is derived from the differential equations that define the problem. The solution of this algebraic equations is the set of parameters of the approximate solution. An "element" consists of a set of functions, defined in the simple domain, used to solve different kinds of problems.

Take for instance the nonlinear problem defined by:

$$D(\phi) = f(\phi) \tag{4.12}$$

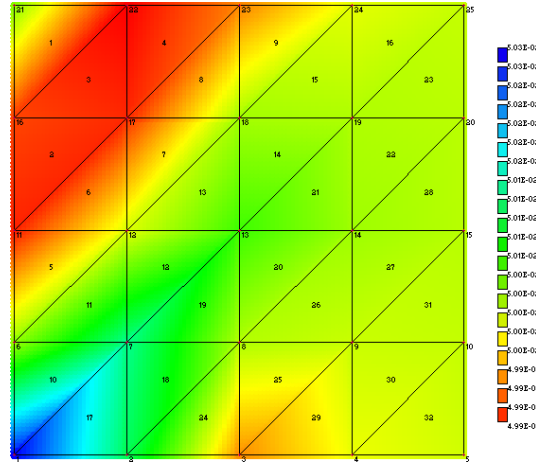


Figure 4.8: The deformation field and the shapes of the elements for a problem of orthotropic elasticity in 2D by means of PEFiCA (an open code finite element implementation, written by Prof. Dorian Luis Linero, [Lin09])

where D represents a differential operator, ϕ is the unknown solution. Within FEM, the solution is the product of a vector of constants and a vector of functions:

$$\phi = \vec{N} \cdot \vec{B} \quad (4.13)$$

where \vec{N} is a vector of coefficients and \vec{B} a vector of functions.

The FEM method is built as an algorithm. The first step is to discretize the domain, generating a set of node points and their coordinates. Secondly, the approximation to the solution is defined, and a set of equations (one for each node) is defined in terms of the unknown nodal values. The third step is to use the integral method (Galerkin's) to find an equation for each nodal value. The system of equations is solved using a linear algebra routine. This gives the final approximated solution to the problem. The last step is to use the approximated function to describe characteristics of the initial physical problem, for example the derivatives of the solution may describe physical quantities of interest.

An example of the FEM would be the problem of finding the magnitude of the strain field σ_{xx} inside a loaded orthotropic material, as show in [Fig. 4.8]. The beam is discretized at an angle of 90 degrees with respect to the axis of the material constants.

The reader interested in a more thorough description of the model can check the extense literature, for instance: [Seg84, Bat96, Hug00, ZTTZ05].

4.3.1 Elasticity FEM problem formulations

In the case of structural and solid mechanics, the FEM method is formulated in a very specific way. Take the Hooke's equation, (Eq.3.4),

$$\sigma_{ij} = \sum_{k,l} C_{ijkl} \epsilon_{kl},$$

Within FEM, the discretization of the solid into elements provides a number of local degrees of freedom, DOFs, corresponding to the relative coordinates of the motion of the different nodes of the element. The Hooke's equation is written for each of the elements of the solid, in which the elasticity matrix encompasses the elastic properties of the element. The constraints of the structure allow the programmer to specify a subset of these DOFs which are fixed. Since the motion of the nodes is relative to the nodes of the neighboring elements, some DOFs are related to two or more elements. The next step corresponds to assembling a single matrix of elasticity, in which every one of its rows and columns is related to a free DOF of the structure. In this way, it is possible to rewrite Hooke's equation for the whole solid, given an assembled matrix for the whole structure and an assembled vector of displacements, as:

$$\mathbb{K} \cdot \vec{U} - \vec{F} - \vec{P} = \vec{0}, \quad (4.14)$$

where \mathbb{K} is the elasticity matrix of the structure; \vec{U} is the vector of displacements; \vec{F} is the vector of element forces, in our case only the shrinkage due to drying; and \vec{P} is the vector of external forces, in our case a null vector. In the model that I present in [Chapter. 6], the object's deformation can only occur in one plane. This corresponds to the case of plane strain, a simplification of 3D problems to 2D geometries.

4.3.2 Strain-displacement equations

Let me take a closer look to the formulation of the elasticity problem in terms of the FEM model (see, for instance [Seg84]). The displacements inside the body are a function of the three coordinate directions:

$$u = f(x, y, z), \quad v = g(x, y, z) \quad \text{and} \quad w = h(x, y, z), \quad (4.15)$$

where the goal of the model is to find f , g and h , approximated by continuous piecewise smooth functions defined over the individual elements. The displacement equations will depend on which type of element is chosen. In general the displacement equations look like:

$$\begin{Bmatrix} u \\ v \\ w \end{Bmatrix} = \mathbb{N} \vec{U}^{(e)} \quad (4.16)$$

where the $\vec{U}^{(e)}$ is the column vector with the nodal displacements, and \mathbb{N} a matrix with the shape element functions. The strain components are obtained from the displacements by:

$$\begin{aligned} \epsilon_{xx} &= \frac{\partial u}{\partial x}, \quad \epsilon_{yy} = \frac{\partial v}{\partial y}, \quad \epsilon_{zz} = \frac{\partial w}{\partial z} \\ \epsilon_{xy} &= \frac{\partial u}{\partial y} + \frac{\partial v}{\partial x}, \quad \epsilon_{xz} = \frac{\partial u}{\partial z} + \frac{\partial w}{\partial x}, \quad \epsilon_{yz} = \frac{\partial v}{\partial z} + \frac{\partial w}{\partial y}. \end{aligned} \quad (4.17)$$

which is valid in the case that thermal strain is zero. Shortly, this can be written as :

$$\epsilon = \mathbb{B} \vec{U}^{(e)}. \quad (4.18)$$

can be proven (see [Seg84]), that the element elastic matrices come from this calculation, as:

$$\mathbb{K}^{(e)} = \int_V \mathbb{B} \mathbb{D} \mathbb{B} dV \quad (4.19)$$

with D the elastic constants matrix.

4.3.3 The plane frame element, PFE

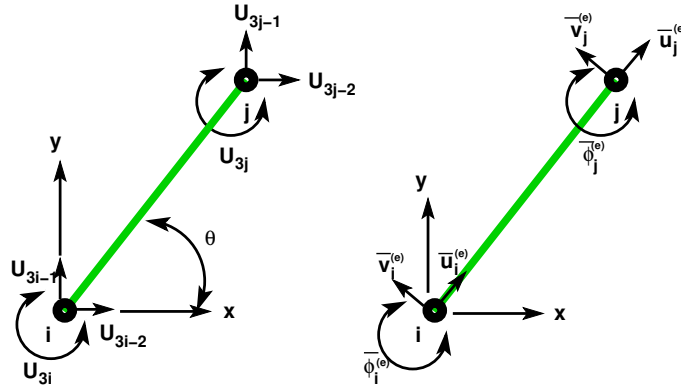


Figure 4.9: (Left) A plane frame Element, showing the nodal displacements. The angle θ describes the orientation of the element. (Right) Each of the nodes and their local displacements, the overline coordinates correspond to the element coordinates.

As was discussed previously, this book is restricted to the study of the plane deformations during drying. Therefore it is possible to do a strictly 2D formulation. The element chosen to model the cell wall, is the plane frame element, or PFE. A PFE models a beam for which both rotation and translation of its two ends are possible, see [Fig. 4.9]. The parameters that define it are its elastic modulus E , cross section area A , area moment I and length L . The vector of displacements in element coordinates is given by:

$$\vec{\bar{u}}_{loc}^{(e)} = \{\bar{u}_i, \bar{v}_i, \bar{\phi}_i, \bar{u}_j, \bar{v}_j, \bar{\phi}_j\} \quad (4.20)$$

The unprimed (global) coordinates are obtained from the local coordinates by means of a rotation matrix T :

$$\mathbb{T}^{(e)} = \begin{bmatrix} \cos(\theta) & \sin(\theta) & 0 & 0 & 0 & 0 \\ -\sin(\theta) & \cos(\theta) & 0 & 0 & 0 & 0 \\ 0 & 0 & 1 & 0 & 0 & 0 \\ 0 & 0 & 0 & \cos(\theta) & \sin(\theta) & 0 \\ 0 & 0 & 0 & -\sin(\theta) & \cos(\theta) & 0 \\ 0 & 0 & 0 & 0 & 0 & 1 \end{bmatrix}, \quad (4.21)$$

The element stiffness matrix is given by (see, for example, [Seg84]):

$$\mathbb{K}_{loc}^{(e)} = \frac{EI}{L^3} \begin{bmatrix} \frac{AL^2}{I} & 0 & 0 & -\frac{AL^2}{I} & 0 & 0 \\ 0 & 12 & 6L & 0 & -12 & 6L \\ 0 & 6L & 4L^2 & 0 & -6L & 2L^2 \\ -\frac{AL^2}{I} & 0 & 0 & \frac{AL^2}{I} & 0 & 0 \\ 0 & -12 & 6L & 0 & 12 & 6L \\ 0 & 6L & 2L^2 & 0 & -6L & 4L^2 \end{bmatrix}. \quad (4.22)$$

As the element rotates in the space of the system, the angle θ changes. The global matrix of the system is constructed by assembling the individual elements, as discussed in [Seg84]. In the [Chapter. 6] two kinds of lattices are introduced, either regular hexagonal or randomized voronoi.

4.3.4 Voronoi construction: gathering of guadua structure and random lattice generation

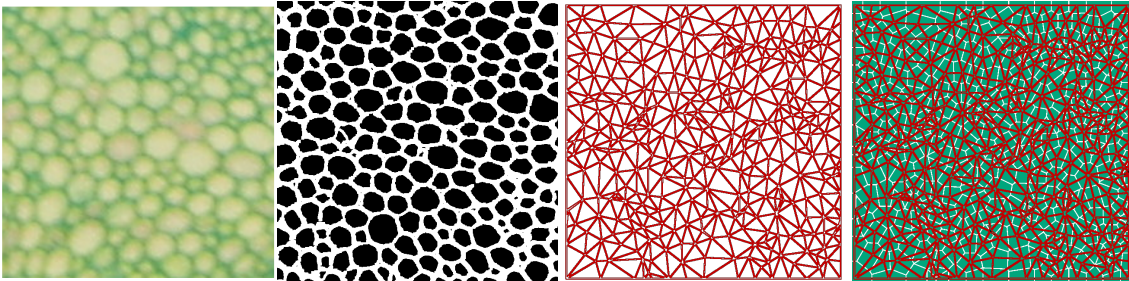


Figure 4.10: Construction of the voronoi lattice corresponding to the real parenchyma tissue. (Left) A picture from the guadua drying, taken from [LVV⁺03]. (Center-Left) the cells are recovered by applying a mask to the imate. (Center-Right) using the centers of the cells, a triangulation can be constructed. (Right) the voronoi lattice is built by intersecting the lines perpendicular to those of the triangulations. The final voronoi tessellation is seen in [Fig. 4.11].

How to capture and regularize the geometry of the guadua tissues? The present section describes the method I used to both capture the geometry of guadua, and generate new geometries that resemble the natural one. The problem here is that even though the cells walls seem straight, they show roughness at the pixel level pictures. As this is not a fundamental aspect of the geometry, i.e., they are lines in mandelbrot's classification, a computational method can be used to obtain straight lines.

Take first the structure of the parenchyma tissue cell wall, as shown in the pictures from the literature [LVV⁺03]. By using a mask over the picture, I obtained the body of the pictures. Afterwards a simple center of mass calculation,

$$X_{CG-l} = \frac{1}{N_l} \sum_{i=1}^{N_l} x_i, \quad Y_{CG-l} = \frac{1}{N_l} \sum_{i=1}^{N_l} y_i, \quad (4.23)$$

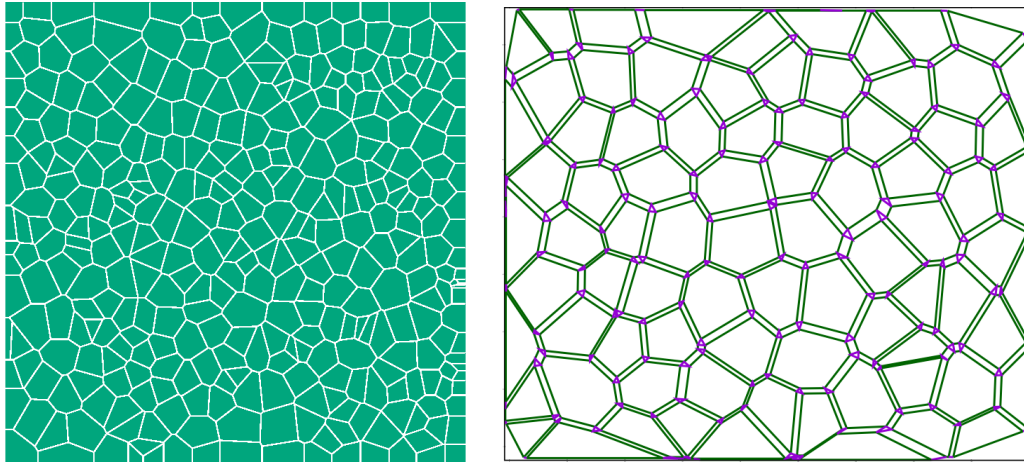


Figure 4.11: (Left) Voronoi lattice build from a photo of bamboo parenchyma tissue. In green the voronoi cells that will correspond to the cells. The cell walls (in white) suffer capillary pit forces perpendicular to them. The tessellation was done using Triangle[She96]. (Rigth) An inhomogeneous lattice, build by displacing the center nodes in an hexagonal lattice and calculating the closest neighbours by means of a Delaunay triangulation, [Fig. 4.11], used in [Chapter. 6].

provides the centers of the cells. The closed shapes generated by the perpendicular lines to the lines that join all this centers constitute the voronoi lattice. The process of building this has been optimized and distributed as open software by means of a Delaunay tessellation ,[She96], therefore I used this implementation.

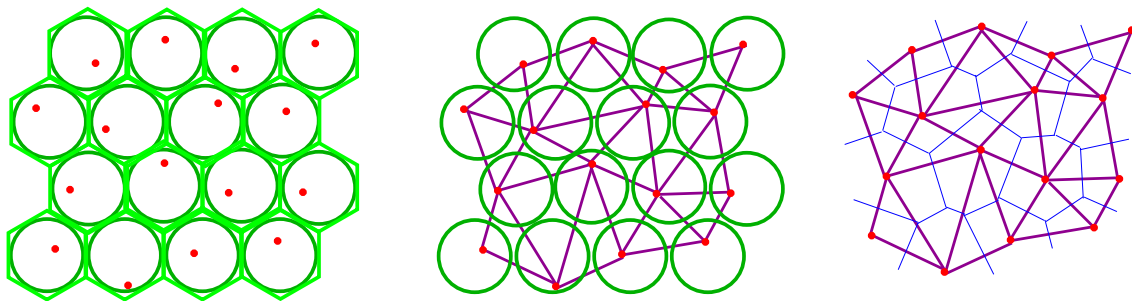


Figure 4.12: Voronoi generation. (Left) Inside each hexagon from the original lattice, build a circle. Take a random point from inside each of the circles. (Center) Make a triangulation, by drawing lines from the points to those in the neighboring circles. (Rigth) The voronoi construction is finished by taking the perpendicular lines to those of the triangulation and extending them until they find another line.

In a similar way an artificial network can be constructed. Take any hexagonal lattice. The hexagons correspond to the voronoi lattice that would correspond to points in their centers. To randomize this lattice, I took circles inside the hexagons and randomly choose a point inside each of them. From the new points a voronoi lattice was constructed. This new lattice resembles the natural one, as seen in [Fig. 4.12]

4.4 Pore network models

The pore network models provide a way of studying the receding of a water front inside a porous material. They consist in pores (sites) connected by throats (bonds). The throat widths are chosen randomly (see [Fig. 4.13]). Initially the whole sample is filled with water. As drying starts, the water will recede into the sample. If the fluid is viscous enough, the simulation will correspond to a laminar flow and the turbulent effects can be ignored. This is the case in drying below the boiling point of water. Furthermore, this “slow drying” simulations allows to disregard the effect of the flux of energy [Pra02].

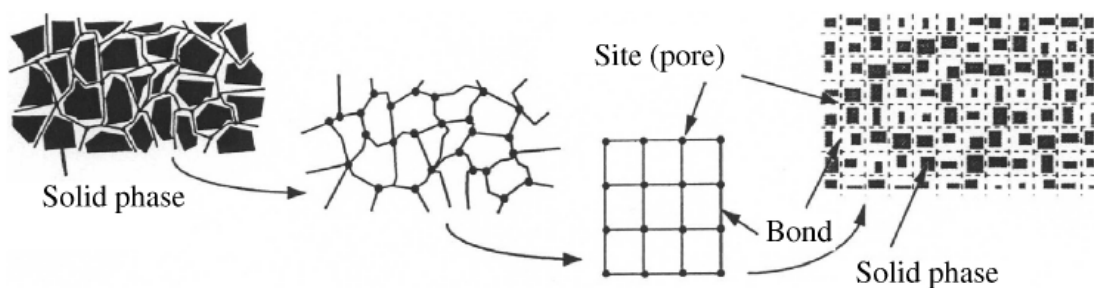


Figure 4.13: Modeling of pore space by a network of pores (sites) and throats (bonds), from [Pra02]

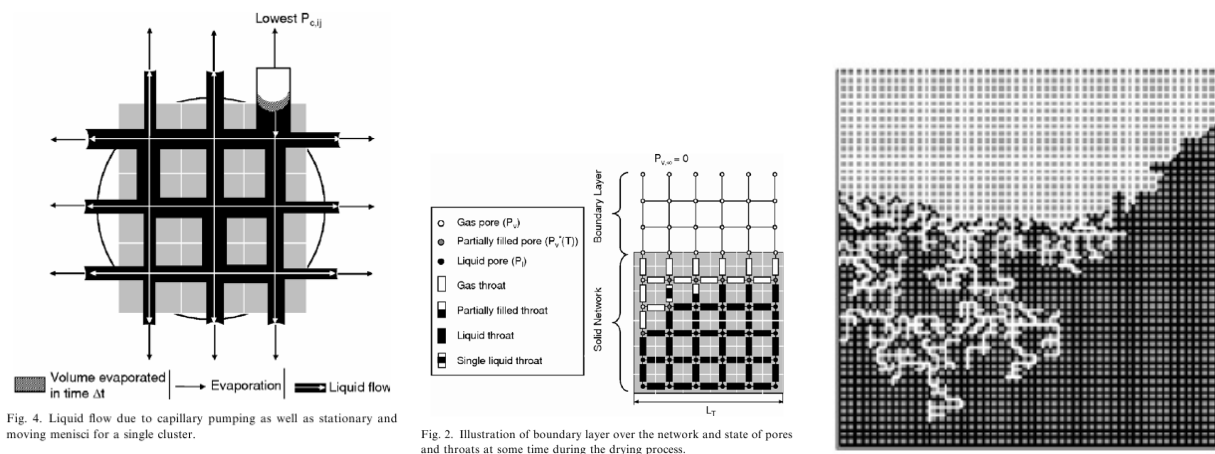


Figure 4.14: (Left) Liquid flow due to *capillary pumping*. (Center) Boundary layer over the network and state of pores and throats, (Right) A given state of the drying interface. From [SMT08]

Even though there is evaporation at all the capillaries, the drying front does not move at the same time in all of the throats. This is because of the capillary pumping: the smallest pore will create the highest Laplace under-pressure and then there will be a net flow to this pore from the others. Furthermore, only the widest pore will be emptying at a time. After this pore has been dried, the next one in order of size will be chosen next and so on (see [Fig. 4.14], this dynamics has been reported experimentally, in [XDSW08]).

The pore network modeling is being actively developed by groups at France (IMFT ,Institut de Mécanique des Fluides de Toulouse, Prat et al.), California (University of Southern California, Yortsos et al.) and Chile (Universidad de Concepción, Segura y Toledo) based on a seminal work by Nowicki.

4.4.1 General description

There is continuity in the liquid phase at the representative elementary volume scale:

$$\epsilon \frac{\partial S}{\partial t} + \nabla \cdot \vec{q}_1 = -\frac{\dot{m}}{\rho_l} \quad (4.24)$$

where ϵ is the porosity, S liquid saturation, \vec{q}_1 the volumetric flux of liquid, \dot{m} the drying rate per unit volume, and ρ_l the liquid density. \vec{q}_1 is related to the pressure gradient by means of Darcy's law :

$$\vec{q}_1 = -\frac{k k_{r,l}}{\mu} \nabla p_1 \quad (4.25)$$

where k is the permeability of the porous medium, $k_{r,l}$ the relative permeability, a function of the liquid saturation, and μ is the liquid viscosity. As we have seen, the pressure difference will be given by capillary forces. The vapor phase transport is assumed as a diffusive process. If continuity for the gas phase is needed it can be expressed as:

$$\epsilon \frac{\partial p_v}{\partial t} = \nabla \cdot (D_{eff} \nabla p_v) + \dot{m} \quad (4.26)$$

with p_v the vapor partial pressure, D_{eff} the vapor effective diffusivity. Pore network models allow to calculate macroscopic parameters (k , k_l , D_{eff}) as functions of the saturation S .

The discretization of this continuum equations is done by expressing the volumetric flow rate between two sites as the difference of pressure at them:

$$q_k = \frac{g_k}{\mu} (p_i - p_j) \quad (4.27)$$

where the pressure at each pore is given by its width. The conductance g_k depends on the shape of the bond. This allows to define a Kirchhoff-like current law, $\sum_k q_k = 0$. The models define four states for bonds -filled, emptied, half filled and with a droplet- and three for sites, liquid filled, gas filled, and partially filled. (see [Fig. 4.14]). The quenched disorder in the pore sizes generates a non trivial drying dynamics (see [Fig. 4.14]). Pore network models have also been extended to include heat flux [SMT08] and shrinking [ST05, QRT05].

4.4.2 Physical evidence of “drying rules”

Lei Xu and collaborators have studied experimentally the drying dynamics of a porous medium by means of confocal microscopy, in [XDSW08]. Their experimental set-up consists on small

particles soaked in an evaporating liquid. The work finds two stages of drying: During compactification, the first one, the particles aggregate and pack into structures creating a network of pores. During the second phase there are abrupt air invasions varying in burst sizes from one to hundreds of particles. This invasion process follows from the strong flow in menisci from large pores to menisci in smaller pores during drying. This dynamics is equivalent to invasion percolation, as is the model that I introduce in [Chapter. 5].

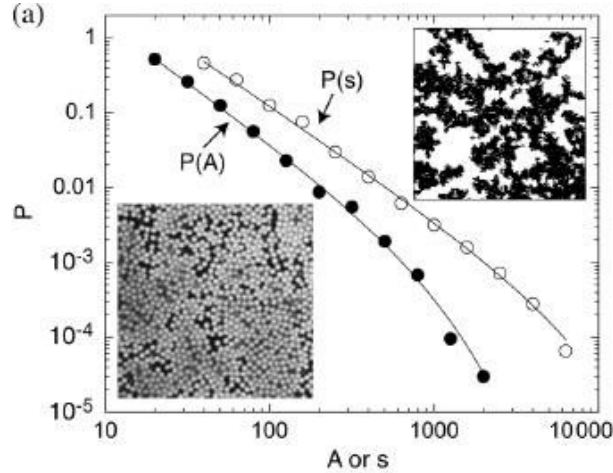


Figure 4.15: Probability distribution of finding a burst of sizes s (2D), or A (3D), from [XDSW08]

Furthermore, they measure the probability of the burst sizes (in 2D) and areas (in 3D), obtaining power-law distributions: (see [Fig. 4.15])

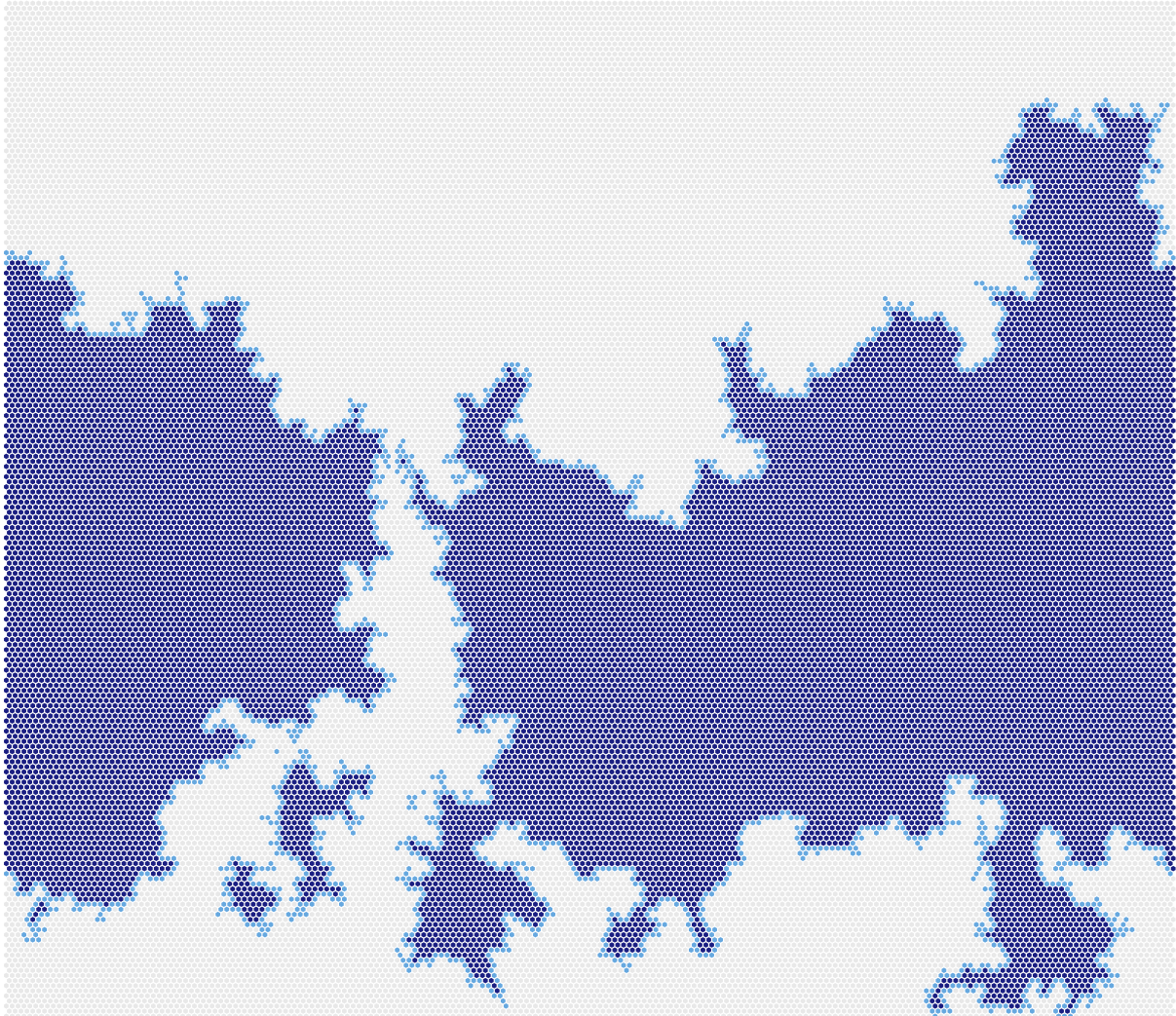
$$P(A) = A^{-\alpha} e^{-A/A^*} \quad \text{with } \alpha = 1.6 \pm 0.1, \quad A^* = 850 \pm 150 \mu m^2 \quad (4.28)$$

$$P(s) = s^{-\tau'} e^{-s/s^*} \quad \text{with } \tau' = 1.5 \pm 0.1, \quad s^* = 6500 \pm 1000 \quad (4.29)$$

In this case the experimental cutoff is related to the liquid redistribution due to the finite size of the sample.

These experimental results prove that the invasion in a porous medium can be approximated to bursts of drying events, in which the pores are emptied. This implies that for the case of my model it is not necessary to model the whole water movement inside the wood, instead one can apply a set of drying rules that follow from the physics of the process.

$$\tau = 11955$$



Hexagonal lattice drying model, at percolation time, $L = 1000$.

A theoretical statistical model of fracture due to capillary pressure

The present chapter introduces a theoretical model of fracture for a cellular material subject to drying induced pressure. This is an inherently probabilistic process, as both the dynamics of the receding front and the value of the pressure depend on the disorder present in the distributions of sizes of pore pits. Therefore the methods of statistical mechanics of fracture provide a characterization that allows to determine the impact that this dynamics may have on the fracture statistics of bamboo.

In the first section of this chapter, I study the evolution of the drying front inside a cellular material. This is done by means of a percolation model for the dynamics of the drying. Turns out that this simple model is completely equivalent to invasion percolation. In the second section I study the effect that the capillary forces, transmitted to the cell walls by the liquid, have on the deformation and fracture process of the bamboo tissue. This is done by means of a discrete element model which can take into account complex interactions in a very simple way.

5.1 Honeycomb lattice non-trapping invasion percolation

As was stated before, drying of a cellular material has two different phases: free water removal and bond water removal. The former starts by emptying the vessels, almost immediately after cutting the bamboo, in a very fast sub-stage. In this chapter I present a model to deal with the following drying sub-stages of this free water removal phase, in which the content from the apoplasm is slowly lost.

In the present model the cellular material is represented as a lattice of geometrically identical hexagonal cells. To account for the ring topology of bamboo, periodic boundary conditions are implemented in the left and right borders. Lattice linear size L is defined as the number of cells in the bottom row. The free water drying is represented as a percolation process where the cells are the sites and the pit pores represent the links. At the beginning of the simulation all of the cells are marked as filled. The initial condition corresponds to labeling which cells have at least one

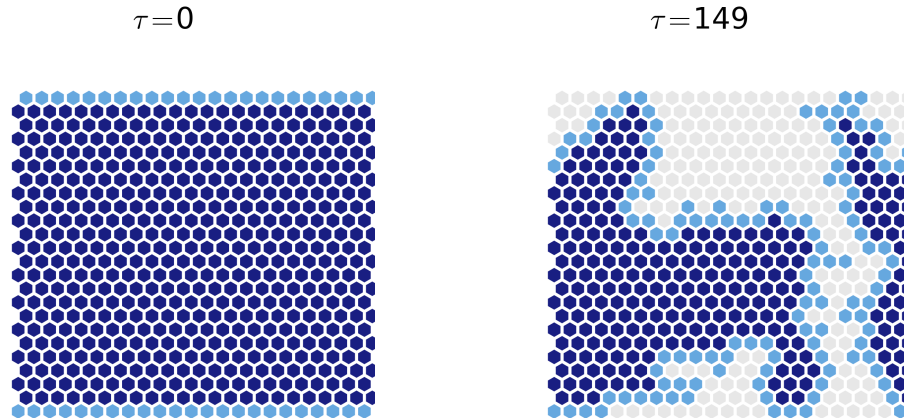


Figure 5.1: Snapshots of percolation drying systems. In gray the empty cells, light blue the drying front cells, and dark blue the inner cells. (Chapter cover) System of linear dimension $L = 200$, at the percolation time. (This page) A system of linear dimension $L = 24$: (Left) Initial state, the drying front corresponds only to upper and lower rows. (Right) State of the system at percolation time.

cell wall who has water on one side and air on the other side as belonging to the drying front . In this subsection’s model this corresponds, in the beginning of the simulation, to those cells in the upper and lower rows. Drying is an stepwise process in which one cell belonging to the drying front is marked as empty at a time, while its remaining filled neighbors are added to the drying front for the next step of the evolution. The drying dynamics itself (in other words “which is the next cell to be marked as dried”), is governed by the quenched disorder present in the structure in the form of a homogeneous distribution of pit pore widths δ_i between neighboring cells (see [Fig. 5.4]). Water would evaporate from the water-air interface at the pores of the drying front, but due to capillary pumping only one cell at a time is emptied: the one with the wider pore pit.

The *filled cells clusters* are set of neighboring filled cells. At the beginning of the simulation, for example, there is just one cluster of cells including all of them. As drying evolves sets of contiguous cells may get detached from the main cluster. One example is the figure on the cover of this chapter, where there are three filled clusters: a huge one, wrapping from left and right boundaries (as there are periodic boundary conditions there); and two smaller ones, in the middle of the graph. As the capillary forces are larger than viscous forces, the flow of water is governed by the capillary pressure, given by the smallest pore in the system. This implies that at a given moment of the drying evolution effectively only the widest pore present empties (at each cluster of filled cells), even though evaporation occurs at every water-air interface. This dynamics is coherent with the results of [XDSW08]; the only difference being that in the present model there are no bursts of drying larger than one, since the volume of the cells is much larger than that of the pits.

The stepwise drying dynamics allows to define a *dried cells time*, τ as the number of cells that have dried on the largest cluster of cells. This discrete quantity is different to t , a continuous variable defined as the *clock measured drying time*. The relation between this two quantities is like this: on an hypothetical experiment clock, the interval Δt between that takes to dry one cell is different at any to different values of τ , simply because the water-air inter-facial area is different. For example take the system of linear extension $L = 24$ represented in [Fig. 5.1]. At $\tau = 1$ (left panel) -the beginning of the simulation- the total area of the interface is given by the pores of the upper and lower rows of cells, in this case 46 cells. At $\tau = 149$, a larger area of 119 cells is responsible for the emptying of the next cell.

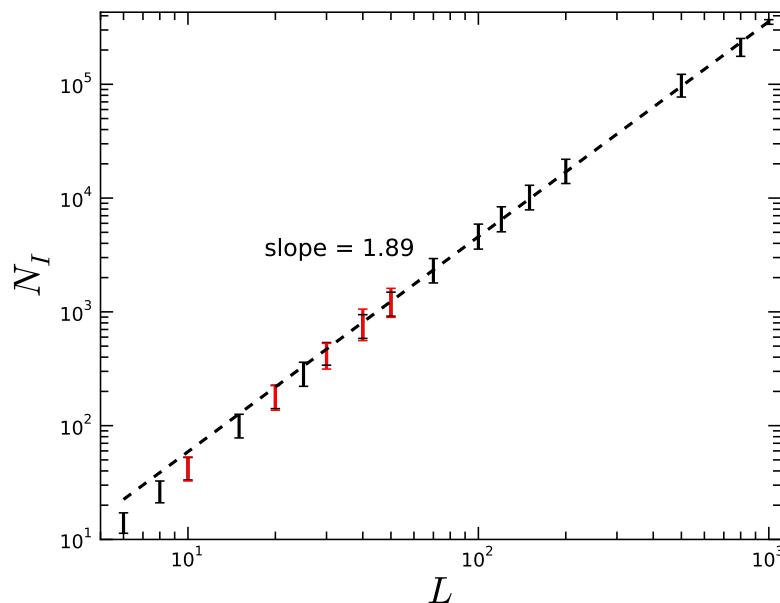


Figure 5.2: Average size of the emptying cluster at percolation time, as function of the linear size of the system. Black points correspond to the size of the cluster for invasion percolation. The red points include the forces and detachments, from section 5.2. Dashed black line corresponds to a power law of 1.8, the known value for invasion percolation from the literature.

In the snapshots of the system, filled cells are represented by blue colors, light for the cells belonging to the drying front and dark for the inner cells. Empty cells are marked by gray. The dynamics of this drying model corresponds to non-trapping invasion percolation [WW83, Sah94, SA94]. ¹ The algorithm of the drying proceeds is the following:

¹Invasion Percolation is related to a wetting fluid displacing a non-wetting fluid, as for instance water displacing oil at a petroleum extracting site. A displaced site is marked as filled. In that case clusters of non-marked cells correspond to a finite amount of non-wetting incompressible fluid. As invasion corresponds to displacement of the fluid, isolated clusters have nowhere to displace to, and therefore they can not be marked anymore; this is called the non-trapping condition. This does not happen in our case: non-marked cells corresponds to clusters of cells filled with water, which can emptied by evaporation.

1. A *drying front* is constructed, having all those cells neighboring either empty cells or the system boundary. In the first step this corresponds to the upper and lower rows of cells.
2. The filled cluster sets, consisting of all those neighboring filled cells is constructed. During drying, branches of cells may get isolated of the rest, and thus belong to different sets. Every set is sorted by the wider open pore of its cells belonging to the drying front.
3. From each set, the cell with the wider pore belonging to the drying front is emptied.

Percolation is defined as the merging of the upper and lower drying fronts. The snapshot plot at the beginning of this chapter was precisely taken at percolation time ([Fig. 5.1]). On an ensemble average, the size of the cluster of empty cells is determined by the *fractal dimension* D_f , by:

$$N_f \sim L^{D_f} \quad (5.1)$$

The validity of this relation for our system is investigated on [Fig. 5.2], where the size of the emptying cluster at percolation time is plotted as function of the system size. The dashed line corresponds to the accepted value for 2D: $\phi = 91/48. \approx 1.896$. The good fit indicates that our model reproduces the standard percolation. Moreover even when the system is extended to include drying induced fractures that could prevent some neighboring filled cells to belong to the same cluster of filled cells, the slope is maintained; implying that the system is still in the same universality class.

Given this geometry of the drying front, the next section would extend this model to take into account the effect of the capillary pressure has on the statistics of detachments of cells.

5.2 Dynamic Model

The objective of the present chapter is to find the role that capillary forces may have over the onset and growth of fractures during a drying process of a cellular material (like bamboo), by means of a theoretical computational model. This implies taking into account the relationship between the capillary forces and the material characteristics; in our case, the distribution sizes of pore pits between cells and the distribution of breaking thresholds of the *middle lamella-tricellular junctures* between neighboring cells. The scheme chosen for the simulation is the time driven discrete element method. This allows us to preserve the cell structure including even the contact forces that may appear between neighboring cells if they are crushed by the capillary forces.

5.2.1 Model Description

As drying in bamboo tissues takes place in the radial-tangential plane, as a good first approximation it is possible to take only a two dimensional model aligned in this directions. A section of bamboo culm is represented in this model as a lattice of geometrically identical hexagonal cells, with lattice size L defined as the number of cells in the bottom row. In turn each cell is composed of six cell walls which are modeled as two dimensional sphero-sticks of unitary mass. They are

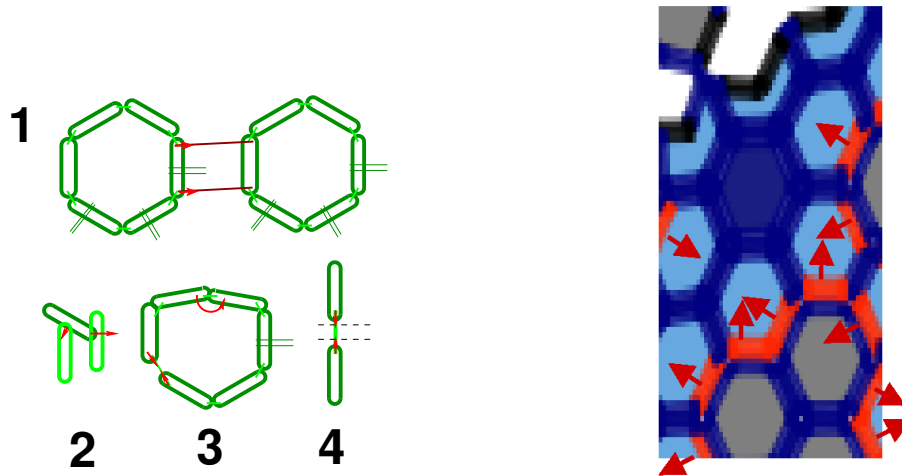


Figure 5.3: (Left) Forces acting on the system. 1. Cohesive junctures lamella. 2. Contact forces due to neighboring cells. 3. and 4. Cohesive forces in keeping the cells walls together. (Right) Capillarity causes a difference of pressure that can be represented as a force acting on those walls on the air-water drying front set of cells which have not plasmolyzed. Key: Gray cell, empty; Light blue cell, drying front; Dark blue cell, inner; colored wall, are not delaminated and the color-scale represents the magnitude of the force; black wall, delaminated.

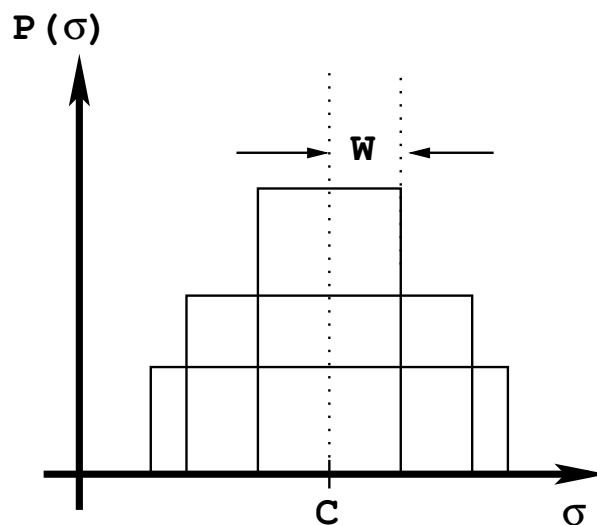


Figure 5.4: Uniform distributions of either breaking thresholds (σ) or pit opening widths (δ) are characterized by a center value (C_σ , C_δ) and a width (W_σ , W_δ).

joined together by both a linear and angular springs; the former just enforce the continuity of the cell, while the latter represent its bending resistance. The combined effect of the middle lamella and the tricellular junctures is represented by joining neighboring cells by a couple of springs in the corners, called the *junctures*. Therefore the following are the forces acting on any particular cell that belongs to the tissue being modeled:

1. Cohesive forces from neighboring cells, transmitted by the middle lamella and the tricellular junctures. This force is represented by central force with constant $k_j = El/A$, with l a natural length, A the uniform cross section and E the Young modulus. (see [Fig. 5.3], panel 1.)
2. Contact forces due to neighboring cells. The overlapping between the cell walls provides a distance x_{ov} . The overlapping force is proportional to this distance, by an elastic constant k_{wn} (see [Fig. 5.3], panel 2.)
3. Capillary forces arising from the interface between the inner apoplasm and the external air due to the drying front receding into the wood. As in the case of capillary adhesion, this implies that the pressure difference between the atmospheric pressure and the liquid pressure can be represented as a force acting on those cell walls which have on one side the air interface and on the other side the water interface. The direction of the force is perpendicular to the wall, (see [Fig. 5.3], panel 3.) and its magnitude is given by the Laplace pressure (equation, (Eq.2.24).):

$$\Delta p = \gamma C = \gamma \left(\frac{1}{R} + \frac{1}{R'} \right),$$

4. Cohesive forces between neighboring walls. A linear elastic spring maintains the cell walls joined together, while an angular spring at the corners represents the resistance to bending. (see [Fig. 5.3], panel 4.)

As discussed in the previous section, the time evolution of the water front is ruled by the set of pit pores openings δ_i , belonging to the drying front at a given dried cell time τ . Those width values are set fixed at the beginning of the simulation, and they distribute homogeneously with a center C and a width W , representing the quenched disorder of the system [Fig. 5.4]. This is, the probability distribution of pore pits is given by:

$$p(\delta_i) = \frac{1}{2W_\delta}, \quad \text{for } C_\delta - W_\delta \leq \delta_i \leq C_\delta + W_\delta \quad (5.2)$$

The present model is focused on studying the capillary forces that act on the cells, therefore keep in mind the fact that the pressure on the liquid phase is given by the smallest pore of the water-air interface for each of the *clusters*. As in the previous section, they are defined as contiguous sets of neighboring filled cells. Furthermore, in the present model two mechanisms can make contiguous cells to belong to different clusters: cracks and plasmolysis (to be described shortly). The magnitude of the pressure is fixed during each time-step τ for each cluster.

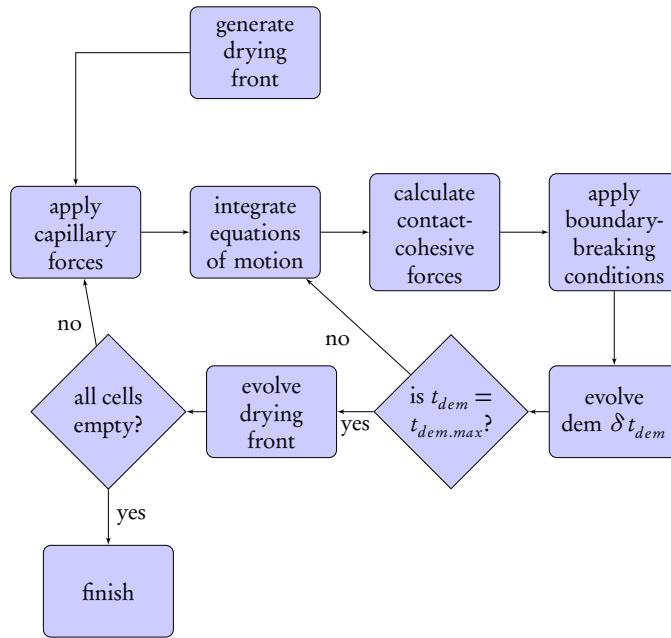


Table 5.1: Flux diagram of the discrete element capillary forces model.

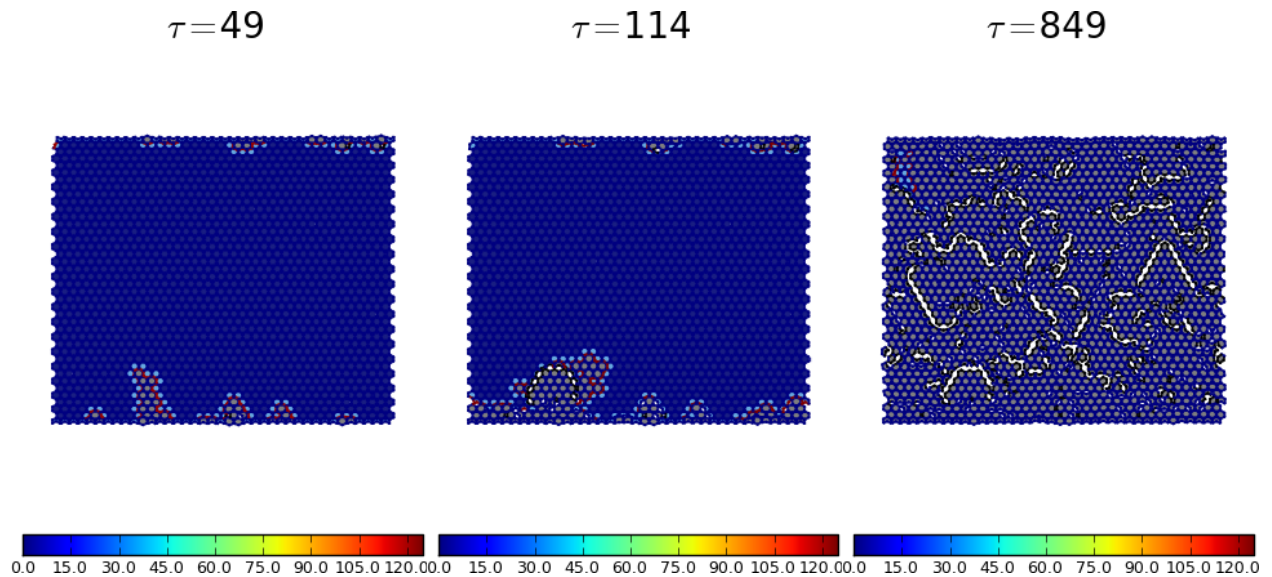


Figure 5.5: Snapshots of a non-homogeneous system with $4 < \sigma < 4.2$, with a distribution of pits characterized by a disorder $\xi = 0.7$: (Left) $\tau = 49$, drying starts; (Middle) $\tau = 114$ some fractures appear on those walls which belong to the drying front; (Right) Final state, some isolated cracks have appeared. Color key: Gray cell, empty; Light blue cell, drying front; Dark blue cell, inner; colored wall, are not delaminated and the color-scale represents the magnitude of the force; black wall, delaminated.

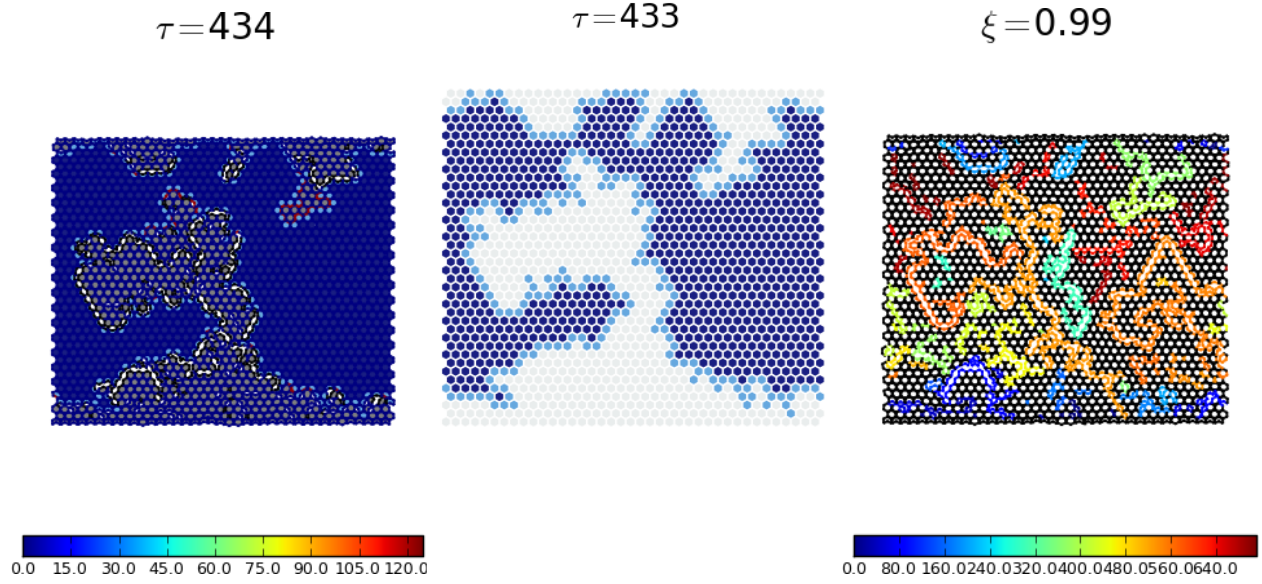


Figure 5.6: Snapshots of a non-homogeneous system with $4 < \sigma < 4.2$, with a distribution of pits characterized by a disorder factor $\xi = 0.7$ (Left) $\tau = 434$, more cracks are generated on the cells belonging to the drying front; (Middle) $\tau = 849$ final state of the system after the drying process has finished; (Right) Individual cracks, characterized by different colors.

The drying dynamics implies that the capillary forces change with τ , both on magnitude (as the narrowest pore may change) and also on which walls it is applied; as the drying of cells changes the character of which cells belong to the interface. This generates an anisotropy of the force field, thus causing tensile forces at specific points of the cellular material on the receding interface of the drying front. As cell walls get displaced, the cohesive and contact forces also change in magnitude and orientation.

The movement of the cell walls is faster than the drying dynamics. Computationally, the kinematics is obtained by integrating the equations of the motion of each cell walls by means of a Verlet algorithm whose time-step is defined as $t_c \ll \tau$. At each step of the Verlet algorithm, the program calculates the instantaneous values of the contact and cohesive forces due to the exact position of the walls. To speed up the evolution, relaxation is ensured by applying a velocity dependent damping force.

In this model fractures are introduced by applying a detachment criteria of neighboring cell walls. This is accomplished by assigning a threshold value for the strength σ_{th} at which every juncture is irreversibly broken; values of these thresholds are chosen automatically by the program from an homogeneous probability distribution, characterized by a center value C , a width W , and a random generator seed s_σ :

$$p(\sigma_i) = \frac{1}{2W_\sigma}, \quad \text{for } C_\sigma - W_\sigma \leq \sigma_i \leq C_\sigma + W_\sigma \quad (5.3)$$

depicted in [Fig. 5.4]. The program applies the breaking condition for every juncture at each value of the molecular dynamics evolution time t_c ; this ensures that the occurrences of the breakings are caused by the changes in capillary forces due to drying rather than being an artifact of the computational model. In other words, one can say that the dynamics due to the capillary, contact and cohesive forces gives a resulting quasi equilibrium system configuration state which implies certain distribution of forces on the junctures. When the stress on any juncture surpasses the strength values σ_i , the particular juncture is removed from the simulation and marked as broken, and a new quasi-equilibrium configuration is calculated. At each time-step τ the number of such detachments $\Delta(\tau)$ is defined as the size of the avalanche having place at that given discrete time.

Let me define *cracks* as contiguous sets of detached neighboring cells and, as in the shrinking model of next chapter (representing bond water removal), they can come from different avalanches. *Plasmolysis* (the separation of the cell membrane from the cell wall) is taken into account by applying a deformation criteria: if any of a cells linear dimensions is reduced by 30%, the capillary force does not affect the plasmolyzed cell anymore, and therefore it is marked to be ignored from further capillary forces calculations.

In the remaining of this chapter I will present the results of the dynamics of the avalanches, for further comparison with the experimental data. This section's plots of the snapshots of the system follows the following convention: cell walls color is picked according to the force acting on it, scaled by the color bar on the bottom of the picture; black cell walls, an exception to the previous rule, correspond to delaminated walls; dark blue cells, filled with water; light blue cells, drying front; gray cells, empty.

5.2.2 Fracture statistics for different drying dynamics and disorder distributions

The fracture of a real material is a fortuitous process, in the sense that mechanical characteristics and the failure mechanisms are intrinsically random. The present section contains the results of the investigation I conducted on the effect that either the disorder of the pit openings δ_i of the links between the cells, the disorder of the breaking thresholds σ_i for the junctures and two different drying dynamics have on the statistics of breakings of the junctures.

Disorder is introduced by means of random number generators. In the current section I used only homogeneous distributions of random numbers, which can be characterized by a dimensionless parameter:

$$\xi = \frac{W}{C} \quad (5.4)$$

with W the width of the distribution and C the center, as mentioned in (Eq.5.2), ranging from 0 (no disorder) to 1 (highest disorder). Different quantities reported correspond to averages over different realizations of disorder, having the same parameters but characterized by different seeds of the corresponding random number generator.

Keep in mind that, due to the inverse proportionality between the pore width and the capillary force (Eq.2.24), when the distribution of pores includes smaller values, the distribution of forces will include larger values. Distributions of widths closer to $\xi = 1$ will include some small pores, with larger capillary forces, as the minimum of the distribution of pit width is closer to 0. On the contrary for too narrow distributions the maximum capillary force can be quite low.

Regarding the units, in the remaining of the chapter I take the breaking threshold in units of $k * w$, with w is the half width of the cell wall and k the value of the elastic constant used in the calculations of wall-wall interactions. Pit pore widths are given in μm . The rest of the numerical constant correspond to those of bamboo, as reported in the literature and in the constants appendix.

In the literature, the avalanche dynamics of the system is usually monitored with two quantities. Firstly, the *average size of the avalanches as function of the drying time* $\overline{\Delta}(\tau)$ as an ensemble average over different instances of the system, characterized by different seeds of the random number generator for the same amount of disorder. This quantity shows when do the large avalanches occur on the system, giving information about the stress concentration. The second quantity is the *probability distribution of avalanches* $P(\Delta)$. This will provide an analogy between the phase transitions not only with the present model, but also with the shrinkage model to be presented in the following chapter.

In what follows I will show the effect that the amount of disorder of both the pit pore and the breaking threshold distributions have on the statistics of avalanches of breakings. Since the dynamics of the drying front relies on having different values for the pit pores, the amount of disorder of pores is always nonzero. Furthermore, to isolate the effect of the width, the center of the distribution of pore pits is fixed at the value of 0.0001.

Homogeneous Material

A homogeneous material is characterized by having a single value of the strength for all of the junctures: $\sigma_0 = 4$. This implies that the only quenched disorder comes from the random distribution of pore pit widths; the control parameter for the simulations being the amount of disorder of that distribution. As the amount of disorder is proportional to the width of the distribution (Eq.5.4), higher values of the disorder imply smaller pit pores and therefore higher pressure forces to be in play. It also implies the existence of a minimum value of the amount of disorder at which the capillary forces are not strong enough to generate any detachments.

For each simulation 300 instances of the system of size $L = 40$ are calculated, corresponding to different seeds of the random number generator. First, let me focus on the average avalanche size as function of τ , [Fig. 5.7](Left). The average curve $\langle \Delta(\tau) \rangle$ shows an almost constant value over almost the whole time of the evolution. Both the starting time τ and the average value achieved increase with the value of the disorder; the process of breaking is homogeneous in time. The distributions of avalanche sizes shows also a single regime, with exponential behavior, for all the values of the disorder [Fig. 5.7](Right). The only difference between the curves is the constant, represented by the slope in the semilogarithmic plot. For the highest disorder the largest avalanche that may happen has a size of 40, about the 0.5% of the junctures of a system of size of $L = 40$ (with a total of 9600 of them).

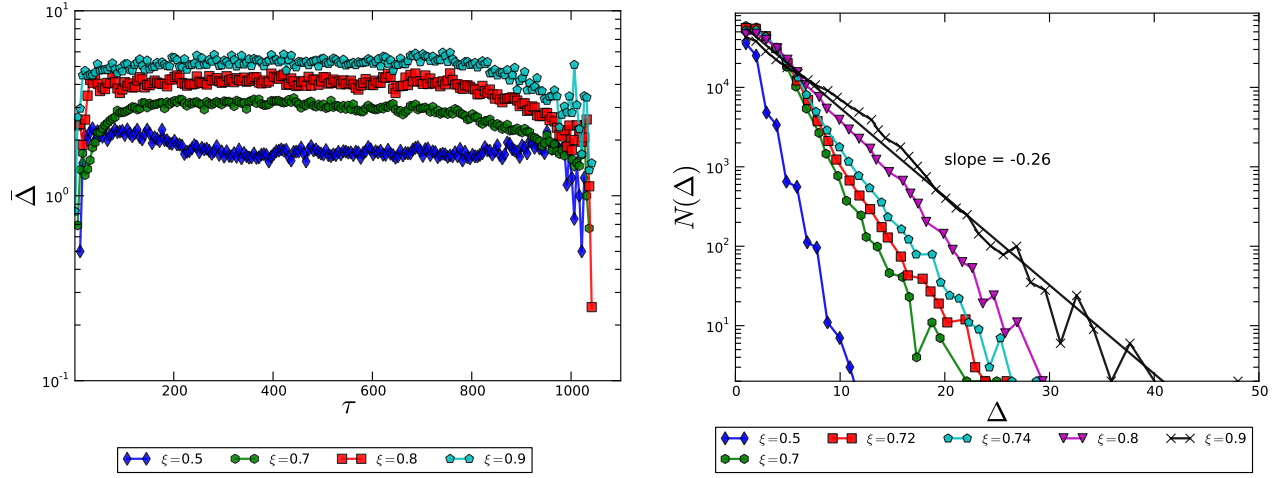


Figure 5.7: Homogeneous system of linear size $L = 30$, $\sigma = 4$, for 300 instances of the system, and several values of the amount of disorder of the pit pore size distributions ξ_{pit} . (Left) Average avalanche size as function of the drying cell time τ , shows that a constant rate of delamination, which starts early and reaches higher values for larger amounts of disorder. (Right) Avalanche size distributions, show exponential behavior.

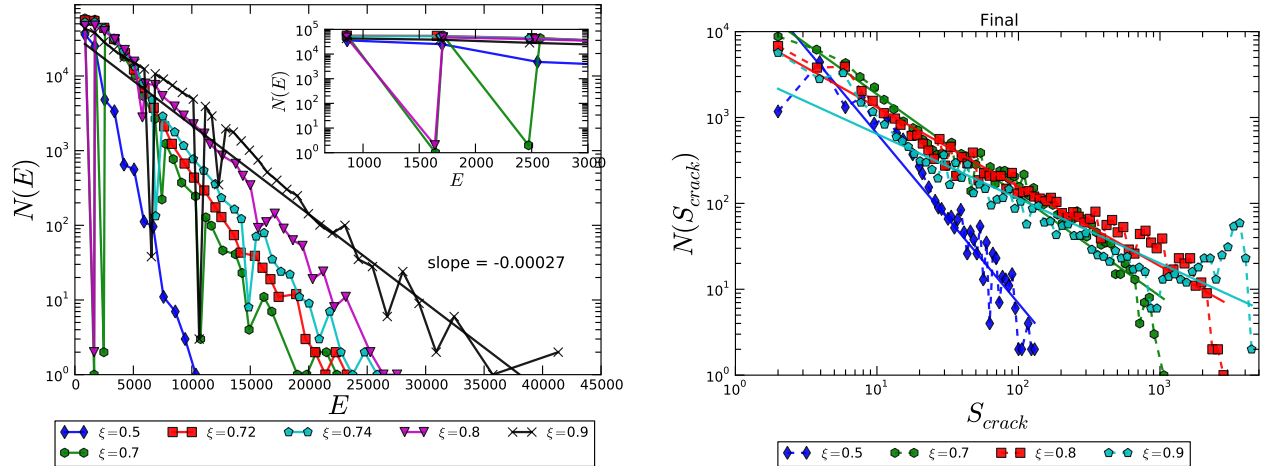


Figure 5.8: Homogeneous system of linear size $L = 30$, $\sigma = 4$, for 300 instances of the system, and several values of the amount of disorder of the pit pore size distributions ξ_{pit} . (Left) Distributions of Energy released in the breakings. For small values of energy the distributions peak in discrete values. (Right) Distributions of final sizes of cracks. The slope of the blue line is -1.98 ± 0.16 , and that of the cyan is -0.75 ± 0.06 ; the flattening comes as higher avalanches happen for higher disorders.

The energy release histograms have also an overall exponential decay [Fig. 5.8](Left). For the small values of E the distribution shows some peaks, but they are a consequence of the fact that the junctures' lengths tendency towards a discrete set; the first peak corresponds to many single breakings of one juncture, the second to two, etc.

The final distribution of avalanche sizes is shown in [Fig. 5.8](Right). There seems to be cracks of every length, as the distribution is a power law. The wider disorders allows the appearance of larger cracks, as the forces involved are stronger.

Inhomogeneous Material

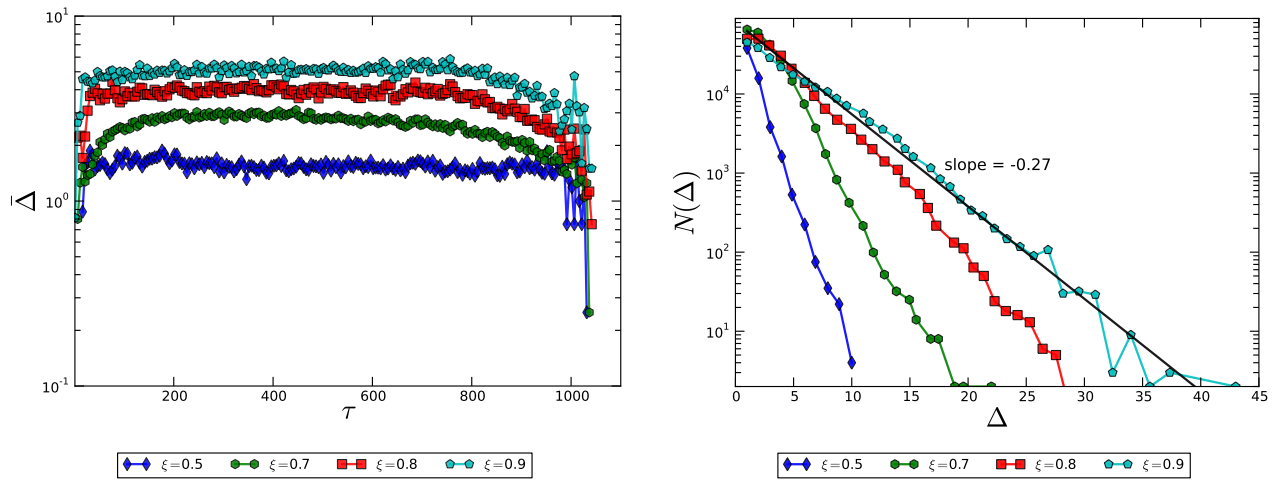


Figure 5.9: Inhomogeneous system of linear size $L = 40$, $4.0 < \sigma < 4.2$, for different values of the amount of disorder of the pit pore size distributions ξ_{pit} , averaged over 300 instances. (Left) Average avalanche size as function of the drying cell time τ , shows that a constant rate of delamination, which starts early and reaches higher values for larger amounts of disorder. (Right) Avalanche size distributions, show exponential behavior.

In the following, an inhomogeneous material will be that for which there is spatial variations of the mechanical properties. In the present chapter I model such system by introducing disorder in the Junctures' strength distribution, σ . Specifically, the breaking thresholds were chosen from an homogeneous probability distribution such that $4.0 < \sigma < 4.2$. The logic behind this distribution is to mimic more closely the structure of the material. Therefore the widths of both distributions of strength and pit pores (W_δ , W_σ) are allowed to change.

The introduction of such disorder does not change the overall behavior of the quantities that were mentioned before, as the reader can see in the figures [Fig. 5.9] and [Fig. 5.10].

On [Fig. 5.11] the average number of dried steps time τ needed to completely dry the system is plotted as function of the disorder of pore pits ξ_δ for two values of the width of breaking thresholds, either 0 or 0.2. This shows how the introduction of disorder of pore pits does not influence on the drying time.

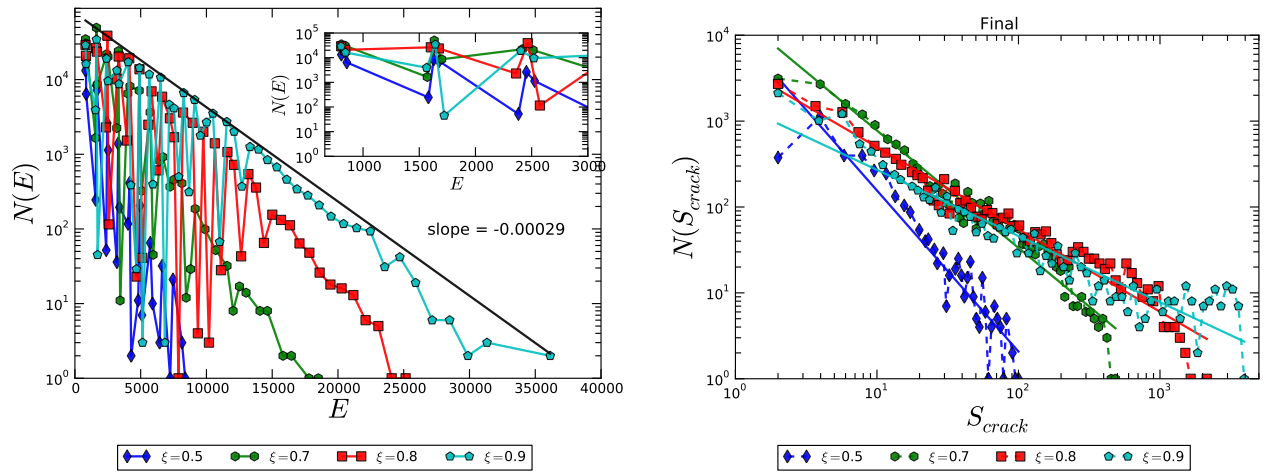


Figure 5.10: Inhomogeneous system of linear size $L = 40$, $4 < \sigma < 4.2$, for several values of the amount of disorder of the pit pore size distributions ξ_{pit} . (Left) Distributions of Energy released in the breakings. For small values of energy the distributions peak in discrete values. (Right) Distributions of final sizes of cracks, the slope of the set $\xi = 0.5$ is calculated as -1.87 ± 0.18 , and for the cyan -0.77 ± 0.06 ; the flattening comes as higher avalanches happen for higher disorders.

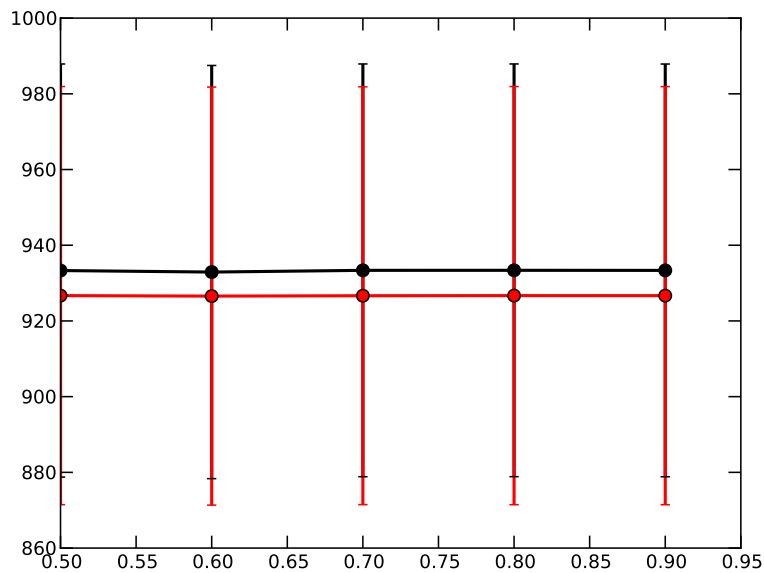


Figure 5.11: Drying time τ needed to dry the sample as function of the disorder of pore pits. The value is constant, independently of the disorder, which implies that the drying process is not affected by the fracturing. Notice that the error bars are one order of magnitude lower than the values.

Guadua drying parameters

Although not the goal of this thesis, it is possible to run systems with similar parameters to the ones measured in the literature of Guadua. The first set of simulations performed wanted to discern whether a reduction of the capillary force would have an impact on the distributions of bursts of detachments. Unsurprisingly, this has the exact same effect that the change in the distribution of pit pore disorder, this is, one obtains distributions completely analogous to [Fig. 5.9] and [Fig. 5.10]. The reason is the fact that the fracture process in this system is ruled by the distribution of forces alone, and there is no force rearrangements in the system. Then the dynamics is the same for both changes of the forces. A second set of simulations were run with a distribution of pore sizes of the order of those found from the micrographs for the pit pores, this means a parameter $\xi =$. There were no fractures in the system due to capillary forces.

5.2.3 Crack sizes and system spanning fractures

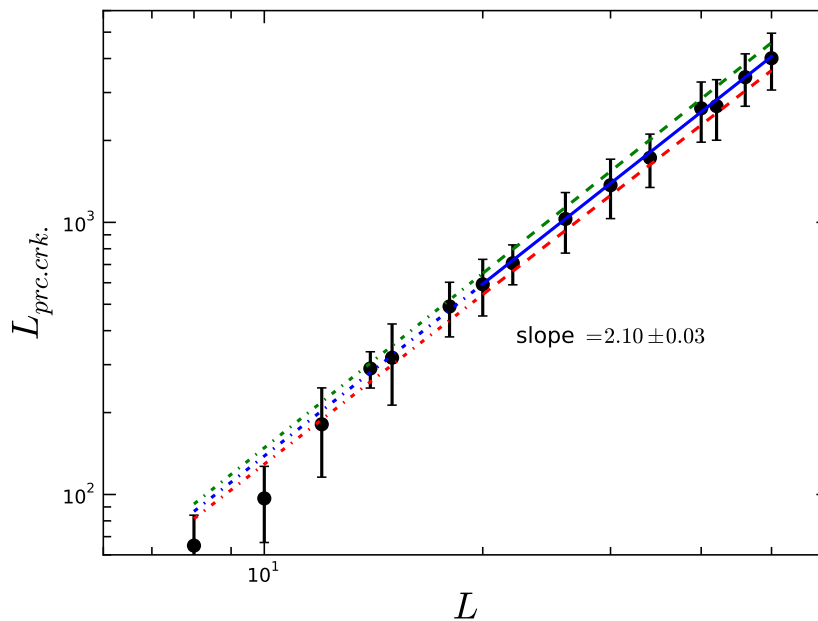


Figure 5.12: Size of the system spanning crack as a function of the size of the system. The slope is different from the percolation one, thus showing that the fracture process is not related to percolation. A disorder value of $\xi = 0.9$ and 300 instances for large systems and 50 for smaller ones were used; however not all the samples had a spanning crack along the sample.

It is also relevant to discuss the distribution of sizes and the geometry of the cracks in the system. [Fig. 5.6](Right) shows a snapshot of the final stage of the system, in which different fractures are labeled with different colors to help differentiating them. Comparing with the snapshot of the drying of the system at the time of the water front percolation, [Fig. 5.6](Middle),

one can see how the fractures follow the previous shape of the drying front; compare the orange cracks at the middle of the plot. This is an evidence that there is a strong correlation between the neighboring breaking junctures.

In [Fig. 5.8](Rigth) and [Fig. 5.10](Right), I show the distribution of sizes of fractures at the end of the drying process for several different values of the disorder of the system. They follow a power law whose power grows (absolute value diminishes) as the disorder of the system is increased; from -1.98 ± 0.16 to -0.75 ± 0.06 for the homogeneous and from -1.87 ± 0.18 to -0.77 ± 0.06 for the inhomogeneous case. The reason for this flattening of the distributions as higher disorders enter in play, is the fact that larger values of the disorder are also related to higher forces; then for those systems there will be both more fractures and larger ones occurring.

In some of the systems there will be a final system spanning fracture. In [Fig. 5.12], I address the question of wether the appearance of this macroscopic fracture can be related to a percolation process. I averaged the longitude of the spanning system cracks for different system sizes, and for a fixed disorder parameter $\xi = 0.9$. 300 instances were used for systems of sizes smaller than 30 and 50 instances for larger ones. The fit of the slope was done by using the larger systems, since smaller ones always tend to fall behind of the curve, as can be seen in the water percolation case. The blue line corresponds to the calculated slope, while the red and green are errorbars. The value of the slope is slightly larger than the expected one, therefore it is not clear that the system spanning crack would be a percolation phenomena. The reason of this different slope is the fact that, unlike in percolation systems, for this case the probability of a detachment to take place is not completely unrelated to the neighboring detachment having occurred.

5.3 Analysis

The numerical evidence on this chapter implies that the disorder in the distribution of pore pits does not have an influence on shape of distribution of avalanches of breakings. This happens because fractures are created on the instantaneous drying front, their dynamics and growth lagging behind that of the cell emptying phenomena; even for high forces the resulting cracks can not affect the path of water between the undried cells. There is no feedback between the two mechanisms.

The mechanical parameters chosen for the cell walls are close to the literature reported values for the Bamboo. If the exact values of the widths of the pore pits are chosen, there are no avalanches of breakings in the system. Even when smaller pores are chosen (stronger forces), the size distributions of the avalanches of breakings do not follow the power law distribution that has been found experimentally. This two facts strongly suggest that capillary forces are not the main mechanism that influences the initiation and growth of drying induced fractures in *Guadua Angustifolia*.

A statistical model of fracture due to shrinkage, the Cell Network Model of fracture

In this chapter I will present and show the results of an statistical model of fractures in which hexagonal cells, joined by junctures at the corners, are subject to shrinkage. The main quantity of study of the dynamics in the micro-scale is the avalanches of breakings of junctures. The model is called the Cell Network Model of Fracture; the results of this section were published in [VKLM11, VLM11]. The code used for this was written from scratch using C++.

The goal of this model is to characterize the avalanches of breakings. Firstly it is key to determine which are the relevant parameters that drive the breaking. Secondly, to characterize the kind of statistics that the avalanches are subject to. As the reader knows from the theory section, in the case that the system presents scale invariant behavior it could be mapped to a simpler system (maybe solvable); on the contrary the system may be equivalent to a simpler random process.

6.1 The Model

As discussed in the literature section, Bamboo culms have two main structures: flexible parenchymatous tissue and stiff fiber bundles surrounding the transport vessels (Figure 6.2). From a structural point of view, the former provide flexibility while the latter carry most of the weight of the plant. During industrial drying, a careful process has to be set up in order to reduce the occurrence of macroscopic cracks that emerge from micro-cracks at the parenchymatous tissue between the fibers [MA06].

The model, from now on the Cell Network Model of Fracture (CNMF), is a 2D version of the mechanical response of the parenchymatous tissue to the stresses produced by the final drying stage, when all intracellular water is gone. The CNMF is a statistical model of fracture, following the breaking of individual elements. In the real bamboo, cells are joined by both the

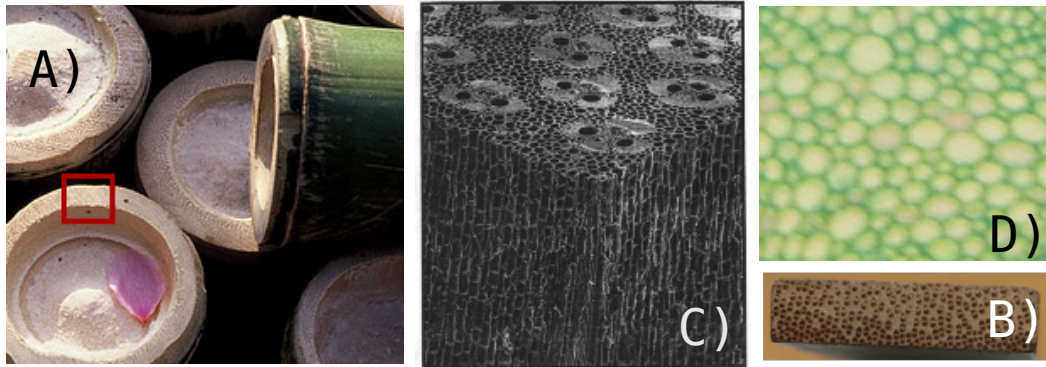


Figure 6.1: A) Bamboo culms [Lin], B) Small *Guadua angustifolia* board showing the fibers embedded into the parenchymatous tissue and their distribution: more dense at the outer than at the inner side. C) 3D Bamboo culm structure. Fiber bundles align along the axis of the culm ([Lie98]). D) 2D photography of the *Guadua* parenchyma ([LVV+03]).

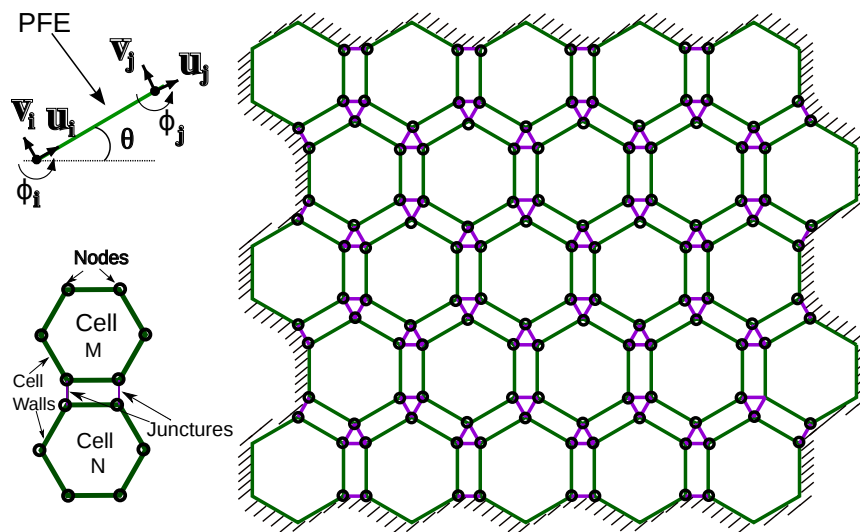


Figure 6.2: Upper left, the plane frame element spanning between the nodes i and j , arbitrarily oriented by an angle θ . Each node has two translational and one rotational degree of freedom. Lower left, two contiguous cells. Right, structure of the CNMF (not at scale). The hexagons represent the cells and the junctures are arranged into triangles. Hashing represents fixed boundary conditions.

middle lamella between neighboring cells and the so-called tricellular junctures (made of pectic polysaccharides and calcium [WB07, JM00]); these are three individual polymer bonds connecting the cell walls by pairs at the corners. The model resembles this structure with uniform hexagonal cells, with six cell walls each, ordered in a honeycomb structure and connected at the corners by triangles of individual junctures.

The structural division of the cell into walls and of the bonds into junctures, makes it natural to choose a computational model in which these biological structures are the individual elements i.e. the building blocks of the problem. This is why I decided to use the Finite Element Method. Both cell walls and junctures are modeled as linear elastic elements, called Plane Frame Elements (PFE) by the FEM literature (see, for instance, [Seg84, Bat96, Hug00]). As was sketched before, these elements have the advantage that a solid made of them models the Cosserat continuum equations when approximations to the bulk are done; i.e. they produce the right physics in the continuum limit.

Each PFE has six degrees of freedom: two translational and one rotational at each of its two nodes; it is characterized by an elastic modulus E , cross sectional area A , area moment I , and length L . The notation for the nodal displacements of an element spanning from node i to node j is $\vec{u}_{loc}^{(e)} = \{u_i, v_i, \phi_i, u_j, v_j, \phi_j\}$, as is pictured on Figure 6.2. In element (local) coordinates, the element stiffness matrix is (Eq.4.22):

$$\mathbb{K}_{loc}^{(e)} = \frac{EI}{L^3} \begin{bmatrix} \frac{AL^2}{I} & 0 & 0 & -\frac{AL^2}{I} & 0 & 0 \\ 0 & 12 & 6L & 0 & -12 & 6L \\ 0 & 6L & 4L^2 & 0 & -6L & 2L^2 \\ -\frac{AL^2}{I} & 0 & 0 & \frac{AL^2}{I} & 0 & 0 \\ 0 & -12 & 6L & 0 & 12 & -6L \\ 0 & 6L & 2L^2 & 0 & -6L & 4L^2 \end{bmatrix}.$$

The representation of this matrix in global coordinates is reached through the transformation (Eq.4.21),

$$\mathbb{T}^{(e)} = \begin{bmatrix} \cos(\theta) & \sin(\theta) & 0 & 0 & 0 & 0 \\ -\sin(\theta) & \cos(\theta) & 0 & 0 & 0 & 0 \\ 0 & 0 & 1 & 0 & 0 & 0 \\ 0 & 0 & 0 & \cos(\theta) & \sin(\theta) & 0 \\ 0 & 0 & 0 & -\sin(\theta) & \cos(\theta) & 0 \\ 0 & 0 & 0 & 0 & 0 & 1 \end{bmatrix},$$

as $\mathbb{K}^{(e)} = (\mathbb{T}^{(e)})^T \mathbb{K}_{loc}^{(e)} \mathbb{T}^{(e)}$. The equilibrium conditions for the whole structure are expressed by

$$\mathbb{K} \cdot \vec{u} = \vec{f}_n, \quad (6.1)$$

where \vec{u} , \mathbb{K} and \vec{f}_n are the displacement vector, the stiffness matrix and the nodal force vector for the whole structure, respectively, obtained by assembling all individual elements [Seg84]. This expression allows us to compute the displacements from the forces, or vice versa.

Disorder is introduced into the system by choosing at random the breaking thresholds of each juncture, between 0.8 and 1.2 in units of EA (juncture Young modulus, cross sectional area). The Young modulus is fixed at literature published values [YFZY07].

The *boundary conditions* are chosen to be fixed nodes at the border. This aims to represent shrinkage of the material subject to a fixed border. As parenchymatous cell walls are ductile and tricellular junctures are brittle, only junctures are allowed to break if their strength surpasses a global failure threshold.

6.1.1 Homogeneous model, Hexagonal geometry

Firstly, let me show the case of an initial regular hexagonal lattice geometry, i.e., the length L and cross sectional area A of all elements are fixed. This simulations were conducted by a system of linear size $L = 5$, (5×5 cell lattice) due to restrictions in the computational resources (Figure 6.2).

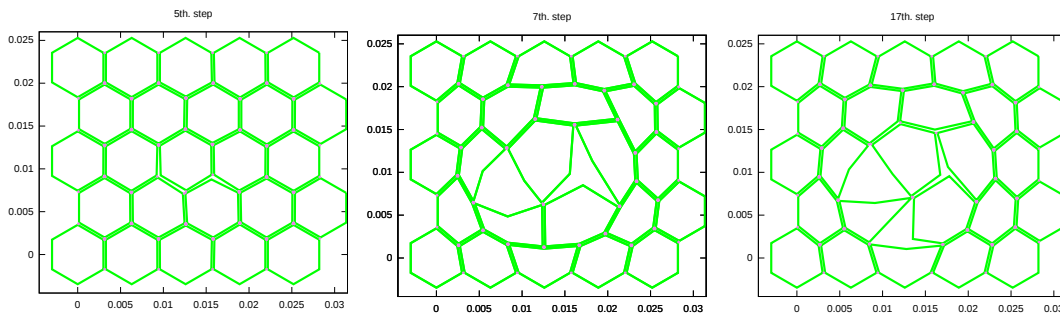


Figure 6.3: Snapshots of the system, for a $L = 5$ geometry. Left(5 steps), a gap appears due to the breaking of some junctures at the center of the sample. Middle, 7 time-steps, right 17 time-steps.

6.1.2 Inhomogeneous model, Voronoi Geometry

A voronoi point is randomly chosen inside every cell of an hexagonal array, and then a Voronoi construction is generated for the cells. The randomized geometry resembles the parenchymatous tissue. Disorder is introduced by the geometry; therefore both Young modulii and breaking thresholds are homogeneous [Fig. 6.5].

6.1.3 Distributions of breaking thresholds

For the CNMF we studied the distribution of avalanche sizes when the juncture stress threshold breaking value σ_{th} at which every juncture is irreversibly broken distributes either by means of a flat distribution of changing width or from Weibull distributions with several characteristic parameters:

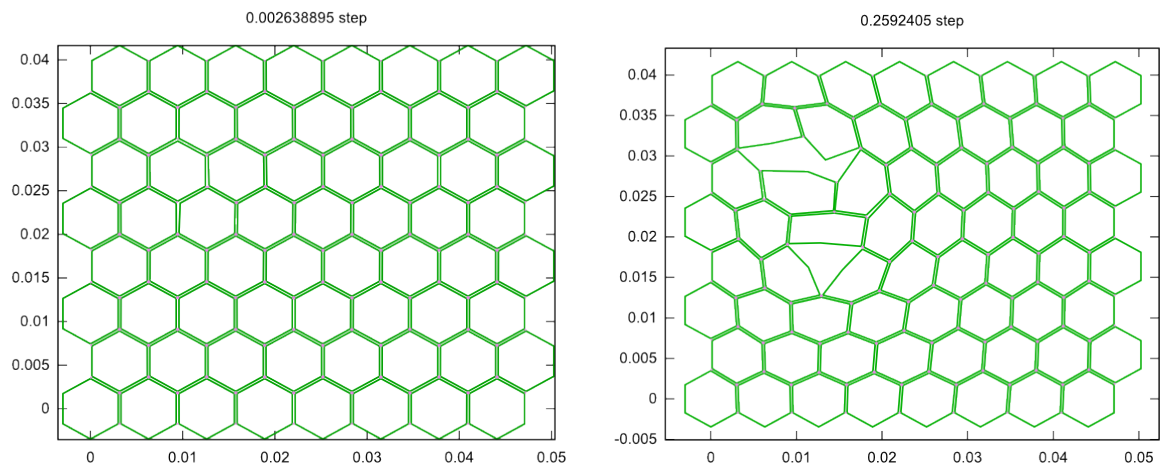


Figure 6.4: Snapshots of the system, for a $L = 8$ geometry. (Left) A few junctures have been removed, causing small displacements of the remaining ones; as for instance the one in the coordinates $x = 0.01$, $y = 0.024$. (Right) As the evolution continues, the removed junctures cause larger displacements in the network.

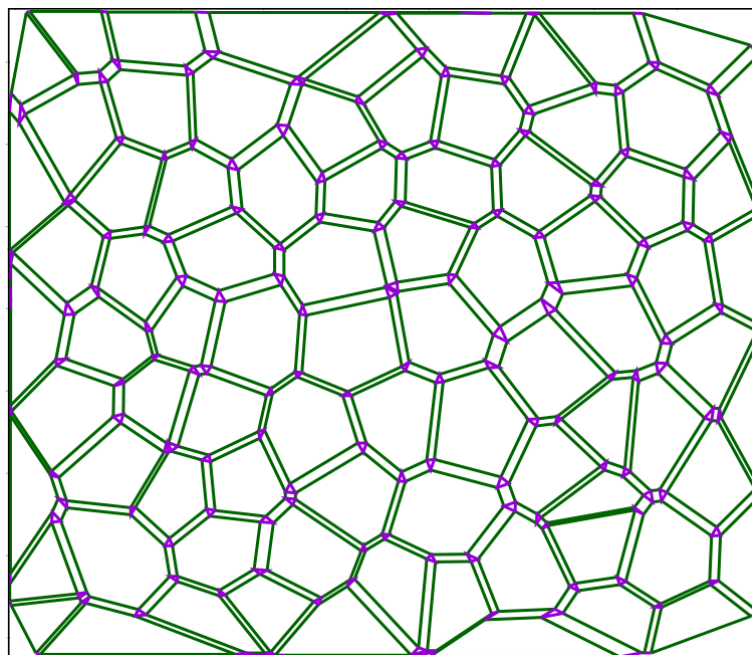


Figure 6.5: Initial network, for the case of an inhomogeneous lattice. The disposition of the cells resemble the randomness in the parenchyma tissue of guadua.

The *homogeneous probability distribution* is characterized by a center value C , a width W , and a random generator seed s_σ :

$$p(\sigma_i) = \frac{1}{2W_\sigma}, \quad \text{for } C_\sigma - W_\sigma \leq \sigma_i \leq C_\sigma + W_\sigma \quad (6.2)$$

The for the *Weibull distribution function* probability density function [Wei51] is given by:

$$f(x; \lambda, m) = \begin{cases} \frac{m}{\lambda} \left(\frac{x}{\lambda}\right)^{m-1} e^{-(x/\lambda)^m} & x \geq 0 \\ 0 & x < 0 \end{cases}, \quad (6.3)$$

where m and λ are free parameters. It is commonly used to describe the breaking thresholds of fibers by fixing $\lambda=1$ and changing m , which is the main parameter controlling the distribution shape.

6.2 Evolution

In the bond water drying stage, after the fiber saturation point when all intracellular water is gone, guadua wood is usually part of a structure and the boundary conditions are fixed (no displacements). Lets impose that all boundary nodes are fixed in space, i.e. with zero displacement zero. The drying process is modeled as a tensile nodal force on all elements that is proportional to the humidity change Δb . This change increases until a first juncture breaks. Then the forces redistribute among the resting elements, eventually causing an avalanche of successive breakings. The simulation includes a linear elastic shrink step, a breaking criteria and a non-linear avalanche step.

Linear elastic shrink step: Drying caused stresses are applied following a two step process. In the shrink step, each cell wall suffers shrinking nodal forces along its axis and acting at its ends,

$$\begin{aligned} \vec{f}_n^{(e)} &= \{-f_n, 0, 0, f_n, 0, 0\} \\ f_n &= EA\alpha_b \Delta b. \end{aligned} \quad (6.4)$$

In analogy with the strain caused by temperature (see, for instance, [WG90]) α_b is a constant defining how much force is caused by a unit humidity change Δb . So, increasing Δb is like advancing in the drying process. These forces are assembled into the global vector \vec{f}_n . In the equilibrium step, the global displacements \vec{u} are computed from Eq.(6.1).

Breaking criterion The element displacement vectors $\vec{u}^{(e)}$ are constructed from the global displacement vector \vec{u} . The actual total force $\vec{f}^{(e)}$ acting on a single element due to the contractions and displacements of the whole structure is given by $\vec{f}^{(e)} = \mathbb{K}^{(e)} \vec{u}^{(e)}$. If the magnitude of the longitudinal component of this vector is larger than the breaking threshold σ_{tb} , the element will break. By taking Δb as control variable, the secant method gives us the minimum value for a first breaking, that is the drying point when the avalanche starts. At this point, Δb is fixed for the whole avalanche and that juncture is broken.

Nonlinear avalanche step. The breaking of a single juncture has two consequences. First, both the global stiffness matrix and the global nodal forces have to be updated. This is achieved by reassembling them from all elements but the broken one, to obtain \mathbb{K}_{new} and $\vec{f}_{n \text{ new}}$. Second, the breaking causes a new global displacement, \vec{u}_{new} , which is computed from Eq.(6.1). This new displacement may cause in turn a new juncture to break, which causes a new displacement, and so on, until no more junctures break and the avalanche stops.

6.3 Breakup process

In this section I will show the changes in the breakup behavior of the system for different configurations (homogeneous versus inhomogeneous geometry), and for different control parameters.

6.3.1 Avalanche dynamics

As was stated before, the avalanche size distribution characterizes the fracture process of the system; scale free phenomena will present a power law distribution of avalanches. Here I show an exploration of the behavior of this quantity with respect to different ways to define the control parameter of the system.

Homogeneous system In the first case the breaking thresholds distribute homogeneously. A control parameter a which defines the range of variation of the breaking thresholds varies both the width and the center of the distribution of breaking thresholds as:

$$\begin{aligned} a \times 0.8EA < \sigma_{th} < a \times 1.2EA, \\ a \in \{1 \times 10^{-5}, 1 \times 10^{-4}, 1 \times 10^{-3}, 1 \times 10^{-2}, 1 \times 10^{-1}, 1\}, \end{aligned} \quad (6.5)$$

with the area of the cross section of the juncture being A and the elastic modulus E . Equivalently, it can be said that the center of the distribution of breaking thresholds is given by $a \times EA$.

The distribution of avalanches for different values of a is shown in Figure 6.6. The system size is $L = 5$. The upper line (+) corresponds to a threshold distribution centered at $10^{-5}EA$; the lower line (o) corresponds to a value of 1 in the same units. Each of the curves corresponds to the average over several different realizations (the number of runs changed for the each curve, since the computing time was not constant).

The behavior of the curves suggests that there is a threshold value where the distribution of avalanches' sizes follows a power law. A good fit occurs at a threshold of $0.35A\bar{E}$, with a power law exponent $-2.93(9)$. This value coincides within the error bars with the reported value of 3.0 ([PHH06, HH94]) for the random fuse model ([HR90]). This will suggest that both systems have the same breaking statistics and may fall in the same universality class.

Homogeneous system, fixed center of distribution The effect of the change of the amount of disorder, i.e., the width of the distribution of breaking thresholds can be isolated by fixing the center of the distribution and changing only its width:

$$p(\sigma_{th}) = \frac{1}{2W}, \quad \text{for } C - W \leq \sigma_{th} \leq C + W. \quad (6.6)$$

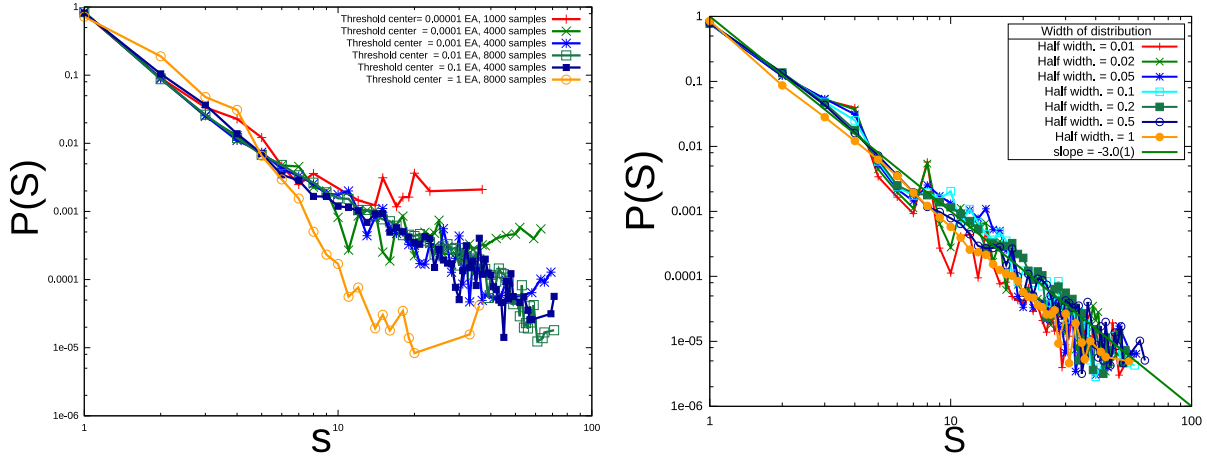


Figure 6.6: Log-log plot of number of events of avalanche size s ($N(s)$) as function of avalanche sizes (s) for the CNMF, for several centers of distribution of breaking thresholds, homogeneously distributed. (Left) A power law with exponent $-2.93(9)$ is gather for a breaking threshold of 0.35 (for an explanation on the units, see Sec. 6.3.1), the breaking thresholds are given by the control parameter is defined in (Eq.6.5) (Right) Histogram of avalanche sizes for several widths of the homogeneous threshold distribution centered at $0.35EA$, for different widths.

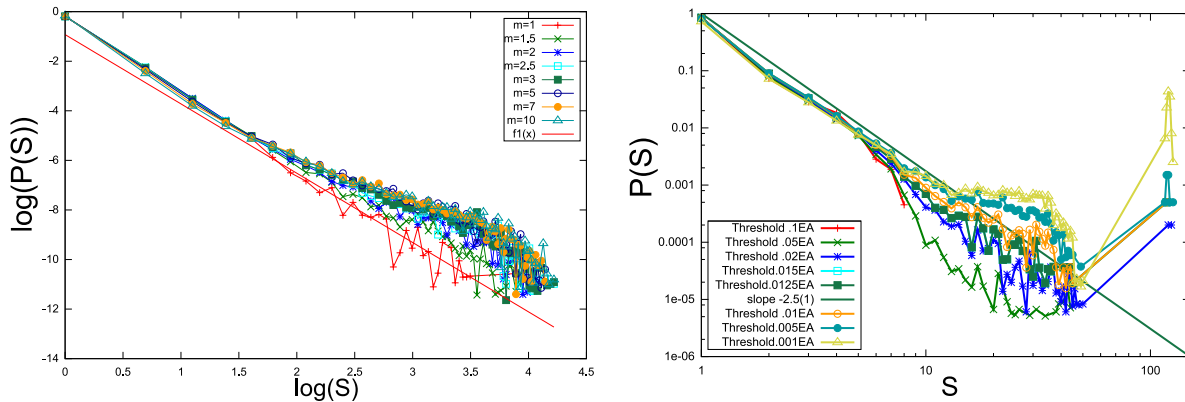


Figure 6.7: Log-log plot of number of events of avalanche size s ($N(s)$) as function of avalanche sizes (s). (Left) Several Weibull distributions of the breaking thresholds, with values of the shape parameters m between 1 and 10. The straight line corresponds to an slope of -2.9 . (Right) Inhomogeneous lattice geometry, the control parameter is the global breaking threshold. The straight line corresponds to an slope of 2.5 .

Flat distributions of the breaking thresholds, all centered at $0.35EA$ but with different widths (spanning on two orders of magnitude), show the same power-law distribution of avalanche sizes, with slopes around -3 [Fig. 6.6]. The data shows that narrower distributions show larger fluctuations around this power law than wider ones.

Weibull distribution of breaking thresholds [Fig. 6.7](Left) shows the avalanche size distributions when the juncture's breaking threshold distribute according to a Weibull distribution. The changes in the shape of the avalanche size distributions is quite slim. On the graph a straight line denoting a power law of exponent -2.9 has been added to guide the eye. For small values of m the distributions seem to fit it better, while for larger values the exponential cutoff is more pronounced.

Voronoi geometry system On [Fig. 6.7](Right) the disorder is introduced by selecting the geometries at random. The breaking threshold is the same for the whole structure and is taken as the control parameter. The system size in this case is $L = 5$. For small values of the breaking threshold most of the junctures break at once, they constitute the peak around 100 bonds. As the threshold is diminished, the peak disappears. For large values of the threshold most of the avalanches are of small size. The best fit for a straight line occurs for the threshold of $0.0125EA$, for which an slope of $2.5(1)$ is obtained.

6.3.2 Distributions of humidity decrement between consecutive avalanches

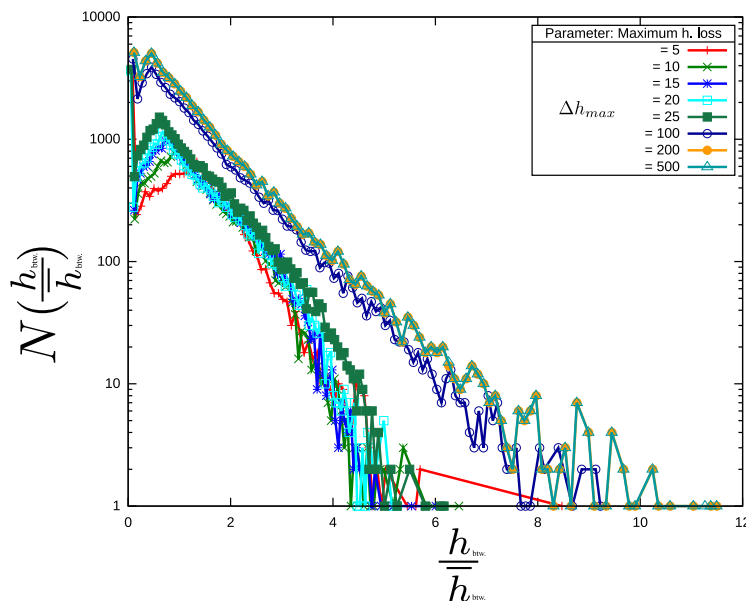


Figure 6.8: Histogram of Normalized Humidity decrements between consecutive avalanches h_{btw} , for different maximum humidity changes Δh_{max} (which is proportional to the Cell Wall strain, (Eq.6.4)). For a maximum humidity change of 25 (in arbitrary units) the slope is fitted to $-0.188(5)$, while for a maximum humidity change of 200 it is $-0.074(1)$. The system corresponds to regular lattice geometry, with breaking thresholds given by (Eq.6.6).

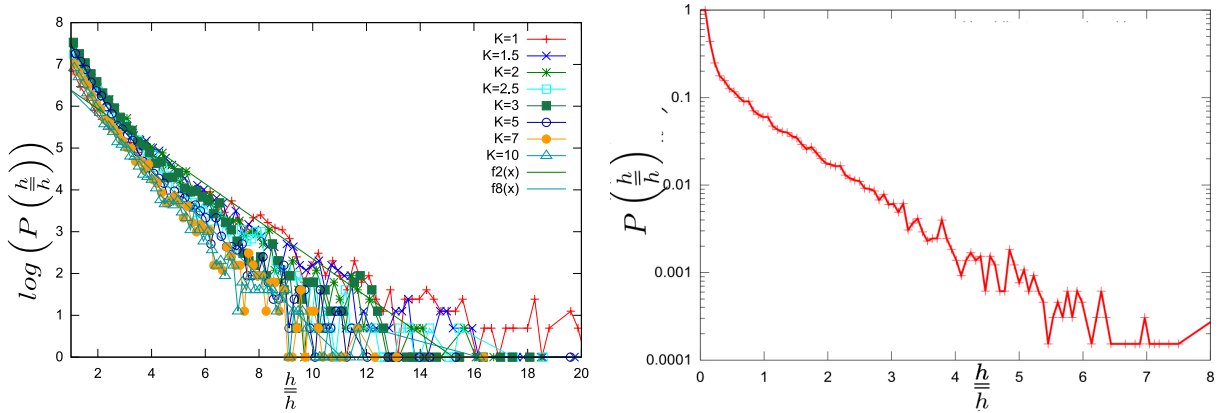


Figure 6.9: Histogram of humidity increments between successive avalanches. (Left) Breaking thresholds following several Weibull distributions, with m between 1 and 10. The green line corresponds to a fit of the series of shape $m = 2$, with slope $-0.45(2)$. The blue line to that for $m = 10$, with slope $-0.63(2)$ (Right) For an inhomogeneous lattice geometry the slope in semi-log axis is $-1.04(2)$.

Homogeneous system, fixed center of distribution The distribution of humidity decrements between successive avalanches provides a description of the path to the global failure of the system. This is the analog to the waiting times between avalanches of other models of fracture. [Fig. 6.8] shows the normalized histograms of humidity decrements for several values of the maximum humidity change allowed Δh , for a regular hexagonal lattice system whose distribution of breaking thresholds follows (Eq.6.6).

To identify the effect that a maximum value of the allowed humidity loss has on the distribution of humidity increments between avalanches, the different curves shown have a set parameter of the final maximum humidity loss. When the breaking process is driven until the end, the histograms can be fitted to an exponential, with a fitted humidity constant of $-0.074(1)$. This implies that there is a lack of correlation between successive avalanches, unlike in the avalanches found in earthquakes, for which the distribution follows a power law.

Weibull distribution of breaking thresholds For the case of breaking thresholds distributed according to (Eq.6.3), the humidity decrements between consecutive avalanches also has an exponential distribution, as can be seen in [Fig. 6.9](Left). There is a change of slope for different values of the disorder, fitted to -0.45 for $m=5$; -0.63 for $m=10$.

Voronoi geometry system For an inhomogeneous geometry system, i.e., when the disorder is introduced by means of disordered lattice, the humidity to cause next breaking also has an exponential behavior, as can be seen in [Fig. 6.9](Right). The slope in semi-log axis has the value of $1.04(2)$.

6.3.3 Fraction of remaining junctures

Lets consider the global load sharing fiber bundle model [PHC10]. Given $U(\sigma)$ as the fraction of remaining fibers at a given stress and σ_c the critical stress causing the global breaking of the system. Thus, $U^*(\sigma) - U^*(\sigma_c)$ behaves as an order parameter for that system. In this section

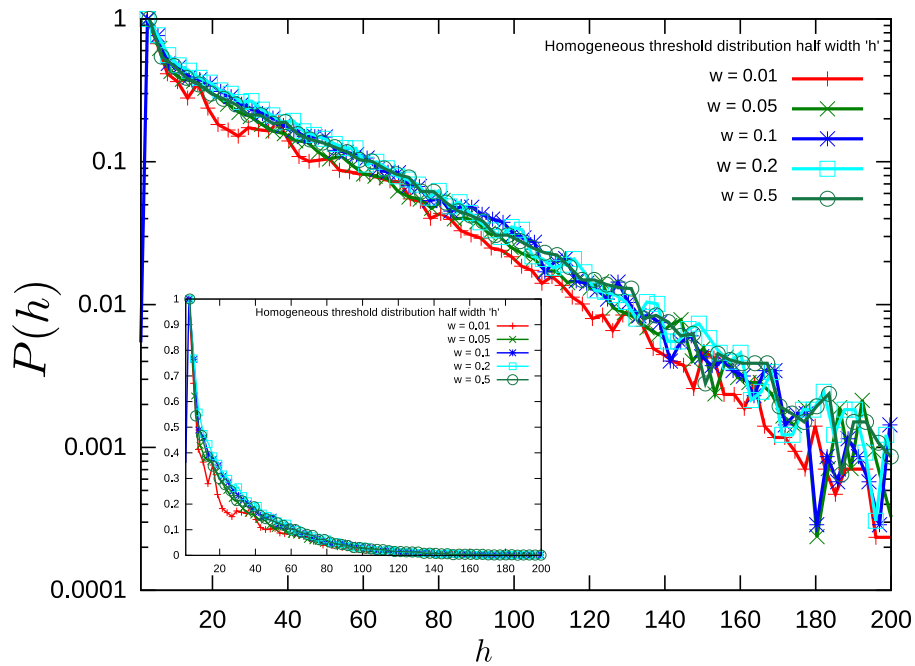


Figure 6.10: Number of intact fibers as function of the humidity change for several homogeneous distribution of the breaking threshold with different widths (semi log). The line is drawn only to guide the eye, the data points are the symbols. The system corresponds to regular lattice geometry, with breaking thresholds given by (Eq.6.6). *Inset*, linear axis.

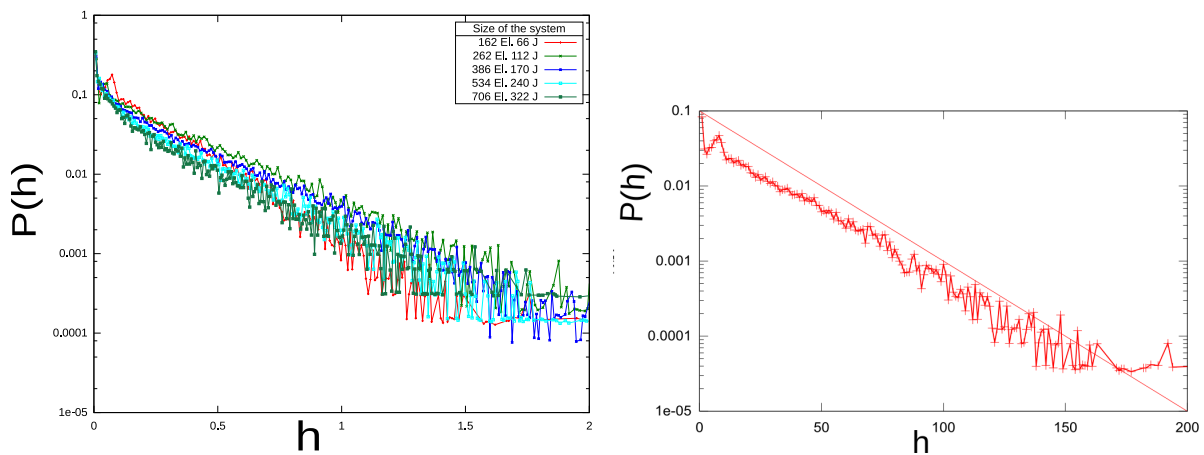


Figure 6.11: Scaled fraction of intact fibers as function of the humidity change (in units of max humidity difference) for different system sizes.

we explore whether the fraction of intact junctures as function of humidity change behave as an order parameter for the CNMF.

Homogeneous system, fixed center of distribution In [Fig. 6.10] shows the number of intact fibers as function of humidity, for different widths of the distribution of breaking thresholds. It is clear how the number of junctures follows an exponential decay. This exponential behavior is independent of the system size. In [Fig. 6.11](Left), the fraction of the population of intact fibers as function of humidity is shown for different sizes of the system. The horizontal axis was rescaled by means of a linear fit on the semi-log data. All histograms show an exponential decay.

Voronoi geometry system In the same way, when the disorder is introduced by the different geometries, the distribution of intact junctures also shows exponential behavior, as can be seen in [Fig. 6.11](Right).

6.4 Damage

Homogeneous system, fixed center of distribution In order to introduce a degradation for the juncture elements we reduce the Young modulus of the juncture elements by a damage factor $0 < a < 1$ each time the juncture fails. When the element has suffered a maximum number of failures k_{max} , it is assumed to be broken and is removed from the structure.

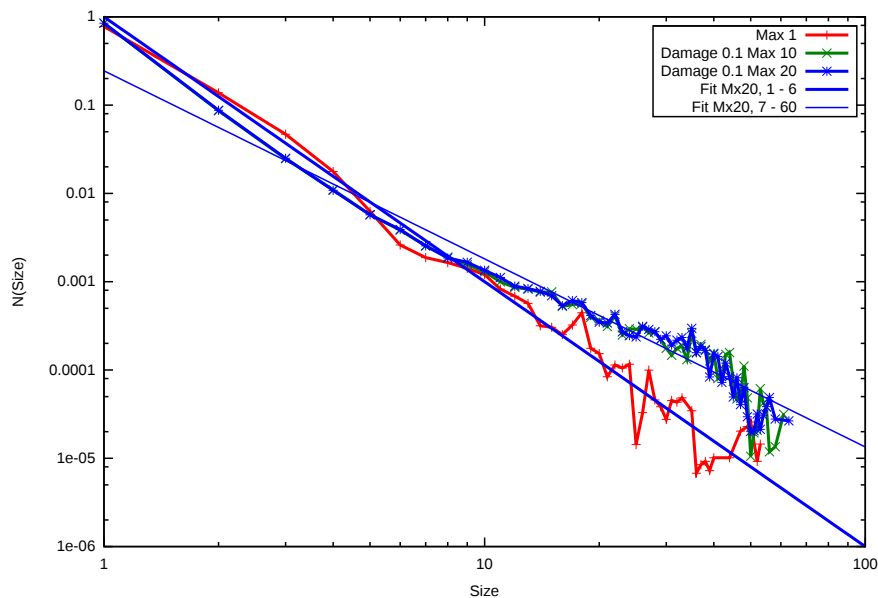
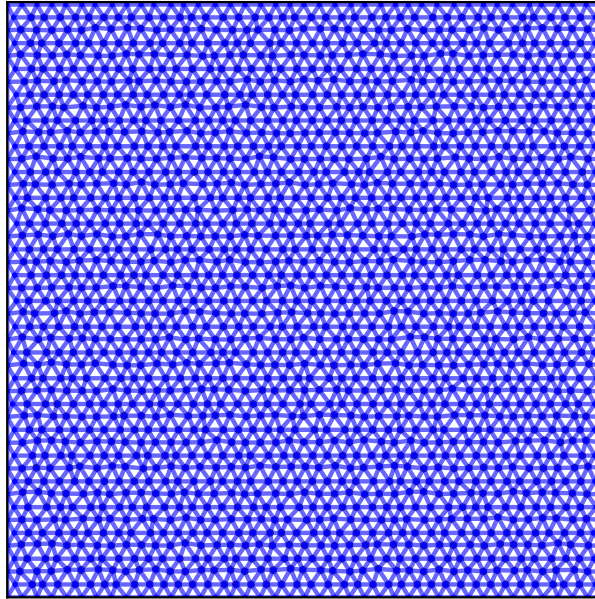


Figure 6.12: Histogram of avalanche sizes for damage parameter $a=0.1$ and several maximal numbers of failures, k_{max} . The bolder line (slope $-2.98(7)$) fits for avalanche sizes between 1 and 7, while the thinner line (slope $-2.1(1)$) fits for avalanche sizes between 7 and 60. The breaking thresholds have a homogeneous threshold distribution centered at $0.35EA$

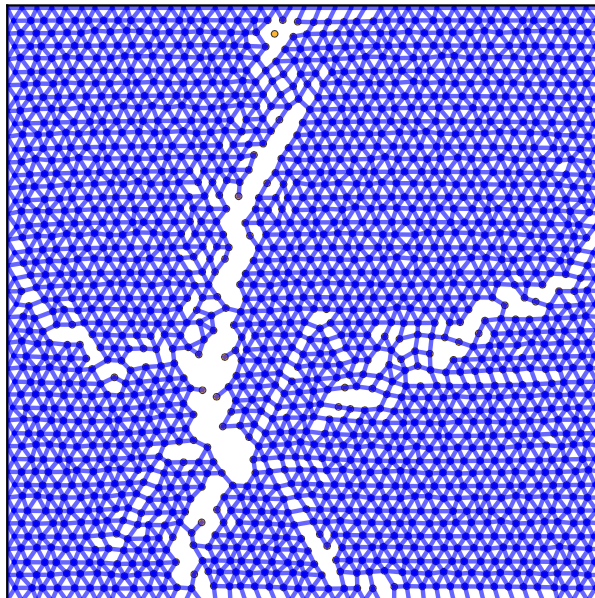
When a small degradation is introduced ($a=0.1$), the slope of the distribution of avalanche

is reduced for large avalanches. In fact, avalanches with sizes smaller than 8 seems to follow a power law of exponent $-2.98(7)$ and for avalanches larger than 8 a power with exponent -2.1 . [Fig. 6.12]. A plausible physical explanation would be that, a damaged juncture (that has not been completely removed) enhances the localization of the stress, in contrast with the case when it is completely removed; therefore, allowing for larger avalanches. Even smaller values of a (not shown) cause the maximum humidity loss (and therefore the forces on the elements) to be much larger.

$\alpha = 0.0$



$\alpha = 0.03658779572$



A theoretical statistical model of fracture due to shrinkage

7.1 Introduction

The present chapter focus on the effect of the amount of quenched disorder on the process of gradual breakup induced by desiccation. A related experimental realization of this system can be found in the drying of a thin slab of mud, as shown in the works of Nakahara and Matsuo [NM07, NM06b, NM06a] and Kitsunozaki [Kit99]. Moreover, this can be seen as a general statistical model of shrinkage, and therefore applicable to a thin homogenized slab of the internode of the bamboo. The section is then discretized into a regular triangular lattice of springs with fixed ends at the boundary. Drying is captured by gradually decreasing the natural length of all springs, inducing unbalanced forces and leading to the final breaking of some bonds. The quenched disorder of the material is represented by a random distribution of the bonds' breaking thresholds, and the amount of disorder is given by distribution's width. There are numerous studies in the literature on the spatial arrangement of cracks [SDT11, NSS⁺10, SMM⁺07, Kit99, SM88, Skj88]. Hereby, we focus on the temporal evolution of the crack by analyzing the statistics of avalanches of breaking bonds. A quasi-static desiccation process is implemented by shrinking all the springs by the same rate until a first bond breaks. This induces a redistribution of loads that can be followed by an avalanche of breaks. Simulations revealed that the layer's breakup proceeds in bursts whose dynamic and statistical features strongly depend on the amount of disorder: At low disorders a dominating crack nucleates, creating an extended free surface inside the system. As a consequence, the size distribution of bursts is discontinuous, i.e. small sized avalanches have an exponential distribution while larger ones show a peak distribution, with a gap in between. At high disorders, in contrast, the breakup process consists of a large number of small-sized avalanches with an exponential distribution. Varying the amount of disorder a transition occurs between the two phases at a critical disorder where the size distribution becomes a power law. Analyzing the finite size scaling behavior of the largest and average burst sizes we demonstrate that the disorder-induced transition of our system is analogous to a continuous phase transition.

7.2 Model construction

An slab of bamboo corresponding to internode portion is represented by a discretized uniform two-dimensional triangular lattice with a slightly distorted arrangement. The nodes represent point masses and the bonds among them provide for cohesive forces. Nodes at the boundaries are set fixed, while internal nodes can move in the two-dimensional plane. This will represent a strong surface on the outer part of the Bamboo. System size L is defined as the number of nodes in the lower boundary row of the lattice, simulations were carried out for the values $L = 16, 24, 30, 36, 42, 50$. The bonds are simple central force springs, each one with a different spring constant $k = El/A$, where l is the natural length of the spring, A is a uniform cross section and E denotes for the Young modulus of the layer's material.

The effect of desiccation is implemented by reducing the natural length of all springs by the same ratio. It is controlled by an increasing parameter α , given by

$$\alpha = \frac{l_0 - l}{l_0}, \quad (7.1)$$

where l is the current natural length of the spring and l_0 denotes its initial value, computed as the initial distance between the two nodes connected by the spring. Springs are assumed to have a finite strength: When the load σ on a spring exceeds its breaking threshold σ_{tb}^i ($i = 1, \dots, N$), the spring breaks instantaneously and it will never be restored (no healing). Notice that in this system, unlike the FBM case, there is no need to imply a re-distributing rule, i.e., the distinction between local- and global- load distribution has no place in this model. The quasi-static process of a very slow drying is assured by looking for the smaller α to break a spring.

The quenched disorder of the material is represented by the randomness of the breaking thresholds σ_{tb} . In order to be able to vary the amount of heterogeneity in the system, we consider a uniform distribution of threshold values centered at $C = 1$ with half-width $0 \leq W \leq 1$, that is with probability density

$$p(\sigma_{tb}) = \frac{1}{2W}, \quad \text{for } C - W \leq \sigma_{tb} \leq C + W. \quad (7.2)$$

Hence, the strength of disorder is characterized by the dimensionless parameter

$$\xi = \frac{W}{C}, \quad (7.3)$$

ranging from 0 (no disorder) to 1 (highest disorder). We note that there is also a slight amount of structural disorder in the system: Even though the spring lattice is almost a triangular regular grid with spacing a , each node is randomly set inside a circle of radius $0.1a$, centered at the regular place. This slight distortion is sufficient to prevent the formation of artificial crack patterns, but otherwise, it does not have any relevant role in the breakup process.

After removing a spring, the system is relaxed by numerically integrating through the Verlet algorithm the equation of motion for each node,

$$m \ddot{\vec{r}}_i = \vec{F}_i - c \vec{v}, \quad i = 1, \dots, N \quad (7.4)$$

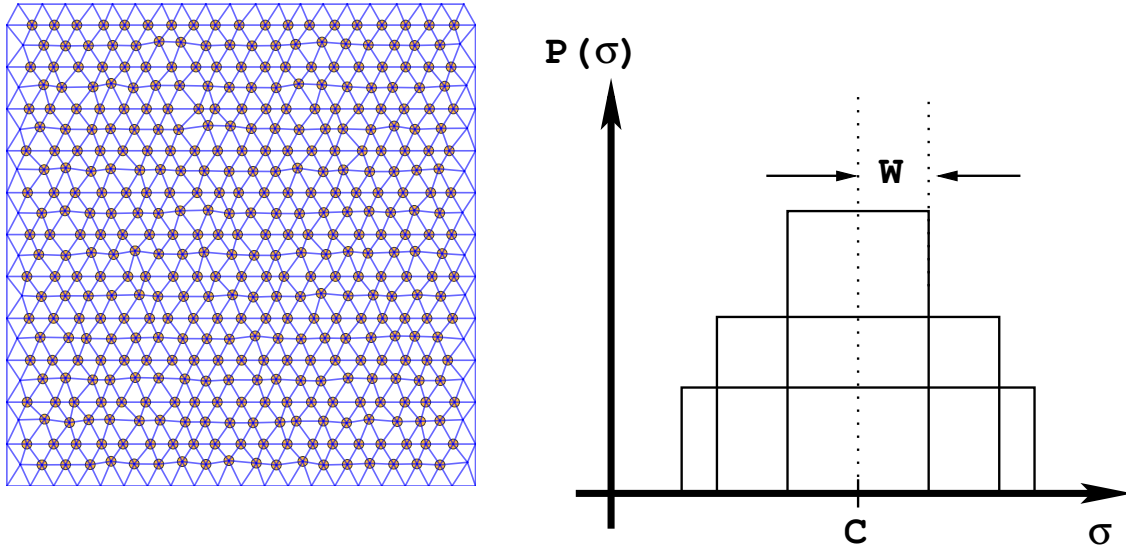


Figure 7.1: (Left) Example of initial randomized geometry. (Right) Uniformly distributed breaking thresholds are centered at $C = 1$ with half-width W . The amount of strength disorder is controlled by varying the value of W between 0 and 1.

where a velocity-dependent damping force (with damping coefficient $c = 10$) has been added to assure for relaxation. The node mass m is proportional to the area of the set of all points closer to this node than to the other ones (that is the Voronoi polygon of the dual lattice for this geometry) [She96]. In the present chapter, because the geometry is close to a regular triangular lattice, $m \approx 0.86$ for all internal nodes, in arbitrary units (which in principle could be scaled for comparison with experiment). The relaxation causes the redistribution of the load dropped by the broken bond over the remaining ones, leading to spatial correlations in the system. It has to be emphasized that this force rearrangement itself may result into subsequent breakings, as more springs surpass their breaking thresholds while keeping their relaxed length fixed. As a consequence, a single spring breaking induced by drying may trigger an avalanche of breakings. The avalanche size Δ is defined as the number of broken bonds during the avalanche, including also the first one whose breaking was provoked by the drying step. Thus *cracks*, defined as clusters of contiguous broken bonds, appear. Due to the long-range load redistribution, a single avalanche can generate several cracks, and it is also possible that several independent avalanches contribute to a given crack.

In the framework of the model, the desiccation is treated as a stepwise process in which the steps t are defined as the number of avalanches occurred. During drying, the amount of shrinkage is characterized by the relative length reduction $\alpha = \Delta l / l_0$ of spring elements, so that we use α as the degree of desiccation. The initial value of α at the beginning of the loading process is $\alpha_0 = 0$; at each time-step t , α corresponds to the minimum value that will cause a breaking. The drying process ends when the humidity content on the sample drops to 0. We consider this to be equivalent to a finite value of the shrinkage parameter α_f , which in the present model is set

to the arbitrary value of $\alpha_f = 0.3$. A large amount of computer simulations were performed in order to understand the effect of the strength of disorder on the breakup process of thin layers of heterogeneous materials. Specifically, $N = 1000$ for $L = 16$, $L = 24$ and $L = 30$, $N = 800$ for $L = 36$, $N = 500$ for $L = 42$ and $N = 50$ for $L = 50$, systems were generated for each value of the amount of disorder ξ by changing the seed of the random number generator.

In the present chapter we focus on the effect of the amount of disorder on the statistics of avalanches.

7.3 Breakup Process

As explained before, the desiccation-induced breakup of our discrete model is not a smooth process, but evolves in bursts (avalanches). The desiccation parameter α grows until a single spring breaks, triggering the burst and leading to load redistributions and additional rearrangements that eventually break more springs. The burst stops when no more springs break with that desiccation factor. Both these temporal fluctuations of the bursting activity and the emerging crack structure are strongly affected by the degree of disorder in the system. To give a quantitative characterization of the effect of disorder on the breakup process, simulations were carried out by varying the value of ξ in a broad range.

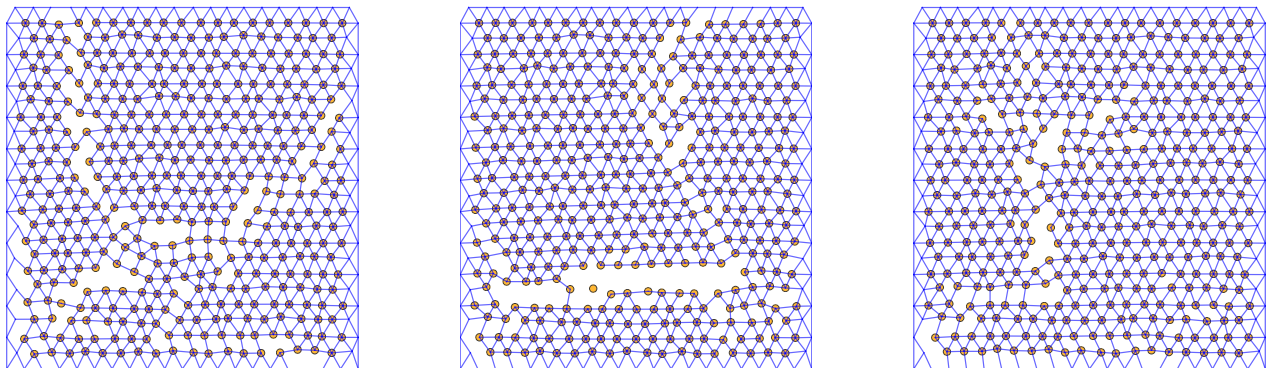


Figure 7.2: First large avalanche for three different widths of disorder, showing how the narrower breaking distributions favor the appearance of large fractures. (Left) $\xi = 0.01$, (Center) $\xi = 0.1$, (Right) $\xi = 0.3$. [VLM11, VKLM11].

Large avalanches consist of spatially correlated bonds being broken; even though not necessarily as a single expanding crack of contiguous bonds. Such spatial correlation takes place at the beginning of the breaking process for low amounts of disorder in the distribution of breaking thresholds, where large avalanches appear early on (see Fig. 7.2, and the videos referenced therein), due to stress accumulations. Conversely, large amounts of disorder do not generate correlated crack growths during the early stages of the evolution. The initial breakings tend to be random, scattered all over the lattice, with small avalanches of size $\Delta \simeq 1$. Only after a

fraction of bonds breaks and small micro-cracks have appeared in the system, these micro-cracks can coalesce by means of *gapping cracks*, that are clusters of broken bonds joining two micro-cracks. As drying continues, both for small and large disorder, the newly created free surfaces hinder the appearance of large avalanches by relaxing the stress in the remaining intact parts of the spring network. The overall shape of cracks is similar to what has been observed for drying processes in composite materials, where the disorder comes from random distributions of the three types of bonds representing the interaction between the ingredients of a composite (see [SDT11, NSS⁺10, SMM⁺07]).

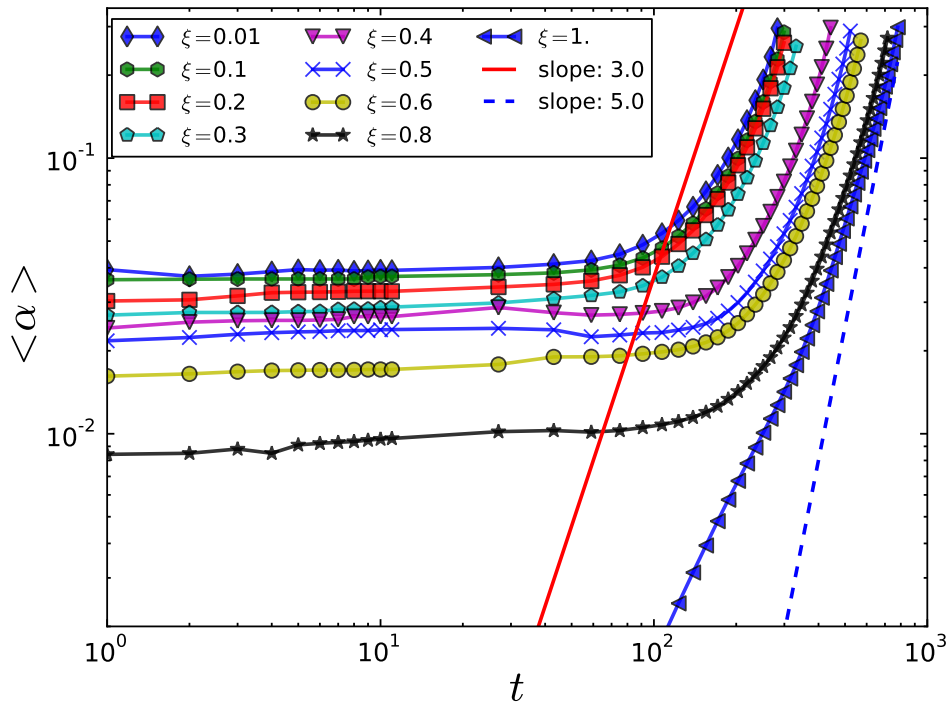


Figure 7.3: The relative length reduction $\langle \alpha \rangle$ of springs as a function of time for several values of the amount of disorder ξ . The system size was set to $L = 30$. Data values are binned with a bin size $\Delta t = 1$ and $\Delta t = 16$ for $0 < t < 10$ and for $t > 10$, respectively.

To follow the time evolution of the process, we evaluated the average value of the desiccation parameter $\langle \alpha \rangle$ as a function of time t . It is important to emphasize that the curves of $\langle \alpha \rangle(t)$ presented for several values of ξ in Fig. 7.3 have two distinct regimes: at the beginning of the drying process the value of $\langle \alpha \rangle$ remains nearly constant over two orders of magnitude in time, which implies a large number of shrinking steps with tiny length changes $\delta \alpha \ll 1$. This slow regime is then followed by a sudden acceleration of the process where springs suffer a considerable length reduction. The reason of the crossover from slow to rapid shrinkage is the formation of a dominating crack spanning the system in one or both directions. Due to the large free surface inside the lattice, a larger reduction in the length of all springs is required to trigger the next

breaking event. The analysis of the spatial structure of damage shows that the transition point can be identified as the exact time when the spanning crack appears. This occurs for all levels of disorder ξ ; nevertheless, the geometrical structure strongly depends on the precise value of ξ .

It can be seen in Fig. 7.3 that the curves of $\langle \alpha \rangle(t)$ shift to the right with increasing values of ξ . It means that the total duration t_f of the process, i.e. the total number of shrinkage steps required to reach some value α_f , is an increasing function of the amount of disorder, as illustrated in Fig. 7.4. In other words, the process slows down with increasing disorder, i. e.

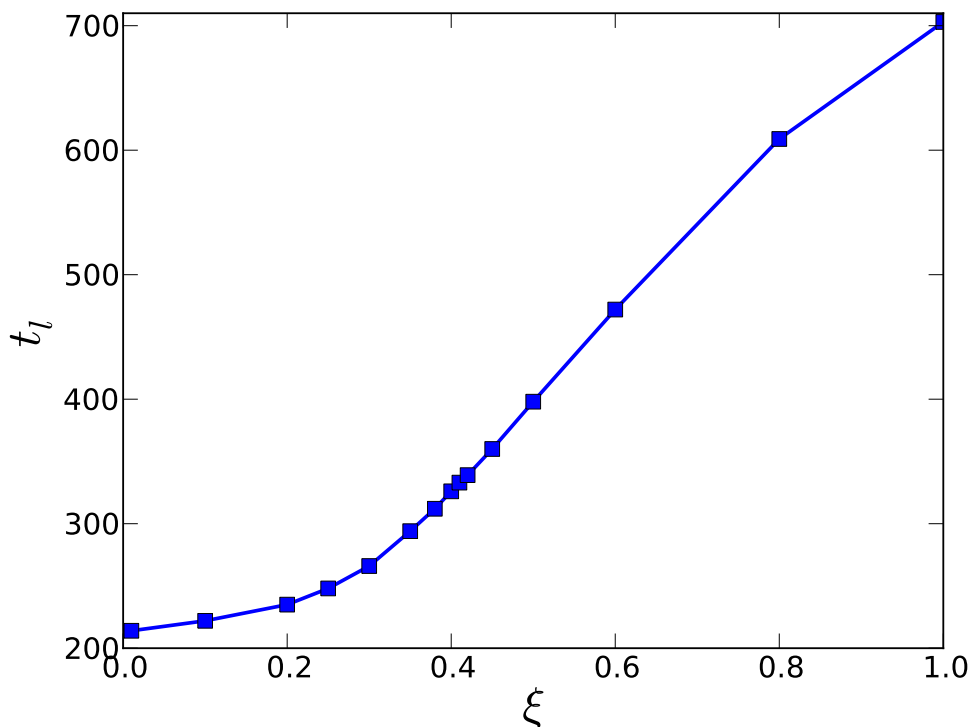


Figure 7.4: Average number of steps t_f needed to reach the shrinkage value of $\alpha_f = 0.7$, for different values of the disorder ξ , for a system of size $L = 30$.

a larger number of smaller steps are required to drive the fracture process. It can be observed in Fig. 7.4 that the monotonically increasing t_f curve has a curvature change around $\xi_c \approx 0.5$, where the slope of the function has a maximum. Looking at the rate of change, the system seems to have two phases depending on the amount of disorder: a rapidly evolving low disorder phase and a slowly proceeding high disorder one, separated by the inflection point. Both quantities we have considered until now are global characteristics of the lattice breaking process. In the following we analyze the statistical features of the individual avalanches of spring breakings.

7.4 Avalanche dynamics

Let us start by analyzing $\bar{\Delta}$, defined as the average size of avalanches decreased by the minimum avalanche size, $\Delta_{min} = 1$, as a function of α .

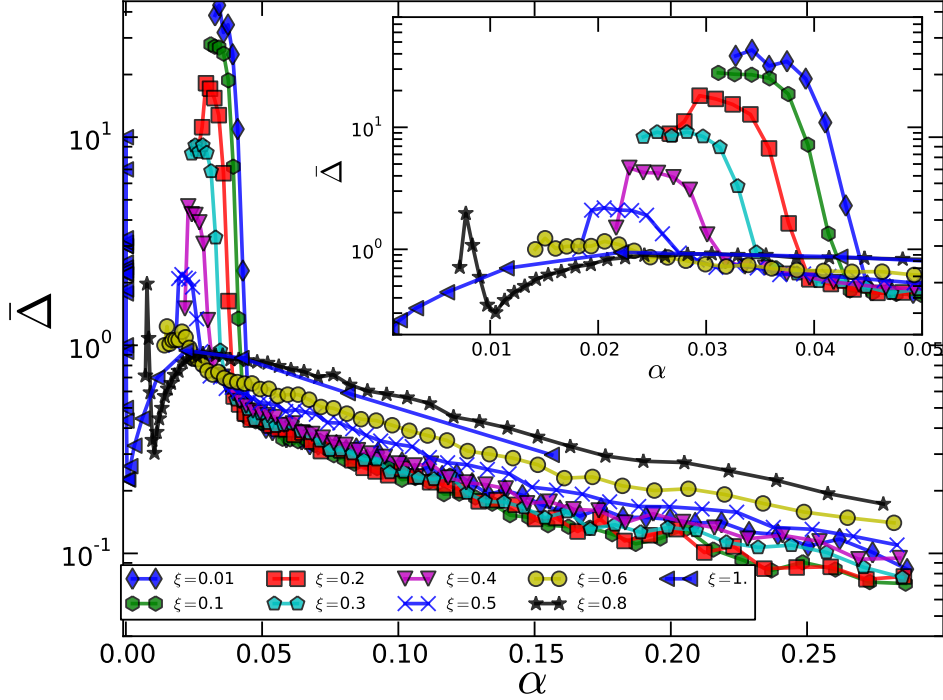


Figure 7.5: Arithmetic average of avalanche sizes $\bar{\Delta}(\alpha)$ as function of the shrinkage α for different values of disorder ξ . Each curve is the average over several instances of the system. *Inset* For very high disorders (for example $\xi = 1.0$), there is a single maximum, corresponding to a single large avalanche, just at the start. This first maximum disappears close to the transition value of disorder $\xi_c = 0.6$ and, thereafter, a second local maximum appears. For all cases, there is an exponential relationship between $\bar{\Delta}$ and α at the end of the process.

It can be observed in Fig. 7.5 that for systems with very high disorder, $\bar{\Delta}(\alpha)$ jumps discontinuously from zero to an isolated maximum, which in turn is orders of magnitude larger than the average of the function over the whole loading process. This corresponds to a large initial avalanche, caused by the release of the strain accumulation in the system. The height of this maximum decreases with increasing disorder and disappears for $\xi \approx 0.7$, where $\bar{\Delta}(\alpha)$ becomes a monotonically decreasing function. This is in agreement with previous results on the geometrical structure of the crack patterns, showing that for large disorders the largest crack appears by coalescence, not by a single large avalanche [SDT11, NSS⁺10]. Also notice that for smaller amounts of disorder (for $\xi \leq 0.6$) a local maximum appears. This implies that the large initial

crack does not completely precludes the appearance of large avalanches; rather, some new cracks can appear at this second value of shrinkage. It is interesting to note that in Fig. 7.5 straight lines are obtained on a semi-logarithmic plot, evidencing that, for large α values, $\overline{\Delta}(\alpha)$ shows an exponential decay

$$\overline{\Delta} \approx e^{-A\alpha}, \quad (7.5)$$

for all amounts of disorder. The multiplication factor A is practically independent of the value of ξ .

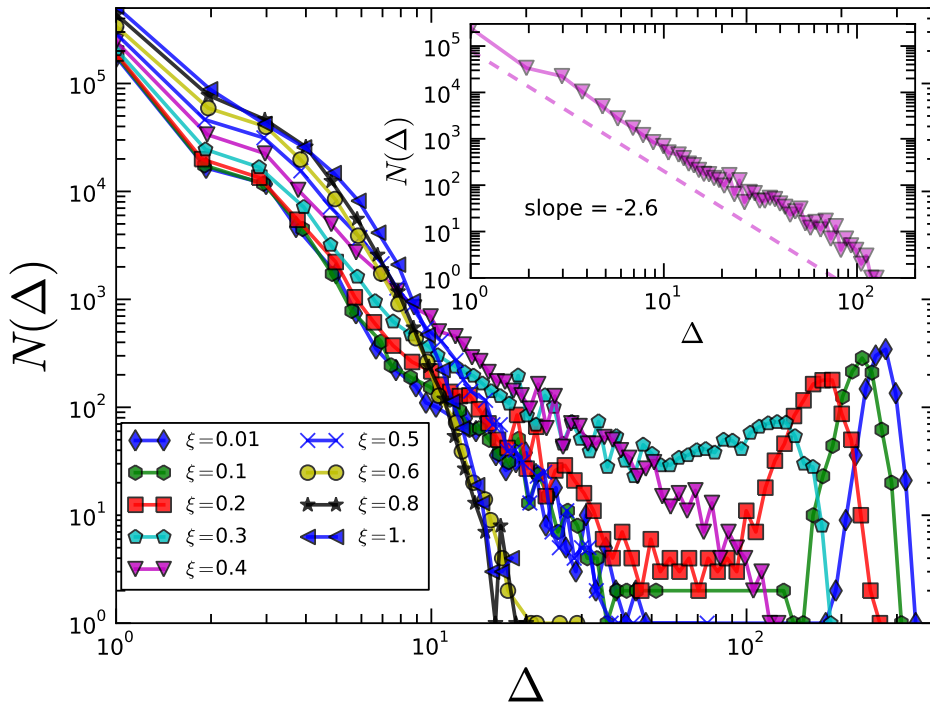


Figure 7.6: Avalanche size distributions $N(\Delta) \propto P(\Delta)$ for a system of linear extension $L = 30$, for several values of disorder ξ . *Inset* avalanche size distribution at the critical point ξ_c , where a good quality power law is obtained.

The distribution of avalanche sizes $N(\Delta)$, proportional to the probability distribution of avalanche sizes $P(\Delta)$, is presented in Fig. 7.6 for several values of the amount of disorder ξ . It can be observed that for small disorders the distribution $P(\Delta)$ clearly separates into two distinct regimes with different functional forms: for small-sized avalanches (say, $\Delta < 10$) the distribution P shows an exponential decay, while for larger ones it shows a well defined peak, corresponding to a single major avalanche at the beginning of the drying (depicted in Fig. 7.2). This rapid exponential decay of small-sized avalanches is due to the appearance of a large dominating crack of almost the same as the linear extension of the system, which creates a free surface that allows for the relaxation of stresses. The drying process later on cannot generate long breaking sequences,

since nodes can easily rearrange to compensate for unbalanced forces. At high amount of disorder, in contrast, the presence of strong springs prevents the formation of a dominating crack at the onset of breaking. The breakup proceeds in short avalanches resulting in a large number of small-sized cracks which eventually merge and relax all unbalanced forces. Consequently, the distribution of avalanches sizes $P(\Delta)$ spans again a limited range and exhibits an exponential decay.

These two different behaviors define the two phases of the system: a first *isolated large crack phase* where the fracture growth is dominated by the appearance of a macroscopic crack at the beginning of the process, almost spanning across the sample; and a second *coalescence phase*, where the large fracture is formed by merging small cracks at the end of the breakup process. The transition between the two phases is controlled by the amount of disorder in the system. At the critical value $\xi_c = 0.40 \pm 0.01$, the probability distribution becomes a power law

$$P(\Delta) \sim \Delta^{-\tau} \quad , \quad (7.6)$$

with no characteristic length scale (see the inset of Fig. 7.6). The value of the exponent τ was determined numerically as $\tau = 2.6 \pm 0.08$. It is interesting to note that this value falls very close to the mean-field exponent $\tau = 5/2$ of fiber bundles [PHC10, PHH06, HKKP09], supporting the idea that the statistics of avalanches in drying induced cracking is dominated by the long range nature of the load redistributions.

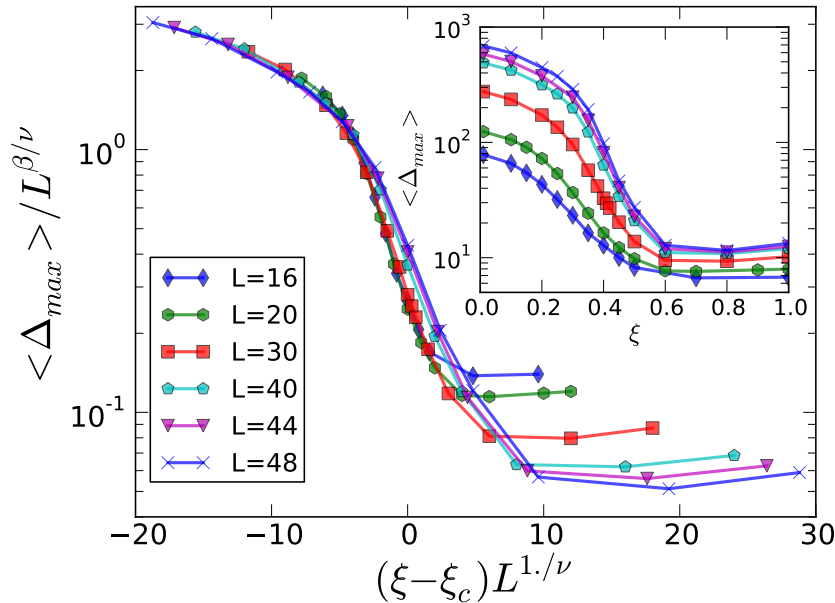


Figure 7.7: Arithmetic average of the largest avalanche, for different system sizes, as a function of the disorder of the system ξ . The different data curves collapse in a single shape when the transformation is applied, implying: $\xi_c = 0.4$, $\beta/\nu = 1.4$ and $1/\nu = 1$. *Inset* Original data without rescaling.

In order to understand the nature of this disorder-induced transition we computed the average value of the largest burst $\langle \Delta_{max} \rangle$, which can be considered as the order parameter of the transition. Indeed, it can be observed in Fig. 7.7 that $\langle \Delta_{max} \rangle$ is a monotonically decreasing function of the amount of disorder ξ , with an inflection point at the transition ($\xi_c \approx 0.6$ for the system size $L = 48$). Increasing the system size L shift the curves of $\langle \Delta_{max} \rangle$ towards higher disorder values, but the functional form remains the same. Actually, Fig. 7.7 shows that all curves for different system sizes L can be collapsed onto a universal master curve by appropriately rescaling both axis on the plot. The good quality data collapse implies the scaling structure

$$\langle \Delta_{max} \rangle(L, \xi) = L^{\beta/\nu} f((\xi - \xi_c)L^{1/\nu}), \quad (7.7)$$

where the value of the critical exponents were obtained numerically as $\beta/\nu = 1.4$ and $1/\nu = 1.0$ in agreement to the value of ν obtained theoretically for the quasi-static damage models in the regime of small damage [TP05]. In this case, the values were obtained by carefully changing the values until a good collapse could be achieved, since higher order cumulants resulted too noisy to try a more elaborated method.

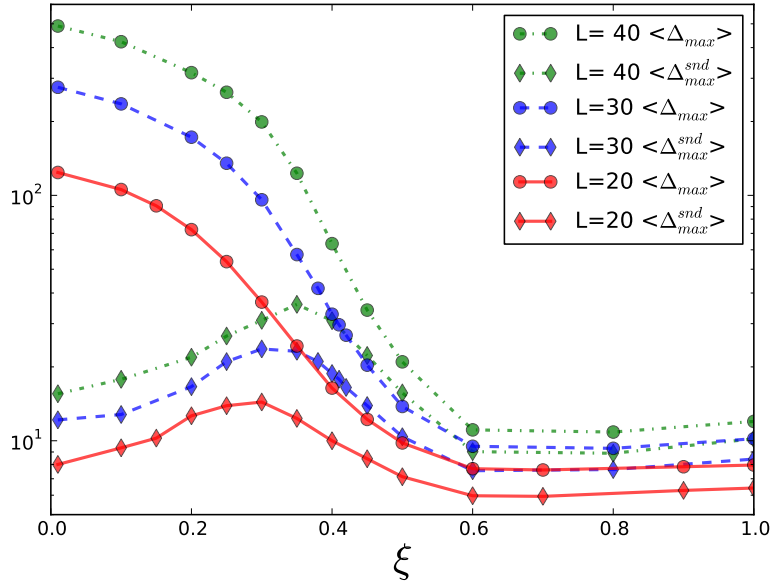


Figure 7.8: Arithmetic average of the largest $\langle \Delta_{max} \rangle$ and second largest $\langle \Delta_{max}^{2nd} \rangle$ avalanches for different system sizes, as a function of the disorder ξ .

Fig. 7.8 compares the average of the largest $\langle \Delta_{max} \rangle$ and second largest $\langle \Delta_{max}^{2nd} \rangle$ bursts. It can be observed that below the critical point $\xi < \xi_c$ the size of the largest avalanche is a finite fraction of the total number of bonds in the lattice, while the second largest burst is orders of magnitude smaller; in contrast, in the high-disorder regime $\xi > \xi_c$ the largest and second largest bursts are similar and decrease together as ξ increases. Based on this behavior, let us define the

average burst size $\langle \Delta \rangle$ as the average value of the ratio of the second m_2 and first moments m_1 of the avalanche size distribution [SA94],

$$\langle \Delta \rangle = \left\langle \frac{m_2}{m_1} \right\rangle , \quad (7.8)$$

where the k th moment of the burst sizes is defined as

$$m_k = \sum_{i=1}^K \Delta^k - \Delta_{max}^k . \quad (7.9)$$

When plotted against ξ , this average burst size exhibits the remarkable feature of showing a maximum at the same critical disorder ξ_c obtained in the previous analysis of the largest bursts (Fig. 7.9). Both results demonstrate that the interplay between strength disorder and stress inhomogeneities around cracks leads to the emergence of a critical state of the system where the bursting activity becomes scale-free. Note that in the evaluation of the average burst size $\langle \Delta \rangle$ the largest burst is always omitted; thus, the maximum in Fig. 7.9 implies that the characteristic avalanche size becomes comparable to the system size at the critical disorder. By increasing the system size L the maximum of the average burst size $\langle \Delta \rangle$ gets sharper, i.e. it becomes a higher and narrower peak. Based on the analogy to phase transitions, we tested the validity of the scaling form

$$\langle \Delta \rangle(L, \xi) = L^{\gamma/\nu} g((\xi - \xi_c)L^{1/\nu}) , \quad (7.10)$$

where $g(x)$ denotes a universal scaling function. It can be observed in Fig. 7.10 that this scaling law allows for a data collapse of very good quality. The value of the exponents were obtained as $\gamma/\nu = 1$ and $1/\nu = 0.9$. It has to be emphasized that these values of ξ_c and $1/\nu$ are consistent with the ones obtained from the scaling analysis of the largest burst $\langle \Delta_{max} \rangle$.

7.5 Discussion

By means of computer simulations the effect of structural disorder on the statistics of cracking for a thin layer of material under uniform and isotropic drying was investigated. The layer was discretized into a triangular lattice of mass and springs elements, in which the nodes were slightly randomly displaced. The effect of the drying is introduced by reducing the natural length every springs by the same factor; while the amount of quenched disorder is controlled by varying the width ξ of the distribution of the random breaking thresholds for the springs. The breaking of a spring causes a redistribution of the forces acting on the nodes, which in turn may trigger an avalanche of breaks; which may or may not be part of the same crack. Computer simulations revealed that the system exhibits a phase transition with the amount of disorder as control parameter: at low disorders, the breaking process is dominated by a macroscopic crack at the beginning, and the size distribution of the subsequent breaking avalanches shows an exponential form. At high disorders, the fracturing proceeds in small-sized avalanches with an exponential distribution, generating a large number of micro-cracks which eventually merge and

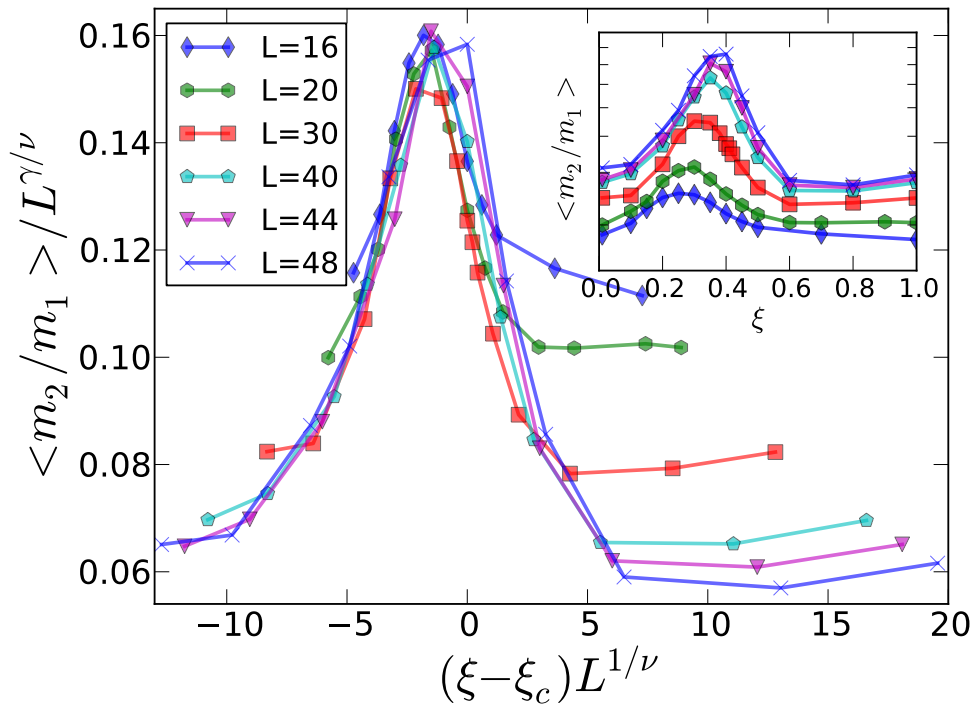


Figure 7.9: Scaling plot of the average avalanche size $\langle m_2/m_1 \rangle$. By rescaling the two axis with appropriate powers of L , all curves obtained for different L values collapse on the top of each other for $\gamma/\nu = 1.$, $1/\nu = 0.9$ and $\xi_c = 0.4$. The inset shows the original data before rescaling.

break the layer. Between both phases a sharp transition occurs at a critical amount of disorder $\xi_c = 0.40 \pm 0.01$, where the avalanche size distribution becomes a power law with exponent $\tau = 2.6 \pm 0.08$, in agreement with the mean-field value $\tau = 5/2$ of the fiber bundle model. Moreover, good quality data collapses from the finite-size scaling analysis show that the average value of the largest burst $\langle \Delta_{max} \rangle$ can be identified as the order parameter, with $\beta/\nu = 1.4$ and $1/\nu \simeq 1.0$, and that the average ratio $\langle m_2/m_1 \rangle$ of the second m_2 and first moments m_1 of the avalanche size distribution shows similar behaviour to the susceptibility of a continuous transition, with $\gamma/\nu = 1.$, $1/\nu \simeq 0.9$. These results suggest that the disorder induced transition of the breakup of thin layers is analogous to a continuous phase transition.

Note that in real systems the drying process might not be quasi-static, i.e. avalanches might be triggered by more than one micro-fractures, which also affects the statistic of avalanches. Recently, it has been shown analytically in the framework of fiber bundles that compared to the quasi-static limit, the power law exponent of the burst size distribution gets higher when the system is driven with finite load increments [PHC10, HP07]. A similar change of the burst size exponent can be expected when increasing the drying rate of the desiccation process.

Desiccation induced cracking of pastes is a good candidate for a possible experimental realization of our theoretical findings. It has been shown recently in several experiments [Kit99, NM06b] that pastes offer several opportunities to control the amount of disorder in the drying material: By varying the composition of the system (for instance by mixing two different materials such as polymers and clay, as in Ref. [Kit99]) a quenched structural disorder of local strength values can be introduced. Another possibility is to consider a single component paste, but varying the size distribution of particles in the colloidal suspension (as in [NM06b]). Both methods might be used to prepare samples with several amounts of quenched disorder, and high-speed imaging techniques could be used to monitor the avalanches by analyzing the temporal fluctuations of the crack pattern, as in [WKHK04, MSST06]. This experimental setup would contrast our results for the order parameter, the critical exponents and the phase transition itself.



Experimental evidence of avalanches of breakings during Bamboo drying

In the present chapter we show acoustic emission measurements of the statistics of avalanches of breakings, pictures of the macroscopic cracks and deformations, as well as microscopic images taken from drying experiments on bamboo culms. Since the computational models follow the main physical characteristics of the drying of bamboo, it is expected that experiments of drying would provide relevant information. Besides this, the goal of the experiments was to characterize the breakup of guadua; to the best of our knowledge there are no published works that study both the evolution of the tissues at the microscopic scale as well as the acoustic emission events that occur during the drying. Our experiments provide evidence of the detachment between neighbouring cells being a key process taking place during the drying. The comparison between experimental and analytical statistics of avalanches shows compelling evidence of the shrinkage induced breaking being the most likely candidate for the creation of drying induced cracks.

Three sets of bamboo drying experiments were conducted. For all of them 4 year old *Phyllostachys Edulis* (also known as *Phyllostachys Pubescens*) culms were used. Firstly, we characterized the *drying speed* by measuring the average weight loss during the oven drying at 100C of 20 internodal bamboo samples of 10 cm as function of time; from this data an experimental curve of moisture content was obtained. The experiment shows a fast mass loss phase, which slows down until the sample weight stabilizes at the dry state value. Pictures taken at the end of the drying process give evidence of macroscopic cracks appearing during drying.

The easily audible evidence of crackings that we heard during drying lead us to do a second set of experiments. In this set, we characterized the intensity of the microscopic cracks by measuring their acoustic emission by means of a microphone in contact with the bamboo culm segments being dried in the oven. The temperature was again 100 C, and the digitalization was performed using a standard microphone and a digital sound card at a rate of 9600 bps.

A final set of experiments was conducted looking for pictorial evidence of the drying induced delaminations, as well as to characterize the deformations of the cell geometry during drying. Due to size restrictions of the microscopy apparatus, the samples had to be cutted down to segments of the arc of the culm. Our results show that there is no large shape distortions during

Experiment	Sample Width	Number of Samples
Moisture content	1 <i>cm</i>	4
Moisture content	10 <i>cm</i>	1
Accoustic emission	1 <i>cm</i>	1
Microscopy	10 <i>cm</i>	1

Table 8.1: Materials used in the drying experiments. The bamboo species used was *Phyllostachys Pubescens*. For the microscopy experiments a single 1 *cm* ring was cut into 9 segments.

drying, and the detachments, are not visible at the microscopic scale.

8.1 Moisture content

As discussed before, in this set of measurements we characterized the moisture content on the sample as function of drying time. The materials and methods are reported in 8.1. We choosed to 4 pieces of 10 *cm* long for the first experiment looking for homogeneity of the material, as they belong to the same internode. Drying was conducted at a 100 C. The moisture content as function of drying time of the bamboo samples is shown in Fig. 8.1.

For the four 1 *cm* pieces, an exponential can be fit to the data with a time constant of $-0.4(3) 1/h$, for the first 3 to 4 hours of drying. In this phase the moisture content falls from the initial value of 60 % to about 10 %. Similar behaviour can be spotted for the single 10 *cm* piece. A slower drying takes place from this point on, until the moisture content goes to 0. This behaviour is an indication of the two phases of drying, first a fast one in which most of the moisture is physically bounded, so the free water can be removed quite easily. On comparison, the last stage of drying corresponds to the removal of chemically bounded water which takes longer time to dry.

During this drying experiment 3 out of the 4 samples presented visible large cracks, which were first spotted at drying times 59 *min*, 286 *min* and 326 *min*. One of the samples also presented large deformations, which we show on [Fig. 8.2]. While it is clear that macroscopic fractures do appear during drying, the sample is too small to quantify the relationship.

8.2 Accoustic emission measurements

The objective of this experiment was to characterize the statistics of avalanches of breakings that are easily heard during the drying process. The measurements we obtained correspond to the first 3 hours of drying, the fast drying stage. A single sample was placed on the oven, with a contact microphone. The voltage increase in the microphone due to the sounds was recorded by means of a computer's sound card. The absolute units of voltage have no special meaning, since there is gain through both the electronics and the software. Then the units of voltage are arbitrary and we only care about the range of variations of the values.

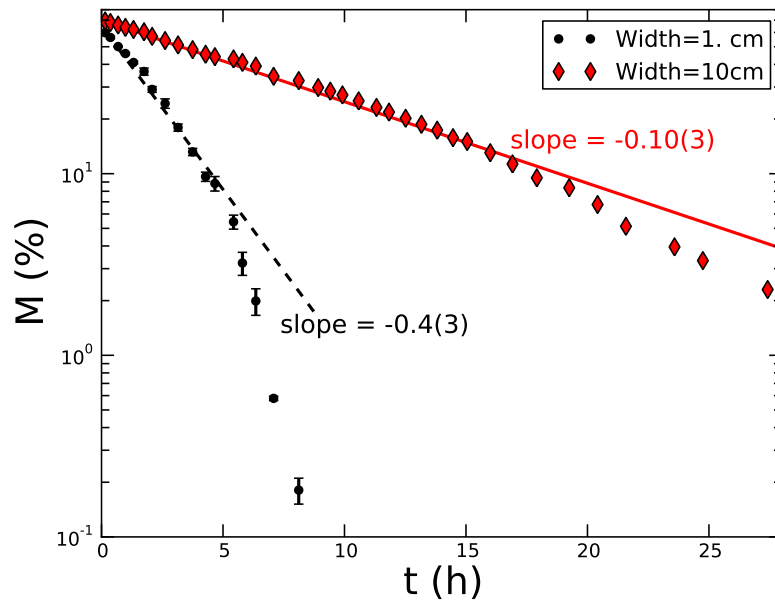


Figure 8.1: Moisture content as function of drying time, for two sets of experiments. Black points corresponds to the measurements of moisture content averaged over 4 segments of internode culm of 1 cm of width. An exponential fit with timeconstant $-0.4(3) 1/b$ is shown in dashed line. The red diamonds correspond to moisture content over a single 10 cm segment, with the red line being an exponential fit with timeconstant $-0.10(3) 1/b$.

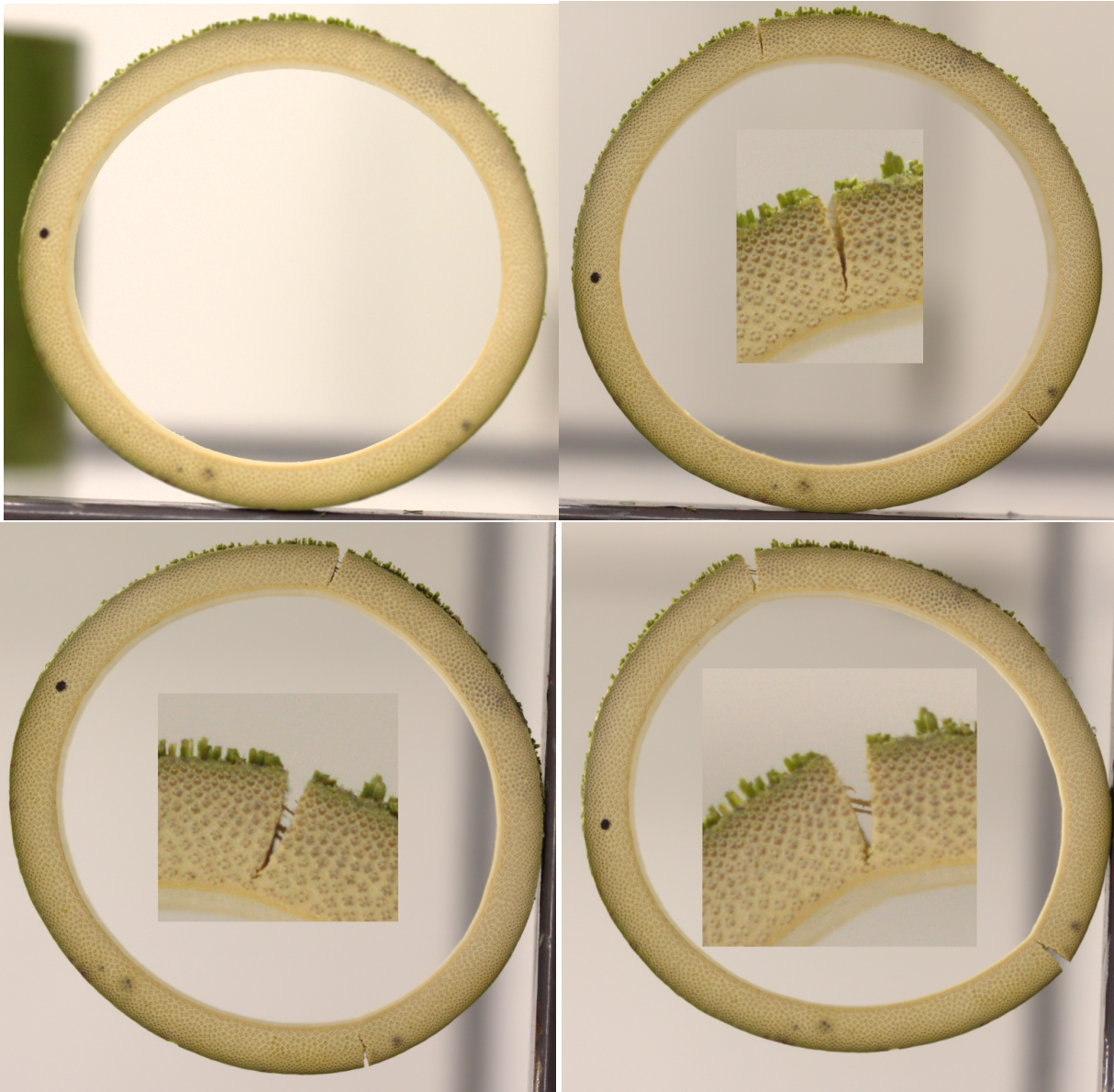


Figure 8.2: Snapshots of the sample 1, at different times during drying, along with enlargements of one of the two catastrophic cracks that appeared on this sample. (Upper left) Minute 41, no visible cracks. (Upper Right) Minute 79, two cracks are clearly visible. (Lower left) Minute 105. (Lower right) Minute 157, large deformation of the ring.

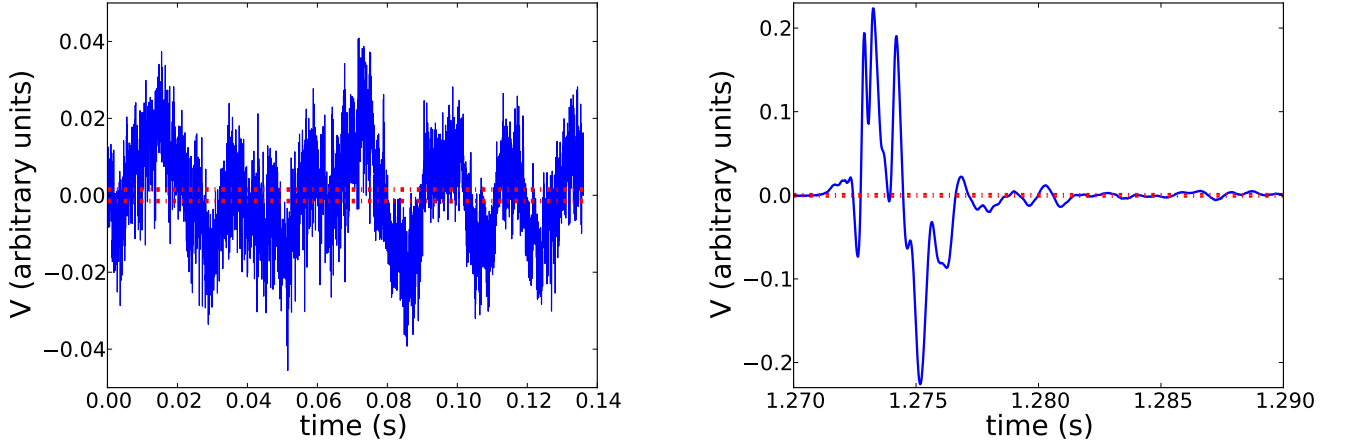


Figure 8.3: (Color Online). Examples of voltage on the microphone, blue continuous line (proportional to the sound intensity), and set noise threshold. a) A cascade of small sized breakings. b) A single large crack. (Sounds included as supplementary material.)

Two procedures were taken in order to clean spurious signals not corresponding to cracks from the sample. Firstly, after the sound was recorded, the whole dataset was manually screened and loud noises not coming from the drying specimen were removed by just not taking this segments into the dataset. The second concern is to identify background noise, both acoustic and from the electronics. This was filtered out by setting a minimum threshold for recording a voltage signal. This threshold compared to two sample signals, a faint and a loud one, shown on Fig. 8.3. Since our main concern is to relate the amplitude and duration of different crack signals, the calibration focused on obtaining a wide range of values keeping out measurements that could not be identified as a snap signal.

The input voltage data is discretized by the transduction electronic-software system at a frequency of $\Delta t_{exp} = 1/14400$. We first identify *snap events*, defined as a contiguous set of voltage measurements whose squared signal are larger than the minimum threshold. Contiguous points are defined by a threshold of $5\Delta t_{exp}$. This definition is coherent with the breaking process, since part of the energy released on fracture is released as acoustic wave. The size of the event is defined as the total energy released at the event, that is, the integral of the square of the voltage measurement. We also measure the waiting times between successive snap sound events.

This dataset allows us to study the distribution of avalanches of sound events. Take first Fig. 8.4, where the probability distribution of the sizes of sound events is presented. The behaviour corresponds to a power law distribution of sizes,

$$P(\Delta) \propto \Delta^{-\alpha}, \quad (8.1)$$

with an exponent of $\alpha = -1.2$.

The waiting times between avalanches, on the other side, show an exponential decay behaviour, as can be seen in Fig. 8.4. In this case the time constant is 0.045. The behaviour

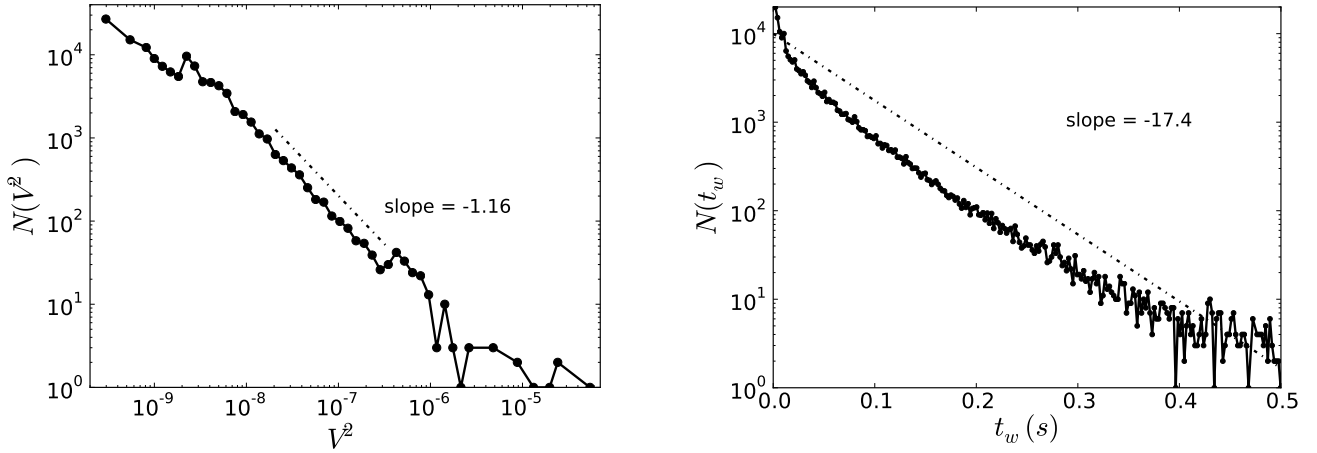


Figure 8.4: (Left) Experimental squared voltage size distributions $N(\Delta)$. The line drawn has a slope of -1.2 . (Right) Experimental waiting times between consecutive avalanches.

is clearly different to that of earthquakes, in which a scale free phenomenon characterized by a power law can be obtained. The difference can be explained from the fact that the allowed number of cracks in the present case is finite, while in earthquakes the possible number of events is always larger than what is measured in any particular measurement.

The correlation between the amount of released energy in an event and its timespan is depicted in Fig. 8.5 as a scatter plot. The lower cutoff comes from the imposed threshold of measurement. The discreteness in time span values is a consequence of the sound sampling rate of the acquisition transducer. Clearly, there is more dispersion on the crack events that take longer and release a larger amount of energy, while the distribution narrows for shorter times.

To identify the evolution of energy release, the size of the avalanche was averaged over 5 second sound intervals, and plotted as function of the number of the sound interval, as can be seen in 8.5. It is possible to identify two stages, early and late, separated by the sound interval number 100. In the first stage the average intensity is in average a growing quantity, while some isolated sound intervals show peaks corresponding to single big cracks. At the late stage, the distribution of average intensities narrows at and overall higher value.

8.3 Microscopy measurements

As stated at the beginning of this chapter, the objective of this measurements was to capture the deformation of the different tissues of the bamboo culm during drying. To be able to mount the samples into the microscope, a single ring of 1 cm width was cut into 9 pieces. Drying was conducted at 100 C .

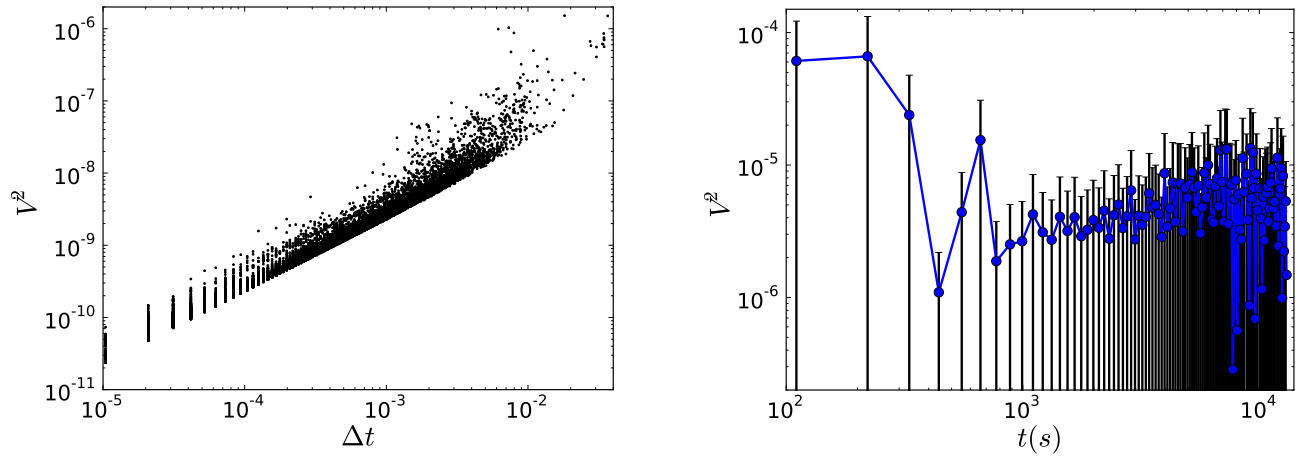


Figure 8.5: (Color online) (Left) Experimental scatter plot of energy as function of avalanche timespan. (Right) Experimental averaged energy release per avalanche as function of time.

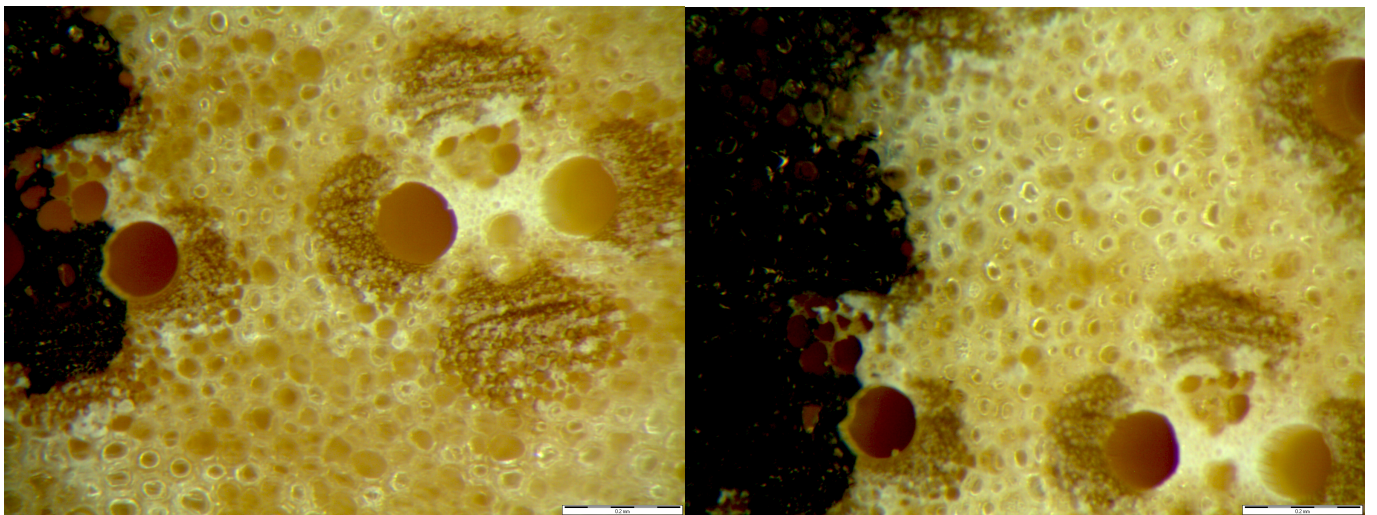


Figure 8.6: Zoom, amplified 57 times a fiber bundle and surrounding parenchyma tissue. (Left) Before drying. (Right) After drying.

Conclusions

The present thesis introduced and developed four statistical models of fracture inspired in the geometry and drying mechanisms of the parenchymatous tissue of *Guadua angustifolia*. All models are two-dimensional, resembling the geometry of this tissue in a perpendicular plane to the culm. Two of them correspond to the first stage of drying, when all cells are saturated with water (called *free water*) and a capillary front advances from cell to cell. The capillary forces play a central role here, eventually driving the collapse of the soft tissue (*capillary induced fractures*). The other two models are related with the second drying stage, when the water (called *bond water*) lies inside the cell walls themselves, and all cells are in contact with the air. Here, the fracture is driven by the shrinkage of the cell walls (*shrinkage induced fractures*).

The main fracturing mechanism during bamboo drying is the shrinkage due to the removal of bond water from the cell wall. Let us start with this second mechanism. If the process is slow enough, all cell walls may shrink by the same uniform factor α , increasing the stresses and eventually driving the brittle junctures among cells to break. The way they break is controlled by the structural disorder. I carried out a theoretical investigation of this fracture process on a thin layer of an heterogeneous material. The study has focused on the temporal evolution of the fractures by analyzing the statistics of avalanches of micro-fractures for several amounts of disorder. Two main models were considered: In the first one, the actual geometry of the parenchymatous tissue is closely resembled. Each polygonal cell is composed of individual cell walls. The cells are organized in a lattice, and each cell is connected with around six neighbors by brittle junctures at the tri-cellular points. The whole system is simulated with the finite element method, FEM ([Chapter. 6]). In the second model, the geometry is over-simplified. Each cell is represented by a single mass, connected to exactly six neighbors by brittle junctions in a slightly randomized triangular lattice of spring elements. This model is simulated with the discrete element method, DEM ([Chapter. 7]).

In the first model, the constitutive elements are the cell walls. They are represented by plane-frame elements in the FEM simulation. Each wall is tightly bond to two other walls in the same cell (building up the cell structure), but loosely joint to the neighboring cell by brittle springs. These springs are set at the tri-cellular junctures. The structural disorder can be included in two ways: either the geometry is uniform and the breaking thresholds ant the junctures are random

distributed or this threshold is the same for all junctures and the geometry is random (9.1(Left)). For the latter, the geometry is generated by a Voronoi construction.¹ The simulation run as follows. First, the effect of shrinkage is introduced by homogeneously reducing the length of all elements, characterized by a global shrinking factor α . Its value is carefully chosen to assure that just one brittle juncture breaks. Then, this juncture is removed from the structural matrix, and the forces are re-calculated to determine if more junctures break. They are removed, and the process iterates until the structure stabilizes and the avalanche stops. The whole process repeats until the matrix cannot be solved. The models were investigated by carrying out extensive computer simulations for several values of the control parameter. This control parameter is the width of the random distribution of breaking thresholds, for the first model; or the value of this threshold, for the second one. The simulations show that both models present power law distributions of the avalanche sizes for a specific value of the control parameter. The exponents are $\Delta^{-2.93}$, for the uniform geometry; and $\Delta^{-2.5}$, for the random one. This provides evidence that the breaking process has a phase transition. The increments in α between consecutive avalanches are analogous to the waiting times between earthquakes, but they show an exponential distribution in all cases, in contrast to the power-law behavior for the earthquake case. Nonetheless, the system sizes computed for the FEM model were too small to unequivocally assess this latter result.

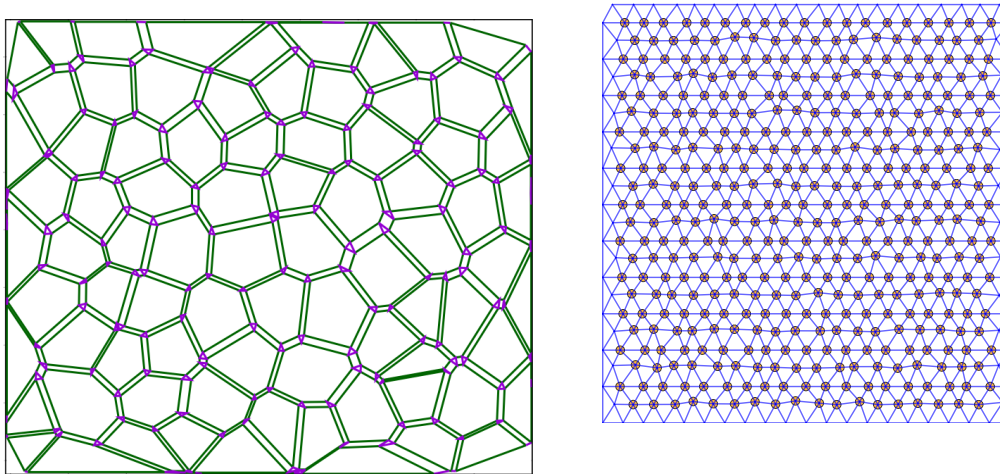


Figure 9.1: (Left) Polygonal, inhomogeneous cellular lattice model geometry, [Fig. 4.11](Right)Randomized triangular lattice model geometry. [Fig. 7.1]

The second shrinkage model consists of a slightly randomized triangular lattice of masses connected by brittle springs (Fig. [Fig. 9.1](Right)) [Chapter. 7]. The system evolves in a similar way as before. The α factor is carefully increased just to drive a first spring to break,

¹ The random geometry was built by means of a Voronoi procedure: An hexagonal array of cells is constructed, afterward a point is chosen at random from circles inscribed inside of the hexagons, then the lines joining every point with the points in the neighboring cells are drawn, and lastly the cells are constructed by using the perpendicular lines to the ones just described.

and the system is relaxed by numerically integrating the Newton's equations of motion; while every juncture is checked for breaking at every time step. The control parameter is the amount of disorder, characterized again by the width of the flat random distribution of breaking thresholds. Two time-like variables are tracked along the simulation: the α factor and the discrete number of avalanches.

As the most remarkable outcome, this study revealed that behind the formation of crack patterns induced by drying there are two well distinguished phases: At low disorders, few large avalanches at the beginning of the drying create a large free surface in the system, and thereafter only small-sized avalanches can emerge; this was called the *isolated large crack* phase. The large avalanches are comparable to the size of the system and they distribute like a peak around a mean size, while the small ones show an exponential distribution of sizes. In the opposite limit of high disorder, the entire breakup of the layer proceeds in small-sized bursts with an exponential distribution of sizes; this was called the *coalescence phase*. Between the high and low disorder phases a sharp transition occurs at a critical amount of disorder of $\xi_c = 0.40 + \pm 0.01$, where the avalanche size distribution becomes a power law with exponent -2.6 ± 0.08 , in agreement with the mean-field value $5/2$ of the fiber bundle model. Moreover, good quality data collapse from the finite-size scaling analysis show that the average value of the largest burst $\langle \Delta_{max} \rangle$ can be identified as the order parameter, with $\beta/\nu = 1.4$ and $1/\nu \simeq 1.0$, and that the average ratio $\left\langle \frac{m_2}{m_1} \right\rangle$ of the second m_2 and first moments m_1 of the avalanche size distribution shows similar to the susceptibility of a continuous transition, with $\gamma/\nu = 1.$, $1/\nu \simeq 0.9$ [Fig. 9.2]. These results suggest that the disorder induced transition of the breakup of thin layers is analogous to a novel continuous phase transition, with critical exponents characterizing probably a new universality class. This amazing result is the most remarkable outcome of this thesis, and can have deep implications in the understanding of drying-induced fractures of thin films, like painted surfaces, thin wood layers, anti reflective and UV-protecting coatings on glasses and thin-film manufacturing processes like chemical-bath and sol-gel depositions. In all these cases, drying proceeds uniform on all the surface. Actually, the controlled desiccation of pastes is a good candidate for a possible experimental realization of our theoretical findings, and we are expectant on the results that can confirm our findings.

The next two models study the first drying stage, when all cells are saturated with water (called *free water*) and a capillary front advances from cell to cell. The goal of the first model was to study the evolution, due to capillarity, of the drying front. The system is a regular hexagonal array of sites, representing the cells, with each site connected to six neighbors by bonds, representing the pit pores [Fig. 9.3](Left). The pore widths are chosen from a random distribution of a certain width. An initially fully saturated lattice of cells is emptied one-by-one by evaporation at the pits in contact with the atmosphere, i.e. at the drying front. The capillary forces in play cause the water to flow from the wider pores to the narrower ones; therefore, the first cell to empty is the one with the larger pit in contact with the atmosphere. This dynamics is equivalent to invasion percolation, and my numerical results are consistent with this. In fact, they are consistent with a fractal dimension of $91/48 \approx 1.896$ for the cluster of empty cells at percolation (the invasion-percolation result).

The second model studies how these capillary forces can produce fractures. It uses the dry-

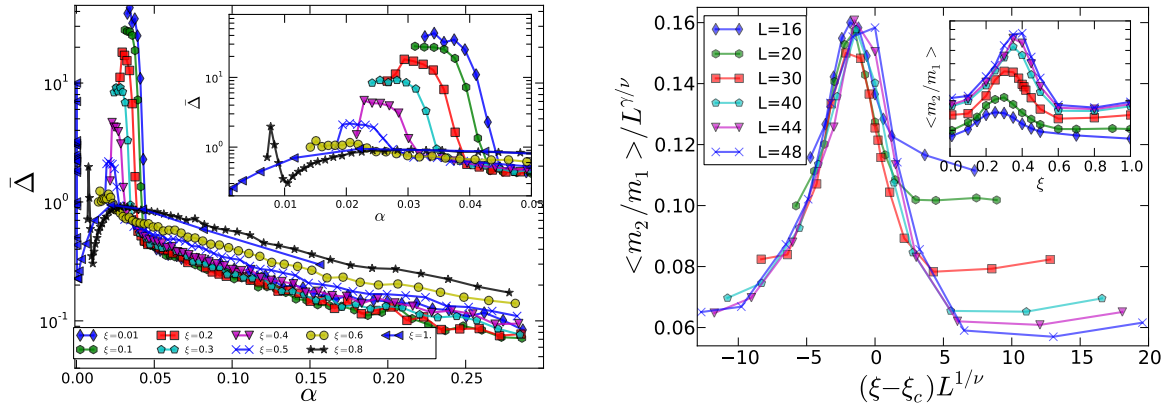


Figure 9.2: (Left) Arithmetic average of avalanche sizes $\overline{\Delta}(\alpha)$ as function of the shrinkage α for different values of disorder ξ [Fig. 9.2] (Right) Scaling plot of the average avalanche size $\langle m_2/m_1 \rangle$. By rescaling the two axis with appropriate powers of L , all curves obtained for different L values collapse on the top of each other for $\gamma/\nu = 1.$, $1/\nu = 0.9$ and $\xi_c = 0.4$. [Fig. 9.2]

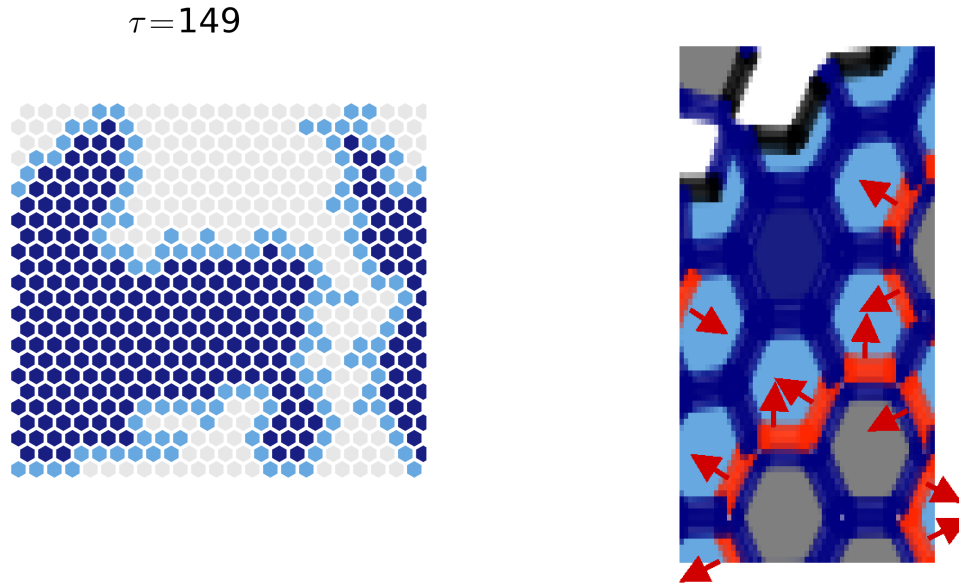


Figure 9.3: (Left) Capillary front model snapshots of percolation drying systems. In gray the empty cells, light blue the drying front cells, and dark blue the inner cells. [Fig. 5] (Right) Capillary induced fractures model. Key: Grey cell, empty; Light blue cell, drying front; Dark blue cell, inner; colored wall, are not delaminated and the color-scale represents the magnitude of the force; black wall, delaminated.[Fig. 5.3]

ing dynamics of the previous one on top of a Discrete Element Method (DEM) , modeling the parenchymatous tissue. The system geometry is again an hexagonal lattice, with each cell composed of six cell walls represented by spheropolygons and subject to contact, cohesion and capillary forces [Fig. 9.3](Left). Each cell wall is connected with the closest cell wall of a neighboring cell by two brittle contacts at the corners, which fail at a given breaking threshold. As the drying front evolves, the cell walls get displaced and the brittle contacts eventually break. Even though the geometry is highly regular, the fractures are not, since the forces are applied on the surface of the drying front, whose geometry is fractal. This breakup process has two interesting aspects to study: the changes that the fracture process can induce on the drying dynamics, and how this drying dynamics causes the fractures.

As the cellular material fractures, the interruption of the water flow between cells might have an impact on the percolation dynamics of drying. Interestingly enough, the numerical calculations showed that there is no appreciable effect, neither on the fractal dimension of the emptying cluster at percolation time nor on the time needed to dry the sample. The snapshots show why this is the case. Because the capillary forces appear on the drying front, the detachments occur behind this front; therefore, they do not significantly alter the drying dynamics.

The second aspect is how this capillary forces produce the detachments between cells (that is, the fractures). Capillary forces can be strong enough to induce a brittle contact to break. Then, the forces may redistribute around, and more contacts can break, rising an avalanche. I took as control parameter the width of the random distribution of pit sizes (the *amount of structural disorder*), and measured the sizes of the avalanches as a function of the number of dried cells for different instances of the same disorder of the system. For a given value of the disorder the average avalanche size (averaged over the realizations ensemble) is almost constant for all times, but depends on the amount of structural disorder. Both the avalanche sizes $P(\Delta)$ and the released energies per event $P(E_i)$ show exponential distributions. These results imply that there is no accumulation of strain in the sample due to the evolution of the forces, rather it is a simple rate process depending on the number of unbroken contacts. In terms of the statistical models of fracture, there load redistribution is not significant, and the contacts seem to break almost independently; therefore, the correlation length between cracks does not evolve. This behavior is robust against the introduction of some disorder on the elastic constants. I also calculated the distribution of sizes for the cracks at the end of the drying process. A crack is here defined as a connected cluster of broken contacts. In this case the distribution tends to a power law, which may indicate a relation to percolation. The fractal dimension shows an exponent of 2.10 ± 0.03 , slightly different to the percolation value. The difference is probably due to the slow correlation among neighboring detachment events, which is contrary to pure percolation, in which these breaks are completely independent events. The main difference between the shrinkage and the capillary model, in terms of the evolution of the forces in the system, is that the former shows accumulation of strain in the sample, which causes correlations among breakings that may generate larger avalanches, and the second does not. This will be relevant in the discussion, when compared with experiments.

Even though providing exact values for drying is beyond the goals of these models, I ran some numerical tests using the values from the literature of bamboo. As expected, a reduction

of the value of the capillary force by either wider pores or a change in the contact angle decreases the number of fractures; thus, capillary induced drying fractures can be controlled by physicochemical methods (as the industry actually does). Nonetheless, according to my numerical calculations, the values of pit sizes for bamboo reported in the literature are not small enough to generate detachments; therefore, is unlikely that this process may be the most relevant one in the drying of bamboo.

The numerical study of these models was complemented by a thorough experimental study. I performed two sets of experiments: acoustic emission and microscopy. Firstly, I characterized the process of water loss during the drying, obtaining an exponential decay. Drying of 1 cm thick culm sections of *Phyllostachys edulis* (a Bamboo similar to *Guadua angustifolia*) took between 5 and 8 hours in an oven at 100 C. Despite the fact that macroscopic cracks grow to break the sample across, the microscopic measurements showed no evidence of collapse or detachments among cells. The acoustic emission measurements had both popping and snapping events. The former are smaller in amplitude for at least one order of magnitude than the later. I implemented the computational code for analysis to isolate single cracks and measure its magnitude, taking into consideration the signal noise. For each event I recovered the area, proportional to the energy released, the time-span the event takes and the waiting time to the following event. The released energies at every crack distribute like a power law with exponent -1.16 , $P(V^2) \propto (V^2)^{-1.16}$. The waiting times between events show an exponential distribution with a characteristic time of -17.4 s. These functional forms (a power-law in the first case and an exponential in the second one) are the same the shrinkage models show, in contrast to earthquakes or fiber bundle models. This fact supports the arguments that the shrinkage induced breaking belongs to a different universality class than earthquakes, and that this is the dominant fracture process in drying Bamboo.

Each crack is characterized by the released energy and the time spanned by the event. A scatter plot of the energy as a function of the time-span does also show a power law behavior over many orders of magnitude. This suggests that most loud events are probably composed of several individual events of approximately the same energy, i.e. that a long event in the system may be in fact an avalanche of similar breaks, caused by some initial event, as assumed in our computational models. Finally, the average energy released as function of the drying time shows a high peak for the first seconds, followed by a drop of about two orders of magnitude. Hereafter on, the energy increases slowly until the measurement ends. The theoretical model of shrinkage shows a similar behavior, with a peak in the first instants of drying and a slow *decrease* thereafter. This could mean that in bamboo there is a backbone of elements with similar values of breaking thresholds, causing the large avalanche at the start.

The shrinkage model presented in this thesis has deep implications, not only for dessication processes but also in general for every process in which the fracturing comes due to homogeneous shrinkage of the whole structure. As we mentioned before, this ranges from macroscopic applications, as the drying of pastes, painted surfaces, thin wood layers, anti reflective and UV-protecting coatings; to microscopic processes like thin-film manufacturing. Driving the system into the high-disordered phase may turn the film more robust, avoiding the appearance of large cracks at the beginning and increasing lifetime. This could be reached by generating inhomoge-

neous mixtures or alternatively by manufacturing processes freezing some glass structure. This is the case, for instance, of glass-metallic films, and a possible explanation on why they are so tough.

The present work opens many new possibilities for the future study of bamboo and composite materials. A first extension of the drying model comes from the fiber-reinforced materials. In these systems a macroscopically homogeneous material is improved by inserting some stronger fibers into the mixture. A simple model would take the latter as a set of randomly distributed nucleation points, the fiber reinforcements, which have different drying characteristics, i.g., timescales for bond and free water removal, rates of swelling and shrinkage due to moisture content changes. This can be easily implemented in the models I have proposed, and has very interesting industrial applications. Moreover, this can also be used to investigate the mechanical consequences of an uneven distribution of fibers, like the one in Bamboos, in which fibers are more numerous toward the outer side of the culm. Recently, it has been shown that the optimized functional structure of natural materials may be related to different values for the strength of some subset of the fibers, its complex geometrical distribution, as well as nonlinear effects on their elastic properties,[CTPB12]. Secondly, both drying and shrinkage models can be extended to a three dimensional geometry. This can be useful to accomplish the study of drying of materials in which shrinkage may also affect the longitudinal direction. Take for instance the field of soil mechanics. It is well known that the amount of moisture in the samples change dramatically the mechanical properties of the soil, from rigid to plastic to liquid. The spheropolygon approach of this thesis can be used to study the different microscopic interactions taking place in this transition. The model may also be used to study the morphological changes that may happen during the drying of the soil and test for the appearance of fault planes in the drying process.

Another direction of future studies is to study the Bamboo strength to tension in the axial direction. The parenchymatous tissue shows in this direction a parallel structure of tubes, each one composed of an alternative ordering of short and long cells. Why are the parenchyma cells ordered this way? Perhaps this arrangement jeopardizes the crack propagation from tube to tube. This hypothesis may be investigated by introducing discrete fracture models resembling this structure, with the correlation length of the distribution of distances between cell limits of neighboring tubes as control parameter. Such models can be simulated by using the discrete element approach. This study may reveal why Bamboo can be several times stronger than wood against tensile stresses and the amazing stability of the culm, as a whole.

This work has introduced several statistical models of fracture inspired in the geometry and drying processes of Bamboo, but the consequences are far reaching. The discrete shrinkage model proposed here shows a novel and well-defined phase transition with interesting applications in materials' sciences. Once, more, the Nature teaches us how to built up structures of optimized performance with simple elements.

Bibliography

- [AJ08] C.M. Altaner and M.C. Jarvis. Modelling polymer interactions of the "molecular Velcro" type in wood under mechanical stress. *Journal of Theoretical Biology*, 253(3):434 – 445, 2008.
- [AM08] F. Alonso-Marroquín. Spheropolygons: A new method to simulate conservative and dissipative interactions between 2D complex-shaped rigid bodies. *EPL (Europhysics Letters)*, 83(1):14001, 2008.
- [Ama97] Fiber texture and mechanical graded structure of bamboo. *Composites Part B: Engineering*, 28(1- 2):13 – 20, 1997.
- [ANZ06] Mikko J. Alava, Phani K. V. V. Nukala, and Stefano Zapperi. Statistical Models of Fracture. *Advances in Physics*, 55(3-4):349, 2006.
- [AVB93] O.A. Arce-Villalobos and Technische Universiteit Eindhoven. Faculteit Bouwkunde. *Fundamentals of the design of bamboo structures*. PhD thesis, 1993.
- [Bat96] K.J. Bathe. *Finite element procedures*. Prentice Hall, 1996.
- [BC06] P. Bhattacharyya and B.K. Chakrabarti. *Modelling critical and catastrophic phenomena in geoscience: a statistical physics approach*. Lecture notes in physics. Springer, 2006.
- [Bha03] K.H. Bhat. Anatomical changes during culm maturation in *Bambusa bambos* (L.) Voss and *Dendrocalamus strictus* Nees. *J. Bamboo and Rattan*, 2(2):153–166, 2003.
- [Car88] John L. Cardy, editor. *Finite-size scaling*. North-holland, 1988.
- [CBI98] E. Charkaluk, M. Bigerelle, and A. Iost. Fractals and fracture. *Engineering Fracture Mechanics*, 61(1):119 – 139, 1998.

- [CDM⁺09] C. Carrasco, M. Douas, R. Miranda, M. Castellanos, P. A. Serena, J. L. Carrascosa, M. G. Mateu, M. I. Marqués, and P. J. de Pablo. The capillarity of nanometric water menisci confined inside closed-geometry viral cages. *Proceedings of the National Academy of Sciences*, 106(14):5475–5480, 2009.
- [Cha06] B.K. Chakrabarti. *Statistical Physics of Fracture and Earthquake*, 2006.
- [Chi05] Jean-Paul Chilés. *Stochastic Modeling of Natural Fractured Media: A Review*, volume 14 of *Quantitative Geology and Geostatistics*, pages 285–294. Springer Netherlands, 2005.
- [CJ11] Michael C. and Jarvis. Plant cell walls: Supramolecular assemblies. *Food Hydrocolloids*, 25(2):257 – 262, 2011. <ce:title>Dietary Fibre and Bioactive Polysaccharides</ce:title>.
- [CM94] Maarten J. Chrispeels and Christophe Maurel. Aquaporins: The molecular basis of facilitated water movement through living plant cells? *Plant Physiology*, 105:9–13, 1994.
- [CM00] E. Crow and R. J. Murphy. Microfibril orientation in differentiating and maturing fibre and parenchyma cell walls in culms of bamboo (*Phyllostachys viridiglaucescens* (Carr.) Riv. & Riv.). *Botanical Journal of the Linnean Society*, 134(1-2):339 – 359, 2000.
- [Coc06] Hervé Cochard. Cavitation in trees. *Comptes Rendus Physique*, 7(9 - 10):1018 – 1026, 2006.
- [Col56] B. D. Coleman. Time dependence of mechanical breakdown phenomena. *J. Mech. Phys. Solids*, 27, 1956.
- [CTPB12] Steven W. Cranford, Anna Tarakanova, Nicola M. Pugno, and Markus J. Buehler. Nonlinear material behaviour of spider silk yields robust webs. *Nature*, 482:72 – 76, 2012. Supplementary material online, <http://www.nature.com/nature/journal/v482/n7383/abs/nature10739.html>.
- [CWKH08] H. A. Carmona, F. K. Wittel, F. Kun, and H. J. Herrmann. Fragmentation processes in impact of spheres. *Phys. Rev. E*, 77:051302, May 2008.
- [DAKH04] G. Drazer, H. Auradou, J. Koplik, and J. P. Hulin. Self-Affine Fronts in Self-Affine Fractures: Large and Small-Scale Structure. *Phys. Rev. Lett.*, 92(1):014501, Jan 2004.
- [Dan45] H. E. Daniels. The Statistical Theory of the Strength of Bundles of Threads. *Proc. R. Soc London A*, 183:405–435, 1945.
- [DARH85] L. De Arcangelis, S. Redner, and H.J. Herrmann. A random fuse model for breaking processes. *Journal de Physique Lettres*, 46(13):585–590, 1985.

- [DD09] P. Deitel and H.M. Deitel. *C++: how to program*. How to program series. Pearson/Prentice Hall, 2009.
- [Elt01] Catedral vegetal para Pereira. El Tiempo, eltiempo.com, March 2001. Retrieved on January the 18th of 2012, url: eltiempo,.
- [Elt10] Un amigo fiel de guadua. El Tiempo, eltiempo.com, August 2010. Retrieved on January the 30th of 2012, url: <http://www.eltiempo.com/archivo/documento/MAM-4106911>.
- [Fis71] M.E. Fisher. In M.S. Green, editor, *Critical Phenomena, Proc. 51st Enrico Fermi Summer School, Varenna*. Academic Press, 1971.
- [FTDG⁺11] C. A. Fuentes, L. Q. N. Tran, C. Dupont-Gillain, W. Vanderlinden, S. De Feyter, A. W. Van Vuure, and I. Verpoest. Wetting behaviour and surface properties of technical bamboo fibres. *Colloids and Surfaces A: Physicochemical and Engineering Aspects*, March 2011.
- [GacP95] Leonardo Golubović and Anatoli Peredera. Mechanism of time-delayed fractures. *Phys. Rev. E*, 51:2799–2804, Apr 1995.
- [GBWQ04] P.G. Gennes, F. Brochard-Wyart, and D. Quéré. *Capillarity and wetting phenomena: drops, bubbles, pearls, waves*. Springer, 2004.
- [GCC99] A. Gabrielli, R. Cafiero, and G. Caldarelli. Statistical properties of fractures in damaged materials, 1999.
- [GKM04] Cristina Sanchis Gritsch, Gunnar Kleist, and Richard J. Murphy. Developmental Changes in Cell Wall Structure of Phloem Fibres of the Bamboo *Dendrocalamus asper*. *Annals of Botany*, 94(4), 2004.
- [GL74] G. Grosser and W. Liese. Verteilung der leitbündel und zellarten in sprossachsen verschiedner bambusarten. *Holz Roh-Werkstoff*, 32:473–482, 1974.
- [GM05] Cristina Sanchis Gritsch and Richard J. Murphy. Ultrastructure of Fibre and Parenchyma Cell Walls During Early Stages of Culm Development in *Dendrocalamus asper*. *Annals of Botany*, 95(4):619–629, 2005.
- [GMABS06] Héctor A. González, Jorge Augusto Montoya Arango, and Jose Rubiel Bedoya Sánchez. Esfuerzo De Tensión Y La Influencia De La Humedad Relativa Del Ambiente Y La Altura A Lo Largo Del Tramo En La Especie De Bambú *Guadua angustifolia* Kunth. *Scientia et Technica*, (12):445–450, 2006.
- [GMABS07] Héctor A. González, Jorge Augusto Montoya Arango, and Jose Rubiel Bedoya Sánchez. Resultados Del Ensayo A Flexión En Muestras De Bambú De La Especie *Guadua Angustifolia kunth*. *Scientia et Technica*, (35):503 – 508, 2007.

- [Gri20] A.A. Griffith. The phenomena of rupture and flow in solids. *Philos. Trans. Roy. Soc. London*, 221:163 – 198, 1920.
- [GSS06] D. Gross, T. Seelig, and T. Seelig. *Fracture mechanics: with an introduction to micromechanics*. Mechanical engineering series. Springer, 2006.
- [Gug45] E. A. Guggenheim. The principle of corresponding states. *The Journal of Chemical Physics*, 13(7):253–261, 1945.
- [Her82] Heinrich Hertz. Ueber die berührung fester elastischer körper. *Journal für die reine und angewandte Mathematik*, 92:156 – 171, 1882.
- [Her91] H.J. Herrmann. *Fractals and Disordered Systems*, chapter Fractures, pages 201–235. Springer-Verlag, 1991.
- [Her10] Igor Herbut. *A Modern Approach to Critical Phenomena*. Cambridge, 2010. www.cambridge.org.
- [HH89] H.J. and Herrmann. Fractal deterministic cracks. *Physica D: Nonlinear Phenomena*, 38(1 - 3):192 – 197, 1989.
- [HH92] Per C. Hemmer and Alex Hansen. The Distribution of Simultaneous Fiber Failures in Fiber Bundles. *Journal of Applied Mechanics*, 59(4):909–914, 1992.
- [HH94] Alex Hansen and P.C. Hemmer. Burst avalanches in bundles of fibers: Local versus global load-sharing. *Physics Letters A*, 184(6):394 – 396, 1994.
- [HKKP09] R. C. Hidalgo, F. Kun, K. Kovács, and I. Pagonabarraga. Avalanche dynamics of fiber bundle models. *Phys. Rev. E*, 80:051108, Nov 2009.
- [HKPK08] R. C. Hidalgo, K. Kovacs, I. Pagonabarraga, and F. Kun. Universality class of fiber bundles with strong heterogeneities. *EPL (Europhysics Letters)*, 81(5):54005 (6pp), 2008.
- [HP00] D. G. Harlow and S. L. Phoenix. *Damage and Fracture of Disordered Materials*, chapter Statistical toolbox for damage and fracture., pages 17 – 101. Springer Verlag, 2000.
- [HP07] Per C. Hemmer and Srutarshi Pradhan. Failure avalanches in fiber bundles for discrete load increase. *Phys. Rev. E*, 75:046101, Apr 2007.
- [HR90] H.J. Herrmann and S. Roux. *Statistical models for the fracture of disordered media*. Random materials and processes. North-Holland, 1990.
- [HT67] C.A. Hart and R.J. Thomas. Mechanism of bordered pit aspiration as caused by capillarity. *Forest Prod J*, 17:61–67, 1967.
- [Hug00] T. J. R. Hughes. *The finite element method*. Dover, 2000.

- [HWK06] Hans J. Herrmann, Falk K. Wittel, and Ferenc Kun. Fragmentation. *Physica A: Statistical Mechanics and its Applications*, 371(1):59 – 66, 2006.
- [HZH08] Raúl Cruz Hidalgo, Stefano Zapperi, and Hans J Herrmann. Discrete fracture model with anisotropic load sharing. *Journal of Statistical Mechanics: Theory and Experiment*, 2008(01):P01004, 2008.
- [Iva] Rafael Ivan. <http://www.flickr.com/photos/rafa64/4374513850/>.
- [Jan81] Julius J.A. Janssen. *Bamboo in building structures*. PhD thesis, Eindhoven University, 1981.
- [JM00] Michael C. Jarvis and Maureen C. McCann. Macromolecular biophysics of the plant cell wall: Concepts and methodology. *Plant Physiology and Biochemistry*, 38(1-2):1 – 13, 2000.
- [KAN11] Eisuke Kanzawa, Shoko Aoyagi, and Takato Nakano. Vascular bundle shape in cross-section and relaxation properties of Moso bamboo (*Phyllostachys pubescens*). *Materials Science and Engineering: C*, 31(5):1050 – 1054, 2011.
- [KCAH08] F. Kun, H. A. Carmona, J. S. Andrade, and H. J. Herrmann. Universality behind basquin’s law of fatigue. *Phys. Rev. Lett.*, 100:094301, Mar 2008. Phys-RevLett.100.094301, arXiv.org:0801.3664.
- [KHH97] M. Kloster, A. Hansen, and P. C. Hemmer. Burst avalanches in solvable models of fibrous materials. *Phys. Rev. E*, 56:2615–2625, Sep 1997.
- [Kit99] So Kitsunozaki. Fracture patterns induced by desiccation in a thin layer. *Phys. Rev. E*, 60:6449–6464, Dec 1999.
- [KMHH03] F. Kun, Y. Moreno, R. C. Hidalgo, and H. J. Herrmann. Creep rupture has two universality classes. *EPL (Europhysics Letters)*, 63(3):347, 2003.
- [Kra11] Crhis Kraul. Colombia architect leads bamboo building crusade. Los angeles times, [articles.latimes.com.](http://articles.latimes.com), November 2011. Retrieved on January the 30th of 2012, url <http://articles.latimes.com/2011/nov/29/world/la-fg-colombia-bamboo-20111129>.
- [KRHH06] F. Kun, F. Raischel, R. C. Hidalgo, and H. J. Herrmann. *Modelling Critical and Catastrophic Phenomena in Geoscience*, chapter Extensions of fiber bundle models. Springer, 2006.
- [Lab08] Marie-Pierre G. Laborie. *The Temperature Dependence of Wood Relaxations: A Molecular Probe of the Woody Cell Wall*, pages 87–94. Blackwell Publishing Professional, 2008.

- [LHH⁺02] Jinxing Lin, Xinqiang He, Yuxi Hu, Tingyun Kuang, and R. Ceulemans. Lignification and lignin heterogeneity for various age classes of bamboo (*Phyllostachys pubescens*) stems. *Physiologia Plantarum*, 114(2):296–302, 2002.
- [Li04] Xiabo Li. *Physical, Chemical, And Mechanical Properties Of Bamboo And Its Utilization Potential For Fiberboard Manufacturing*. PhD thesis, Louisiana State University, 2004.
- [Lie98] Walter Liese. *The Anatomy of Bamboo Culms*. INBAR, 1998. ISBN 81-86247-26-2.
- [Lin] LinkesAuge. www.flickr.com/photos/linkesauge/135501932.
- [Lin09] Dorian Luis Linero. *Programa de elementos finitos a código abierto - PEFiCA*. Universidad Nacional de Colombia, 2009.
- [LVAG06] Bieke Lybeer, Joris Van Acker, and Paul Goetghebeur. Variability in fibre and parenchyma cell walls of temperate and tropical bamboo culms of different ages. *Wood Science and Technology*, 40:477–492, 2006. 10.1007/s00226-006-0078-5.
- [LVV⁺03] Ximena Londoño, Marcelo Villegas, Simón Velez, Jesús Velez, Gabriel G. Londoño, and Götz Schmitt. *Guadua Arquitectura y Diseño*. 2003.
- [MA06] Jorge Augusto Montoya Arango. *Trocknungsverfahren für die Bambusart Guadua angustifolia unter tropischen Bedingungen*. PhD thesis, Universität Hamburg, Von-Melle-Park 3, 20146 Hamburg, 2006.
- [MA07] Jorge Augusto Montoya Arango. Determinación De Las Curvas Isotermas De Sorción Y El Psf-Punto De Saturación De Fibra-De La Especie De Bambú *Phyllostachys Pubescens* Mazel . *Scientia et Technica*, (35), 2007.
- [MAGBS07] Jorge Augusto Montoya Arango, Héctor A. González, and Jose Rubiel Bedoya Sánchez. Dureza Brinell Y La Influencia De La Humedad Relativa Del Ambiente, De La Edad Y La Altura A Lo Largo Del Tramo En La Especie De Bambú *Guadua angustifolia*. *Scientia et Technica*, (34):619 – 624, 2007.
- [MGMP01] L Moral, J B Gómez, Y Moreno, and A F Pacheco. Exact numerical solution for a time-dependent fibre-bundle model with continuous damage. *Journal of Physics A: Mathematical and General*, 34(47):9983, 2001.
- [MGP00] Y. Moreno, J. B. Gómez, and A. F. Pacheco. Fracture and Second-Order Phase Transitions. *Phys. Rev. Lett.*, 85:2865–2868, Oct 2000.
- [MSST06] Knut Jørgen Måløy, Stéphane Santucci, Jean Schmittbuhl, and Renaud Toussaint. Local Waiting Time Fluctuations along a Randomly Pinned Crack Front. *Phys. Rev. Lett.*, 96:045501, Jan 2006.

- [MTN08] Peter J. Mohr, Barry N. Taylor, and David B. Newell. CODATA recommended values of the fundamental physical constants: 2006. *Rev. Mod. Phys.*, 80:633–730, Jun 2008.
- [Nie08] P. Niemz. *Holzphysik und Holzwerkstoffe, Taschenbuch der Holztechnik*. Fachbuchverlag Leipzig im Hanser Verlag, 2008.
- [NM06a] A Nakahara and Y Matsuo. Imprinting memory into paste to control crack formation in drying process. *Journal of Statistical Mechanics: Theory and Experiment*, 2006(07):P07016, 2006.
- [NM06b] Akio Nakahara and Yousuke Matsuo. Transition in the pattern of cracks resulting from memory effects in paste. *Phys. Rev. E*, 74(4):045102, 2006.
- [NM07] Akio Nakahara and Yousuke Matsuo. Morphological Change of Crack Patterns Induced by Memory Effect of Drying Paste. In Andreas Schadschneider, Thorsten Pöschel, Reinhart Kühne, Michael Schreckenberg, and Dietrich E. Wolf, editors, *Traffic and Granular Flow'05*, pages 181–186. Springer Berlin Heidelberg, 2007.
- [Nob09] Park S. Nobel. *Physicochemical and Environmental Plant Physiology*. Elsevier Academic Press, 2009.
- [NSS+10] S. Nag, S. Sinha, S. Sadhukhan, T. Dutta, and S. Tarafdar. Crack patterns in desiccating clay-polymer mixtures with varying composition. *J. Phys.-Condens. Mat.*, 22:015402., 2010.
- [OGP05] Eiichi Obataya, Joseph Gril, and Patrick Perré. Shrinkage of cane (*arundo donax*) ii. effect of drying condition on the intensity of cell collapse. *Journal of Wood Science*, 51(2):130 – 135, 2005.
- [OGT04] Eiichi Obataya, Joseph Gril, and Bernard Thibaut. Shrinkage of cane (*Arundo donax*) I. Irregular shrinkage of green cane due to the collapse of parenchyma cells. *Journal of Wood Science*, 50:295–300, 2004. 10.1007/s10086-003-0578-y.
- [OKY07] Eiichi Obataya, Peter Kitin, and Hidefumi Yamauchi. Bending characteristics of bamboo (*Phyllostachys pubescens*) with respect to its fiber-foam composite structure. *Wood Sci Technol*, 41:385 – 400, 2007.
- [ON09] Yoshimi Ohmae and Takato Nakano. Water adsorption properties of bamboo in the longitudinal direction. *Wood Science and Technology*, 43:415–422, 2009. 10.1007/s00226-008-0225-2.
- [OWA06] Steffen Orso, Ulrike Wegst, and Eduard Arzt. The elastic modulus of spruce wood cell wall material measured by an in situ bending technique. *Journal of Materials Science*, 41:5122–5126, 2006. 10.1007/s10853-006-0072-1.

- [PB00] S. LEIGH PHOENIX and IRENE J. BEYERLEIN. *1.19 - Statistical Strength Theory for Fibrous Composite Materials*, pages 559 – 639. Pergamon, Oxford, 2000.
- [PC03] S. Pradhan and B. K. Chakrabarti. Failure properties of Fiber bundle models. *Int. J. Mod. Phys.*, 17:5565–5581, 2003.
- [PHC10] Srutarshi Pradhan, Alex Hansen, and Bikas K. Chakrabarti. Failure processes in elastic fiber bundles. *Rev. Mod. Phys.*, 82:499–555, Mar 2010.
- [PHH05] Srutarshi Pradhan, Alex Hansen, and Per C. Hemmer. Crossover Behavior in Burst Avalanches: Signature of Imminent Failure. *Phys. Rev. Lett.*, 95:125501, Sep 2005.
- [PHH06] Srutarshi Pradhan, Alex Hansen, and Per C. Hemmer. Crossover behavior in failure avalanches. *Phys. Rev. E*, 74(1):016122, Jul 2006.
- [PJKJ01] Mikael Perstorper, Marie Johansson, Robert Kliger, and Germund Johansson. Distortion of norway spruce timber part 1. variation of relevant wood properties. *European Journal of Wood and Wood Products*, 59:94–103, 2001. 10.1007/s001070050481.
- [PLZA09] Clara B. Picallo, Juan M. López, Stefano Zapperi, and Mikko J. Alava. Optimization and Plasticity in Disordered Media. *Phys. Rev. Lett.*, 103:225502, Nov 2009.
- [Pra02] M. Prat. Recent advances in pore-scale models for drying of porous media. *Chemical Engineering Journal*, 86(1-2):153 – 164, 2002.
- [PT02] P. Perré and I.W. Turner. A heterogeneous wood drying computational model that accounts for material property variation across growth rings. *Chemical Engineering Journal*, 86(162):117 – 131, 2002.
- [QRT05] Javier R. Quispe, Roberto E. Rozas, and Pedro G. Toledo. Permeabilityóporosity relationship from a geometrical model of shrinking and lattice Boltzmann and Monte Carlo simulations of flow in two-dimensional pore networks. *Chemical Engineering Journal*, 111(263):225 – 236, 2005.
- [RK89] John B. Rundle and W. Klein. Nonclassical nucleation and growth of cohesive tensile cracks. *Phys. Rev. Lett.*, 63:171–174, Jul 1989.
- [RKH08] Frank Raischel, Ferenc Kun, and Hans J. Herrmann. Continuous damage fiber bundle model for strongly disordered materials. *Physical Review E (Statistical, Non-linear, and Soft Matter Physics)*, 77(4):046102, 2008.
- [SA94] D. Stauffer and A. Aharony. *Introduction to Percolation Theory*. Taylor & Francis, London, second edition, 1994.

- [SA98] D. Sornette and J.V. Andersen. Scaling with respect to disorder in time-to-failure. *The European Physical Journal B - Condensed Matter and Complex Systems*, 1:353–357, 1998. 10.1007/s100510050194.
- [Sah94] M. Sahimi. *Applications of Percolation Theory*. Taylor & Francis, London, 1994.
- [SC03] R.M. Stallman and Gcc Developer Community. *Using GCC: the GNU compiler collection reference manual*. Free Software Foundation, 2003.
- [Sch97] James Schooley. *Introduction to Botany*. Delmar publishers, first edition, 1997.
- [SdBH04] Erwin Stein, René de Borst, and Thomas J.R. Hughes, editors. *Encyclopedia of Computational Mechanics*, volume 1, Fundamentals, pages 311–337. John Wiley And Sons, 2004.
- [SDM01] James P. Sethna, Karin A. Dahmen, and Christopher R. Myers. Crackling Noise. *Nature*, 410:242 – 250, 2001.
- [SDT11] Supti Sadhukhan, Tapati Dutta, and Sujata Tarafdar. Crack formation in composites through a spring model. *Physica A: Statistical Mechanics and its Applications*, 390(4):731 – 740, 2011.
- [Seg84] Larry J. Segerlind. *Applied Finite Element Analysis*. 1984.
- [SH06] George J. Simitzes and Dewey H. Hodges. *Fundamentals of Structural Stability*. Elsevier, 2006.
- [She96] Jonathan Richard Shewchuk. Triangle: Engineering a 2D Quality Mesh Generator and Delaunay Triangulator. In Ming C. Lin and Dinesh Manocha, editors, *Applied Computational Geometry: Towards Geometric Engineering*, volume 1148 of *Lecture Notes in Computer Science*, pages 203–222. Springer-Verlag, May 1996. From the First ACM Workshop on Applied Computational Geometry.
- [Sia84] Jhon F. Siau. *Transport Processes in Wood*. Springer Series in Wood Science. Springer - Verlag, 1984.
- [Skj88] A Skjeltorp. Fracture experiments on monolayers of microspheres. In H. E. Stanley and N. Ostrowsky, editors, *Random Fluctuations and Pattern Growth*. Kluwer, 1988.
- [SM88] A. T. Skjeltorp and Paul Meakin. Fracture in microsphere monolayers studied by experiment and computer simulation. *Nature*, 335:424 – 426, September 1988.
- [SMM⁺07] Supti Sadhukhan, Shashwati Roy Majumder, Dibyendu Mal, Tapati Dutta, and Sujata Tarafdar. Desiccation cracks on different substrates: simulation by a spring network model. *Journal of Physics: Condensed Matter*, 19(35):356206, 2007.

- [SMO09] Hiroki Sakagami, Junji Matsumura, and Kazuyuki Oda. In situ visualization of hardwood microcracks occurring during drying. *Journal of Wood Science*, 55:323–328, 2009. 10.1007/s10086-009-1041-5.
- [SMT08] V.K. Surasani, T. Metzger, and E. Tsotsas. Consideration of heat transfer in pore network modelling of convective drying. *International Journal of Heat and Mass Transfer*, 51(9 - 10):2506 – 2518, 2008.
- [Sor89] D Sornette. Elasticity and failure of a set of elements loaded in parallel. *Journal of Physics A: Mathematical and General*, 22(6):L243, 1989.
- [Sou07] Juan Soulié. C++ language tutorial. Online at <http://www.cplusplus.com/doc/tutorial/>, June 2007.
- [ST05] Luis A. Segura and Pedro G. Toledo. Pore-Level Modeling of Isothermal Drying of Pore Networks Accounting for Evaporation, Viscous Flow, and Shrinking. *Drying Technology*, 23(9-11):2007–2019, 2005.
- [Sta73] Alfred J. Stamm. Maximum effective lumen and pit pore sizes of the earlywood and the latewood of never dried loblolly pine sapwood. *Wood Science and Technology*, 7:212–217, 1973. 10.1007/BF00355551.
- [Sta87] H. Eugene Stanley. *Introduction to Phase Transitions and Critical Phenomena*. Oxford, 1987.
- [SWP06] Emílio Carlos Nelli Silva, Matthew C. Walters, and Glaucio H. Paulino. Modeling bamboo as a functionally graded material: lessons for the analysis of affordable materials. *Journal of Materials Science*, 41:6991–7004, 2006.
- [Tob07] *An introduction to computer simulation methods, applications to physical systems*. Pearson Education, 3rd. edition, 2007.
- [TP05] Renaud Toussaint and Steven R. Pride. Interacting damage models mapped onto ising and percolation models. *Phys. Rev. E*, 71(4):046127, Apr 2005.
- [TZ02] M.T. Tyree and M.H. Zimmermann. *Xylem structure and the ascent of sap*. Springer series in wood science. Springer, 2002.
- [VAH08] André P. Vieira, José S. Andrade, and Hans J. Herrmann. Subcritical Crack Growth: The Microscopic Origin of Paris’ Law. *Phys. Rev. Lett.*, 100:195503, May 2008.
- [Vél] Simón Vélez. Simón Vélez, the architectural league NY exposition.
- [vK11] T. von Kármán. Festigkeitsversuche unter alleseitgem druck. *Z. Ver. Dt. Ing*, 55:1749 – 1757, 1911.

- [VKLM11] Gabriel Villalobos, Ferenc Kun, Dorian L. Linero, and José D. Muñoz. Size distribution and waiting times for the avalanches of the Cell Network Model of Fracture. *Computer Physics Communications*, 182(9):1824 – 1827, 2011.
- [VKMn11] Gabriel Villalobos, Ferenc Kun, and José D. Muñoz. Effect of disorder on temporal fluctuations in drying-induced cracking. *Phys. Rev. E*, 84:041114, Oct 2011.
- [VLM11] Gabriel Villalobos, Dorian L. Linero, and José D. Muñoz. A statistical model of fracture for a 2D hexagonal mesh: The Cell Network Model of Fracture for the bamboo *Guadua angustifolia*. *Computer Physics Communications*, 182(1):188 – 191, 2011.
- [Wal06] John C.F. Walker. *Primary Wood Processing, Principles and Practice*. Springer, 2006.
- [WB07] Keith W. Waldron and Christopher T. Brett. *Plant Cell Separation and Adhesion*, chapter The role of polymer cross-linking in intercellular adhesion. Blackwell Publishing, 2007.
- [Wei51] Waloddi Weibull. A statistical distribution function of wide applicability. *ASME Journal of Applied Mechanics*, pages 293 – 297, 1951.
- [WG90] William Weaver and James M. Gere. *Matrix Analysis of Framed Structures*. Van Nostrand Reinhold, 3rd. edition, 1990.
- [Whi77] Stephen Whitaker. *Advances in heat transfer*, volume 13, chapter Simultaneous Heat, Mass, and Momentum Transfer in Porous Media: a Theory of Drying. Elsevier, 1977.
- [WKHK04] F. Wittel, F. Kun, H. J. Herrmann, and B. H. Kröplin. Fragmentation of Shells. *Phys. Rev. Lett.*, 93:035504, Jul 2004.
- [WW83] D Wilkinson and J F Willemsen. Invasion percolation: a new form of percolation theory. *Journal of Physics A: Mathematical and General*, 16(14):3365, 1983.
- [XDSW08] Lei Xu, Simon Davies, Andrew B. Schofield, and David A. Weitz. Dynamics of Drying in 3D Porous Media. *Phys. Rev. Lett.*, 101:094502, Aug 2008.
- [Xu10] Feng Xu. Structure, Ultrastructure, and Chemical Composition. In *Cereal Straw as a Resource for Sustainable Biomaterials and Biofuels*, pages 9 – 47. Elsevier, Amsterdam, 2010.
- [YFZY07] Yan Yu, Benhua Fei, Bo Zhang, and Xiang Yu. Cell-Wall Mechanical Properties of Bamboo Investigated by In-Situ Imaging Nanoindentation. *Wood and Fiber Science*, 39(4):527 – 535, October 2007.

- [YJHS08] H. Q. Yu, Z. H. Jiang, C. Y. Hse, and T. F. Shupe. Selected physical and mechanical properties of moso bamboo (*Phyllostachys pubescens*). *Journal of Tropical Forest Science*, 20(4):258–263, 2008.
- [Zim83] *Xylem Structure and the Ascent of Sap*. Springer-Verlag, 1983.
- [ZJLL09] Linhua Zou, Helena Jin, Wei-Yang Lu, and Xiaodong Li. Nanoscale structural and mechanical characterization of the cell wall of bamboo fibers. *Materials Science and Engineering: C*, 29(4):1375 – 1379, 2009.
- [ZRSV97] Stefano Zapperi, Purusattam Ray, H. Eugene Stanley, and Alessandro Vespignani. First-Order Transition in the Breakdown of Disordered Media. *Phys. Rev. Lett.*, 78:1408–1411, Feb 1997.
- [ZRSV99a] Stefano Zapperi, Purusattam Ray, H. Eugene Stanley, and Alessandro Vespignani. Avalanches in breakdown and fracture processes. *Phys. Rev. E*, 59:5049–5057, May 1999.
- [ZRSV99b] Stefano Zapperi, Purusattam Ray, H. Eugene Stanley, and Alessandro Vespignani. Analysis of damage clusters in fracture processes. *Physica A: Statistical Mechanics and its Applications*, 270(1 - 2):57 – 62, 1999.
- [ZTTZ05] O.C. Zienkiewicz, R.L. Taylor, R.L. Taylor, and J.Z. Zhu. *The finite element method: its basis and fundamentals*. The Finite Element Method. Elsevier Butterworth-Heinemann, 2005.

Appendix A

Numerical constants

Name	Value	source
\bar{V}_w (dilute solution)	$18 \times 10^{-6} m^3 mol^{-1}$	[Nob09]
$\sum c_i$ (active partcl. plant)	$0.3 mol$	[Nob09]
Vacuole Volume ^a	$\approx 90\%$ of cell or $4 \times 10^4 \mu m^3$	[Nob09]
Y (dry cotton fibers)	$10^4 MPa$	[Nob09]
ϵ (volum. elast. modul) ^b	1 to 50 MPa	[Nob09]
ΔP_{max} (tonoplast) ^c	$0.5 \times 10^{-3} MPa$	[Nob09]
Re (reynolds in plants) ^d	10^{-3}	
γ_w (water surface tension) ^e	$73 mN/m$	[GBWQ04]
R (gas constant)	$8.314472(15) JK^{-1} mol^{-1}$	[MTN08]
v_{xylem} (speed of sap in xylem)	$\approx 10 cm/s$	[Zim83]
$1D$ (Darcy)	$\approx 10^{-9} cm^2$ ^f	
E (Elastic Modulus Spruce Cell Wall)	$\approx 28 GPa$	[OWA06]
Hardness Fiber Cell wall(GPa)	0.44 ± 0.09	[ZJLL09]
Hardness Parenchyma Cell wall(GPa)	0.43 ± 0.22	[ZJLL09]

^amesophyll cells in leaves

^bIs reported as that for a complete cell, means changes of 0.2 to 10% for each atmosphere of pressure (0.1 MPa) applied.

^cRoughly $\Delta P = \frac{2t\sigma}{r}$

^dUsing, $v \approx 1 cm/s$, $L \approx 10 \mu m$, $\eta_w = 10^{-1} kg/(ms)$, $\rho_w = 1000 kg/m^3$, and $R = \frac{\rho v L}{\eta}$

^eAt 20° C

^f $\frac{1 cm^3 \cdot dot 1 mPa \cdot s \cdot 1 atm}{1 s \cdot 1 cm^2 \cdot 1 atm / cm \cdot 101325 Pa}$

Name	Value	source
Elastic Modulus Fiber Cell wall(<i>GPa</i>)	10.4 ± 1.8	[ZJLL09]
Elastic Modulus Parenchyma Cell wall(<i>GPa</i>)	3.4 ± 1.3	[ZJLL09]
Longitudinal Elastic Modulus Fiber Cell wall Bamboo(<i>GPa</i>)	16.1 ± 1.8	[YFZY07]
Transverse Elastic Modulus Fiber Cell wall Bamboo(<i>GPa</i>)	5.91 ± 1.8	[YFZY07]
Longitudinal Elastic Modulus Parenchyma Cell wall Bamboo (<i>GPa</i>)	5.8 ± 1.3	[YFZY07]
Transverse Elastic Modulus Parenchyma Cell wall Bamboo(<i>GPa</i>)	0.23 ± 1.8	[YFZY07]
Pit size (μm) latewood	0.8 [Sta73]	
Pit size (μm) earlywood	0.28 [Sta73]	

For Hooke's constant, if one takes the distances in micrometers and the forces in meganewtons, then the change of variables is $x = y_0 y$ and $k = \kappa k_0$. Where $k_0 = 10^6$ $y_0 = 10^{-6}$. Then,

$$F(N) = -\kappa k_0 y_0 y \quad (A.1)$$

$$F(N)/k_0 y_0 = F(N) = -\kappa y \quad (A.2)$$

The units of force are Newtons.

For the surface tension,

$$F = N_p \cdot A \cdot \frac{\gamma}{R} \quad (A.3)$$

where

- N_p : Number of pores
- A : Area of Wall
- γ : Water-air surface tension
- R : Pit size

Then, as $A = l^2 * 4 * \pi$, $\gamma \approx 70 \cdot 10^{-3} N/m$ taking $N_p = 10$, and redefining γ , one has:

$$F_\gamma \approx 70 \frac{10^{-3} N}{m} \cdot 100 \cdot 12 \cdot \frac{l^2}{R} \quad (A.4)$$

$$F_\gamma \approx \gamma' \cdot \frac{l^2}{R} \quad (A.5)$$

For l and R in μm ,

$$\gamma' = 70 \cdot 10^{-3} \cdot 100 \cdot 12 \cdot 10^{-6} \frac{N}{m} \quad (\text{A.6})$$

$$\gamma' = 84 \cdot 10^{-6} \frac{N}{m} \quad (\text{A.7})$$

Similarly, the hydrostatic pressure is given by:

$$F_b = \rho \cdot g \cdot h \cdot A \quad (\text{A.8})$$

Where $\rho = 10^3 \text{ kg/m}$, $g \approx 10 \text{ m/s}^2$ and $h \approx 10 \text{ m}$ for bamboo. The area is again of the order of $L^2 = l^2 \cdot 10^{-12}$, with l in μm . Then :

$$F_b \approx 10^3 \cdot l \cdot 10^{-12} \cdot 10 \approx l^2 \cdot 10^{-8} \text{ N} \quad (\text{A.9})$$

Publications

The following is the list of posters, talks and publications derived from this work, published up to the date of writing this thesis.

1. “A statistical model of fracture for a 2D hexagonal mesh: the cell network model of the bamboo *Guadua Angustifolia*“. Poster, CCP2009 Taiwan. [Fig. B.1].
2. “A statistical model of fracture for a 2D hexagonal mesh: the cell network model of the bamboo *Guadua Angustifolia*“. Article, Computer Physics communications, [VLM11].
3. “Size distribution and waiting times for the avalanches of the Cell Network Model of Fracture“. Article, Computer Physics Communications [VKLM11].
4. “Size distribution and waiting times for the avalanches of the Cell Network Model of Fracture“. Talk, CCP2010 Norway. [Fig. B.2]
5. “Avalanche distributions in an inhomogeneous cell network model of fracture“. Poster, STATPHYS24, Australia. [Fig. B.3]
6. “Effect of disorder on temporal fluctuations in drying-induced cracking“. Article, Physical Review E. [VKMn11]
7. “A Statistical model of fracture applicable to the drying of the Bamboo *Guadua Angustifolia*. Poster, School and Conference on Mathematics and Physics of Soft and Biological Matter, Italy, 2011 [Fig. B.6].
8. “Statistical models of Fracture inspired in drying of Bamboo *Guana angustifolia*“. Talk. Seminar Computational Physics for Engineering Materials, Switzerland.

A Statistical Model of Fracture for a 2D Hexagonal Mesh: the Cell Network Model of the Bamboo *Guadua angustifolia*

Villalobos G., Linero D.L., and Muñoz J.D.

gvillalobosc@bt.unal.edu.co, Simulation of Physical Systems Group, CEIBA Complejidad, Physics Department, Universidad Nacional de Colombia and Grupo de Análisis, Diseño y Materiales, Department of Civil Engineering, Universidad Nacional de Colombia

ABSTRACT
Introduction and Background:

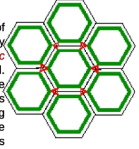
Guadua angustifolia is a Colombian Bamboo widely used for construction and handicrafts. It optimizes longitudinal stress and bends elastically. Longitudinal cracks may appear due to drying induced shrinkage [Mon.]

Statistical Models of Fracture characterize failure by statistics of individual breakings [Kun, Kun05]. The elements follow a constitutive relationship and damage law. The phase transition critical point and exponents are determined by the damage law and the geometry of the connecting elements.

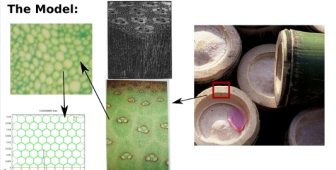
Methods: The parenchyma tissue of *guadua* is modeled as a regular array of hexagonal cells. Cell walls are joined by rotational springs to conform the cell. Elastic junctures join the cells. Boundaries are fixed. The stresses are computed by FEM. The evolution consists in shrinking the cell walls until a juncture reaches a fixed breaking threshold, changing the elastic matrix. The Young modulus of cell walls and junctures are chosen at random between some intervals. The statistics of cracks of junctures is recorded.

Results: The system seems to exhibit a phase transition at a critical breaking threshold. At that point, the avalanche sizes distribute as a power law with exponent of $-2.93(8)$.

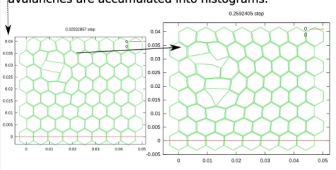
Conclusion: An statistical model of fracture for a 2D system resembling the structure of the parenchyma tissue of the bamboo *Guadua angustifolia* has been constructed. The system seems to exhibit a phase transition at a critical fracture threshold. This model may give insights on the drying induced fractures of this bamboo.



The Model:

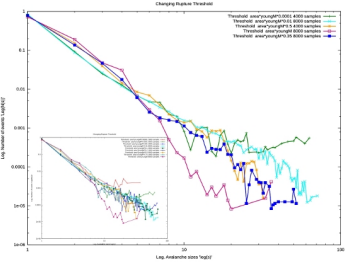


Drying will shrink the cell walls, generating a stress field over the whole structure. Individual junctures fail at a fixed threshold, while the cell walls remain intact. A break may cause avalanches of different sizes, until the system does not brake anymore. This procedure is repeated thousands of times and the sizes of all avalanches are accumulated into histograms.



Results and conclusions:

The size distribution of avalanches changes with the breaking threshold, which can be taken as the control parameter. At breaking thresholds around $0.35 \text{ Young} \cdot \text{Area}$, the avalanches distribute like a power law, with an exponent of $-2.93(8)$.



Above and below this value, the distribution deviates from the power law. Further simulations with larger systems should be run in order to establish if this exponent differs of the value of $5/2$ of the literature.

Funding

This work has been partially funded by the project Micromechanical and Macromechanical Models of Granular Media and Composite Materials, CEIBA complejidad and by Colciencias, Departamento Administrativo de Ciencia, Tecnología e Innovación.

Bibliography:

[Kun] Transition from damage to fragmentation in collision of solids. Phys. Rev. E 59, 2623 - 2632. (1999).

[Kun05] Extension of fiber bundle models for creep rupture and interface failure. Int. Journ. of Fract. 140 1- 4. July 2006.

[Mon] Jorge Augusto Montoya Arango. Trocknungsverfahren furr die Bambusart *Guadua angustifolia* unter tropischen Bedingungen. PhD thesis, Universitat Hamburg, 2006.

[Seg] Segerlind, L. Applied Finite Element Analysis. Jhon Wiley and Sons, 1984.

[GSL] M. Galassi et al, GNU scientific Library Reference Manual (3rd Ed.) ISBN 0954612078

[Lie98] Walter Liese. The Anatomy of Bamboo Culms. 1998. ISBN 81-86247-26-2.




Figure B.1: Poster, presented at the 2009 Conference on Computational Physics, Taiwan

CCP 2010
 CONFERENCE ON COMPUTATIONAL PHYSICS
 23RD - 26TH OF JUNE 2010 - TRONDHEIM, NORWAY

NTNU

Power law behaviour of the size distribution of avalanches in the Cell Network Model of Fracture

Gabriel VILLALOBOS, Ferenc KUN, José Daniel MUÑOZ, Dorian L. LINERO
 Universidad Nacional de Colombia
 Debrecen University



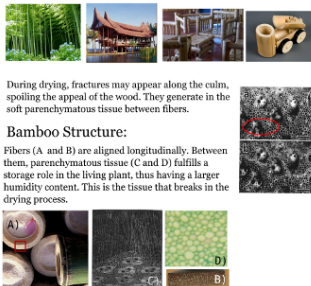
Figure B.2: Talk, presented at the 2010 Conference on Computational Physics, Norway

Avalanche distributions in an inhomogeneous cell network model of fracture

Gabriel VILLALOBOS, Ferenc KUN, Dorian L. LINERO, José D. MUÑOZ

*Simulation of Physical Systems Group, CEIBA - Compijélab, Department of Physics, National University of Colombia - Bogotá, Colombia; Research Group on Structures and Materials, Department of Civil and Agricultural Engineering, National University of Colombia - Bogotá, Colombia; Department of Theoretical Physics, University of Debrecen - Debrecen, Hungary

Introduction:
Guadua crantziifolia is an Andean Bamboo used throughout Colombia for: house building, furniture and handicrafts. *Guadua* structure is optimized to withhold stresses along its axis and bend elastically perpendicular to it.



Bamboo Structure:
 Fibers (A and B) are aligned longitudinally. Between them, parenchymatous tissue (C and D) fulfills a storage role in the living plant, thus having a larger humidity content. This is the tissue that breaks in the drying process.

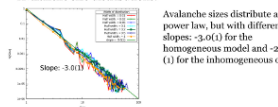
The Model:
 Cell walls and junctures are modeled by plane frame elements within an FEM model. Cell are built up by beams connected by angular springs, and do not break. Junctures are little springs, allowed to break. The cell walls at the border are fixed, they are not allowed to move. The drying process starts by thickening all the cell walls by a uniform rate, until a first juncture breaks. This breaking can generate an avalanche. The shrinking continues until a new avalanche occurs.

Homogeneous Model
 The geometry of the homogeneous model consists in an uniform array of hexagonal cells. The Young modulus is the same for all junctures, and all cell walls, but the breaking thresholds of the junctures is randomly distributed.

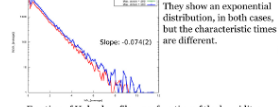
Inhomogeneous Model
 A Voronoi point is randomly chosen inside every cell of an hexagonal array, and then a Voronoi construction is generated for the cells. The randomized geometry resembles the parenchymatous tissue. Disorder is introduced by the geometry; therefore both Young modulus and breaking thresholds are homogeneous.

Main Results: Homogeneous vs Inhomogeneous

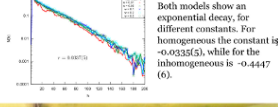
Avalanche size distributions:
 Avalanche sizes distribute as a power law, but with different slopes: $-3.0(1)$ for the homogeneous model and $-2.5(1)$ for the inhomogeneous one.



Humidity decrement among breakings (analogous to waiting times):
 They show an exponential distribution, in both cases, but the characteristic times are different.



Fraction of Unbroken fibers as function of the humidity:
 Both models show an exponential decay, for different constants. For homogeneous the constant is $-0.0335(5)$, while for the inhomogeneous is $-0.4447(6)$.



Conclusions:
 Despite the fact that both models show similar behaviors, they exhibit different exponents and characteristic times, suggesting different universality classes.

Bibliography
 (1) G. Villalobos et al., A statistical model of fracture for a 2D hexagonal mesh. The Cell Network Model of Fracture for the bamboo *Guadua crantziifolia*, *Computer Physics Communications* (2010), doi:10.1016/j.cpc.2010.06.015 (and references therein)

Acknowledgments
 We thank CEIBA - Compijélab, Colciencias and Faculty of Sciences of National University of Colombia for financial support. We also thank Professor András Mészáros (Technological and Pedagogical University of Pereira) and Professor Csaba Tóth (National University of Colombia) for very enlightening discussions and bibliography.




Figure B.3: Poster, presented at the 2010 iupap conference on statistical mechanics STATPHYS24, Australia



Contents lists available at ScienceDirect

Computer Physics Communications

www.elsevier.com/locate/cpc



A statistical model of fracture for a 2D hexagonal mesh: The Cell Network Model of Fracture for the bamboo *Guadua angustifolia*

Gabriel Villalobos^{a,*}, Dorian L. Linero^b, José D. Muñoz^a

^a CeiBA – Complejidad, and Simulation of Physical Systems Group, Department of Physics, Universidad Nacional de Colombia – Bogotá, Crr 30 # 45-03, Ed. 404, Of. 348, Bogota, Colombia
^b Analysis, Design and Materials Group, Department of Civil Engineering, Universidad Nacional de Colombia – Bogotá, Crr 30 # 45-03, Ed. 406 IEL, Of. 301, Colombia

ARTICLE INFO

Article history:

Received 15 February 2010

Accepted 12 June 2010

Available online xxxxx

Keywords:

Statistical models of fracture

Finite Element Method

Computational mechanics of solids

ABSTRACT

A 2D, hexagonal in geometry, statistical model of fracture is proposed. The model is based on the drying fracture process of the bamboo *Guadua angustifolia*. A network of flexible cells are joined by brittle junctures of fixed Young moduli that break at a certain thresholds in tensile force. The system is solved by means of the Finite Element Method (FEM). The distribution of avalanche breakings exhibits a power law with exponent $-2.93(9)$, in agreement with the random fuse model (Bhattacharyya and Chakrabarti, 2006) [1].

© 2010 Elsevier B.V. All rights reserved.

1. Introduction

Guadua angustifolia is an Andean Bamboo that is widely used both as a construction material, for structural frames and walls [2], and as raw material for handicrafts, furniture and vessels, throughout Colombia [3,4]. Moreover, *Guadua* forests play a crucial ecological role, fostering native species, helping to regulate the water cycle, consuming CO₂, and injecting water into the soil. Nowadays, it is having a revival as construction material for building houses, [5], due to recent advances in research about bamboo structural properties and behavior [6] as well as structural laminated bamboo [7].

Guadua structure is optimized to withhold stresses along its axis, with a high Young modulus in this direction, and to bend elastically for deformations perpendicular to it, as all bamboos do. To achieve this performance, all fibers are oriented along the culm axis, more of them being nearer the outer radius than the inner one [8]. Thus, cracks appear mostly along the axis as a consequence of the drying process, due to the avalanche of parenchyma cells collapse.

The statistical models of fracture (SMF) describe macroscopic cracks by following the failure of individual elements [9]. An SMF can be tracked by means of computer simulations, which can exhaustively explore the statistical properties of the model. For instance, fiber bundle models are 1D analytically solvable SMFs describing the degradation and failure of materials [10–14]. Furthermore, fracture models have also used to investigate the fractal nature of the cracks [15,16], the size distribution on impact

fragmentation [17] and the hydraulic fracture as used on the oil industry [18]. All these models consist on individual elements interacting by some known force with their neighbors, where the breaking of a single element redistributes the load on the surrounding ones, causing an avalanche of breaks. Many of them exhibit a phase transition that shows itself in a power-law distribution of these avalanches [17,19,20,13]. On the other side, the finite element method has been successfully implemented in the field of computational failure mechanics to study discontinuities and failure [21–23].

In the present work we propose a 2D statistical model of fracture, inspired in the geometry and the mechanical processes of fracture of an Andean Bamboo, *Guadua angustifolia*. This model is explained in Section 2, and resembles the geometry of the *dry foam* models [24], but with key differences: the rule for breaking a juncture here is not random but chosen from the internal forces on the system, the individual hexagonal cells do not share walls and there is no coalescence of neighboring cells. As in other SMF models, the breaking of a single juncture redistributes the stress on the surrounding ones; but here it is done not by following a simple rule but by computing the new equilibrium state of the whole system. Actually, we use the Finite Element Method (FEM) to model the cell walls and junctures and compute such equilibrium state. All cells are similar in shape, but breaking thresholds are chosen at random. We explore the distribution of avalanches and found that this model exhibits a power-law behavior (an indication of a phase transition), as other SMF models do.

2. *Guadua* structure and model

Bamboo culms have two main structures (see Fig. 1): flexible parenchymatous tissue and stiff fiber bundles surrounding the

* Corresponding author.

E-mail address: gvillalobosc@bt.unal.edu.co (G. Villalobos).

0010-4655/\$ – see front matter © 2010 Elsevier B.V. All rights reserved.

doi:10.1016/j.cpc.2010.06.015

Please cite this article in press as: G. Villalobos et al., A statistical model of fracture for a 2D hexagonal mesh: The Cell Network Model of Fracture for the bamboo *Guadua angustifolia*, Computer Physics Communications (2010), doi:10.1016/j.cpc.2010.06.015



Size distribution and waiting times for the avalanches of the Cell Network Model of Fracture

Gabriel Villalobos^{a,*}, Ferenc Kun^c, Dorian L. Linero^b, José D. Muñoz^a

^a Simulation of Physical Systems Group, CeIBA-Complejidad, Department of Physics, Universidad Nacional de Colombia, Crr 30 # 45-03, Ed. 404, Of. 348, Bogotá D.C., Colombia

^b Analysis, Design and Materials Group, Department of Civil and Environmental Engineering, Universidad Nacional de Colombia, Crr 30 # 45-03, Ed. 404, Of. 348, Bogotá D.C., Colombia

^c Department of Theoretical Physics, University of Debrecen, P.O. Box 5, H-4010 Debrecen, Hungary

ARTICLE INFO

Article history:

Received 3 August 2010

Received in revised form 27 October 2010

Accepted 28 October 2010

Available online 3 November 2010

Keywords:

Statistical models of fracture

Finite Element Method

Computational mechanics of solids

ABSTRACT

The Cell Network Model is a fracture model recently introduced that resembles the microscopical structure and drying process of the parenchymatous tissue of the Bamboo *Guadua angustifolia*. The model exhibits a power-law distribution of avalanche sizes, with exponent -3.0 when the breaking thresholds are randomly distributed with uniform probability density. Hereby we show that the same exponent also holds when the breaking thresholds obey a broad set of Weibull distributions, and that the humidity decrements between successive avalanches (the equivalent to waiting times for this model) follow in all cases an exponential distribution. Moreover, the fraction of remaining junctures shows an exponential decay in time. In addition, introducing partial breakings and cumulative damages induces a crossover behavior between two power-laws in the histogram of avalanche sizes. This results support the idea that the Cell Network Model may be in the same universality class as the Random Fuse Model.

© 2010 Elsevier B.V. All rights reserved.

1. Introduction

The Cell Network Model of Fracture (CNMF [1]), is a two-dimensional statistical model of fracture [2] inspired in the stress field caused by drying of the bamboo *Guadua angustifolia* [3,4]. At the parenchymatous tissue level, bamboos shrink during drying, causing the detaching of neighboring cells and the appearance of fractures. The CNMF models this tissue as a hexagonal array of cell elements (each of them made of six plane frame elements), fixed by rotational springs and joined by brittle springs called the junctures (Fig. 1). Shrinking forces – due to drying – acting along the elements distort the structure and cause breaking avalanches of the junctures among cells.

Interestingly enough, when a homogeneous distribution of breaking thresholds of junctures and fixed Young's moduli are used, the histogram of avalanche sizes of the CNMF shows power law behavior with an exponent of $-2.93(8)$ [1]. This is by all means equal to avalanche size distribution of the random fuse model, which shows a power law with exponent of -3 [5,6]. The analytical solution of both models has been elusive.

Global load sharing fiber bundle systems have provided models for the thoroughly study of critical phenomena. Universality, the effect of damage and the critical exponents have been found analytically (see [7,8] and references therein). Moreover, the random

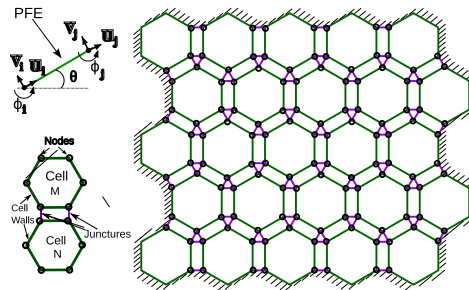


Fig. 1. Cell Network Model of Fracture (CNMF). Upper left. The plane frame element spanning between the nodes i and j , oriented by an angle θ . Each node has two translational and one rotational degrees of freedom. Lower left. Two contiguous cells. Right. Structure of the CNMF. The hexagons represent the cells and the junctures are arranged into triangles. Hashing denotes fixed boundary conditions. From [1], not at scale.

fuse model has allowed to investigate the fracture properties of biological materials, as in the case of brittle nacre, [9], describing the toughness of the material by its microscopical architecture. Beam models similar to the CNMF have also been used to model fracture in concrete [10].

In the present paper, to characterize the path to global failure, we study both the distribution of humidity decrement among con-

* Corresponding author.

E-mail address: gvillalobosc@bt.unal.edu.co (G. Villalobos).



A statistical model of fracture applicable to the drying of the Bamboo *Guadua Angustifolia*

Gabriel VILLALOBOS¹, Ferenc KUN², Dorian L. LINERO³, José D. MUÑOZ¹

¹ Simulation of Physical Systems Group, CoEBA - Compihedral, Department of Physics, National University of Colombia - Bogotá, Colombia. Research group on Structures and Materials.
² Department of Civil and Agricultural Engineering, National University of Colombia - Bogotá, Colombia.
³ Department of Theoretical Physics, University of Debrecen - Debrecen, Hungary



Introduction:

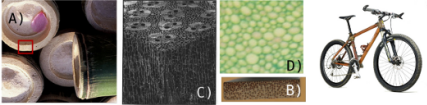
Guadua antustifolia is an Andean Bamboo used throughout Colombia for house building, furniture, and handicrafts. *Guadua* structure is optimized to withstand stresses along its axis and bend elastically perpendicular to it.



During drying, fractures may appear along the culm, spoiling the appeal of the wood. They generate in the soft parenchymatous tissue between fibers.

Bamboo Structure:

Fibers (A and B) are aligned longitudinally. Between them, parenchymatous tissue (C and D) fulfills a storage role in the living plant, thus having a larger humidity content. This is the tissue that breaks in the drying process.

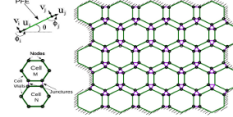


The Model:

Cell walls and **junctures** are modeled by plane frame elements within an FEM model. Cell are build up by beams connected by angular springs, and do not break. Junctures are breakable brittle springs, allowed to break. The cell walls at the border are fixed. The drying process starts by shrinking all the cell walls at a uniform rate, until a first juncture breaks. This breaking can generate an avalanche. The shrinking continues until a new avalanche occurs.

Homogeneous Model

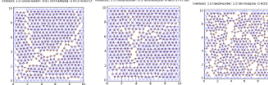
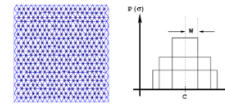
The geometry of the homogeneous model consists in a uniform array of hexagonal cells. The Young modulus is the same for all junctures, and all cell walls, but the breaking thresholds of the junctures are randomly distributed.



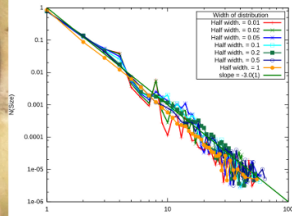
Lattice Model

A drying model is discretized in a framework of a triangular lattice with slightly disordered arrangement. The nodes correspond to point masses and the bonds between them provide cohesive forces. The mass of the nodes is proportional to the area of the several dual lattices associated with it. The bonds are linear springs where the spring constant is determined as kE/A , with k the natural length. If the young modulus is A and the cross section, the degree of deterioration is characterized by a shrinkage parameter, ξ . The equation of motion of the nodes is:

$$m_i^2 \ddot{x}_i = F_i - \sigma_i, \text{ the presence of disorder causes that the breakup process proceeds in bursts. Both this temporal fluctuations are strongly affected by the degree of disorder in the system.}$$



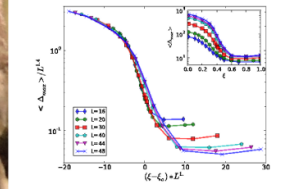
Main Results:



Avalanche size distributions:

Avalanche sizes distribute as a power law, $s^{-3.0}$ for the homogeneous model and $s^{-2.5}$ for the lattice model.

Average of the largest avalanche and average avalanche size.



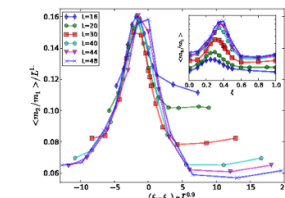
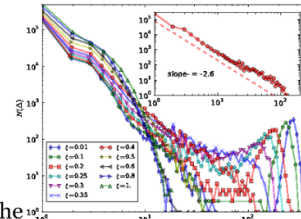
$$\langle \Delta_{max} \rangle(L, \xi) = L^{\beta/\nu} f((\xi - \xi_c) L^{1/\nu}),$$

$$\beta/\nu = 1.4 \text{ and } 1/\nu = 1$$

$$\langle \Delta \rangle(L, \xi) = L^{\gamma/\nu} g((\xi - \xi_c) L^{1/\nu}),$$

$$\gamma/\nu = 1, \text{ and } 1/\nu = 0.9.$$

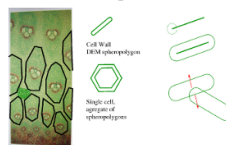
$$\langle \Delta \rangle = \left\langle \frac{m_2}{m_1} \right\rangle, \quad m_k = \sum_{i=1}^K \Delta^i - \Delta_{max}^k.$$



Concluding remarks:

Phase transitions between brittle and slow damage controlled by disorder. For the experimentalist of drying: characterize the disorder of the material. Future work: characterize the free water removal.

Under development:



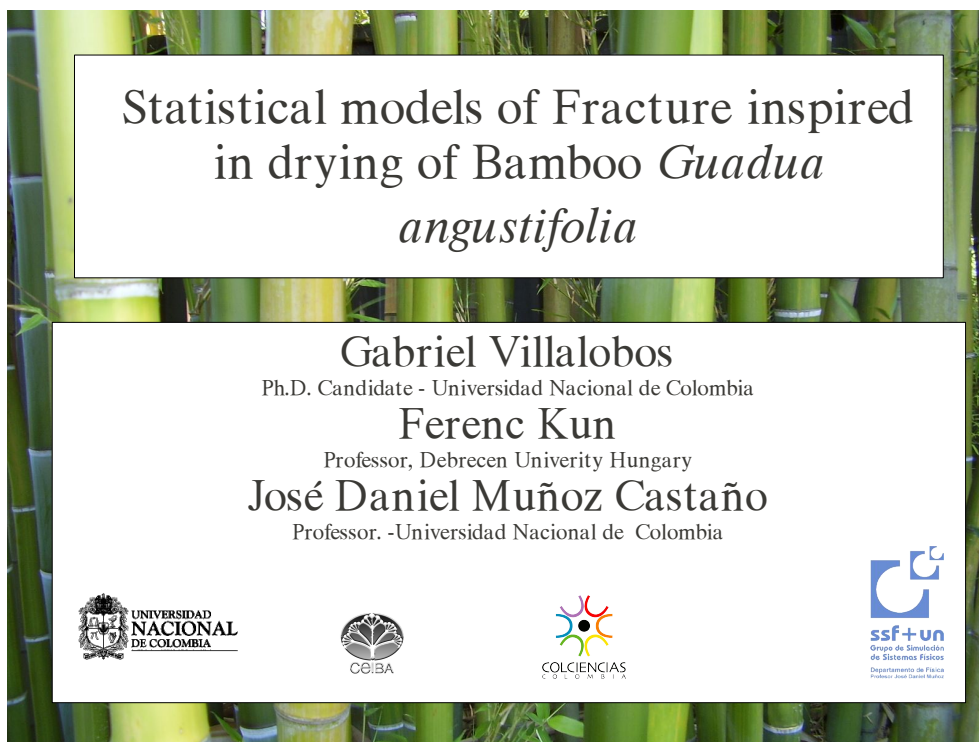
Bibliography

[1] G. Villalobos et al., A statistical model of fracture for a 2d hexagonal mesh: The Cell Network Model of Fracture for the bamboo *Guadua angustifolia*, Computer Physics Communications (2010), doi:10.1016/j.cpc.2010.06.015 (and references therein)

Acknowledgments

We thank CoEBA - Compihedral, Colciencias and Faculty of Sciences of National University of Colombia for financial support. We also thank Professor. Augusto Montoya (Technological and Pedagogical University of Pereira) and Professor. Csorj Takacs (National University of Colombia) for very enlightening discussions and bibliography.

Figure B.6: Poster, presented at School and Conference on Mathematics and Physics of Soft and Biological Matter The Abdus Salam International Centre for Theoretical Physics - ICTP, Trieste, Italy 2 - 13 May 2011



Statistical models of Fracture inspired
in drying of Bamboo *Guadua*
angustifolia

Gabriel Villalobos
Ph.D. Candidate - Universidad Nacional de Colombia

Ferenc Kun
Professor, Debrecen University Hungary

José Daniel Muñoz Castaño
Professor. -Universidad Nacional de Colombia







Figure B.7: Talk, presented at the Seminar Computational Physics for Engineering Materials, Zurich Switzerland, April 2011.

Effect of disorder on temporal fluctuations in drying-induced crackingGabriel Villalobos,^{1,2,*} Ferenc Kun,^{3,4,†} and José D. Muñoz^{1,2,‡}¹Grupo de Simulación de Sistemas Físicos, Departamento de Física, Universidad Nacional de Colombia, Carrera 30 45-03, Ed. 404, Of. 348, Bogota D.C., Colombia²CeiBA-Complejidad, Carrera 19A 1-37, Este Of., C222 Bogota, Colombia³Department of Theoretical Physics, University of Debrecen, H-4010 Debrecen, P.O. Box 5, Hungary⁴Institute of Nuclear Research (ATOMKI), H-4001 Debrecen, Pf.51, Hungary

(Received 1 July 2011; published 11 October 2011)

We investigate by means of computer simulations the effect of structural disorder on the statistics of cracking for a thin layer of material under uniform and isotropic drying. For this purpose, the layer is discretized into a triangular lattice of springs with a slightly randomized arrangement. The drying process is captured by reducing the natural length of all springs by the same factor, and the amount of quenched disorder is controlled by varying the width ξ of the distribution of the random breaking thresholds for the springs. Once a spring breaks, the redistribution of the load may trigger an avalanche of breaks, not necessarily as part of the same crack. Our computer simulations revealed that the system exhibits a phase transition with the amount of disorder as control parameter: at low disorders, the breaking process is dominated by a macroscopic crack at the beginning, and the size distribution of the subsequent breaking avalanches shows an exponential form. At high disorders, the fracturing proceeds in small-sized avalanches with an exponential distribution, generating a large number of microcracks, which eventually merge and break the layer. Between both phases, a sharp transition occurs at a critical amount of disorder $\xi_c = 0.40 \pm 0.01$, where the avalanche size distribution becomes a power law with exponent $\tau = 2.6 \pm 0.08$, in agreement with the mean-field value $\tau = 5/2$ of the fiber bundle model. Moreover, good quality data collapses from the finite-size scaling analysis show that the average value of the largest burst $\langle \Delta_{\max} \rangle$ can be identified as the order parameter, with $\beta/\nu = 1.4$ and $1/\nu \simeq 1.0$, and that the average ratio $\langle m_2/m_1 \rangle$ of the second m_2 and first moments m_1 of the avalanche size distribution shows similar behavior to the susceptibility of a continuous transition, with $\gamma/\nu = 1$, $1/\nu \simeq 0.9$. These results suggest that the disorder-induced transition of the breakup of thin layers is analogous to a continuous phase transition.

DOI: 10.1103/PhysRevE.84.041114

PACS number(s): 64.60.av, 46.50.+a, 02.50.-r

I. INTRODUCTION

Desiccation-induced cracking of a thin layer of materials is an interesting scientific problem with a broad spectrum of technological applications. Painted surfaces, thin wood layers, antireflective and UV-protecting coatings on glasses, and thin-film manufacturing processes such as chemical-bath and sol-gel depositions are just a few of a large set of examples where desiccation-induced cracks might be avoided. In contrast with fractures induced by collisions or tensile stresses, drying of a thin-layer material is a homogeneous and isotropic process occurring everywhere inside the layer, the statistical behavior of which could be different from those previously studied cases.

During the past decades, experiments have revealed that the competition of crack formation inside the layer with the delamination from the substrate leads to a gradual breakup into pieces of polygonal shapes, the characteristic length scale of which is determined by the layer's thickness. Recently, Nakahara and Matsuo addressed the possibility of controlling the structure and time evolution of crack patterns in pastes, i.e., dense colloidal suspensions, by subjecting the paste to vibration or flow before the onset of drying [1–3]. Detailed

experiments showed that those mechanical excitations induce structural rearrangements and plastic deformations getting imprinted onto the patterns of the drying crack network. A large number of experiments have been performed to understand the microscopic mechanism leading to this memory effect. They conclude that the interaction (attractive or repulsive) among the colloidal particles and the amount of disorder (shape regularity) govern the pattern formation [4]. A very interesting effect of the amount of disorder has recently been pointed out in other types of fracture processes as well. Fiber bundle models with equal load sharing exhibit a power-law distribution of the bursts' sizes [5–8]. Mixing fibers with widely different breaking strengths reveals a phase transition between two regimes with different power-law exponents of the bursts' distribution. The transition takes place at a well defined system composition, and it has shown to be analogous to a continuous phase transition [9].

In this paper, we focus on the effect of the amount of quenched disorder on the process of gradual breakup induced by desiccation, motivated by the works of Nakahara and Matsuo [1–3] and Kitsunezaki [10]. The thin layer of paste is discretized into a regular triangular lattice of springs with fixed ends at the boundary. Drying is captured by gradually decreasing the natural length of all springs, inducing unbalanced forces and leading to the final breaking of some bonds. The quenched disorder of the material is represented by a random distribution of the bonds' breaking thresholds, and the amount of disorder is given by the distribution's width. There are

*gvillalobosc@bt.unal.edu.co

†feri@ntp.atomki.hu

‡jdmunozc@unal.edu.co

Index

- algorithm
 - verlet, 91
- apoplasm, 34
- Arundo donax, 22
- avalanche
 - probability distribution of, 116
 - average size as function of time, 116
 - dynamics, 116
 - size, 115
- bamboo
 - cortex, 30
 - culm, 30
 - isotherm curves, 46
- Bambusa vulgaris, 35
- beam models, 79
- boundary conditions, 125
- brittle, 58
- capillary
 - pumping, 103
- capillary induced fractures, 157
- cell wall, 38
- clusters, 112
 - filled cells, 108
- coalescence phase, 159
- Cohesion - Tension, 33
- collapse, 22, 35, 53
- concentration gradient, 49
- correlation length, 69
- crack
 - initiation, 62
 - intensity factor, 82
- cracks, 115, 138
- critical
 - exponent β , 69
- critical phenomena, 64, 69
- critical point, 64
- critical value, 74
 - p_c , 68
- Damage mechanics, 78
- dilation, 93
- discrete element methods, 89
- Discrete Element Method, 88
- discrete element method, 161
 - event driven, 91
 - time driven, 91
- discrete element model, 107
- discretization, 23
- disorder
 - quenched, 24
- displacement field, 58
- distribution rule, 23
- drying
 - dynamics, 52
 - front, 108, 110
 - speed, 150
- ductile, 58
- Equilibrium moisture content, 42
- erosion, 93

extreme statistics, 63
 failure condition, 62
 failure law, 23
 failure surface, 62
 fiber saturation point, 46
 Fiber Saturation Point(FSP), 42
 Finite Element Method, 88
 finite element method, 97
 finite size scaling, 70
 fractal, 161
 fractal dimension, 110
 fracture, 61
 Fracture process zone, 62
 fractures
 drying induced, 55
 shrinkage induced, 157
 gapping cracks,, 140
 guadua
 drying induced shrinkage, 47
 Guadua angustifolia, 20, 35, 162
 Hamiltonian systems, 89
 homogeneous probability distribution, 127
 homogenization, 43
 integration
 verlet, 91
 Ising symmetry, Z_2 , 65
 isolated large crack, 159
 junctures, 38
 law
 Darcy's, 104
 Hooke's, 99
 Law of Young-Dupré, 51
 Matric Potential, 49
 micro-fibril angle, 36
 Moisture content, 42
 object oriented programing, 89
 order parameter, 64, 69
 parenchyma, 30, 39
 percolation
 bond, 68
 invasion, 25, 105, 109
 site, 68
 threshold, 68
 phase transition
 continuous, 64
 phase transition, 64
 discontinuous, 64
 phloem, 33
 phyllostachys
 edulis, 40, 150
 nigra, 35
 pubescens, 40, 150, 151
 vidiriglaucescens, 38
 Phyllostachys edulis, 162
 pit, 22, 33, 40, 41, 49, 52
 plane frame element, 100
 plasma membrane, 38
 plasmolysis, 54, 115
 poacea, 22
 Pore Network Method, 88
 pore network model, 103
 potential
 osmotic, 49
 pressure
 gravitational, 49
 Laplace, 49
 turgor, 54
 Protoplasm, 38
 Relative Humidity, 42
 renormalization group , 66
 Reynolds number, 22
 Saturated Vapor Pressure, 42
 scaling, 67
 shrinkage driven fractures, 22
 simulation
 event driven, 90
 snap events, 154
 sorption, 46

- isotherm, 42
- sphero-cow, 94
- sphero-poligons, 92
- spontaneously symmetry breaking, 66
- strain tensor
 - symmetric, 58
- strength, 58
 - yield, 58
- stress
 - ultimate, 58
- structural disorder
 - ammount of, 161
- surface tension, 50
- sympiasm, 34

- time
 - clock measured, 109
 - dried cells, 109
- tonoplast, 38
- tractions, 59

- universal, 67, 72
- universality, 66, 69
 - classes, 69

- vascular bundle, 30

- water
 - absorbed, 42
 - adsorbed, 42
 - bond, 157
 - free, 107, 157, 159
- Weibull distribution function, 127
- wetting
 - partial, 51
 - total, 51

- xylem, 33